



universität  
wien

# DISSERTATION

Titel der Dissertation

„The Role of the Moon on Close Encounters and Impacts  
of Near-Earth Asteroids with the Earth“

Verfasser

Mag. rer. nat. Ákos Bazsó

angestrebter akademischer Grad

Doktor der Naturwissenschaften (Dr. rer. nat.)

Wien, 2015

Studienkennzahl lt. Studienblatt: A 791 413  
Dissertationsgebiet lt. Studienblatt: Astronomie  
Betreuerin / Betreuer: ao. Univ.-Prof. i. R. Dr. Rudolf Dvorak



The Role of the Moon on  
Close Encounters and Impacts  
of Near-Earth Asteroids with the Earth

Ákos Bazsó



# Dedication

I dedicate this work to the memory of my grandparents Ferenc, Gyula, Klára, and Margit, who will never have the chance to read it.

Some of you passed away long ago, and memories become faint, but I will never forget you loving me.

We might be far apart, but you will always be with me in my heart.



# Abstract

**Aims:** This thesis examines the question how the Moon influences the dynamics of Near-Earth Asteroids. In most former studies the Earth-Moon system was treated as a single body at the system's barycenter. For certain NEAs it was found that it is essential to include the Moon as a separate body to accurately follow their motion.

Earth-orbit crossing asteroids have frequent close encounters to the Earth-Moon system and are a major source of impacts on both bodies. The main objective is to investigate qualitatively the lunar influence on these asteroids. It is quantified to which degree the Moon is able to modify the trajectories of Near-Earth Asteroids, and whether or not it can prevent potential impactors from reaching Earth.

**Methods:** Two types of numerical experiments are carried out. In the first kind of experiments long-time calculations are performed for a large subset of the real NEA population; the Lie-series and the Mercury hybrid-symplectic integrators are employed for this part. The pairs of runs span 10 Myr and compare the dynamical behaviour of NEAs when the Moon is present or not. A series of dynamical models include all main perturbing planets.

The second kind of experiments investigates asteroids in the vicinity of the Earth-Moon system in the circular restricted three-body problem. The simulations are divided into a part investigating the deflection of incoming impactors, and another part examining the lunar contribution to impacts. A large number of test particles are set-up using various random distributions for the initial conditions. Three configurations for the Earth-Moon system are tested: (i) the real system, (ii) a configuration with increased lunar mass, and (iii) one with decreased lunar distance.

**Results:** In the long-term integrations no clear lunar effect is discernible for the model pairs. The number of close encounters and impacts detected show statistical fluctuations, but no evidence for an important lunar contribution. Only  $P = 0.0052$  % of all encounters fulfill the constraints for a deflection by the Moon. As a by-product of the integrations the impact probability for the Amor, Apollo and Aten groups is determined, and mixing effects between them are studied.

From the impact experiments it turns out that the Moon is able to remove  $\sim 0.8$  % of potential impactors, and forces  $< 0.2$  % of previously non-impacting objects to hit Earth. When the lunar mass is increased and its distance decreased the deflection efficiency rises to 2.2 % and 3.7 %, respectively.



# Zusammenfassung

**Ziele:** Diese Arbeit untersucht wie der Mond die Dynamik von erdnahen Asteroiden (NEAs) beeinflusst. Die meisten früheren Studien betrachteten das Erde-Mond System als Einzelkörper im gemeinsamen Schwerpunkt. Für manche NEAs wurde jedoch festgestellt, dass es wesentlich ist den Mond als eigenständiges Objekt zu betrachten, um ihre Bahnen genau zu bestimmen.

Erdnahe Asteroiden haben häufig nahe Begegnungen mit dem Erde-Mond System und sind eine Hauptquelle von Einschlägen auf diesen Körpern. Das Hauptziel ist die qualitative Untersuchung des Mondeinflusses auf diese Asteroiden. Es wird berechnet inwieweit der Mond in der Lage ist die Bahnen von NEAs zu verändern, und ob er die Erde vor potentiellen Impaktoren schützen kann oder nicht.

**Methoden:** Zwei Arten von numerischen Experimenten werden benutzt. Erstens werden Langzeitberechnungen für einen Großteil der vorhandenen NEA Population durchgeführt; dazu werden der Lie-Reihen und Mercury hybrid-symplektische Integrator verwendet. Die Berechnungen erstrecken sich über 10 Millionen Jahre und vergleichen das dynamische Verhalten der NEAs in An-/Abwesenheit des Mondes. In einer Reihe von dynamischen Modellen werden alle wichtigen störenden Planeten berücksichtigt.

Die zweite Art von Experimenten untersucht Asteroiden in der Nähe des Erde-Mond Systems im eingeschränkten kreisförmigen Dreikörperproblem. Die Simulationen sind aufgeteilt in einen Teil zur Untersuchung der Ablenkung von ankommenden Impaktoren, und einen anderen Teil, der den lunaren Beitrag zu Einschlägen überprüft. Eine große Anzahl von Testpartikeln wird erzeugt, deren Anfangsbedingungen verschiedenen Verteilungen gehorchen. Für das Erde-Mond System werden drei Konfigurationen getestet: (i) das tatsächliche System, (ii) eine Konfiguration mit erhöhter Mondmasse, sowie (iii) eine mit reduziertem Mondabstand.

**Ergebnisse:** Die Langzeitberechnungen zeigen keinen wahrnehmbaren Effekt des Mondes auf die Modellpaare. Es treten zwar statistische Schwankungen bei der Anzahl naher Begegnungen und der Häufigkeit von Impakten auf, jedoch gibt es keine eindeutigen Hinweise auf einen Beitrag des Mondes. Nur  $P = 0.0052\%$  aller naher Begegnungen erfüllen die Vorbedingungen dafür, dass der Mond für eine Ablenkung sorgen kann. Zusätzlich werden die Impaktwahrscheinlichkeiten für Amor, Apollo und Aten Asteroiden ermittelt, und die Effekte untersucht, welche zu ihrer Durchmischung führen.

Bei den Impaktexperimenten stellt sich heraus, dass der Mond in der Lage ist  $\sim 0.8\%$

aller potentiellen Impaktoren zu beseitigen, er lenkt aber auch  $< 0.2\%$  jener Objekte zur Erde, die keine Einschläge erzeugt hätten. Mit einer erhöhten Mondmasse steigt die Ablenkungseffizienz auf  $2.2\%$ , bei halbiertem Mondentfernung ist diese sogar  $3.7\%$ .

# Contents

<b>English abstract</b>	<b>iii</b>
<b>German abstract</b>	<b>v</b>
<b>List of Figures</b>	<b>xi</b>
<b>List of Tables</b>	<b>xiii</b>
<b>1 Introduction</b>	<b>1</b>
1.1 Minor objects in the solar system . . . . .	1
1.1.1 At the very beginning . . . . .	2
1.1.2 Comets . . . . .	2
1.1.3 Asteroids . . . . .	3
1.2 Dynamics of Near-Earth Asteroids . . . . .	4
1.2.1 Orbital classes . . . . .	4
1.2.2 Number of NEOs . . . . .	6
1.2.3 Long-term dynamical evolution and origin . . . . .	7
1.3 Physics of Near-Earth Asteroids . . . . .	10
1.3.1 Taxonomic classes . . . . .	10
1.3.2 Space missions . . . . .	11
1.3.3 Masses and densities . . . . .	15
1.4 Motivation . . . . .	17
<b>2 Concepts and Definitions</b>	<b>19</b>
2.1 Coordinate systems . . . . .	19
2.1.1 Barycentric coordinates . . . . .	20
2.1.2 Heliocentric coordinates . . . . .	20
2.1.3 Discussion . . . . .	21
2.2 Solving the equations of motion . . . . .	22
2.2.1 Lie series integrator . . . . .	22
2.2.2 Mercury integrator . . . . .	24
2.3 Circular restricted three-body problem . . . . .	25
2.3.1 Equations of motion . . . . .	25
2.3.2 Manifold correction . . . . .	28

2.4	Estimating the domain of planetary influence . . . . .	30
2.4.1	Hill sphere . . . . .	31
2.4.2	Sphere of influence . . . . .	33
2.4.3	Comparison . . . . .	35
2.5	Hyperbolic trajectories . . . . .	37
2.5.1	Hyperbolic $f$ and $g$ functions . . . . .	38
2.5.2	Solving the hyperbolic Kepler equation . . . . .	39
2.6	Distribution of points on a sphere . . . . .	42
<b>3</b>	<b>Long-time dynamics of Near-Earth Asteroids</b>	<b>47</b>
3.1	Dynamical models . . . . .	47
3.1.1	General aspects . . . . .	47
3.1.2	Details of models . . . . .	49
3.1.3	Justification of models . . . . .	49
3.1.4	Summary . . . . .	50
3.2	Initial conditions . . . . .	51
3.2.1	The Planets . . . . .	51
3.2.2	The Near-Earth Asteroids . . . . .	51
3.3	Results . . . . .	57
3.3.1	Preliminary checks . . . . .	58
3.3.2	Models M2/M3 . . . . .	61
3.3.3	Models M4/M5 . . . . .	70
3.3.4	Models M6/M7 . . . . .	82
3.4	Discussion . . . . .	90
3.4.1	Recurrence of close encounters . . . . .	90
3.4.2	Statistics of close encounters . . . . .	92
3.4.3	Statistics of impacts . . . . .	97
3.4.4	Comparison of collision probabilities . . . . .	104
3.4.5	Impact velocities . . . . .	105
3.4.6	Surviving objects . . . . .	107
<b>4</b>	<b>Impact simulations</b>	<b>109</b>
4.1	Dynamical models . . . . .	109
4.1.1	Background . . . . .	109
4.1.2	General aspects . . . . .	111
4.1.3	Model 1: the Moon's role for deflecting impacts . . . . .	112
4.1.4	Model 2: the Moon's contribution to impacts . . . . .	113
4.1.5	Summary . . . . .	114
4.2	Simulation . . . . .	114
4.2.1	Numerical integrator and manifold correction . . . . .	115
4.2.2	Model 1: initial positions . . . . .	116
4.2.3	Model 1: initial velocities . . . . .	118

4.2.4	Model 2: initial conditions . . . . .	123
4.3	Results . . . . .	125
4.3.1	Model 1 . . . . .	125
4.3.2	Model 2 . . . . .	136
4.4	Discussion . . . . .	141
4.4.1	Results for Model 1 . . . . .	142
4.4.2	Results for Model 2 . . . . .	143
4.4.3	Comparison to other results . . . . .	145
4.4.4	Captured objects . . . . .	146
<b>5</b>	<b>Summary</b>	<b>149</b>
	<b>Bibliography</b>	<b>153</b>
	<b>Acknowledgements</b>	<b>165</b>
	<b>Curriculum Vitae</b>	<b>167</b>



# List of Figures

1.1	Semi-major axis distribution of asteroids . . . . .	4
1.2	Definition of NEA groups by aphelion/perihelion distance . . . . .	5
1.3	Relative frequency of NEA groups in the years 2011 and 2015 . . . . .	6
1.4	Timeline of completed spacecraft missions to asteroids . . . . .	11
2.1	Sketch of the circular restricted three-body problem . . . . .	26
2.2	Example for the effect of MFC in the two-body problem . . . . .	31
2.3	Mass-ratio dependency of Hill sphere and SOI . . . . .	36
2.4	Critical-mass ratio as function of eccentricity . . . . .	36
2.5	Comparing the sizes of planetary Hill spheres and SOI . . . . .	38
2.6	Influence of parameters $(e, H_0)$ on modified hyperbolic Kepler equation .	40
2.7	Performance of starting values for modified hyperbolic Kepler equation .	42
2.8	Projection of the vertices of a polyhedron onto the plane . . . . .	43
2.9	Snapshots from iteration process for constructing polyhedra . . . . .	45
3.1	NEA groups in semi-major axis vs eccentricity plot . . . . .	54
3.2	Histograms of $(a, e, i)$ distributions for NEA groups . . . . .	56
3.3	Tisserand parameter $T$ vs parameter $w$ for NEA groups . . . . .	58
3.4	Comparison of total energy and angular momentum conservation . . . . .	59
3.5	Time evolution of the lunar distance in different models . . . . .	61
3.6	Time evolution of $(a, q, T)$ for (1943) Anteros . . . . .	63
3.7	Time evolution of $a$ for (1862) Apollo in models M2/3 . . . . .	64
3.8	Relative variation of semi-major axis for NEA groups . . . . .	66
3.9	Orbital element distributions $(a, e, i)$ at close encounters . . . . .	68
3.10	Time evolution and cumulative membership fraction for Amors . . . . .	71
3.11	Time evolution and cumulative membership fraction for Apollos . . . . .	72
3.12	Time evolution and cumulative membership fraction for Atens . . . . .	73
3.13	Time evolution of $a$ for (2062) Aten in models M4/5 . . . . .	74
3.14	Time evolution of $a$ for (1221) Amor in models M4/5 . . . . .	76
3.15	Comparison of two methods to compute relative velocities . . . . .	77
3.16	Statistical check of relative velocity differences with Öpik's method . . . .	79
3.17	Distribution of relative velocities for Apollos in different models . . . . .	80
3.18	Minimum encounter distances for relative velocities $< 5$ km/s . . . . .	81
3.19	Exchange of NEAs between groups with time . . . . .	83
3.20	Percentage of objects remaining in the integrations versus time . . . . .	84

3.21	A test case for computing and extrapolating the relative velocity . . . . .	85
3.22	Impact velocity distributions for all NEA groups in models M6/7 . . . . .	87
3.23	Comparison of impact velocity distributions in models M6/7 . . . . .	88
3.24	Linear fit for encounter frequency vs distance . . . . .	89
3.25	Collision probabilities extrapolated for different NEA groups . . . . .	89
3.26	Recurring close encounters of NEAs within a time span of 1 year . . . . .	91
3.27	Close encounter histograms for comparison of the integrators . . . . .	95
3.28	Impacts per object histograms for comparison of the integrators . . . . .	100
3.29	Percentage of surviving objects at the end of integration time . . . . .	108
4.1	Example for the effect of MFC in the spatial CR3BP . . . . .	116
4.2	Distribution types for initial positions in Model 1 . . . . .	119
4.3	Probability density functions for velocity distributions . . . . .	122
4.4	A 3D view of initial conditions on the Earth surface . . . . .	123
4.5	Examples for successful deflections by the Moon . . . . .	126
4.6	Histogram for lunar impact velocity of equatorial particles . . . . .	128
4.7	Minimum distances to Earth and Moon for deflected particles . . . . .	129
4.8	Histograms of Earth miss distance and minimum distance to Moon for deflected particles . . . . .	130
4.9	Origin of deflected particles on the Earth surface . . . . .	132
4.10	Initial velocity distribution of deflected particles . . . . .	133
4.11	Histograms of minimum distance to Moon in Model 2 . . . . .	137
4.12	Comparison of initial parameters for impacting particles in Model 2 . . . . .	139
4.13	Comparison of models and configurations . . . . .	142
4.14	Deflection angle as function of impact parameter and velocity . . . . .	144

# List of Tables

1.1	Masses and densities for Near-Earth Asteroids . . . . .	16
2.1	Parameters to calculate the Hill and SOI radius for planets . . . . .	37
2.2	Number of vertices of a polyhedron after $i$ iterations . . . . .	44
3.1	Initial conditions for planets in the long-term simulations . . . . .	52
3.2	Absolute and relative frequency of objects from different NEA groups . .	52
3.3	Statistical summary of NEA orbital elements $e$ and $i$ . . . . .	55
3.4	NEA group membership statistics for models M2/3 . . . . .	69
3.5	Parameters for linear fit to impact frequency . . . . .	90
3.6	Percentage of objects with close encounters to Earth in all models . . . .	92
3.7	Statistics of close encounters to planets in all dynamical models . . . . .	94
3.8	Statistics of close encounters to Earth inside lunar distance . . . . .	95
3.9	Statistics of impacts on planets in all dynamical models . . . . .	99
3.10	Statistics of impacts on Earth for Lie data . . . . .	100
3.11	Impact frequency estimates for models M6 and M7 . . . . .	103
3.12	Statistical summary of NEA impact velocities . . . . .	106
4.1	Comparison of surface area in latitude zones to total area of a sphere . .	118
4.2	Statistical summary for Model 1 with standard configuration . . . . .	127
4.3	Statistical summary for Model 1 with increased lunar mass . . . . .	134
4.4	Statistical summary for Model 1 with decreased lunar distance . . . . .	135
4.5	Statistical summary for Model 2 with standard configuration . . . . .	137
4.6	Statistical summary for Model 2 with increased lunar mass . . . . .	140
4.7	Statistical summary for Model 2 with decreased lunar distance . . . . .	141



# Chapter 1

## Introduction

The Earth is target to a number of celestial bodies: asteroids, comets, dust particles, and nowadays also man-made space debris from former missions returning from orbit. Among these objects Earth-orbit crossing asteroids, termed Near-Earth Asteroids (NEAs), received special attention in recent years, since they are numerous and can represent an immanent threat to our planet (Chesley, 2006). Observations of the surfaces of terrestrial planets (e.g. Mercury, Mars) as well as the Moon made clear that they were subject to impact cratering since the very beginning of the solar system (Ivanov, 2008). This cratering is still ongoing and NEAs are a major source of the younger craters on the terrestrial planets (Brown et al., 2002).

As of January 2015 altogether 185 terrestrial impact structures are known<sup>1</sup>, but this record is not complete. There is a lack of evidence regarding impact processes in the first 2.5 billion years (Koeberl, 2006); the 2 billion year old Vredefort crater in South Africa is the oldest preserved impact structure on Earth (Kamo et al., 1996). The Earth exhibits plate tectonics so that the surface is continuously renewed. In addition, signs of past impacts are lost by erosion, or are obscured by water that covers two-thirds of the Earth surface. Thus it is very difficult to investigate in detail how NEAs affected the Earth. For this reason impact processes and rates in the distant past can be better studied by means of the lunar surface.

### 1.1 Minor objects in the solar system

The solar system is dominated by the Sun, the central star which comprises 99.9 % of the total mass. There are eight planets with very different characteristics in mass and composition. One can distinguish the four rocky terrestrial planets in the inner part from the four gas giants in the outer part of the solar system. Additionally, there are a number of so-called dwarf planets. These objects are orbiting the Sun, they are dominated by self-gravity, but have not cleared the neighbourhood of their orbits from smaller objects. All the remaining natural bodies are the minor objects, namely asteroids and comets.

---

<sup>1</sup>see Earth impact database at <http://www.passc.net/EarthImpactDatabase/>

### 1.1.1 At the very beginning

To understand where asteroids and comets come from, we need to understand the circumstances of the beginning and early phases of the solar system. Updated and revised models of planet formation provide now a consistent scenario for the origin of our solar system as well as for other extra-solar planetary systems (see reviews of Morbidelli et al., 2012; Alibert et al., 2010). These models incorporate the new findings and improved knowledge from 20 years of research in the field of extra-solar planets. The origin of asteroids and comets results naturally as a by-product of planet formation.

According to the canonical scenario a planetary system forms from an accretion disk surrounding a protostellar object. This protoplanetary disk is mainly composed of gas with some solid material (dust particles) embedded into it. These dust particles are subject to various processes, which tend to increase their sizes. The continuous growth leads from nanometer-sized particles to meter-sized objects, which grow further on different time-scales. They form planetesimals with typical sizes of the order of one kilometer, the precursors of the asteroids. Some of these planetesimals can quickly increase their mass by the process of “runaway-growth” (Kokubo and Ida, 2002; Aarseth et al., 1993), when their gravitational attraction starts to dominate their surroundings. The largest of these objects form protoplanets (also called planetary embryos) with sizes of the order of 1000 kilometers. Today the dwarf planets – (1) Ceres and (4) Vesta in the main-belt, together with the biggest trans-neptunian objects (134340) Pluto, (136108) Haumea, (136199) Eris, and (136472) Makemake – seem to be the sole remnants of that population. Eventually some of the protoplanets grow further to become the cores of the giant planets, or they collide and merge to form the terrestrial planets. The debris from this turbulent phase resulted in the population of asteroids and comets in our solar system with sizes ranging from some meters to hundreds of kilometers (Weidenschilling, 2011).

### 1.1.2 Comets

Comets are minor bodies that are rich in water and various volatile substances. When they approach the Sun the increasing temperatures cause a partial sublimation of the volatiles which results in an outgassing. They develop the typical coma and tail structure observable with telescopes or bare eyes.

Comets come from the outer parts of the solar system, from beyond the orbit of Neptune. Following the review of Rickman (2010) on cometary dynamics, it is common to divide comets into classes based on their orbital periods. Long-period comets have orbital periods  $P > 200$  years, whereas short-period comets have  $P < 200$  years. The latter type of comets can be further divided based on their Tisserand parameter ( $T$ ) values with respect to Jupiter, for the definition see equation (3.2.1) in section 3.2. The short-period comets with  $T > 2$  are called Jupiter-family comets, those with  $T < 2$  are the Halley-type comets (Levison and Duncan, 1994).

The main source regions of comets are the Trans-Neptunian Objects (TNO) from

the Edgeworth-Kuiper belt between 30 – 50 astronomical units (AU), and the Oort cloud ranging from about  $10^4 - 10^5$  AU. It is believed today that both reservoirs are of secondary origin, created by large scale chaotic processes associated with the orbital migration of the giant planets (Tsiganis et al., 2005). After the formation of the gas planets there remained a disk of icy planetesimals that was subsequently destabilised by the outward migration of Uranus and Neptune (Levison et al., 2008). These two planets and their associated orbital resonances created a scattered disk that extended outwards to several hundred AU. This scattered disk could then have supplied the Kuiper belt and the Oort cloud.

The dynamics of comets is influenced by various external forces, among them are close encounters to planets (e.g. Jupiter), tides from passing stars or the galactic disk which are important for Oort cloud comets, and the solar radiation when comets approach the Sun near perihelion (see Rickman, 2010, and references therein). Secular effects can strongly influence the perihelion distances of comets and lead to an exchange of objects between the different populations in the inner and outer solar system. Such effects would transfer objects from the Oort cloud – in a direct way, or indirectly via the scattered disk – to the Kuiper belt or vice versa.

### 1.1.3 Asteroids

Asteroids are minor objects that consist of solid material; they show a wide range of different compositions involving silicates, carbonaceous or metallic material. Most asteroids are located in a region called main asteroid belt between the orbits of Mars and Jupiter, roughly spanning from 2 – 4 AU. There also exist co-orbital asteroids (called Trojans) in a 1:1 mean-motion resonance with Mars, Jupiter, or Neptune (they were also detected for Earth and Uranus), that occupy the region around the Lagrangian equilateral equilibrium points  $L_4$  and  $L_5$ .

It has been recognised by Kirkwood that there exist certain regions in the main belt where asteroids are less abundant or completely lacking – these regions are called the Kirkwood gaps. The gaps are a consequence of mean-motion resonances (MMR) primarily with Jupiter, which occur whenever the orbital frequencies of Jupiter and an asteroid form an integer ratio. The most prominent MMRs are: 2:1 at  $\approx 3.3$  AU, 3:1 at 2.5 AU, 4:1 at 2.0 AU, and 5:2 at 2.8 AU. Figure 1.1 plots a histogram for the semi-major axis distribution<sup>2</sup>, where the mentioned MMR are clearly visible.

Hirayama has found that at some places in the main belt there is an accumulation of asteroids. These objects share similar orbital elements and belong to a so-called asteroid family, which indicates an origin from a common parent body by collisional processes (see review by Cellino and Dell’Oro, 2010).

A special class of minor objects are planetary orbit crossing objects, called Near-Earth Objects (NEOs) in case of the Earth. Any minor object that has a perihelion

---

<sup>2</sup>based on data from the Minor Planet Center <http://www.minorplanetcenter.org/>

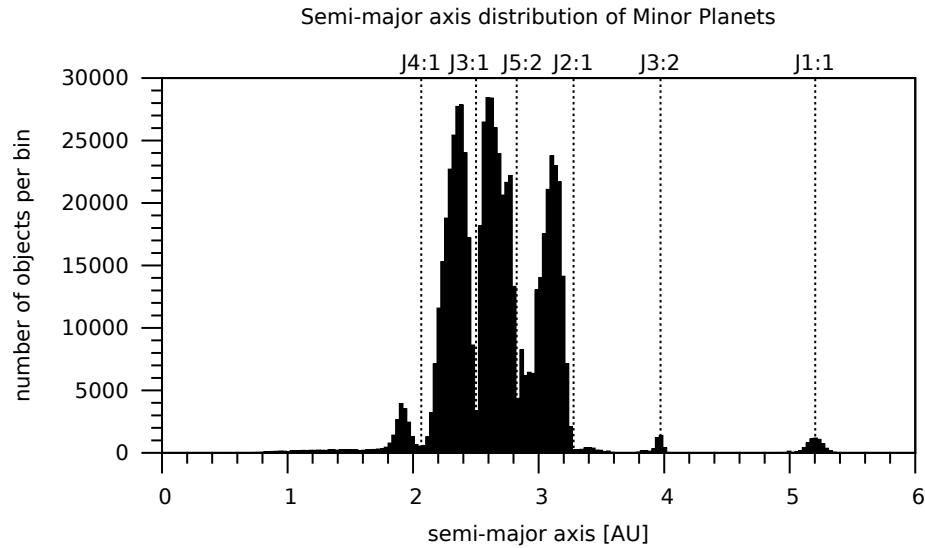


Figure 1.1: Semi-major axis distribution of asteroids from the inner solar system to beyond the orbit of Jupiter. The vertical lines indicate the major mean-motion resonances with Jupiter in the main-belt. This image is based on more than 670 000 asteroids from the Minor Planet Center database; the bin-width is  $\Delta a = 0.03$  AU.

distance  $q < 1.3$  AU is called a NEO, but sometimes the semi-major axis is constrained to  $a < 5$  AU to exclude Jupiter family comets. The population of NEOs thus consists of Near-Earth Asteroids (NEAs, of asteroidal origin) together with the Near-Earth Comets (NECs). In the following we will mainly be interested in NEAs.

## 1.2 Dynamics of Near-Earth Asteroids

In this section we review the dynamics of NEAs, in particular their relation to main-belt asteroids (MBAs) and the mechanisms that are responsible for delivering them to the near-Earth space.

### 1.2.1 Orbital classes

Shoemaker et al. (1979) divided the Earth-orbit crossing asteroids into three orbital classes based on osculating orbital elements: Amors, Apollos, and Atens. Each of these classes was named after a prototype object: (1221) Amor (= 1932 EA1), (1862) Apollo (= 1932 HA), (2062) Aten (= 1976 AA). The definition of NEA groups is based on semi-major axis ( $a$ ), aphelion ( $Q$ ) and perihelion ( $q$ ) distances:

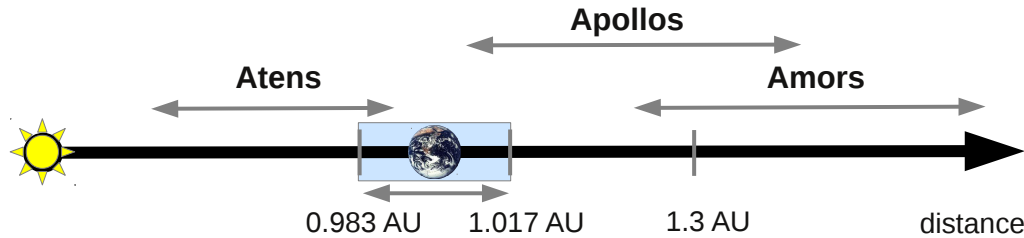


Figure 1.2: A schematic definition of the (classical) NEA groups based on aphelion and perihelion distances. The Earth moves between 0.983 and 1.017 AU at its current orbital eccentricity (indicated by the blue rectangle).

- Amors** have perihelion distances  $1.017 < q < 1.3$  AU and  $a > 1$  AU
- Apollos** have perihelion distances  $q < 1.017$  AU and  $a \geq 1$  AU
- Atens** have aphelion distances  $Q > 0.983$  AU and  $a < 1$  AU
- Atiras** have aphelion distances  $Q < 0.983$  AU and  $a < 1$  AU

Amors and Atiras are not Earth-orbit crossing asteroids in the strict sense, but they are adjacent to the other two groups and can become Earth crossers when their eccentricities increase during one secular period. Figure 1.2 provides a sketch of the one-dimensional definition of the classical NEA groups.

The above list contains the new class of Atiras that was named after object (163693) Atira (= 2003 CP20). Atiras belong to the more general class of Interior-Earth Objects (IEOs, sometimes also denoted as Inner-Earth objects) which move in orbits that are completely interior to Earth's orbit. Currently, in January 2015, there are only 14 known Atiras ( $\approx 0.1\%$  of the discovered NEA population<sup>3</sup>). However, Greenstreet et al. (2012) studied the theoretical steady-state orbital distribution of NEAs interior to Earth's orbit and estimated that IEOs (Mercury and Venus crossers) should amount to about 1.6% of the total NEA population.

The long-term behaviour of NEAs is quite complicated because of resonances and close-encounters, so the Shoemaker classification based on osculating elements turned out to be of limited use for a dynamical classification. Milani et al. (1989) proposed a new classification scheme based on the results of numerical integration of 410 planet orbit crossing asteroids for  $2 \times 10^5$  years. They divided NEAs into 6 classes: Alinda, Eros, Geographos, Kozai, Oljato, and Toro. Each class defines a different kind of dynamical behaviour, like MMR with Earth for the Toro class, or with Jupiter for the Alinda class.

<sup>3</sup>see Near Earth Object Program discovery statistics at <http://neo.jpl.nasa.gov/stats/>

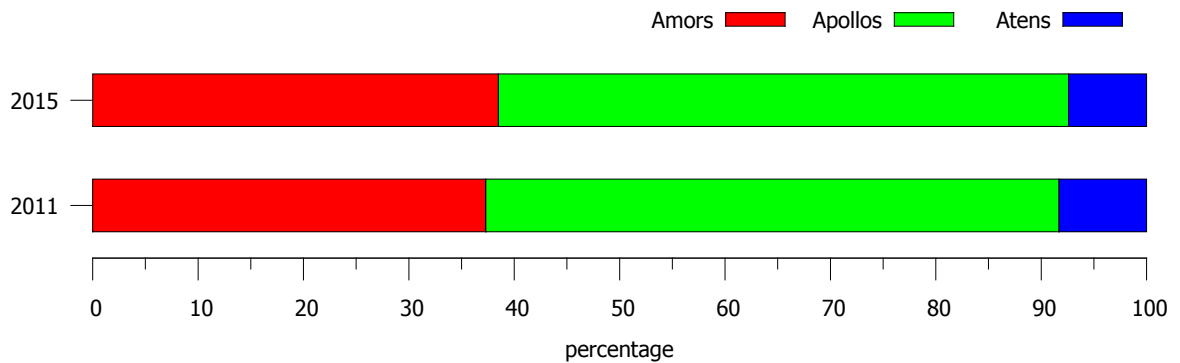


Figure 1.3: The relative frequency of NEA groups in the years 2015 (upper bar) and 2011 (lower bar). Colours distinguish different groups: Amors (red), Apollos (green), Atens (blue).

Nevertheless, on still longer time-scales also these classes tend to blur and mix, which is inevitable because of the inherently chaotic nature of the NEAs.

To overcome the difficulties posed by a rigid classification Freistetter (2009) proposed a new approach based on fuzzy logic. The fuzzy classes for NEAs allow one object to be a member of different classes at the same time, where the degree of membership to a specific class is quantified by a real number  $\alpha \in [0; 1]$ . One possible fuzzy classification would be based on the number of close encounters of NEAs to each of the terrestrial planets Venus, Earth, and Mars.

## 1.2.2 Number of NEOs

Figure 1.3 summarises the percentage of asteroids that belong to one of the three classical NEA groups. In the year 2011, when the data for this work was gathered, there were about 8000 NEAs, since then their number has increased by 50 % to about 12 000 NEAs at the end of the year 2014. Table 3.2 in section 3.2 contains the absolute number of objects for reference. Note that the currently discovered Atiras would not be visible in that figure as they make up for only  $\sim 0.1$  % of the total population.

Shoemaker et al. (1979) reported on the number of NEAs with absolute visual magnitude of  $H_V \leq 18$  mag. These are asteroids with diameters larger than about 1 km, apart from inherent uncertainties in the conversion of absolute magnitude to diameter (which depends on the albedo). The estimates were based on the Palomar planet-crossing asteroid survey (Helin and Shoemaker, 1979) and gave 100 Atens, 700 Apollos, and 500 (Earth-crossing) Amors for a total of 1300 kilometer-sized NEAs; the ratios of these estimates still describe very well the current numbers (see table 3.2).

The population size of Earth-crossing NEAs was re-examined by Rabinowitz et al.

(1994). They used a Monte-Carlo model that took into account the orbital evolution of asteroids, observational biases, and some physical properties (such as the size distribution and albedos). The resulting overall population was estimated to be 1500 objects with diameters  $d \geq 1$  km; currently there are about 860 discovered NEAs exceeding this limit.

Another model for the orbital element and magnitude distribution of NEOs was created by Bottke et al. (2002). Their model incorporated NEOs originating from source regions in the main-belt and from short-period comets. They estimated  $960 \pm 120$  NEOs to  $H < 18$  mag, of which  $\sim 94$  % are NEAs (900) and  $\sim 6$  % (extinct) Near-Earth comets.

More recently Mainzer et al. (2011) estimated a number of  $981 \pm 19$  NEAs (*not* NEOs) larger than 1 km in diameter based on observational data from the wide-field infrared survey explorer spacecraft (NEOWISE).

The amount of cometary contribution to the NEO population is more debated, and theoretical estimates range from 5 – 15 % (see Lupishko et al., 2007, section 6). The large-scale observational surveys<sup>4</sup> have detected 15 NECs so far, this is merely  $\sim 0.1$  % of the total NEO population.

### 1.2.3 Long-term dynamical evolution and origin

In the reviews of Novaković (2013) and Morbidelli et al. (2002) the current standard model for the origin and evolution of NEAs is outlined, which has emerged in the middle of the 1990s and has superseded the classical model. The following paragraphs summarise the transition from the classical model to the new one.

The importance of mean-motion resonances (MMR) and secular resonances (SR) in the main-belt had already been recognized in the 1970s. Shoemaker et al. (1979) explicitly mentioned regions in the main-belt adjacent to the 3:1 and 5:2 MMR with Jupiter along with the  $\nu_5$  and  $\nu_6$  SR with Jupiter and Saturn, respectively, to be the principal sources of NEAs. Collisional processes (fragmentation or catastrophic disintegration) lead to the “creation” of new asteroids in the main-belt, some of which would be transported to the near-Earth region by the resonances mentioned before.

When Wetherill (1979) discussed the steady-state population of Amors and Apollos he had to assume a dominant cometary contribution (from Encke-type comets), since the rate of resupplied asteroids from the main-belt (1.5 objects per million years) would seem too low to support the required rate of 15 objects per million years. However, in the same work Wetherill also reported on the amplitude of forced eccentricity oscillations close to the  $\nu_6$  resonance. These forced amplitudes can lead to an increase of the eccentricity of asteroids to values large enough to become Mars-orbit or even Earth-orbit crossers. Then a subsequent close encounter with a terrestrial planet can change the asteroid’s semi-major axis and displace it from the main-belt to the NEA region.

A similar effect was found by Wisdom (1982) for the 3:1 MMR with Jupiter. He could

---

<sup>4</sup>see list at <http://neo.jpl.nasa.gov/programs/>

recover the formation of the Kirkwood gap for this resonance on a time-scale of  $10^6$  years by means of a mapping technique for the dynamical behaviour of test particles. Even asteroids with low initial eccentricity can obtain values of  $e > 0.3$  when evolving inside this resonance. The 3:1 MMR with Jupiter is important for its connection to the delivery of achondrite meteorites that have been shown to be related to (4) Vesta (Binzel and Xu, 1993; McSween et al., 2011).

Following these results Froeschle and Scholl (1989) reviewed the linear secular resonances  $\nu_5$ ,  $\nu_6$ , and  $\nu_{16}$  and found indications of chaotic motion due to the overlapping of these resonances with MMR or other SR. Thus all of these resonances can potentially supply asteroids from the main-belt to the NEA region via eccentricity pumping on a rather short time-scale of  $10^5 - 10^6$  years.

Progress was not only made on the theoretical side, but also through direct numerical integrations of the orbital evolution of NEAs. Hahn and Lagerkvist (1988) investigated the orbits of 26 NEAs over a timespan of  $10^5$  years including perturbations from all planets except for Mercury. That work was a precursor to the Spaceguard project of Milani et al. (1989), who investigated 410 NEAs over  $2 \times 10^5$  years. These studies helped to better understand the long-term dynamical evolution of NEAs and to identify important mechanisms such as protection from close encounters by MMR (Toro class) and SR (Kozai class).

The basic perturbing mechanisms – close encounters, resonances and secular perturbations – were later thoroughly discussed in Michel et al. (1996) for different dynamical models. They demonstrated that the simplified assumption of a random walk in  $(a, e, i)$  space along a constant value of the Tisserand parameter (for non-resonant objects) breaks down in a realistic dynamical model including at least Earth, Jupiter, and Saturn as the major perturbers. This was a central assumption in the models of Wetherill – as summarised in Greenberg and Nolan (1993) – who worked out a number of evolutionary paths for main-belt asteroids to become NEAs on different time-scales (from  $10^5 - 10^8$  years).

Farinella et al. (1994) found that also NEAs can become sun-grazers or hit the Sun; before this was only known for comets (Bailey et al., 1992). In their integrations 19 out of 47 NEAs, which were initially located near to the  $\nu_6$  resonance and various low-order MMR, collided with the Sun within the integration time of  $2 \times 10^6$  years. These results showed that the eccentricities of NEAs could in principle increase without bound in rather short time, which in turn places an upper limit on the dynamical lifetime of these objects.

As a consequence Gladman et al. (1997) studied the dynamical lifetimes of several hundred main-belt asteroids from different families located in resonances. They observed a completely different behaviour for the 3:1 MMR with Jupiter and the  $\nu_6$  SR in the inner main-belt when compared to the 5:2, 2:1 MMR and others in the middle to outer main-belt. In the former cases the median half-lives for the resonant objects are of the order of 2 million years and most of them ( $\geq 70\%$ ) impact the Sun, whereas for the 5:2 MMR the half-life is of the order of only 0.5 million years and objects are preferably scattered

by Jupiter outwards beyond the orbit of Saturn. Gladman et al. (2000) extended their study to NEAs and checked the final states after an integration time of 60 Myrs. They found a NEA median life-time of 10 Myr, and that about 50 % of them impact the Sun,  $\leq 15$  % impact the terrestrial planets, and another 10 % are ejected from the solar system.

These results indicate that a large fraction of NEAs would originate from the main-belt region  $2 \leq a \leq 2.5$  AU (between the  $\nu_6$  and J3:1 MMR). However, the rather short dynamical lifetimes pose a difficulty to sustain the observed number of NEAs with sizes of 1 km or above.

Migliorini et al. (1998) and Michel et al. (2000) emphasized that there are far more multi-kilometer size Mars-orbit crossing asteroids than Earth-orbit crossing NEAs of comparable size (by about a factor of 35). They defined four groups of potential Mars crossers ( $q < 1.78$  AU), which are themselves supplied by main-belt regions, e.g. the Hungaria and Phocaea family. Asteroids become Mars crossers because they are driven by MMR with Mars, some MMR with Jupiter, and a number of weaker three-body resonances with either Jupiter/Saturn or Mars/Jupiter.

It was shown by Murray et al. (1998) and Nesvorný and Morbidelli (1998b) that three-body resonances are dense in the main-belt regions considered, and can lead to a slow diffusion of the eccentricity to Mars-orbit crossing values. Mars crossers then evolve into Earth crossing asteroids on timescales of 20 – 60 Myr (Migliorini et al., 1998). Michel et al. (2000) estimated that 50 % of the large Earth-orbit crossing asteroids evolved from Mars crossers.

Galiazzo et al. (2013a) investigated the evolution of objects from the Hungaria group in more detail. They found that about 6 % of the investigated asteroids evolved into Mars crossers within 100 Myr, among them 25 – 50 % will become Earth and Venus crossers on timescales of 60 Myr. This rather slow evolution to the NEA region is caused by the inclinations of Hungarias ( $12 < i < 31$  degrees) that make close encounters to Mars unlikely. Hungarias can reach Earth-orbit crossing semi-major axes by decreasing their inclinations and being extracted by close encounter with Mars, or by finding another “escape route”, e.g. the J4:1 MMR or the  $\nu_{16}$  SR with the nodal precession rate of Saturn.

The Yarkovsky effect (Hartmann et al., 1999; Vokrouhlický et al., 2000), a non-gravitational effect from the absorption of sun-light and its re-emission at infrared wavelengths, was discussed to be another important ingredient for the placement of MBAs into resonances. Morbidelli et al. (2002) even argue that the Yarkovsky effect should be more efficient than collisional processes for delivering asteroids to resonances.

Based on all these constraints Bottke et al. (2002) computed the contribution of various sources to the NEO population, they also included Jupiter-family comets but not the long-period comets. The model results showed that  $\sim 60$  % of NEOs originate in the inner main-belt (up to the J3:1 MMR at  $a = 2.5$  AU), another  $\sim 24$  % from the middle main-belt (between J3:1 and J5:2 MMR,  $2.5 < a < 2.8$  AU), while the other sources share the rest.

## 1.3 Physics of Near-Earth Asteroids

This section summarises a subset of the known physical parameters of asteroids, with a focus on the spectral classification, their masses and densities. A limited number of asteroids could be intensely studied by space missions, for these objects a review is compiled.

### 1.3.1 Taxonomic classes

Astronomical observations of asteroids rely on the reflected sunlight and emitted (infrared) radiation from their surfaces. The method of photometry measures the intensity (amplitude) of the lightcurve with time. Spectrometry investigates the (absorption) spectrum and allows to probe the surface properties and mineralogical composition.

Chapman (1979) summarised the observational progress in the 1970s. He pointed out that asteroids were readily distinguishable from one another based on photometry using the Johnson UBV filters and albedo data. These observations resulted in establishing three categories: C-type, S-type, and M-type; additionally also an U-type for unclassifiable objects was defined. The C-type objects have low albedo ( $< 0.07$ ) and flat spectra; they are related to carbonaceous chondrite meteorites. S-type asteroids have moderate albedos ( $< 0.24$ ) and spectra with a positive slope to the red, spectral absorption bands indicate olivine and pyroxene. S-types are related to stony-iron meteorites (ordinary chondrites). M-types were attributed to enstatite chondrites or nickel-iron meteorites.

Tholen introduced a taxonomy for asteroids based on albedo and spectral measurements (using eight data points from  $0.31 - 1.06 \mu\text{m}$ ) for almost 1000 asteroids in the 1980s (Tholen, 1989). There were three major groups: C-group, S-group, and X-group, where each of them contained several subtypes. A total of 14 types were defined, but most asteroids were assigned to the C-type (in the C-group), S-type (or group), or M-type (in the X-group). Some peculiar asteroids (like Vesta) had a type of their own, independent from any group.

Later the Tholen taxonomy was enhanced by Bus and Binzel (2002) by including higher resolution spectra (48 points) for nearly 1500 asteroids in the wavelength range  $0.44 - 0.92 \mu\text{m}$ . They kept the C-, S- and X-groups as broad categories, but introduced 26 types which partly differed from the former meaning. The C-group still contains carbonaceous objects, the S-group objects are made of silicates, while the X-group comprises metallic asteroids. This scheme introduced combinations of letters (like CG) for new transition types that combined properties from both previous Tholen types.

Another extension of the taxonomy was presented by DeMeo et al. (2009). They used the spectral range  $0.45 - 2.45 \mu\text{m}$  (with 40 data points), which includes the near-infrared for more useful absorption features. The 24 types are mostly carried on from the Bus & Binzel scheme, with some minor adjustments.

Reddy et al. (2011) presented four examples for the analysis of the mineralogical composition of NEAs. They used a ground-based near-IR spectrograph ( $0.7 - 2.5 \mu\text{m}$ )

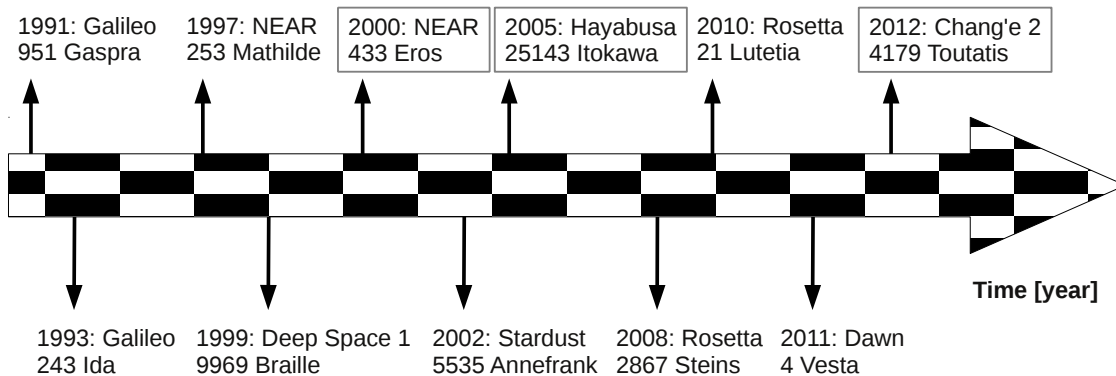


Figure 1.4: Chronological timeline of spacecraft missions to asteroids; a grey box marks missions to NEAs. Each entry gives the year of the mission, the name of the spacecraft, and the catalogue number and name of the asteroid.

to determine the position and width (area) of absorption bands at  $1 \mu\text{m}$  and  $2 \mu\text{m}$  that are indicative for the presence of olivine and pyroxene. The ratio of the absorption band-areas allows to determine the relative fraction of olivine to (ortho)pyroxene.

### 1.3.2 Space missions

The knowledge about the physical properties of asteroids in general – and of NEAs in particular – has been extended by spacecraft that have investigated some objects in detail. Some missions were only fly-bys of short duration, but others were devoted to a long-term survey where the spacecraft would orbit the asteroid, land on it or even return a sample from its surface. These missions revealed a large diversity of surface features, and allowed to investigate a number of physical parameters (mass, density, thermal conductivity, etc.) and the mineralogical composition.

Up to the begin of the year 2015 eight space missions were conducted which made in-situ measurements of eleven asteroids. In the course of 2015 the Dawn mission will arrive to Ceres and investigate it as the twelfth asteroid. Figure 1.4 gives a chronological overview of all those space missions; the three missions to NEAs are emphasized by a box.

The following paragraphs give a summary of all these missions, most of the data are taken from the extensive reviews of Bertini (2013) and Shevchenko and Mohamed (2005), for further references see those publications.

### **(951) Gaspra**

The Galileo spacecraft's main goal was to orbit Jupiter and to study the planet as well as its moons. On the way to its destination Galileo had to fly through the main-belt and was guided to pass two asteroids.

The fly-by to Gaspra on 29 October 1991 was the first time that a spacecraft had visited an asteroid. The minimum fly-by distance was 1600 km; from the images taken an irregular shape for Gaspra was determined with dimensions of  $18.2 \times 10.5 \times 8.8 \text{ km}^3$ . The surface exhibited many impact craters, the (visual geometric) albedo is 0.23. From spectral absorption bands at  $1 \mu\text{m}$  and  $2 \mu\text{m}$  the surface composition was inferred to be 90 % olivine and 10 % orthopyroxene. Gaspra belongs to the S-type taxonomic class.

### **(243) Ida**

Galileo's second target was the S-type asteroid Ida, first observed in 1884 by J. Palisa in Vienna. The fly-by took place on 28 August 1993 with a minimum distance of 2400 km. Ida also turned out to be of irregular shape with  $59.8 \times 25.4 \times 18.6 \text{ km}^3$ . The albedo is 0.21 which is consistent with the value found for Gaspra; the surface composition is 65 % olivine plus 35 % orthopyroxene.

The big surprise was that Ida has a small moon named Dactyl of about 1.4 km diameter. This allowed to determine the mass of Ida ( $4.2 \pm 0.6 \times 10^{16} \text{ kg}$ ) and its density ( $2.6 \pm 0.5 \text{ g/cm}^3$ ).

### **(253) Mathilde**

The second space mission to visit asteroids was the Near-Earth Asteroid Rendezvous (NEAR) targeted to investigate for the first time a NEA. Before the main target (433) Eros was reached, the spacecraft had a fly-by to the main-belt asteroid Mathilde. This asteroid was also detected by J. Palisa in 1885 at the Vienna observatory (Schmadel, 2012).

The fly-by happened on 27 June 1997, the minimum distance was about 1200 km. Mathilde is a C-type asteroid with very low albedo of 0.047, and dimensions of  $66 \times 48 \times 44 \text{ km}^3$ . The mass ( $1.03 \times 10^{17} \text{ kg}$ ) and density ( $1.3 \pm 0.2 \text{ g/cm}^3$ ) of the asteroid could be determined. Several large craters were found; the fact that Mathilde survived those cratering events and the low bulk density led to speculations about a rubble-pile internal structure.

### **(9969) Braille**

On 28 July 1999 the Deep Space 1 mission passed the Mars orbit crossing main-belt asteroid Braille in a distance of 28 km. The spacecraft later also encountered comet 19P/Borrelly.

Braille is a rather small object with an estimated size of  $2 \times 1 \times 1 \text{ km}^3$ . From the near-IR spectrum a composition of pyroxene/olivine was deduced, the albedo was measured to be 0.34. The spectral type is given as Q-type, which is intermediate between S- and V-type, the spectrum indicated similarities to (4) Vesta.

### **(433) Eros**

The NEAR spacecraft had a first fly-by to Eros in December 1998, on 14 February 2000 it entered into an orbit about Eros, and finally on 12 February 2001 the spacecraft successfully landed on the asteroid. This was the first orbiter and lander mission, and the first one to a NEA.

Eros has dimensions of  $34.4 \times 11.2 \times 11.2 \text{ km}^3$  which make it the second largest NEA after (1036) Ganymed, both being Amor class NEAs. It was discovered in 1898 and was the first NEA ever known.

The complete surface was mapped, the mass ( $6.69 \times 10^{15} \text{ kg}$ ) and mean density ( $2.67 \pm 0.03 \text{ g/cm}^3$ ) could be reliably determined due to the long mission duration; the albedo is 0.25.

### **(5535) Annefrank**

The Stardust mission had the aim to investigate comet 81P/Wild 2, but prior to that it had a fly-by to the main-belt asteroid Annefrank. The encounter took place on 2 November 2002 in a distance of 3100 km. Although only part of the surface could be observed the size of the asteroid was fitted as  $3.3 \times 2.5 \times 1.7 \text{ km}^3$ . An albedo of 0.24 indicates that Annefrank is an S-type, but its size could be a hint for an origin as a collisional fragment.

### **(25143) Itokawa**

The Apollo class NEA Itokawa was the target for the orbiter and sample return mission Hayabusa of the Japanese space agency. From September until December 2005 the spacecraft orbited the asteroid, and two touchdowns were attempted for collecting surface material. In 2010 the samples were returned to Earth and the  $\mu\text{m}$ -sized grains could be analysed in laboratories.

Itokawa is an S-type asteroid, with size of  $0.535 \times 0.294 \times 0.209 \text{ km}^3$ . The density is  $1.95 \pm 0.14 \text{ g/cm}^3$ , which is well below the value for LL ordinary chondrites ( $3.2 \text{ g/cm}^3$ ) that are analogous to the samples returned. The shape of this NEA was interpreted as a contact binary, made of at least two larger fragments and having a rubble-pile structure.

### **(2867) Šteins**

The Rosetta spacecraft was dedicated to fly to and observe comet 67P/Churyumov-Gerasimenko. During its ten years of flight Rosetta had also two fly-bys to asteroids,

one of them was the main-belt asteroid Šteins.

The encounter took place on 5 September 2008, the minimum distance was 800 km. Šteins has an unusual shape with equatorial radius of 3.1 km and polar radius of 2.2 km. Thanks to the many instruments on-board of Rosetta the spectrum could be measured in a wide range of wavelengths, spanning from ultraviolet to near infrared. Previously the asteroid had been determined to be an E-type, a type that is common among the Hungaria family. As for most E-types the visual albedo of 0.4 is rather high, however, in the ultraviolet at  $\lambda < 200$  nm the albedo was as low as 0.04.

### **(21) Lutetia**

Rosetta's second asteroid fly-by was on 10 July 2010 to the main-belt asteroid Lutetia, which took the spacecraft up to a minimum distance of about 3100 km.

Lutetia has dimensions of  $121 \times 101 \times 75$  km<sup>3</sup>; its mass was determined to be  $1.70 \pm 0.02 \times 10^{18}$  kg, which results in a density of  $3.4 \pm 0.3$  g/cm<sup>3</sup>. Observations in the wavelength range from 0.24 – 3.4  $\mu$ m gave a mean visual albedo of 0.19, but did not indicate notable absorption features, thus no evidence was found for olivine to be present in the surface layer. The composition is believed to be a mixture of enstatite chondrite and carbonaceous chondrite, although the density is larger than for chondrite meteorites, so probably Lutetia contains some metal rich regions in its interior. Parts of the surface were dated to be up to 3.6 Gyrs old from crater counting.

### **(4) Vesta**

The second most massive main-belt object Vesta was the first target of the Dawn spacecraft. It arrived at Vesta on 16 July 2011 and orbited the asteroid until 4 September 2012, when Dawn left orbit and headed for Ceres.

Vesta is nearly spherical with a mean diameter of 530 km, but the images revealed two large impact structures near the southern pole which distort its shape. Those two impact basins, the  $\sim 1$  Gyr old Rheasilvia and the underlying  $\sim 2$  Gyr old Veneneia, are the probable source for the Vesta family, V-type asteroids, and the HED meteorites (McSween et al., 2011).

From the Dawn data a density of 3.46 g/cm<sup>3</sup> was determined, and the mass is estimated as  $2.67 \pm 0.02 \times 10^{20}$  kg, equivalent to  $1.34 \pm 0.01 \times 10^{-10}$  solar masses (Baer and Chesley, 2008). Vesta is large enough to be differentiated; the measured  $J_2$  moment of the gravitational field indicates a dense (nickel-iron) core of 220 km diameter.

### **(4179) Toutatis**

The Chinese Chang'e 2 spacecraft had a very close fly-by to within 1 km to this Apollo class NEA on 13 December 2012 (Huang et al., 2013). Toutatis is an S-type asteroid, but with a moderate albedo of 0.13. On-board visual and ground-based radar observations

showed that Toutatis consists of at least two parts, which is interpreted as a contact binary configuration. The asteroid's length and width are 4.8 and 2.0 km.

### 1.3.3 Masses and densities

Asteroid masses and (bulk) densities are among the most important physical parameters that need to be known. Aside from the examples mentioned above the masses have been determined for a limited number of asteroids.

Hilton (2002) reviewed the advantages of various techniques for mass determinations. The classical astrometric mass determination method measures an asteroid's gravitational perturbation on another test object, which can be a smaller asteroid, a satellite's orbit, or a spacecraft. This method is limited by the rather small masses of even the largest asteroids – being of the order of  $10^{-10}$  solar masses – and the long observation time intervals needed (often some decades). Modern methods include radar time-delay measurements, which are also used in connection with the perturbations of spacecraft trajectories.

The tables in Hilton (2002) include the published masses for 24 asteroids having masses between  $5 \times 10^{-10}$  solar masses for (1) Ceres down to  $5 \times 10^{-21}$  solar masses for 2000 UG11 (an Apollo group NEA). He also listed the densities for 16 asteroids, in the range  $1.2 - 3.5 \text{ g/cm}^3$ , but these values depend strongly on an accurate shape model to give the correct volume. In total the masses and densities for 4 NEAs are given: (433) Eros, 1999 KW4, 2000 DP107, and 2000 UG11.

In Lupishko et al. (2007) the bulk densities for 8 NEAs were reported. The densities for (433) Eros and (25143) Itokawa are well determined from spacecraft observations; for the other NEAs values of  $1.1 - 3.3 \text{ g/cm}^3$  are given with rather large error margins like for (2100) Ra-Shalom (see table 1.1).

Baer and Chesley (2008) used an iterative least-squares process to determine the masses of large main-belt asteroids from a sample of 300 objects. They found reliable mass and density estimates for 21 objects, in total they summarised the masses for 38 asteroids of which 5 are NEAs. The relative errors for the masses are on average  $\geq 10 \%$ , except for (1) Ceres and (4) Vesta where the errors are much lower.

They also collected empirical values for the bulk densities of taxonomic classes. The C-class density is assumed to be between  $1.3 - 2.1 \text{ g/cm}^3$ , for the S-class it is  $2.4 - 2.8 \text{ g/cm}^3$ , while the M-class has  $4.0 - 5.3 \text{ g/cm}^3$ . However, they demonstrated that there is a correlation between the size of an asteroid and its density, the latter can be expressed as a linear function of the mean radius.

Carry (2012) reviewed the published masses and densities for 287 minor objects (NEAs, MBAs, TNOs and comets) and carefully selected the most reliable estimates. Besides that he also computed the average density for the taxonomic classes. He included a section on the measured bulk density of meteorites for comparison to that of asteroids:

asteroid	mass [ $M_{\odot}$ ]	density [ $\text{g cm}^{-3}$ ]
(433) Eros	$(3.36 \pm 0.01) \times 10^{-15}$	$2.67 \pm 0.03$
(2100) Ra-Shalom	—	1.1 – 3.3
(6489) Golevka	—	$2.7^{+0.4}_{-0.6}$
(25143) Itokawa	$(1.76 \pm 0.05) \times 10^{-20}$	$1.95 \pm 0.14$
1996 FG3	$(2.1 \pm 0.7) \times 10^{-18}$	$1.4 \pm 0.3$
1999 KW4	$(1.1 \pm 0.2) \times 10^{-18}$	$1.97 \pm 0.24$ (primary)
	—	$2.81^{+0.82}_{-0.63}$ (secondary)
2000 DP107	$(2.3 \pm 0.4) \times 10^{-19}$	$1.7 \pm 1.1$
2000 UG11	$(4.7 \pm 0.8) \times 10^{-21}$	$1.5^{+0.6}_{-1.3}$
2002 CE26	$(9.8 \pm 1.3) \times 10^{-18}$	$0.9^{+0.5}_{-0.4}$

Table 1.1: Masses (in units of the solar mass) and densities for Near-Earth Asteroids. For Golevka and Ra-Shalom the densities were derived from radar data (Lupishko et al., 2007).

- ordinary chondrites have an average density of  $3.5 \text{ g/cm}^3$ ,
- carbonaceous chondrite densities range from  $1.6 \text{ g/cm}^3$  (CI) to  $3.1 \text{ g/cm}^3$  (CR),
- enstatites have  $3.5 \text{ g/cm}^3$ ,
- achondrites (HED type) have  $3.3 \text{ g/cm}^3$ ,
- and stony-iron meteorites have densities of  $\geq 4.2 \text{ g/cm}^3$ .

The effective density of asteroids will generally be lower than that of meteorites; their density will be determined by their porosity and whether or not they are monolithic or rubble-piles.

Table 1.1 collects all available data on masses and densities of Near-Earth Asteroids from Hilton (2002); Lupishko et al. (2007); Baer and Chesley (2008); Carry (2012). No masses are available for Ra-Shalom, Golevka and 1996 FG3 in the JPL small-body database<sup>5</sup>, but obviously some estimate must exist to calculate the densities. The mass of 1996 FG3 is taken from Carry (2012). The NEAs 1999 KW4, 2000 DP107 and 2002 CE6 are binary asteroids; for the first and third object the primary’s mass is given, whereas the mass for 2000 DP107 is the total mass of the system.

<sup>5</sup>see online tool at <http://ssd.jpl.nasa.gov/sbdb.cgi>

## 1.4 Motivation

A unique feature of the Earth, as opposed to the other terrestrial planets Mercury, Venus and Mars, is that it owns a companion—the Moon—of considerable size and mass, that potentially can alter the orbits of approaching bodies.

The majority of dynamical investigations neglect the Earth’s moon, or Earth and Moon are replaced by their combined center of mass. There are a few exceptions, though, that point out what a crucial role the presence of the Moon can have.

### Outline of current state

Yeomans and Chodas (1994) performed a numerical survey to predict which near-Earth objects (both asteroids and comets) would approach the Earth in the near future, and how many of them can become a threat. In their work they used the best available ephemerides, including radar astrometry data. Although the authors employed a sophisticated dynamical model by using the general relativistic equations of motion, including perturbations from all planets, Yeomans and Chodas (1994) stated:

For objects making close Earth encounters, the Earth and Moon perturbations must be treated separately. In extreme cases, a satisfactory orbit cannot be computed without separating the Earth and Moon perturbations. [...]

The orbital solution for 1991 VG was not successful until we abandoned the approximation of having the combined Earth and lunar masses located at the Earth-Moon barycenter.

It must be stressed, however, that this survey searched for close encounters in the next 200 years. On still longer timescales there are other (non-gravitational) effects that will become important.

Kankiewicz (2002) analysed the motion of about 1000 NEAs for up to 1000 years in two dynamical models including all perturbing planets. In the first model the Earth-Moon barycenter was included as a single body, while the second model handled Earth and Moon as separate objects. He compared the difference in the final positions of the asteroids from both models. The key result was that including the Moon into the models resulted in a significant change of the final positions. This was demonstrated for seven selected objects that showed the largest difference; all of them had close encounters to the Earth-Moon system with low to moderate relative velocity ( $v_{\text{rel}} \leq 13$  km/s).

The study of Domingos et al. (2004) is of special importance for the current work. They studied the Moon’s contribution to collisions with the Earth. For hypothetical NEAs with relative velocities below 5 km/s in a planar four-body problem they found that the Moon is able to deflect incoming impactors in 2.6 % of cases, but also induces additional collisions in 0.6 % of cases that otherwise would not have happened without the Moon.

## **Objectives for this work**

In this thesis my goal is to investigate qualitatively and quantitatively the influence of the Moon on close encounters of Near-Earth Asteroids to the Earth, and how the impact frequency depends on the lunar parameters. Here are the key questions that will serve as a guidance:

1. How does the Moon influence the trajectories of real Near-Earth Asteroids in the long-term?
2. Does the presence of the Moon increase or decrease the number of impacts on Earth?
3. Would changes in the lunar (orbital or physical) parameters affect the impact rate?

The first question will be addressed in chapter 3, where the lunar gravitational effect on NEAs is investigated in different dynamical models. For answering the second question we have to take into consideration results that are spread over both chapters 3 & 4. In chapter 4 I present the impact simulations that give insight to the third question.

# Chapter 2

## Concepts and Definitions

In this chapter I will introduce the necessary definitions on which the following chapters rely, and will present the concepts applied in this work.

The coordinate systems used in this work are introduced in section 2.1, and the equations of motion are formulated for barycentric and heliocentric coordinates.

The equations of motion of the  $N$ -body problem have to be solved by numerical integration methods, the two methods applied here (Lie series and symplectic integrator) are detailed in section 2.2.

Section 2.3 introduces the Circular Restricted Three-body problem as a simplified dynamical model; additionally it is shown how the accuracy for its numerical solution can be increased by the method of manifold correction.

In section 2.4 two concepts are presented, that allow to estimate the region of dominating gravitational influence of a planet that is orbiting a much more massive star. The “Hill sphere” and “Sphere of Influence” are important when motion near a planet (or a moon) is considered.

The basics of hyperbolic motion in the two-body problem are summarized in section 2.5, including the hyperbolic  $f$  and  $g$  functions and the related hyperbolic Kepler equation.

Another important issue is the generation of initial conditions with certain properties for the simulation of virtual impactors. Section 2.6 presents a method for uniformly distributing points on the surface of a sphere.

### 2.1 Coordinate systems

A number of different coordinate systems are in use in celestial mechanics, e.g. barycentric, heliocentric, Jacobian, and Poincaré coordinates (also known as democratic heliocentric) (Beaugé et al., 2007; Milani and Gronchi, 2010). These coordinate systems are used to express the accelerations (forces) arising from the Newtonian gravitational interaction of several point-masses. Depending on the type of application each of those systems has certain advantages. Here, the two most common systems are presented, the barycentric coordinate system and the heliocentric coordinate system.

By Newton's law the gravitational force is a radial-symmetric central-force of the type

$$\mathbf{F} = f(r) \mathbf{e}_r$$

with some scalar dependence  $f(r)$  only on the distance from the attracting mass, the direction given by the radial unit vector  $\mathbf{e}_r$ . In the classical Newtonian case for point masses  $m_1, m_2$  the function is

$$f(r) = \frac{G m_1 m_2}{r^2}.$$

### 2.1.1 Barycentric coordinates

When describing the motion of  $N$  point masses the natural choice would be to use an inertial system, as for every inertial system the linear momentum is conserved. As a consequence the barycenter (center of mass) of the  $N$  point masses is moving at most with a constant velocity vector relative to the chosen reference system. A simple formulation of the equations of motion is obtained by choosing the barycenter as the origin of the reference system.

Let the position vectors of the  $N$  point masses  $m_n$  be  $\mathbf{r}_n$  ( $n = 1, \dots, N$ ) in any chosen inertial system. Then the barycenter is

$$\mathbf{b}_0 = \frac{1}{M} \sum_{n=1}^N m_n \mathbf{r}_n, \quad M = \sum_{n=1}^N m_n,$$

with  $M$  being the total mass of the system.

We introduce barycentric positions (velocities) by  $\mathbf{b}_i = \mathbf{r}_i - \mathbf{b}_0$  ( $\dot{\mathbf{b}}_i = \dot{\mathbf{r}}_i - \dot{\mathbf{b}}_0$ ). The equations of motion for object  $i$  in barycentric coordinates are

$$\ddot{\mathbf{b}}_i = G \sum_{\substack{n=1 \\ n \neq i}}^N m_n \frac{\mathbf{b}_n - \mathbf{b}_i}{\|\mathbf{b}_n - \mathbf{b}_i\|^3} \quad (2.1.1)$$

where  $G$  is the universal gravitational constant.

The barycentric coordinates are used for the numerical integrations of the long-time dynamics of Near-Earth Asteroids in section 2.2.1.

### 2.1.2 Heliocentric coordinates

The motion of objects in the solar system can alternatively be described by heliocentric coordinates. The origin of the reference system is moved into the Sun, and the set of equations of motion is reduced by three equations for the Sun.

For the following derivation we set  $m_0$  to be the mass of the central object (in general the most massive object, i.e. the Sun) and  $\mathbf{b}_0$  its position vector (*not* the barycenter). Then, by subtracting this vector from all barycentric coordinates, we obtain the heliocentric coordinates of object  $i$  as  $\mathbf{h}_i = \mathbf{b}_i - \mathbf{b}_0$  ( $i = 1, \dots, N$ ).

The heliocentric equations of motion follow from the second derivatives  $\ddot{\mathbf{h}}_i = \ddot{\mathbf{b}}_i - \ddot{\mathbf{b}}_0$  by inserting the appropriate equations (2.1.1)

$$\ddot{\mathbf{h}}_i = G \sum_{\substack{n=0 \\ n \neq i}}^N m_n \frac{\mathbf{b}_n - \mathbf{b}_i}{\|\mathbf{b}_n - \mathbf{b}_i\|^3} - G \sum_{\substack{n=1 \\ n \neq 0}}^N m_n \frac{\mathbf{b}_n - \mathbf{b}_0}{\|\mathbf{b}_n - \mathbf{b}_0\|^3}$$

and splitting off parts that involve  $m_0$  and  $m_i$ .

When switching from barycentric to heliocentric coordinates, the vectorial differences transform like  $\mathbf{b}_n - \mathbf{b}_i = \mathbf{h}_n - \mathbf{h}_i$ . Also note that  $\mathbf{h}_0 \equiv \mathbf{0}$  (the zero vector), as it is chosen to be the origin of the coordinate system. So we have

$$\ddot{\mathbf{h}}_i = -G m_0 \frac{\mathbf{h}_i}{\|\mathbf{h}_i\|^3} - G m_i \frac{\mathbf{h}_i}{\|\mathbf{h}_i\|^3} + G \sum_{\substack{n=1 \\ n \neq i}}^N m_n \frac{\mathbf{h}_n - \mathbf{h}_i}{\|\mathbf{h}_n - \mathbf{h}_i\|^3} - G \sum_{\substack{n=1 \\ n \neq i}}^N m_n \frac{\mathbf{h}_n}{\|\mathbf{h}_n\|^3}.$$

Finally, the equations of motion for object  $i$  in heliocentric coordinates are

$$\ddot{\mathbf{h}}_i = -G (m_0 + m_i) \frac{\mathbf{h}_i}{\|\mathbf{h}_i\|^3} + G \sum_{\substack{n=1 \\ n \neq i}}^N m_n \left( \frac{\mathbf{h}_n - \mathbf{h}_i}{\|\mathbf{h}_n - \mathbf{h}_i\|^3} - \frac{\mathbf{h}_n}{\|\mathbf{h}_n\|^3} \right). \quad (2.1.2)$$

Changing the coordinate system's origin (e.g. to geocentric coordinates) is equally simple for both barycentric and heliocentric coordinates. This task is performed by subtracting the new central object's position vector from all other vectors (for the velocities the same procedure holds). We will make use of heliocentric coordinates in the following section.

### 2.1.3 Discussion

In contemporary applications there is little difference between barycentric and heliocentric coordinates from the point of view of computing speed. The advantage of heliocentric coordinates is, that the system of differential equations is reduced by three equations for the motion of the Sun. This used to be an advantage only when a small number of celestial bodies was considered, and where the difference in the number of equations saved a considerable amount of computing time.

Today there remain a limited number of special applications for using one system exclusively, e.g. barycentric coordinates are more appropriate for observations of exoplanetary systems, whereas heliocentric coordinates are still preferred for analytical investigations where the expansion of the disturbing function is required.

Apart from these cases, in most applications there is no significant advantage in computing speed for either coordinate system. The large number (hundreds to thousands) of objects computed simultaneously in recent numerical studies renders insignificant the savings of three differential equations.

However, there is a minor advantage in favour of the barycentric coordinates. The barycentric equations of motions (2.1.1) contain fewer terms than their heliocentric counterparts (2.1.2), which allows to translate them into a more compact and potentially more efficient computer code.

## 2.2 Solving the equations of motion

The equations of motion for the  $N$ -body problem consist of three differential equations of second-order, or equivalently of six differential equations of first-order, per object. As Poincaré has shown a general solution of the equations of motion does not exist for more than two bodies due to the lack of integrals of motion. Even the most basic case – a single Near-Earth Asteroid in orbit about the Sun being perturbed by the Earth, posing a restricted three-body problem – cannot be handled analytically in general.

This obstacle makes it necessary to resort to numerical procedures to calculate the orbital evolution of Near-Earth Asteroids under the influence of the planets. These numerical procedures have to be rather efficient, since we consider thousands of asteroids over millions of orbital periods. A typical numerical integration scheme accumulates all the accelerations on an individual object by directly summing all contributions from massive “perturbers”, a process for which the complexity grows quadratically with the number of involved objects. Once the accelerations have been calculated for every object, the positions (and eventually velocities) are updated for the next time step. Typically the time steps are smaller than the orbital period of any body, such that tens to hundreds of time steps are needed per orbital period, depending on the accuracy of the computation.

In the following sections I describe the two numerical integration methods that were mainly used to obtain the data for the long-term evolution of Near-Earth Asteroids.

### 2.2.1 Lie series integrator

The use of Lie-series for solving differential equations has been pioneered by Gröbner and Knapp (1967), while they were introduced as a numerical integration method by Hanslmeier and Dvorak (1984). A detailed introduction can be found in Eggl and Dvorak (2010), while just a short summary will be given here.

Let  $\mathbf{z} = (z_1, \dots, z_n)$  be the vector of dependent variables. The system of differential equations to be solved is given by

$$\frac{dz_i}{dt} = f_i(\mathbf{z}), \quad i = 1 \dots n.$$

The linear Lie-differential operator is defined as

$$D := \sum_{i=1}^n f_i(\mathbf{z}) \frac{\partial}{\partial z_i}$$

which is merely a linear combination of the functions  $f_i$ , representing the right-hand side of the system of differential equations, and the partial derivatives with respect to the variables  $z_i$ .

The Lie-series is defined as

$$L(\mathbf{z}, t) := \sum_{k=0}^{\infty} \frac{t^k}{k!} D^k f(\mathbf{z}) = \exp(tD) f(\mathbf{z}).$$

Using these two definitions it can be shown (Gröbner and Knapp, 1967; Hanslmeier and Dvorak, 1984) that the solutions of the differential equations become

$$z_i(t) = \exp(tD) z_i(0) \quad i = 1 \dots n,$$

where  $z_i(0)$  represent the initial conditions. It was assumed here that the initial conditions are given at  $t_0 = 0$ , but the method is not restricted to that. In fact any point  $z_i(t_0)$  of the trajectory can be used to compute the next time-step  $z_i(t_0 + \tau)$ .

Essentially the Lie-series method is a Taylor-series expansion of the a-priori unknown solution  $\mathbf{z}(t)$ , which is why the derivatives  $D^k f(\mathbf{z})$  have to be computed. In practice, this is done by making use of a recurrence relation to calculate  $D^{k+1}$  from the already known  $\{D^1, \dots, D^k\}$ . The so-called ‘‘Taylor’’ method of Jorba and Zou (2005) also uses recurrence relations for a high order approximation of the Taylor series, but with the distinctive difference that the latter uses recurrence formulas for the variables  $z_i$ , while the Lie-series method applies recurrence formulas for the derivatives  $D^k$  (by introducing auxiliary variables).

The Lie-series method can be classified as an explicit one-step method, i.e. a method that needs only one single (previous) point of the trajectory, or – in other words – that does not use or need past information about the solution.

Comparing the Lie-series method to other common numerical methods, like Runge-Kutta or multistep methods, one can find several advantages:

1. The Lie-series method (like the linear multistep methods) only needs one evaluation of the right-hand side of the differential equation system per time-step, which renders it more efficient than Runge-Kutta methods that need several substeps (stages) per time-step.
2. The adaptive adjustment of the step-size is fairly easy, like in the case of (embedded) Runge-Kutta methods. Changing the step-size when needed makes it well suited for  $N$ -body dynamics, especially in the case when the mutual separation between pairs of objects becomes small.
3. The variable and high-order approximation of the Taylor-series allows for a large average step-size and small truncation errors at the same time.

The Lie-series method has been applied to the  $N$ -body problem given in barycentric coordinates (as described in section 2.1.1) using the formalism of Hanslmeier and Dvorak (1984).

### 2.2.2 Mercury integrator

A different class of numerical integration methods relies on the fact that for Hamiltonian systems the phase-space volume is conserved due to a theorem by Liouville. Methods that conserve the phase-space volume are called symplectic integrators, and they have been successfully applied to the  $N$ -body problem (Kinoshita et al., 1990; Yoshida, 1993).

Hamilton's equations of motion for generalised coordinates  $q_i$  and momenta  $p_i$  in a  $2n$ -dimensional phase space ( $i = 1 \dots n$ ) read

$$\begin{aligned}\frac{dq_i}{dt} &= \frac{\partial H}{\partial p_i} \\ \frac{dp_i}{dt} &= -\frac{\partial H}{\partial q_i}.\end{aligned}$$

The variables can be gathered into a single vector  $\mathbf{z} = (\mathbf{q}, \mathbf{p})$ . This allows to write the above equations as

$$\dot{\mathbf{z}} = \{\mathbf{z}, H(\mathbf{z})\}$$

by defining the differential operator  $D_H := \{\cdot, H\}$  for a given Hamiltonian function  $H$ , and using the Poisson bracket

$$\{A, B\} = \sum_{i=1}^n \frac{\partial A}{\partial q_i} \frac{\partial B}{\partial p_i} - \frac{\partial A}{\partial p_i} \frac{\partial B}{\partial q_i}.$$

In analogy to the Lie-series, the solution can now formally be written as

$$\mathbf{z}(t) = \exp(\tau D_H) \mathbf{z}(t_0)$$

with  $\tau = t - t_0$ . To actually obtain a solution, the Hamiltonian  $H$  has to be separated into parts that can be solved independently. Often the Hamiltonian will be split into kinetic and potential energy of the form  $H = T(\mathbf{p}) + U(\mathbf{q})$ , but other forms are also admissible and can be advantageous.

One such alternative splitting was proposed by Chambers (1999), where he used mixed coordinate variables, namely heliocentric positions and barycentric velocities. This allows to split the Hamiltonian into three parts  $H = H_A + H_B + H_C$ , being the two-body part  $H_A$  for Keplerian motion about the Sun, the interaction part  $H_B$  involving the perturbations from all other bodies, and a part  $H_C$  including the kinetic energy of the Sun. Apart from close encounters it holds that  $H_A \gg H_B$  and  $H_A \gg H_C$ ; as a consequence the symplectic integrator has a local error of  $\mathcal{O}(\epsilon \tau^3)$ , with  $\epsilon \propto m_i/m_0$ .

Close encounters need a special handling in order to cope with the fixed step size. When objects  $\alpha$  and  $\beta$  approach each other their mutual distance  $r_{\alpha,\beta}$  becomes small and then  $H_A \sim H_B$ . Chambers introduced a changeover function  $K(r_{i,j})$ , which has the properties that  $K \rightarrow 0$  for  $r_{i,j} \ll 1$  and  $K \rightarrow 1$  for large separation  $r_{i,j}$ . The interaction terms are split between  $H_A$  ( $\propto 1 - K(r_{i,j})$ ) and  $H_B$  ( $\propto K(r_{i,j})$ ), so it is guaranteed that

$H_A \gg H_B$  at all times. When the objects are well separated  $K \rightarrow 1$  and  $H_A$  represents still the two-body motion; on the other hand for a close encounter  $H_A$  will contain the three-body problem including Sun and the two objects  $(\alpha, \beta)$ . Any objects not involved in the close encounter will still move on nearly two-body orbits.

The three-body problem cannot be solved analytically, so in practice the close encounters of two bodies are treated numerically by a conventional Bulirsch-Stoer integrator (Press et al., 1992). This integrator is able to handle large time-steps by splitting them into a sequence of (increasingly smaller) sub-steps, and then to extrapolate them to the limit of step-size  $\tau \rightarrow 0$  (see Eggl and Dvorak, 2010). The accuracy of the Bulirsch-Stoer extrapolation method can be tuned by a user-defined parameter, a typical value for the local error tolerance is  $10^{-12}$ , but also values close to machine precision are possible.

The changeover function  $K(r_{i,j})$  depends on another free parameter, the critical distance  $r_{\text{crit}}$ , which determines the begin of a close encounter. Chambers (and other authors) recommend a value of  $r_{\text{crit}} = 3 - 10$  times the Hill-radius of the involved bodies.

The hybrid symplectic integrator of the Mercury package (Chambers, 1999) combines a high speed (and moderately accurate) second-order symplectic method with the accuracy of the Bulirsch-Stoer method during close encounters, the whole integration method remains symplectic. The advantage of this method is that the angular momentum of the system is very well conserved, which is a common property of symplectic integrators. This integrator has been applied to the  $N$ -body problem to follow the orbital evolution of Near-Earth Asteroids.

## 2.3 Circular restricted three-body problem

The Circular Restricted Three-Body Problem (CR3BP) is a special case of the general three-body problem. It might seem to be an overly simplistic model of not much practical importance, but in fact it serves as a reasonable first approximation in many cases, e.g. for the dynamics of Trojan asteroids in the solar system; for a more complete list of applications see Dvorak and Lhotka (2013, chapter 6). The CR3BP consists of two massive objects  $(m_1, m_2)$  – called primary and secondary – that move on circular orbits about their common barycenter; and one object of negligible mass (the particle).

In the derivation of the equations of motion for the spatial CR3BP I will follow the example of Murray and Dermott (1999) and Szebehely (1967). Figure 2.1 shows a sketch of the configuration of the CR3BP. The graph collects the most important parameters that are defined and used in the following sections.

### 2.3.1 Equations of motion

The massless particle does not perturb the orbits of  $m_1, m_2$  which stay on circular orbits forever. Consequently there is no need to solve for their equations of motion, and

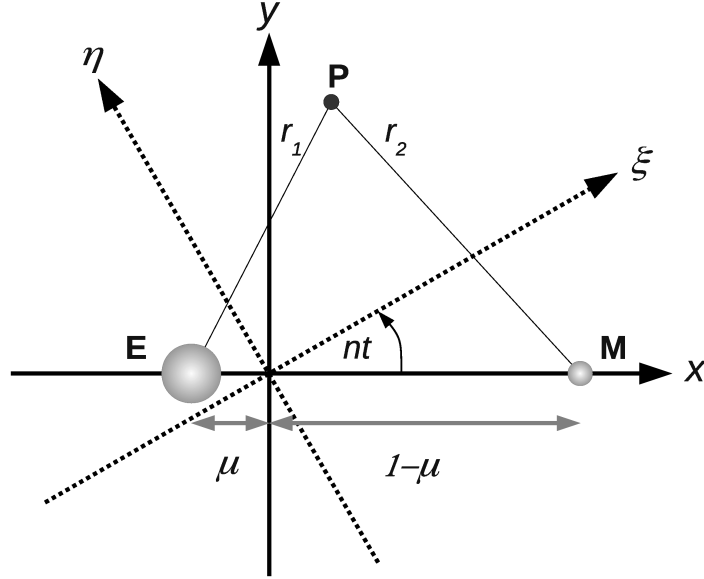


Figure 2.1: A schematic overview of the CR3BP. This planar view shows the two coordinate systems: the inertial (sidereal) system  $(\xi, \eta)$ , and the rotating (synodic) system  $(x, y)$ . The latter rotates with constant angular frequency  $n$  relative to the inertial system. The primaries Earth and Moon are fixed on the  $x$ -axis and their distance is normalised to 1. The massless particle  $P$  moves under the influence of both primaries.

it is sufficient to solve three coupled second-order ordinary differential equations for the motion of the particle.

Let  $(\xi, \eta, \zeta)$  be the coordinates (“sidereal coordinates”) of the particle in an inertial frame, and let the origin be the center of mass. It is common to use units for which the gravitational constant becomes unity; this is achieved by setting the unit-distance to the distance between  $m_1$  and  $m_2$ , and the unit-mass to the sum of masses  $m_1 + m_2$ . Then the masses can be expressed as  $\mu_1 = m_1/(m_1 + m_2)$ ,  $\mu_2 = m_2/(m_1 + m_2)$ , where usually  $\mu_2 < \mu_1$  is assumed. The unit-time must be chosen appropriately in order to fulfill the required condition  $G \equiv 1$ .

We can obtain the sidereal equations of motion by using the barycentric coordinate formulation from equation (2.1.1) (for  $i = 3, n = 1, 2$ )

$$\begin{aligned}
 \ddot{\xi} &= \mu_1 \frac{\xi_1 - \xi}{\rho_1^3} + \mu_2 \frac{\xi_2 - \xi}{\rho_2^3} \\
 \ddot{\eta} &= \mu_1 \frac{\eta_1 - \eta}{\rho_1^3} + \mu_2 \frac{\eta_2 - \eta}{\rho_2^3} \\
 \ddot{\zeta} &= \mu_1 \frac{\zeta_1 - \zeta}{\rho_1^3} + \mu_2 \frac{\zeta_2 - \zeta}{\rho_2^3},
 \end{aligned} \tag{2.3.1}$$

where the distances of the particle to  $m_1$  and  $m_2$  are given by:

$$\begin{aligned}\rho_1^2 &= (\xi - \xi_1)^2 + (\eta - \eta_1)^2 + (\zeta - \zeta_1)^2 \\ \rho_2^2 &= (\xi - \xi_2)^2 + (\eta - \eta_2)^2 + (\zeta - \zeta_2)^2.\end{aligned}$$

The variables  $(\xi_n, \eta_n, \zeta_n)$  (for  $n = 1, 2$ ) are the time dependent components of the primaries' position vectors in the inertial frame; explicit expressions will be stated below.

Now, instead of an inertial reference frame, we change to a rotating coordinate system. Let  $(x, y, z)$  be Cartesian coordinates in a rotating reference system ("synodic coordinates"), in which both massive objects are always located on the  $x$ -axis at

$$(x_1, y_1, z_1) = (-\mu_2, 0, 0), \quad (x_2, y_2, z_2) = (\mu_1, 0, 0).$$

This setup of the CR3BP uses the definition of Murray and Dermott (1999), note that Szebehely (1967) uses the opposite configuration with  $\mu_1$  and  $\mu_2$  being exchanged in the formulas above. The coordinate system  $(x, y, z)$  rotates with constant angular speed  $n = 1$  relative to  $(\xi, \eta, \zeta)$ , because of the normalised units of length, mass, and time.

We use the standard rotation matrix  $R_z$  for rotations about the  $z$ -axis to transform between the sidereal and synodic coordinate systems for arbitrary times  $t$ :

$$\begin{pmatrix} \xi \\ \eta \\ \zeta \end{pmatrix} = \begin{pmatrix} \cos t & -\sin t & 0 \\ \sin t & \cos t & 0 \\ 0 & 0 & 1 \end{pmatrix} \begin{pmatrix} x \\ y \\ z \end{pmatrix}. \quad (2.3.2)$$

From this rotation matrix it is clear that after each complete revolution at times  $t = 2\pi k$  ( $k \in \mathbb{N}$ ) the two coordinate systems are aligned. This coordinate transform also enables us to express the inertial coordinates of  $m_1$  and  $m_2$  as functions of time  $t$  and the fixed synodic positions:

$$\begin{aligned}(\xi_1, \eta_1, \zeta_1) &= (-\mu_2 \cos t, -\mu_2 \sin t, 0) \\ (\xi_2, \eta_2, \zeta_2) &= (+\mu_1 \cos t, +\mu_1 \sin t, 0).\end{aligned}$$

For the accelerations we take the time derivatives  $d^2/dt^2$  on both sides of equation (2.3.2) to obtain

$$\begin{pmatrix} \ddot{\xi} \\ \ddot{\eta} \\ \ddot{\zeta} \end{pmatrix} = \begin{pmatrix} \cos t & -\sin t & 0 \\ \sin t & \cos t & 0 \\ 0 & 0 & 1 \end{pmatrix} \begin{pmatrix} \ddot{x} - 2\dot{y} - x \\ \ddot{y} + 2\dot{x} - y \\ \ddot{z} \end{pmatrix}.$$

Using this last relation and inserting equations (2.3.1) we find – after some algebra – the synodic equations of motion

$$\begin{aligned}\ddot{x} - 2\dot{y} &= x - \mu_1 \frac{x + \mu_2}{r_1^3} - \mu_2 \frac{x - \mu_1}{r_2^3} \\ \ddot{y} + 2\dot{x} &= y - \mu_1 \frac{y}{r_1^3} - \mu_2 \frac{y}{r_2^3} \\ \ddot{z} &= -\mu_1 \frac{z}{r_1^3} - \mu_2 \frac{z}{r_2^3},\end{aligned} \quad (2.3.3)$$

where now the distances of the particle to the primaries  $m_1$  and  $m_2$  are given by

$$\begin{aligned} r_1^2 &= (x + \mu_2)^2 + y^2 + z^2 \\ r_2^2 &= (x - \mu_1)^2 + y^2 + z^2. \end{aligned}$$

The right hand side of equations (2.3.3) can be written as the gradient of the pseudo-potential

$$U(x, y, z) = \frac{1}{2}(x^2 + y^2) + \frac{\mu_1}{r_1} + \frac{\mu_2}{r_2}$$

in which the first term is due to the rotating coordinate system, the other terms stem from the gravitational potential of the massive bodies.

Szebehely (1967) points out that the CR3BP can be defined to depend on the single parameter  $\mu$  by setting

$$\mu_2 \rightarrow \mu \equiv \frac{m_2}{m_1 + m_2}, \quad \mu_1 \rightarrow 1 - \mu.$$

In the rotating system there exists a constant of motion, the so called Jacobi constant (or Jacobi integral)

$$C = 2U - v^2 = x^2 + y^2 + 2 \left( \frac{\mu_1}{r_1} + \frac{\mu_2}{r_2} \right) - (\dot{x}^2 + \dot{y}^2 + \dot{z}^2). \quad (2.3.4)$$

It is this constant that will play an important role in the following section.

### 2.3.2 Manifold correction

The accurate and efficient numerical integration of the equations of motion requires highly skilled solver methods. It is common to monitor some known conserved quantities (integrals) of the problem – such as the total specific energy or the total angular momentum in the  $N$ -body problem – to measure the quality of an integration method.

Instead of only passively monitoring the errors via integrals of motion, it was proposed by Nacozy (1971) to actually use the integrals to ensure that the numerical solution satisfies the conserved quantities. This is achieved by forcing corrections to the integrated variables at every integration step; this procedure is equivalent to projecting the variables back onto the integral’s manifold (Hairer et al., 2006), hence the name “manifold correction” (MFC).

Murison (1989) applied Nacozy’s MFC to the CR3BP by using Lagrange multipliers to correct errors in the integrated coordinates. He demonstrated that with MFC one can achieve an accuracy of  $10^{-14}$  in the accumulated Jacobi constant error (in the absence of collisions), where for comparison with regularisation the error is of order  $10^{-15}$  (see his Table 1).

Fukushima (2003) extended the MFC method by including integral invariant relations, and presented an application to the perturbed two-body problem. An integral invariant

is an analytical function  $I = I(\mathbf{r}, \mathbf{v})$  of position ( $\mathbf{r}$ ) and velocity ( $\mathbf{v} = \dot{\mathbf{r}}$ ). The method of Fukushima extends the equations of motion by the equation for the time evolution of the integral invariant, i.e. he adds  $dI/dt$  to the system of differential equations to be solved. By integrating it in parallel to the variables, it is possible to compare its integrated value  $I(t)$  with the one obtained from the integrated variables  $I(\mathbf{r}(t), \mathbf{v}(t))$ . After each integration step ( $\mathbf{r}, \mathbf{v}$ ) are modified by a scale transform

$$(\mathbf{r}, \mathbf{v}) \mapsto (s\mathbf{r}, s\mathbf{v}),$$

where the scale factor  $s \in \mathbb{R}$  must be determined such that the integrated  $I(t)$  and the evaluated  $I(\mathbf{r}(t), \mathbf{v}(t))$  are identical.

I have derived the necessary transformations to achieve the ‘‘Jacobi constant consistency’’ for the CR3BP. This new MFC method is independent of the work of Murison (1989), it is rather related to the work of Fukushima (2003) for the ‘‘Kepler energy consistency’’ in the two-body problem.

The Jacobi constant in equation (2.3.4) can be written in a form similar<sup>1</sup> to the total energy in the two-body problem

$$-\frac{C}{2} = T - U = \frac{1}{2}v^2 - \left( \frac{1}{2}(x^2 + y^2) + \frac{\mu_1}{r_1} + \frac{\mu_2}{r_2} \right)$$

with the kinetic energy  $T$  and the potential energy  $-U$ . When the scaling transform from above is applied, we have

$$\begin{aligned} v^2 &\mapsto \hat{v}^2 = s^2v^2 \\ T &\mapsto \hat{T} = s^2T \\ r_1^2 &\mapsto \hat{r}_1^2 = s^2 \left( x + \frac{\mu_2}{s} \right)^2 + s^2y^2 + s^2z^2 = s^2\hat{r}_1^2 \\ r_2^2 &\mapsto \hat{r}_2^2 = s^2 \left( x - \frac{\mu_1}{s} \right)^2 + s^2y^2 + s^2z^2 = s^2\hat{r}_2^2 \\ U &\mapsto \hat{U} = \frac{1}{2}s^2(x^2 + y^2) + \frac{\mu_1}{s\hat{r}_1} + \frac{\mu_2}{s\hat{r}_2}. \end{aligned}$$

To simplify the expressions and to make clear the analogy to Fukushima’s paper, let us define

$$\tilde{C} = -\frac{C}{2}; \quad \tilde{T} = T - \frac{1}{2}(x^2 + y^2); \quad \tilde{U} = -\frac{\mu_1}{\tilde{r}_1} - \frac{\mu_2}{\tilde{r}_2},$$

so that after executing the scale transform it follows

$$\tilde{C} = s^2\tilde{T} + \frac{\tilde{U}}{s}.$$

<sup>1</sup>As Murray and Dermott (1999) point out, the Jacobi constant is *not* an energy integral, in the CR3BP the energy and angular momentum are not conserved.

The scale factor  $s$  can then be computed from

$$f(s) = \tilde{T}s^3 - \tilde{C}s + \tilde{U} = 0$$

by some numerical root-finding procedure, for instance the standard Newton-Raphson method<sup>2</sup>. This type of transformation is similar to the near-identity transformations from perturbation theory, so  $s_0 = 1$  is a natural choice. Using this initial guess, the first Newton-Raphson iteration delivers the refined approximation

$$s_1 = \frac{2\tilde{T} - \tilde{U}}{3\tilde{T} - \tilde{C}}.$$

The iteration process continues until some prescribed accuracy  $\|f(s_n)\| < \varepsilon$  is achieved, usually this happens after one or two iterations ( $n \leq 2$ ); the value of  $s$  always remains close to 1.

There are some points worth mentioning:

- It is not necessary to integrate the time evolution of the Jacobi constant, because  $dC/dt = 0$  anyway. The synodic equations of motion (2.3.3) remain unaltered.
- We need to scale  $(\mathbf{r}(t), \mathbf{v}(t))$  to fit with  $\tilde{C} = -C/2$ , which is a constant obtained once and for all from the initial conditions  $C = C(\mathbf{r}(t=0), \mathbf{v}(t=0))$ .
- The modified distances  $\tilde{r}_i$  involve a rescaling of the masses  $\mu_i/s$ , which leads to the interesting effect that not only the coordinates, but also the masses are modified.

Figure 2.2 shows an example of the MFC method. The two-body problem with eccentricity  $e = 0.8$  was integrated with a Runge-Kutta (RK) type method (error tolerance  $10^{-12}$ ) without correction (left panel), and with correction of the Kepler energy (right panel). The RK method exhibits a linear error growth in the conserved quantities (black curve for the theoretical behaviour). The other constants of motion (green: magnitude of the angular momentum vector; blue: magnitude of the Laplace-Runge-Lenz vector, which points to the pericenter) are included to show that they have a similar error growth. In the corrected case they still show the linear error trend, but note that the error is lower by about 1–2 orders of magnitude. After MFC the Kepler energy does not have a linear trend, but the remaining error comes from the accumulation of round-off errors (Quinn and Tremaine, 1990).

## 2.4 Estimating the domain of planetary influence

There are different ways to characterise the region around a planet, where its own gravitational attraction is the major source acting on a test particle. Here the concepts of the “Hill sphere” and the “sphere of influence” (SOI) are presented.

---

<sup>2</sup>Fukushima discusses the possibility of using the analytic formula for cubic equations (Cardano’s formula), but prefers the numerical method for its higher speed.

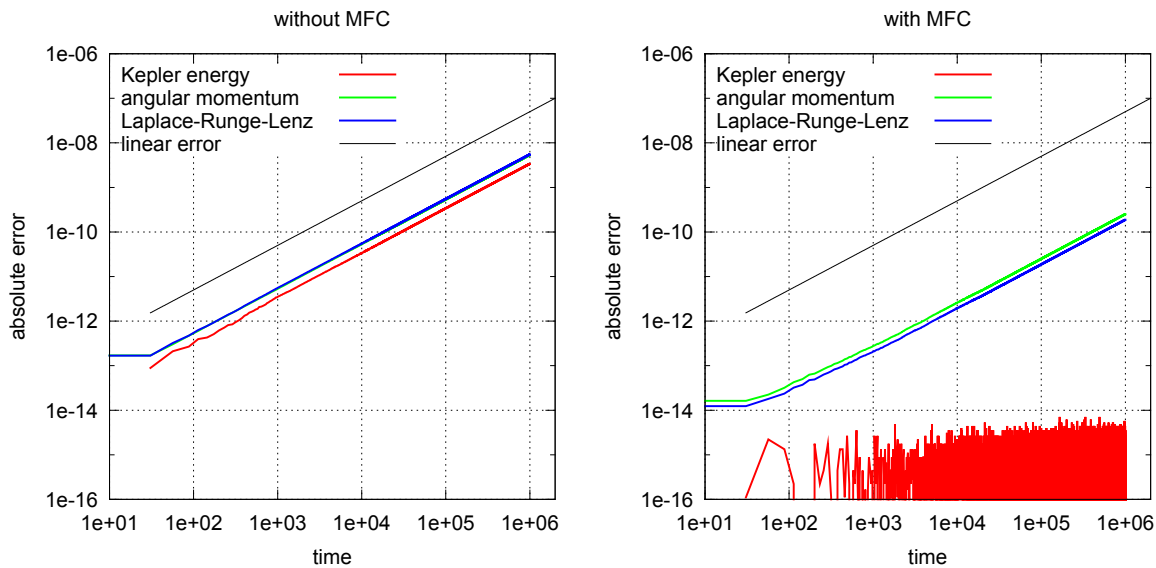


Figure 2.2: An example for the effect of the manifold correction method in the two-body problem for an eccentricity  $e = 0.8$ . On the left no correction is applied, on the right the Kepler energy is corrected only. MFC improves also the errors of the uncorrected integrals of motion by about an order of magnitude.

### 2.4.1 Hill sphere

For the case of a nearly massless object (e.g. a Near-Earth Asteroid) under the gravitational influence of the Sun and a planet, the latter will affect the asteroid's orbit appreciably only at close approaches. The exact boundary for a “close approach” (or close encounter) is not well defined. Based on the work of Hill the notion of the “Hill sphere” has become common as an estimate for the region around a planet where it dominates the dynamics of approaching smaller objects.

The derivation of the Hill sphere starts from the equations of motion (2.3.3) for the circular restricted three-body problem (CR3BP) in section 2.3 (Murray and Dermott, 1999, chapter 3.13).

We recapitulate the definition of the normalised mass-ratio  $\mu$  of the planet to the total mass of the system

$$\mu = \frac{m_2}{m_1 + m_2},$$

and that the synodic reference frame rotates with the constant angular speed of  $n = 1$ .

Then some simplifications can be applied, namely:

1. we consider the planar case ( $z = \ddot{z} = 0$ ) only,
2. the mass-ratio is assumed to be very small  $\mu \ll 1$ ,
3. and the origin of the coordinate system is shifted to the location of the second mass (by  $x \mapsto 1 + x, y \mapsto y$ ).

The simplifications from above result in the transformed equations of motion:

$$\begin{aligned}\ddot{x} - 2\dot{y} - (1 + x) &= - \left( \frac{1 + x + \mu}{r_1^3} + \mu \frac{x}{r_2^3} \right) \\ \ddot{y} + 2\dot{x} - y &= - \left( \frac{y}{r_1^3} + \mu \frac{y}{r_2^3} \right)\end{aligned}$$

As the mass-ratio  $\mu$  is very small, terms of  $\mathcal{O}(\mu)$  and higher are neglected, the mutual distances are expressed as

$$r_1 \approx (1 + 2x)^{1/2}, \quad r_1^{-3} \approx 1 - 3x, \quad R \equiv r_2 = (x^2 + y^2)^{1/2},$$

and the equations from above are transformed into

$$\begin{aligned}\ddot{x} - 2\dot{y} &= \left( 3 - \frac{\mu}{R^3} \right) x \\ \ddot{y} + 2\dot{x} &= -\frac{\mu}{R^3} y.\end{aligned}$$

The stationary solutions of this system for  $\dot{x} = \dot{y} = \ddot{x} = \ddot{y} = 0$  are

$$\begin{aligned}0 &= \left( 3 - \frac{\mu}{R^3} \right) x \\ 0 &= -\frac{\mu}{R^3} y\end{aligned}$$

and – excluding the trivial solution  $(x, y) = (0, 0)$  – it follows from the first equation for the Hill radius  $R_{\text{Hill}}$  that

$$R_{\text{Hill}} = \left( \frac{\mu}{3} \right)^{\frac{1}{3}}.$$

Changing back from normalised units to physical units that involve the planet's distance  $a$  and its eccentricity  $e$ ,

$$R_{\text{Hill}} = a(1 - e) \left( \frac{\mu}{3} \right)^{\frac{1}{3}} \tag{2.4.1}$$

with  $\mu$  being the mass ratio of planet to host star (e.g. Earth to Sun). This form for the Hill radius is a somewhat conservative estimate, because the eccentricity is usually negligible for planets, but the perihelion distance  $q = a(1 - e)$  gives a tighter bound for the Hill sphere than the distance  $a$  alone.

Within the Hill sphere the major gravitational attraction stems from the planet, while the Sun and all other planets can be considered as perturbers.

## 2.4.2 Sphere of influence

The “sphere of influence” (SOI) (Stumpff, 1965) is another concept to assess where the motion of a test particle (considered to be massless) is dominated by a planet instead of the Sun. Stumpff (1965) pointed out that the SOI cannot be expressed unambiguously, because it depends on the choice of the reference system used (e.g. barycentric or heliocentric coordinates). The straight-forward way would be to compare the magnitudes of the resulting forces (accelerations) by the Sun and a planet on the test particle. If one used barycentric coordinates, one would obtain values that underestimate the real influence of the planet. A better estimate uses heliocentric and planetocentric coordinates and compares the relative perturbative accelerations in both systems to estimate a region of a planet’s influence.

The underlying dynamical model is the restricted three-body problem consisting of the Sun, a planet (e.g. Earth), and a massless object (e.g. Near-Earth Asteroid), where the respective masses are  $m_1 \gg m_2 \gg m_3 \approx 0$ . The following derivation follows that in Stumpff (1965).

### Equations of motion in heliocentric coordinates

In heliocentric coordinates the acceleration  $\ddot{\mathbf{h}}_3$  of  $m_3$ , under the influence of  $m_1$  and  $m_2$ , is given by equation (2.1.2)

$$\ddot{\mathbf{h}}_3 = -G m_1 \frac{\mathbf{h}_3}{r_{1,3}^3} - G m_2 \left( \frac{\mathbf{h}_2}{r_{1,2}^3} + \frac{\mathbf{h}_3 - \mathbf{h}_2}{r_{2,3}^3} \right). \quad (2.4.2)$$

The first part  $F_S$  is the acceleration due to the Sun, and the second part  $F_P$  is due to the planet. When comparing the magnitudes one usually finds that  $|F_P| < |F_S|$ , as long as the asteroid is not in the vicinity of the planet, so (with  $|\mathbf{h}_2| = r_{1,2}$ ,  $|\mathbf{h}_3| = r_{1,3}$ ,  $|\mathbf{h}_3 - \mathbf{h}_2| = r_{2,3}$ )

$$F_P/F_S = \left( m_2 \left| \frac{\mathbf{h}_2}{r_{1,2}^3} + \frac{\mathbf{h}_3 - \mathbf{h}_2}{r_{2,3}^3} \right| \right) / \left( \frac{m_1}{r_{1,3}^2} \right). \quad (2.4.3)$$

### Equations of motion in planetocentric coordinates

The situation is contrary to the one before, when the asteroid has approached the planet closely enough so that the main source of acceleration is the planet itself, and the Sun is the perturber.

The heliocentric acceleration of the planet  $m_2$  is completely determined by the two-body problem

$$\ddot{\mathbf{h}}_2 = -G (m_1 + m_2) \frac{\mathbf{h}_2}{r_{1,2}^3}, \quad (2.4.4)$$

which involves only the Sun  $m_1$ , as  $m_3$  is negligible and does not contribute.

Switching to planetocentric coordinates  $\mathbf{p} = \mathbf{h}_3 - \mathbf{h}_2$ , the acceleration is now  $\ddot{\mathbf{p}} = \ddot{\mathbf{h}}_3 - \ddot{\mathbf{h}}_2$ . This expression can be assembled from the heliocentric acceleration  $\ddot{\mathbf{h}}_3$  of the asteroid, and the corresponding heliocentric acceleration  $\ddot{\mathbf{h}}_2$  of the planet.

Combining the two expressions (2.4.2) and (2.4.4) leads to

$$\ddot{\mathbf{p}} = \ddot{\mathbf{h}}_3 - \ddot{\mathbf{h}}_2 = -G m_2 \frac{\mathbf{p}}{r_{2,3}^3} - G m_1 \left( \frac{\mathbf{h}_3}{r_{1,3}^3} - \frac{\mathbf{h}_2}{r_{1,2}^3} \right).$$

Here, the first part  $F'_P$  is the acceleration from the planet, which is larger in magnitude than the second part  $F'_S$  from the Sun, as long as the asteroid is close enough to the planet (remember that  $|\mathbf{p}| = |\mathbf{h}_3 - \mathbf{h}_2| = r_{2,3}$ ):

$$F'_S/F'_P = \left( \frac{m_2}{r_{2,3}^2} \right) / \left( m_1 \left| \frac{\mathbf{h}_3}{r_{1,3}^3} - \frac{\mathbf{h}_2}{r_{1,2}^3} \right| \right). \quad (2.4.5)$$

### Comparison of the perturbations

Now the task is to find the distance from the planet at which the relative perturbations become equal in magnitude. After equating equations (2.4.3) and (2.4.5) and squaring them, it follows (with the mass-ratio  $\mu = m_2/m_1$ )

$$r_{2,3}^4 \left( \frac{\mathbf{h}_3 \cdot \mathbf{h}_3}{r_{1,3}^6} - 2 \frac{\mathbf{h}_2 \cdot \mathbf{h}_3}{r_{1,2}^3 r_{1,3}^3} + \frac{\mathbf{h}_2 \cdot \mathbf{h}_2}{r_{1,2}^6} \right) = \mu r_{1,3}^4 \left( \frac{\mathbf{h}_2 \cdot \mathbf{h}_2}{r_{1,2}^6} + 2 \frac{\mathbf{h}_2 \cdot \mathbf{p}}{r_{1,2}^3 r_{2,3}^3} + \frac{\mathbf{p} \cdot \mathbf{p}}{r_{2,3}^6} \right).$$

To simplify this equation one introduces the angle  $\theta$  between  $\mathbf{h}_2$  and  $\mathbf{p}$ , and the parameter  $u < 1$  in  $r_{2,3} = u r_{1,2}$ , which expresses that the asteroid must be closer to the planet than its distance to the Sun (i.e.  $r_{2,3} < r_{1,2}$ ). For the distance of the asteroid to the Sun  $r_{1,3}$  it follows from trigonometric relations that

$$r_{1,3}^2 = r_{1,2}^2 + r_{2,3}^2 + 2 r_{1,2} r_{2,3} \cos \theta = r_{1,2}^2 (1 + 2u \cos \theta + u^2).$$

Inserting all the relevant expressions from above and simplifying the formula one obtains

$$\begin{aligned} u^8 \left( 1 - 2(1 + u \cos \theta) \sqrt{1 + 2u \cos \theta + u^2} + (1 + 2u \cos \theta + u^2)^2 \right) = \\ = \mu^4 (1 + 2u \cos \theta + u^2)^4 (1 + 2u^2 \cos \theta + u^4). \end{aligned}$$

We need to solve the above equation for  $u = u(\mu, \theta)$ . Since  $u$  is a small parameter, one can perform a Taylor expansion of the square-root which leads to

$$u^{10} (1 + 3 \cos^2 \theta + \mathcal{O}(u^1)) = \mu^4 (1 + \mathcal{O}(u^1))$$

and by ignoring the higher-order terms in  $u$  it follows that

$$u(\mu, \theta) = \frac{\mu^{2/5}}{(1 + 3 \cos^2 \theta)^{1/5}}.$$

This can be further simplified by ignoring the denominator, which is bounded between 0.87 and 1. Then the SOI in physical units is obtained from  $r_{2,3} = r_{1,2} u$ , by using the semi-major axis  $a$  instead of  $r_{1,2}$ ,

$$R_{\text{SOI}} = a \mu^{\frac{2}{5}}. \quad (2.4.6)$$

### 2.4.3 Comparison

Comparing the two equations (2.4.1) and (2.4.6) one will notice a distinctive difference: the Hill sphere includes the planet's eccentricity while the SOI does not. This asymmetry is somewhat unfortunate, and a remedy would be to introduce the eccentricity also into the formula for SOI (or remove it from the Hill sphere formula)<sup>3</sup>.

Still it has to be remarked that – strictly speaking – the use of  $\mu$  in both equations means different things. As the Hill radius has been derived from the restricted three-body problem, the meaning is  $\mu = m_2/(m_1 + m_2)$ , while for the SOI it is  $\mu = m_2/m_1$ . Remembering the assumption of small mass ratio for the Hill sphere ( $m_2 \ll m_1$ ), it can be argued that in practice the mass ratio is meaning the same  $\mu \approx m_2/m_1$ .

The admissible parameter range for  $\mu$  is  $0 \leq \mu \leq 0.5$  (using the original form as for the CR3BP), which means that the higher power of  $\mu$  for the SOI will result in smaller values for typical planetary mass ratios of  $\mu < 10^{-3}$ . For higher mass ratios the situation changes with the SOI being larger than the Hill sphere (typically for binary stars or star–brown-dwarf pairs).

Figure 2.3 shows the functional dependence on the mass ratio  $\mu$  for the case of circular orbits and using a normalised distance  $a = 1$ . Due to the higher power in  $\mu$  the SOI grows faster and is bigger for high mass ratios, while the Hill sphere is bigger for small mass ratios. Both spheres are equal for a planet of about 4 Jupiter masses (at  $e = 0$ , see formula below).

Until this point the eccentricity has been ignored. Now, using the eccentricity in the equation for the Hill sphere, but not for the SOI, the two expressions (2.4.1) and (2.4.6) are equal if

$$\mu(e) = (1 - e)^{15}/3^5,$$

independent of the semi-major axis  $a$  (the other case for  $\mu \rightarrow 0$  is not of interest). Obviously there is a strong dependence on the eccentricity. Consequently one has to take care of this fact even when low mass ratios are considered.

Figure 2.4 shows how the curve  $\mu(e)$  behaves for a wide range of eccentricities. In the area below the curve the Hill sphere is larger than the SOI, while everywhere above the curve the case is opposite. As an example even a moderate eccentricity of  $e \geq 0.1$  leads to a transition of  $R_{\text{Hill}} < R_{\text{SOI}}$  for mass ratios typical of the solar system (the grey shaded area).

---

<sup>3</sup>Doing so I have to admit that the following discussion becomes pointless, but both definitions can be found in the textbooks like they are given here, so I will go on using the eccentricity only for the Hill sphere.

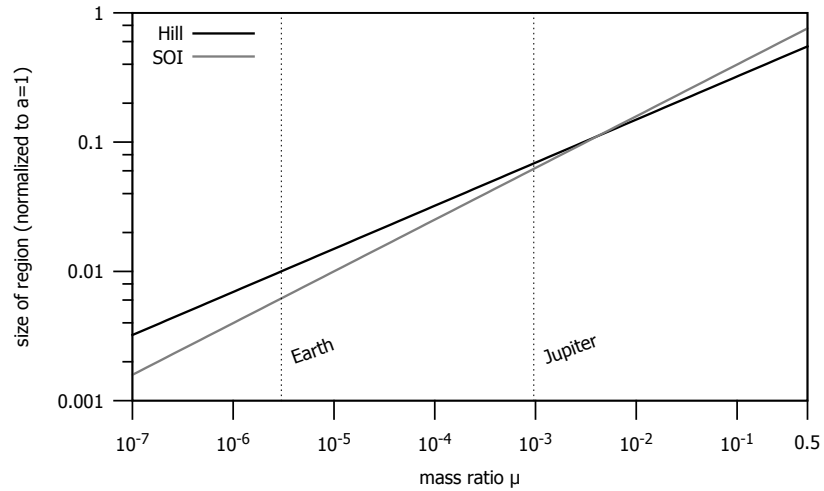


Figure 2.3: Showing the dependence of Hill sphere and SOI on the mass ratio for circular orbits ( $e = 0$ ). The different slopes result from the different powers of  $\mu$ ; they indicate that the SOI is smaller for small  $\mu$ , but it grows quicker for large  $\mu$ . The size of the region is normalised to unit distance  $a = 1$ ; vertical lines indicate the corresponding mass ratios for Earth and Jupiter.

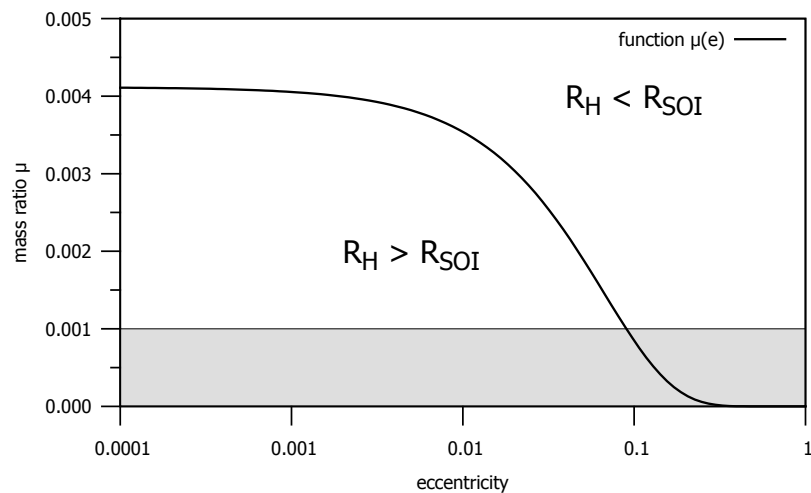


Figure 2.4: Limit mass ratio  $\mu(e)$  depending on the eccentricity where Hill sphere and SOI become equal. Above the curve the SOI is the better estimate for the region of dominating planetary influence, while below the curve the Hill sphere is more appropriate. The shaded area represents typical mass ratios in the solar system with  $\mu < 0.001$  (Jupiter's mass ratio). Note that the horizontal axis is given in logarithmic scaling, while the vertical axis uses linear scaling.

planet	a [AU]	eccentricity	mass [ $M_{\odot}$ ]	$R_{\text{Hill}}$ [ $10^6$ km]	$R_{\text{SOI}}$ [ $10^6$ km]
Mercury	0.39	0.206	$1.66 \times 10^{-7}$	0.175	0.112
Venus	0.72	0.007	$2.45 \times 10^{-6}$	1.004	0.616
Earth	1.00	0.017	$3.00 \times 10^{-6}$	1.472	0.925
Mars	1.52	0.093	$3.23 \times 10^{-7}$	0.983	0.577
Jupiter	5.21	0.049	$9.55 \times 10^{-4}$	50.56	48.23
Saturn	9.58	0.056	$2.86 \times 10^{-4}$	61.83	54.80
Uranus	19.23	0.044	$4.37 \times 10^{-5}$	67.15	51.90
Neptune	30.10	0.011	$5.18 \times 10^{-5}$	115.1	86.92

Table 2.1: Parameters for the calculation of the Hill radius and SOI radius for the planets in the solar system. Note that  $R_{\text{Hill}}$  and  $R_{\text{SOI}}$  depend linearly on  $a$ , but only with some fractional power on the mass.

The transition point, where the SOI becomes larger than the Hill sphere, can be shifted to such low mass ratios, that the usual assumption of the Hill sphere being the right measure for the gravitational influence of a body might be invalid. This can be true especially for highly eccentric exo-planetary systems consisting of two or more Jupiter-size planets.

After this discussion lets compare the two estimates for the solar system, table 2.1 provides the data. The values are visualised in figure 2.5 for better comparison. Due to the mostly low eccentricities in general the SOI is smaller than Hill sphere, while Jupiter is close to the transition mass ratio.

One important use of the Hill sphere and SOI is in numerical integrations of the motion of minor bodies. A close encounter between a planet and an asteroid is often defined to occur whenever the latter comes closer to the planet than several Hill radii.

## 2.5 Hyperbolic trajectories

In the two-body problem the trajectory of an object is determined by the initial conditions for all times (in the absence of external perturbations). Depending on the actual value of the Hamiltonian (total energy) either bounded motion (circular or elliptic) or unbounded motion (parabolic or hyperbolic) can occur; a third special case is rectilinear motion that will not be considered here.

To follow the trajectory of an object,  $(\mathbf{r}(t), \mathbf{v}(t))$  for  $t \in \mathbb{R}$ , the  $f$  and  $g$  functions provide an easy way by means of simple analytical formulae.

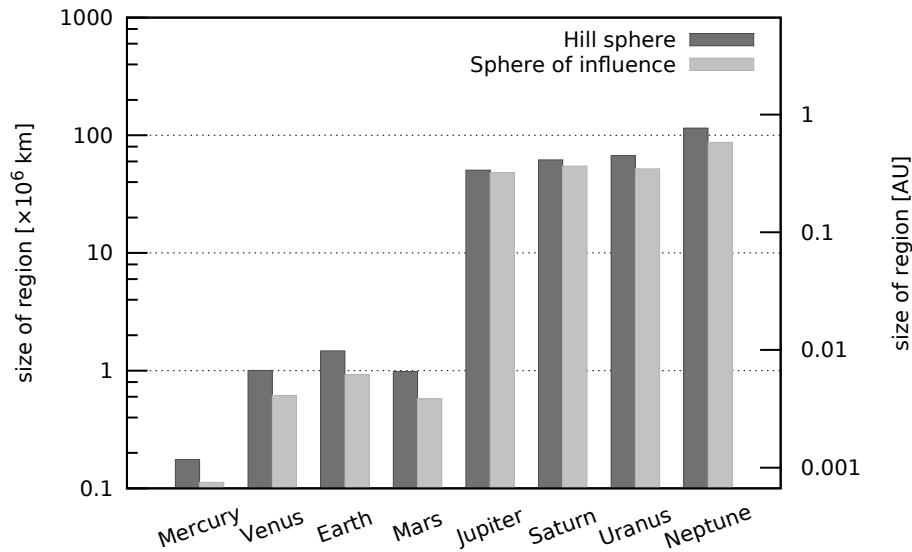


Figure 2.5: Comparison of the Hill radius and sphere of influence for planets in the solar system. Note the logarithmic scaling of the vertical axis; units are in millions of kilometers.

### 2.5.1 Hyperbolic $f$ and $g$ functions

The  $f$  and  $g$  functions map a given initial condition  $(\mathbf{r}(t_0), \mathbf{v}(t_0)) = (\mathbf{r}_0, \mathbf{v}_0)$  at time  $t_0$  to time  $t$ , as long as the angular momentum  $\mathbf{L} \neq 0$  (the reason will become clear a bit later). The new position and velocity are given by

$$\begin{aligned} \mathbf{r}(t) &= f(t, t_0) \mathbf{r}_0 + g(t, t_0) \mathbf{v}_0 \\ \mathbf{v}(t) &= \frac{\partial f(t, t_0)}{\partial t} \mathbf{r}_0 + \frac{\partial g(t, t_0)}{\partial t} \mathbf{v}_0 \end{aligned}$$

The  $f$  and  $g$  functions can be expressed either in terms of the eccentric anomaly, or of the true anomaly. In Danby (2003) and other literature preferentially the corresponding expressions for the elliptical case are discussed. For later purposes the hyperbolic forms are required here, and a short derivation will be presented.

For hyperbolic motion the eccentricity is  $e > 1$ , and hyperbolic trigonometric functions have to be used (Burkardt and Danby, 1983). Besides the true anomaly  $\varphi$ , an auxiliary variable – called hyperbolic eccentric anomaly  $H$  (in analogy to the elliptic eccentric anomaly  $E$ ) – is defined. In the orbital plane the position and velocity components are

parametrised by

$$\begin{aligned}
 x(H) &= a(e - \cosh H) \\
 y(H) &= a\sqrt{e^2 - 1} \sinh H \\
 \dot{x}(H) &= -\frac{na^2}{r(H)} \sinh H \\
 \dot{y}(H) &= \frac{na^2\sqrt{e^2 - 1}}{r(H)} \cosh H
 \end{aligned} \tag{2.5.1}$$

with the radial distance given by  $r(H) = a(e \cosh H - 1)$ .

The hyperbolic form of Kepler's equation (KE), relating the time  $t$  to the hyperbolic anomaly  $H$ , after Taff (1985) reads

$$e \sinh H - H = n(t - T) \tag{2.5.2}$$

where  $T$  is the time of pericenter passage (here it can be regarded as an arbitrary constant). Like its elliptic counterpart this equation is transcendental, meaning that no closed-form solution can be given.

To obtain the  $f$ ,  $g$  functions one starts from

$$\begin{aligned}
 f &= \frac{1}{D}(x \dot{y}_0 - \dot{x}_0 y) \\
 g &= \frac{1}{D}(x_0 y - x y_0) \\
 D &= x_0 \dot{y}_0 - \dot{x}_0 y_0 = |\mathbf{L}|
 \end{aligned}$$

and has to insert the corresponding expressions from equation (2.5.1), and must also use equation (2.5.2). After some time twiddling with the resulting equations we arrive at

$$\begin{aligned}
 f(t, t_0) &= 1 + \frac{a}{r_0}(1 - \cosh(H - H_0)) \\
 g(t, t_0) &= (t - t_0) + \frac{1}{n}((H - H_0) - \sinh(H - H_0)) \\
 \dot{f}(t, t_0) &= -\frac{na^2}{r r_0} \sinh(H - H_0) \\
 \dot{g}(t, t_0) &= 1 + \frac{a}{r}(1 - \cosh(H - H_0))
 \end{aligned} \tag{2.5.3}$$

where we have used  $\dot{f} = \frac{\partial f}{\partial t}$ ,  $\dot{g} = \frac{\partial g}{\partial t}$  for the third and fourth formula.

## 2.5.2 Solving the hyperbolic Kepler equation

In the way that the equations (2.5.3) are formulated, the only unknown parameter  $H$  is linked to time  $t$  (under the assumption that  $H_0$  for  $t_0$  has already been calculated). It would be possible to use directly equation (2.5.2) to determine  $H$ , but the slightly modified version (2.5.4) below proves to be more useful.

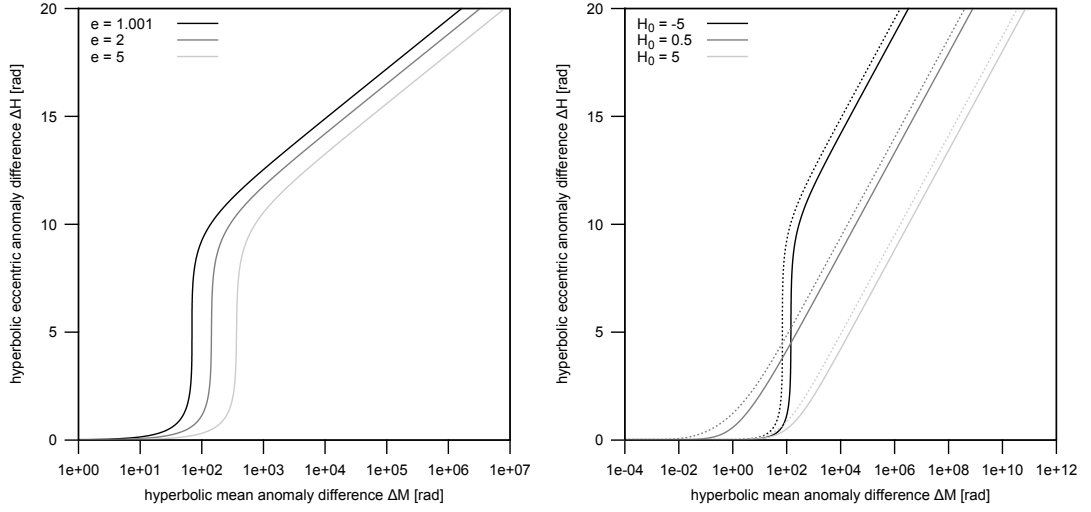


Figure 2.6: The influence of the parameters eccentricity  $e$  and initial hyperbolic anomaly  $H_0$  on the shape of the modified hyperbolic Kepler equation. Left panel:  $e$  is varied for a fixed value of  $H_0 = -5$  rad. Right panel:  $H_0$  is varied for two fixed values of  $e$  (solid line:  $e = 2$ , dotted line:  $e = 1.001$ ).

### The modified hyperbolic Kepler equation

The original hyperbolic Kepler equation (2.5.2) is written for the times  $t$  and  $t_0$

$$\begin{aligned} e \sinh H - H &= n(t - T) \\ e \sinh H_0 - H_0 &= n(t_0 - T). \end{aligned}$$

By subtracting the two equations from each other the arbitrary constant  $T$  cancels out, and it remains

$$e \sinh H - e \sinh H_0 - (H - H_0) = n(t - t_0).$$

This can be further simplified with  $x = \Delta H = H - H_0$ ,  $\Delta t = t - t_0$ , and using trigonometric addition theorems to expand into the modified hyperbolic Kepler equation (or extended KE)

$$e \cosh H_0 \sinh x + e \sinh H_0 (\cosh x - 1) - x = n \Delta t = \Delta M. \quad (2.5.4)$$

As there are three parameters now ( $e, H_0, \Delta M$ ), it is not intuitive to get a feeling for the influence of each of them. A visualisation of a few random cases is provided in figure 2.6. In the left part the initial hyperbolic eccentric anomaly is fixed to  $H_0 = -5$  radians, with increasing eccentricity the curves are shifted horizontally to the right along the  $\Delta M$  axis. It is obvious that around  $\Delta M \approx 100$  there is a sharp transition; and based on the exponential nature of the hyperbolic trigonometric functions a little change in

$\Delta H$  has to be compensated by a tremendous increase of  $\Delta M$  in equation (2.5.4). In the right part the influence of the parameter  $H_0$  is shown, where each pair of curves represents two different eccentricities, namely  $e = 2$  for the solid curves and  $e = 1.001$  for the dotted ones. The third parameter is the mean anomaly difference  $\Delta M$ , from which, together with the other two parameters, the value of  $\Delta H$  has to be computed.

Finally the remaining obstacle is to solve the modified (or extended) form of the hyperbolic Kepler equation

$$\begin{aligned} h(x) &= e_x \sinh x + e_y (\cosh x - 1) - x - \Delta M = 0, \\ e_x &= e \cosh H_0, \\ e_y &= e \sinh H_0, \end{aligned}$$

by any suitable numerical root-finding procedure, e.g. the well-known Newton-Raphson method. The computational details are discussed in the paper of Fukushima (1997). It is important to note that the parameter domain is large compared to the elliptic case, as  $1 < e < \infty$  and  $0 \leq \Delta M < \infty$  is admissible, which raises the problem to find a good starting value.

### Small $\Delta M$ region

A suitable starting value  $x_0$  is found by the natural choice  $x_0 = 0$  and by inserting this into the Newton-Raphson method. The first iteration gives

$$x_0 = \frac{\Delta M}{e_x - 1}$$

which is well suited for the “small  $\Delta M$  region”. By numerical experiments it was found to be suitable for values of  $0 \leq \Delta M < 100$  radians. Additionally, this starting value initially overestimates the hyperbolic eccentric anomaly difference  $x$ , which has been shown to be optimal for the convergence of the Newton-Raphson method (Charles and Tatum, 1997).

### Large $\Delta M$ region

For larger values of  $\Delta M$  Burkardt and Danby (1983) have presented the starting value

$$x_0 = \ln \left( \frac{2\Delta M + 1.8e}{e_x + e_y} \right).$$

It uses the fact that for values of  $x > 10$  the hyperbolic trigonometric functions  $\sinh(x)$  and  $\cosh(x)$  behave like  $\exp(x)$ .

Both starting value formulas can be used successfully for a wide range of  $\Delta M$  values (i.e. for long time spans), two examples are shown in figure 2.7. The small  $\Delta M$  region extends to about  $\Delta H = 1$  ( $\Delta M < 100$ ). The curves present the magnitude of the

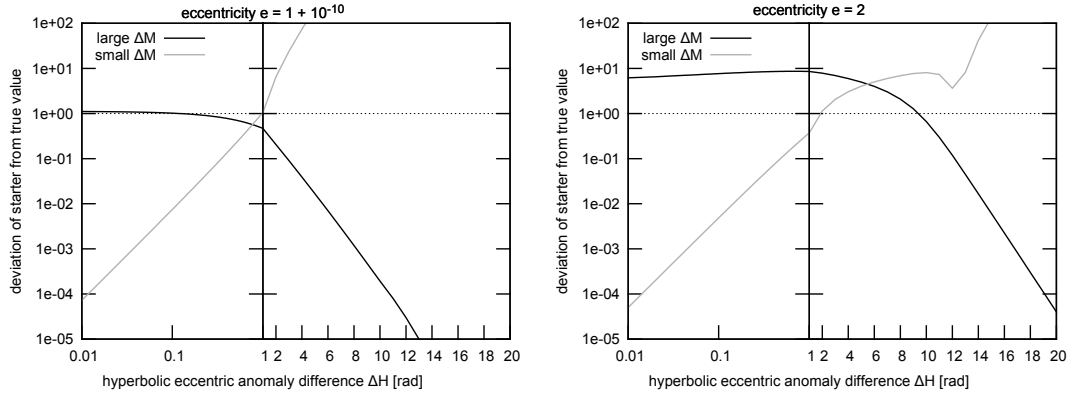


Figure 2.7: The starting values for iteration procedures provide good results only on limited intervals. Here two cases are shown: on the left for an eccentricity slightly above 1 and  $H_0 = 1.71$ , on the right for an eccentricity of  $e = 2$  and  $H_0 = -5$ . The black curves show the starting value designed for large  $\Delta M$ , the grey curves represent the small  $\Delta M$  starting value.

deviation by which the starting value differs from the true solution; as a visual aid the horizontal line for an error equal to 1 is plotted as a dotted line. The grey curve shows the small  $\Delta M$  starting value, whereas the black curve shows the large  $\Delta M$  starting value. One case is for an eccentricity of  $e = 2$  and  $H_0 = -5$ , a particularly difficult case for the large  $\Delta M$  formula, which starts to become acceptable only for  $\Delta M > 1000$ , but quickly increases in accuracy. The other part of the figure shows a challenging case for a very low hyperbolic eccentricity of almost 1, which is typical for an object on a nearly parabolic orbit hitting the Earth with a speed of just slightly above the escape velocity.

In chapter 4 the hyperbolic  $f$  and  $g$  functions will be used to trace back the trajectories of objects that have impacts with the Earth.

## 2.6 Distribution of points on a sphere

An iterative procedure is applied to uniformly distribute points on the surface of a sphere. Following the description of Reyes-Ruiz et al. (2012) the Fuller spherical distribution is constructed using the method of Saff and Kuijlaars (1997). Starting from the geometrical figure of an icosahedron, the number of vertices is increased exponentially to cover the surface of the sphere with uniformly distributed points.

An icosahedron has 12 vertices, the set of those points is

$$I = \{(0, \pm 1, \pm \varphi), (\pm 1, \pm \varphi, 0), (\pm \varphi, 0, \pm 1)\},$$

where  $\varphi = \frac{1}{2}(1 + \sqrt{5}) \approx 1.618$  is the golden number. Every vertex point has five neighbouring points, together they form an equilateral pentagon (see figure 2.9). The

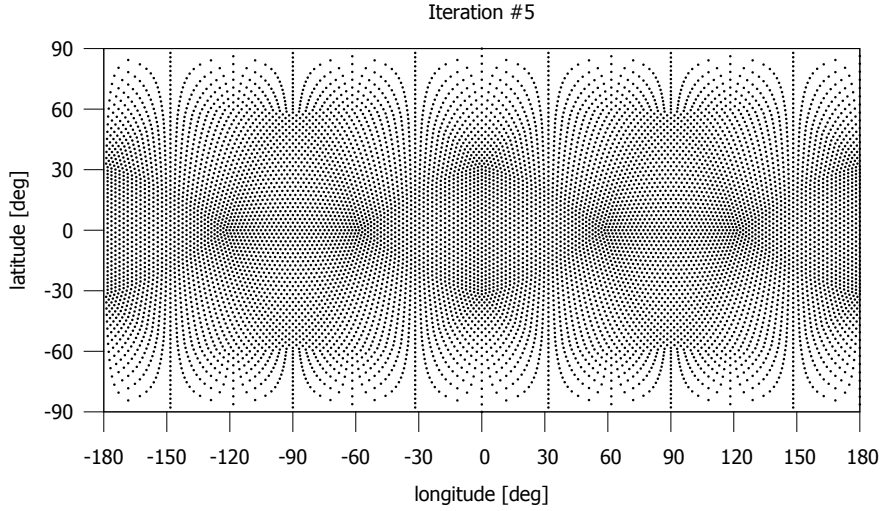


Figure 2.8: Projection of the vertices of a polyhedron onto the plane after 5 iterations.

length of each edge is  $\|P_m P_n\| = 2$  ( $m \neq n$ ), and the radius of the circumscribed sphere to the icosahedron is  $r = \sqrt{1 + \varphi^2}$ .

The process of constructing additional points consists of the following steps:

1. choose any point  $P_m \in I$  of the icosahedron and find its 5 nearest neighbours  $P_n$ ;
2. find the middle point  $M_{m,n} = \frac{1}{2}(P_m + P_n)$  on the line connecting these two points and add it as a new vertex;
3. repeat this for all other vertices excluding pairs already processed ( $M_{m,n} \equiv M_{n,m}$ );
4. and finally project all vertices to the (unit) sphere.

Let us denote by  $N_i$  the number of vertices at iteration  $i$ , so by definition  $N_0 = 12$ . This procedure gives 30 lines connecting neighbouring vertices and thus 30 new middle points, leading to  $N_1 = 12 + 30 = 42$  vertices after the first iteration,  $N_2 = 162$  after the second, and  $N_3 = 642$  after the third. Table 2.2 gives an overview of the number of vertices  $N_i$  after  $i$  iterations. One can notice that the last digit is always 2, while the other digits form a number that is a power of 2.

Reyes-Ruiz et al. (2012, eq.(2)) gave a recursive formula to compute the number of vertices after  $i$  iterations. By presuming an (obvious) exponential increase, from the ansatz  $N_i \propto a^i$ , I derived a simple *explicit* formula:

$$N_i = 10 \times 2^{2i} + 2.$$

iteration $i$	0	1	2	3	4	5	6	7
vertices $N_i$	12	42	162	642	2562	10242	40962	163842

Table 2.2: Number of vertices of a polyhedron after  $i$  iterations, starting from an icosahedron with 12 vertices. The numbers grow exponentially.

The two-dimensional projection of the point distribution in the latitude-longitude plane is shown in figure 2.8 by transforming the Cartesian coordinates into spherical coordinates. The points cover the surface of the sphere uniformly in three-dimensions, but in a two-dimensional projection this is distorted to an apparently non-uniform coverage.

The distribution of vertices on the surface of a unit sphere is visualised in figure 2.9. Four steps from the sequence of iterations are shown:  $i = 0$  for an icosahedron (top left),  $i = 2$  (top right),  $i = 4$  (bottom left),  $i = 6$  (bottom right). This last step (6th iteration) gives a mutual distance of two neighbouring points of  $2/2^6$ , resulting in an angular separation of approximately 1.8 degrees (or about 200 points along the circumference). Thus the coverage is quite complete already at this stage, and consequently this number of vertices will be used in the simulations for the virtual impactors.

The method presented here will be used later in section 4.2.2 to construct initial conditions with a uniform distribution on the surface of the Earth for virtual impactors.

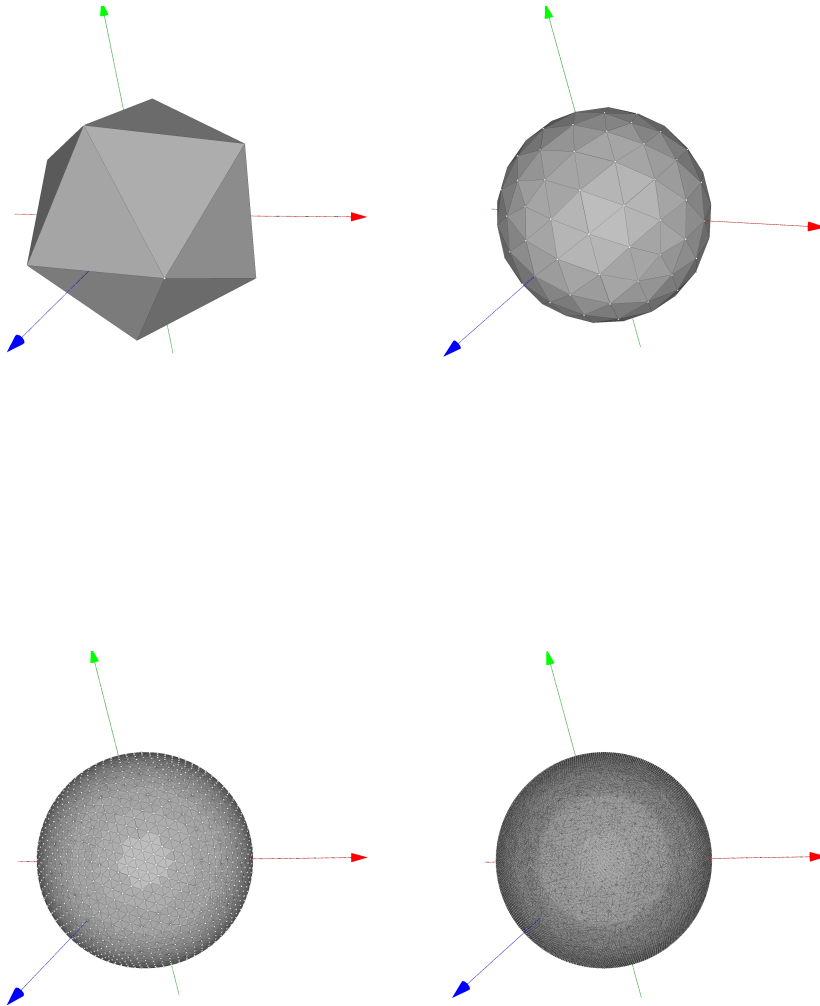


Figure 2.9: Visualisation of the iteration process to construct vertices of polyhedra that uniformly cover the surface of a sphere. The more iterations are performed, the closer the shape resembles a sphere. Top left: the initial stage of an icosahedron, top right: after two iterations, bottom left: after four iterations, bottom right: after six iterations. A Delaunay triangulation has been used to construct the faces based on the vertices.



# Chapter 3

## Long-time dynamics of Near-Earth Asteroids

This chapter's purpose is to investigate the dynamical evolution of an extensive subset of the current Near-Earth Asteroid population over a long period of time by taking into account the gravitational influence of the relevant planets.

A number of different dynamical models is used to quantify the role of the Earth's moon for the frequency of close encounters and impacts of NEAs with the Earth and other terrestrial planets. The dynamical models are presented in section 3.1.

In section 3.2 the initial conditions for the simulations are described, including the osculating elements for the planets, the Moon, and the NEAs. In addition to that, some properties of the NEA population are shown.

The results of the simulations can be found in section 3.3, and the data obtained is analysed with respect to the different dynamical models, but also a comparison of the two integration methods is performed.

Finally, these results are discussed in the context of previous investigations and published work in section 3.4.

### 3.1 Dynamical models

The investigation of the lunar influence on Near-Earth Asteroids requires a number of different dynamical models. The properties of these different models are discussed in the following.

#### 3.1.1 General aspects

In this section we will always use the term  $N$ -body problem regardless of how many massive objects are involved. Besides the massive bodies – the Sun and a variable number of planets – every model also includes up to several thousand massless Near-Earth Asteroids, restricted by the limitations of the numerical integration method.

A common feature of all models is that only point masses are considered. The non-sphericity (flattening) of the Sun or of individual planets (e.g. the Earth) is neglected

and, as a consequence, no higher order terms are used in the spherical harmonic expansion of the potential.

Another restriction is that only the pure (Newtonian) gravitational  $N$ -body problem is applied. At the required level of accuracy there is no need to add relativistic forces to the equations of motion, although this would be possible using a modified Lie-series integrator described in Bancelin et al. (2012).

Various non-gravitational forces also act on asteroids, and it has been shown that especially the Yarkovsky effect – which leads to a slow drift in semi-major axis – is an important factor (Hartmann et al., 1999; Vokrouhlický et al., 2000). An accurate description of the Yarkovsky effect requires a number of parameters that are currently not well constrained for the vast majority of asteroids. In order to simplify the analysis of the lunar gravitational effect on Near-Earth Asteroids I have decided to exclude the Yarkovsky effect from the models.

The time interval for the numerical integration is fixed to  $10^7$  years. This value is a compromise that balances the computational cost (and overhead in recalculating the planetary orbits repeatedly for the different models) and the various dynamical time scales involved. It was shown in Gladman et al. (1997, 2000) that asteroids, directly inserted into mean-motion or secular resonances in the main-belt, can evolve into Earth orbit crossing objects within  $10^6$  years. The median dynamical lifetime of these objects in the near-Earth region was about 10 million years, they were removed by collisions or ejections. In the published literature there is considerable disagreement on the dynamical lifetimes, the values range from  $10^6$ – $10^9$  years, and some authors give only collisional lifetimes, that neglect other effects like resonances.

However, according to the results of Gladman et al. (2000) the chosen integration time seems reasonable, but there is another point to be kept in mind. As the Near-Earth Asteroids evolve in time, they will be subject to different orbital resonances: mean-motion resonances have rather short time-scales, while the secular resonances have associated time-scales of  $10^4$  –  $10^6$  years. For instance, the secular fundamental frequency  $g_5$  of Jupiter has a period of  $3 \times 10^5$  years, while  $g_8$  for Neptune has a period of  $2 \times 10^6$  years (Laskar, 1990). To include the effect of these resonances, the integration time has at least to cover these time-scales, and again the above value represents a sensible choice.

As it is well known the lunar orbit is evolving in time not only due to planetary perturbations, but also due to the secular tidal acceleration of its orbit (Goldreich, 1966; Touma and Wisdom, 1994). Angular momentum is transferred from the spin of the Earth to the orbit of the Moon, leading to an increase in the spin period of the Earth and the orbital period of the Moon. From the Lunar Laser Ranging (LLR) experiments one can observe that currently the Moon recedes from the Earth at a rate of 38 mm/year (Calame and Mulholland, 1978; Williams et al., 1978). A quick estimate of the magnitude of this tidal evolution over  $10^7$  years reveals that it would sum-up to an increase of 380 km in the average lunar distance. Comparing this to the current mean distance of 384 400 km yields a relative error of only 0.1% when neglecting the tidal acceleration in the dynamical models.

### 3.1.2 Details of models

The dynamical models consist of three pairs of models with increasing completeness and complexity. Completeness means that gradually more and more dynamically relevant planets are added to the models; while complexity simply means that the phase-space becomes higher dimensional as more massive objects increase the degrees of freedom and number of interactions.

Here are the dynamical models:

**M2** Sun, Earth, and NEA

**M3** Sun, Earth, Moon, and NEA

**M4** Sun, Venus, Earth, Mars, and NEA

**M5** Sun, Venus, Earth, Mars, Moon, and NEA

**M6** Sun, Venus, Earth, Mars, Jupiter, Saturn, and NEA

**M7** Sun, Venus, Earth, Mars, Jupiter, Saturn, Moon, and NEA

The number associated to each model indicates the number of massive objects only, as opposed to the classical sense of giving the total number of objects. For each pair of models, in one of the models the Moon is present while in the other model it is not.

The first pair M2/M3 represents the simplest case of a restricted three-/four-body problem. These models serve to assess the dynamics of Near-Earth Asteroids in the absence of any perturbers except for Earth and Moon.

The second pair M4/M5 can be labelled “Inner Solar System” (ISS), it contains the relevant bodies that influence the orbits of NEAs by close encounters.

The last pair of models M6/M7 is the almost complete (in terms of planets) “Solar System”. Jupiter and Saturn are the major perturbers of Near-Earth Asteroids among the planets by virtue of their dominating masses.

In the models M2, M4, and M6 the Earth-Moon system is actually modelled as a single body (called “Earth” henceforth) with the combined mass of Earth and Moon located at the common barycenter. For the real Earth-Moon system the barycenter is always located inside the physical radius of the Earth, it lies approximately 1700 km below the Earth’s surface (Roncoli, 2005). In all other models the Earth and Moon are separate objects with their respective masses.

### 3.1.3 Justification of models

With the two models M2/M3 statistical effects and the qualitative differences in the long-term dynamics of Near-Earth Asteroids can be compared. It is not claimed that they represent well the dynamics of real NEAs, but they allow to determine the lunar perturbations most clearly. In many investigations the Earth-Moon system is not treated

as separated bodies, but as one single object with the combined mass of the two located at their barycenter (Earth-Moon-Barycenter model, EMB). In contrast to this, it was shown by Kankiewicz (2002) that it is absolutely necessary to treat the Earth and Moon as separate objects for asteroids having close encounters with the Earth, or otherwise the computed orbits are not precise enough.

The models M4/M5 involve those planets, whose orbits are crossed by the majority of Near-Earth Asteroids. Main-belt asteroids that first become Mars crossers can evolve into Amor group objects. Later these Amors may become Earth crossing Apollo group or even Aten group asteroids. Finally Atens can also cross the orbit of Venus. Mercury is excluded from this model partly due to its low mass, but also because there are no close encounters with this planet, except for some Atens and the very few known Inner Earth Objects (IEOs, or Atiras). A positive side-effect of ignoring Mercury in the models is that the numerical calculations are faster, the step-size need not be decreased to account for Mercury's rather short orbital period.

As of the models M6/M7 one has to remark that both Jupiter and Saturn are essential to get a rather complete picture of the dynamics of asteroids in general. Nesvorný and Morbidelli (1998a) have shown that main-belt asteroids are not only suffering from mean-motion resonances with Jupiter, but that three-body resonances with Jupiter and Saturn also play a crucial role. Another aspect of the dynamical influence of Jupiter and Saturn on the inner solar system was shown in Pilat-Lohinger et al. (2008), who found that a strong secular resonance could destabilise the orbits of test particles in the Venus to Earth region. Contrary to this, Uranus and Neptune do not seem to play such an important role for the dynamics of the ISS; partly because there are neither (linear) secular resonances (Michel et al., 1997) nor important mean-motion resonances with those planets (Gallardo, 2006). In Bazzó et al. (2010) it was shown – by using a set of dynamical models similar to the present work – that Uranus and Neptune can be safely ignored when studying the dynamics of the ISS.

### 3.1.4 Summary

Finally, here I give an overview of the key features and limitations of the models. This shall serve as a quick reference if questions arise when reading later sections.

The main points about the dynamical models are:

- three pairs of models (M2/M3, M4/M5, M6/M7) including a variable number of planets are defined;
- we can compare models using a combined Earth-Moon barycenter to those with the separated Earth + Moon;
- neither relativistic effects nor non-gravitational forces are taken into account, only purely Newtonian gravitational forces;

- all objects are point masses, no higher order terms arising from the spherical harmonic expansion of the potential are used;
- the integrations cover a time interval of  $10^7$  years;
- the tidal acceleration of the lunar orbit is neglected.

## 3.2 Initial conditions

For the actual integrations a number of preliminary parameters have to be fixed. Among others, one parameter is the initial epoch that determines the (osculating) orbital elements for the planets and asteroids. A second important point is the choice of the sample of NEAs, and the intrinsic properties of the NEA groups.

### 3.2.1 The Planets

The main focus of this part of the thesis is on the dynamics of Near-Earth Asteroids over long time intervals, so it is of minor importance on which exact date the integrations start.

The osculating heliocentric elements of the planets have been obtained from the JPL Horizons<sup>1</sup> on-line ephemeris system (Giorgini et al., 1996) for the Julian date JD 2451545.0, corresponding to the calendar date of 2000/January/01 at 12:00 UT. The reference epoch is J2000.0 for the planets and the Moon.

The osculating heliocentric elements for the given epoch for each planet are shown in table 3.1; note that the numbers are given only with a limited precision, the full precision numbers can be retrieved as described above. For the masses of the planets in units of the solar mass see table 2.1.

The Moon itself is treated as another “planet” in the corresponding models, i.e. it moves in a heliocentric elliptical orbit about the Sun. Note that the *geocentric* elements of the Moon are quite different from what the numbers in table 3.1 suggest: the mean semi-major axis is 384 400 km or about 0.00257 AU, the mean eccentricity is  $e = 0.0549$ , and the mean inclination to the ecliptical plane is  $i = 5.15^\circ$ . For the Earth-Moon mass-ratio I used the value 81.3. All these numbers were taken from Roncoli (2005).

### 3.2.2 The Near-Earth Asteroids

The osculating elements for the Near-Earth Asteroids used in the integrations were also obtained from the JPL Horizons ephemeris system in the year 2011. The NEA’s elements were defined for different epochs, and consequently at the begin of every integration the

---

<sup>1</sup>see homepage at <http://ssd.jpl.nasa.gov/?horizons>

planet	$a$ [AU]	$e$ [ $\times 10^2$ ]	$i$ [ $\times 10^4$ , deg]	$\omega$ [deg]	$\Omega$ [deg]	$M$ [deg]
Venus	0.723 327	0.6756	33946	55.19	76.68	49.31
Earth	1.000 372	1.7042	2.6736	297.77	163.97	358.19
Moon	0.971 418	2.9829	142.61	213.88	359.35	249.94
Mars	1.523 678	9.3315	18499	286.54	49.56	19.09
Jupiter	5.205 109	4.8923	13047	275.12	100.49	18.72
Saturn	9.581 452	5.5599	24843	335.90	113.69	320.38

Table 3.1: The initial osculating heliocentric orbital elements of the planets at JD 2451 545.0 for the long-term simulations. The orbital elements are: semi-major axis  $a$ , eccentricity  $e$ , inclination  $i$ , argument of perihelion  $\omega$ , longitude of ascending node  $\Omega$ , mean anomaly  $M$ . The numbers are not given to full accuracy here; also note that the eccentricities and inclinations are scaled by the indicated number.

	NEA group			
	Amor	Apollo	Aten	total
number of objects (2011)	2940	4291	652	7883
fraction of total [%]	37.3	54.4	8.3	100
number of objects (2015)	4600	6448	888	11936
fraction of total [%]	38.5	54.0	7.4	100

Table 3.2: The absolute and relative frequency of objects belonging to the different NEA groups. The data for the integrations were acquired in 2011. For comparison the current number of NEAs (in January 2015) is included.

planetary elements have to be propagated forward in time to meet the NEA’s initial epoch.

In total 7883 Near-Earth Asteroids are contained in the data files, but they are not equally distributed among the different NEA groups. Most NEAs belong to the Apollo group, the Amor group is the second most numerous, and the Atens form the smallest group. In table 3.2 the absolute number of objects in each group is shown, as well as the corresponding fraction of this group to the total population for the years 2011 and 2015. Since, at that time and still today, the Near-Earth Asteroids constituted about 99% of all Near-Earth Objects (NEOs), the results and conclusions obtained from the integrations (discussed later) are only negligibly affected by ignoring this minor rest of 1%.

Another issue is the continuously increasing number of NEAs, due to effective automatic monitoring programs covering large areas of the sky. Although the absolute numbers were constantly increasing during the last couple of decades<sup>2</sup>, the relative fraction of the groups did not change appreciably. Comparing the data from 2011 to current numbers (January 2015) one can see that the total number was only about 66% of the current population (almost 12 000 objects), but the fractions changed only by some tenths of a percent (most notably the Amor group fraction increased by  $\sim 1\%$  while the Aten group fraction decreased by the same amount).

### Selection of samples

For the simulations with the Lie-series integrator a sample of 300 objects per NEA group was chosen, for a total of 900 objects. This had to be done in order to overcome technical limitations on the number of objects that can be integrated simultaneously. For models M6 and M7 the sample was further reduced to 100 NEAs per group, due to a lower performance of the integration process. This reduction of the sample size will play a role in the calculation of quantities that need to be normalised by the number of objects in the sample, such that the associated uncertainties will be higher than for a larger sample.

There was no sophisticated selection process, I took the first 300 objects from the data files. In those data files the NEAs were sorted according to their official designation, or by detection date in case they had no designation yet, so that effectively objects with a higher number of observations and more reliable orbital elements were selected. The equal number of NEAs in the samples does not take into account the unequal absolute number of objects of the real NEA groups. In this way 46 % of the Aten group was sampled, but only 10 % and 7 % of the Amor and Apollo group, respectively. Unless it is stated otherwise, I will perform comparisons only on a per-object basis, i.e. with values normalised by the number of objects in the sample.

Using the Mercury package the whole NEA population of 7883 objects was included into the simulations, since the performance of this method allows for a higher number of objects than the Lie series integrator.

The results from the Mercury integrations will be interpreted as being representative for the respective NEA group for two reasons: (i) because the whole population (known at that time) was considered, (ii) because the validity of the results depends only weakly on the absolute number of NEAs, but rather on the relative fraction of objects in the different NEA groups, which (as discussed above) remained quite constant since then.

Bottke et al. (2002) provide a synthetic NEO population that by design should eliminate the effects of observational bias on the currently detected NEO population. The orbital element distributions suggest that a considerable fraction of NEOs at high eccentricities and moderate to high inclinations have not been discovered yet. For the aim

---

<sup>2</sup>see discovery statistics <http://neo.jpl.nasa.gov/stats/>

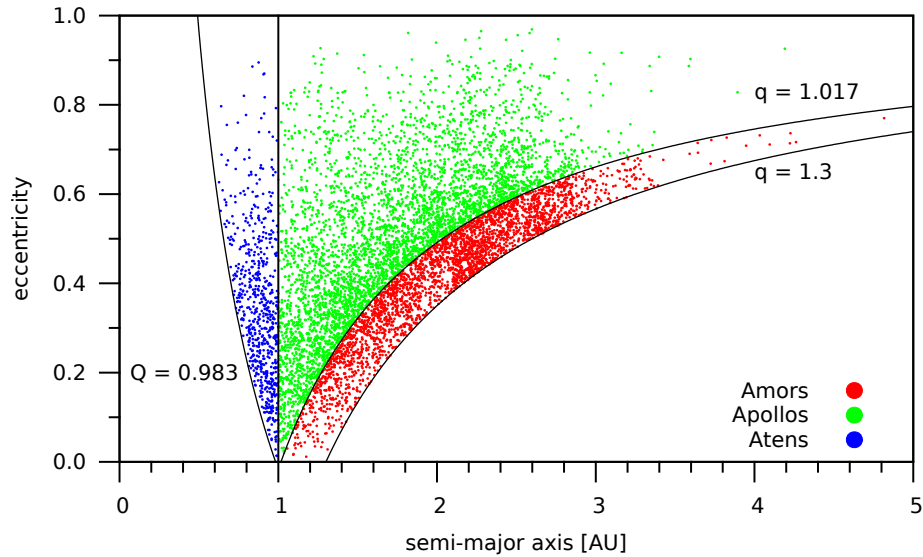


Figure 3.1: In a semi-major axis versus eccentricity plot the NEA groups based on the Shoemaker classification become apparent. The various curves display the borders defined for the NEA population based on the aphelion distance  $Q$  (for  $a < 1$  AU) and perihelion distance  $q$  (for  $a \geq 1$  AU).

of this work I see no point in considering a population of currently undiscovered objects. The lunar effect on NEAs will become clear already from the known population, any additional objects would not much improve the results.

### Properties of the NEA population

We can take a look at the (osculating) orbital elements of the Near-Earth Asteroids and derive some properties of the population.

The original Shoemaker classification of the NEA groups (Shoemaker et al., 1979) depends only on the semi-major axis and eccentricity. In figure 3.1 the division of the three NEA groups is shown. An asteroid must have an aphelion distance  $Q \geq 0.983$  AU (for  $a < 1$  AU) or a perihelion distance  $q \leq 1.3$  AU (for  $a \geq 1$  AU) in order to be qualified as a Near-Earth Asteroid. Apollos and Atens are distinguished by their semi-major axis being greater and smaller than 1 AU, respectively; Apollos have perihelion distances smaller than 1.017 AU while Amors have larger values. The figure shows clearly that many NEAs actually have semi-major axes that would be considered typical for a main-belt asteroid (between 2 – 4 AU), and it is only thanks to their rather high eccentricities that they are Earth (and/or Mars) orbit crossing asteroids.

In figure 3.2 the distribution of the different orbital elements is visible, from top to bottom for semi-major axis, eccentricity, and inclination.

	eccentricity		inclination	
	mean $\pm$ std. dev.	median	mean $\pm$ std. dev.	median
Amors	$0.42 \pm 0.14$	0.45	$14.6 \pm 11.8$	10.9
Apollos	$0.51 \pm 0.18$	0.52	$13.5 \pm 12.5$	9.4
Atens	$0.35 \pm 0.16$	0.33	$13.6 \pm 10.5$	10.7

Table 3.3: A statistical summary of the eccentricity and inclination (in degrees) for the NEA groups at the initial epoch. These values are based on the entire NEA population, as given in table 3.2. For easier comparison both the mean plus standard deviation and the median values are shown.

The histograms in the top row show the semi-major axis distribution extending out up to a limit of 5 AU for the Amor and Apollo group (with a few objects having even larger values). The width of the bins is  $\Delta a = 0.1$  AU for all three images; but note that the Atens occupy a much narrower semi-major axis interval. Although these images are based on osculating elements, there is an indication of some important mean motion resonances (MMR). One can observe a decrease in the number of Amor and Apollo objects at 1.5 AU (MMR 1:1 with Mars), at around 2 AU (MMR 4:1 with Jupiter) and at 2.5 AU (MMR 3:1 with Jupiter). Also observe that the Amors show a pronounced bimodal distribution for the semi-major axis. Interestingly there seem to be no Atens with semi-major axes smaller than 0.6 AU. The abrupt cut at 1 AU for Atens and Apollos is caused by the definition of the groups.

In the middle row are the histograms for the eccentricity. They show the different locations of the peaks of the distribution: the peak for Amors is at around 0.5, that for the Apollos at 0.6, while for the Atens at 0.35; the width of each bin is  $\Delta e = 0.05$ . It follows that on average the Apollos have the highest eccentricities, which in turn is an important parameter for the relative velocities at close encounters.

The bottom row gives the histograms for the inclination, with a bin-width of  $\Delta i = 5^\circ$ . The maximum value displayed is  $90^\circ$ , only two objects have higher values and move on retrograde orbits. All three groups have peak values below 10 degrees, but the tails extend to relatively high inclinations.

A statistical summary of the eccentricity and inclination of the NEAs is given in table 3.3. The mean and median values are shown based on the data for the entire population at the given initial epoch. Those numbers underline again, that the Apollos have the highest eccentricities on average, and that the majority of NEAs (regardless of the group) have moderately inclined orbits of up to 20 degrees.

Before going on with the discussion of the properties of the NEAs, we have to introduce two parameters that combine (some of) the orbital elements to form a new relation.

1. The Tisserand parameter  $T$  is derived from the conservation of the Jacobi constant

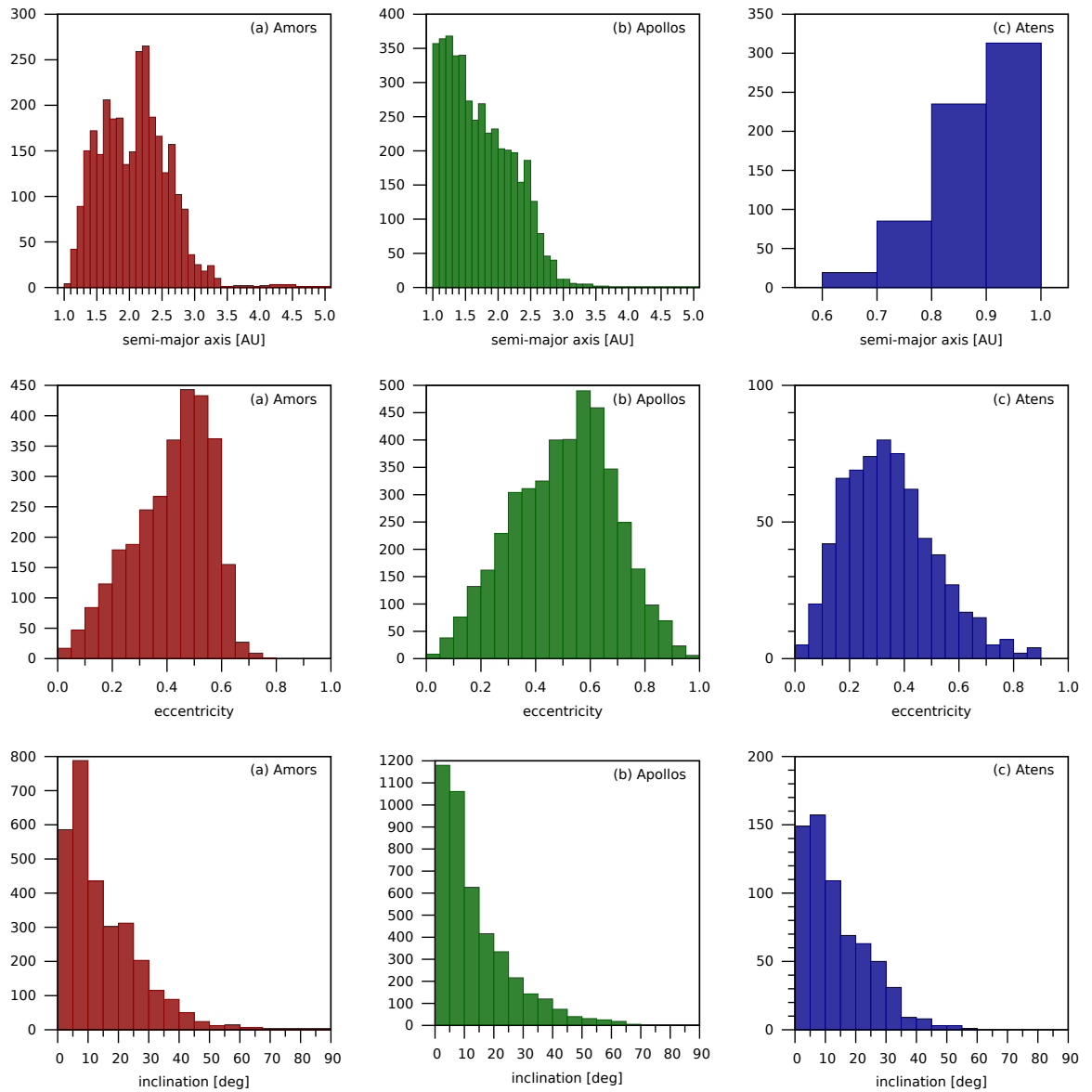


Figure 3.2: Histograms of the frequency distribution of the orbital elements semi-major axis (top row), eccentricity (middle row), and inclination (bottom row) for the different NEA groups: (a) Amors, left column, (b) Apollos, center column, (c) Atens, right column. The width of the histogram bins is the same in each row; the vertical axis gives the number of objects per bin, and so it depends on the number of NEAs per group.

in the restricted three-body problem. When  $T$  is expressed in orbital elements it reads (Michel et al., 1996)

$$T(a, e, i) = \frac{a_P}{a} + 2 \cos i \sqrt{\frac{a}{a_P} (1 - e^2)}, \quad (3.2.1)$$

where  $(a, e, i)$  are the orbital elements of the NEA, and  $a_P$  is the semi-major axis of the corresponding planet to which the Tisserand parameter is related. It was shown in Michel et al. (1996) that for small  $e, i$  and  $a \approx a_P = 1$  the lowest order Taylor-expansion becomes  $T = 3 + \mathcal{O}(e^2, i^2)$ . Consequently, NEAs with nearly circular and co-planar orbits will stay close to  $T = 3$ . The Tisserand parameter is a constant only in the restricted three-body problem, but while the NEA's orbital elements are modified by close encounters, it will change only slightly.

2. The  $w$  parameter is defined after Chapman (1979) as

$$w(e, i) = \sqrt{e^2 + \sin^2 i}. \quad (3.2.2)$$

This parameter provides a measure of the deviation from a circular and planar orbit. The natural range of  $w$  is  $0 \leq w \leq 2$  for  $0 \leq e \leq 1$ , and  $0 \leq i \leq 180$  degrees. However, note that in Chapman (1979) the definition was slightly different, as it did not include the sine of the inclination, but the inclination itself directly. The current definition seems more appropriate when applying the  $w$  parameter to highly inclined NEAs.

From the definitions given above, it is obvious that a relation exists between  $T$  and  $w$  via the expression  $e^2 = w^2 - \sin^2 i$ , that can be inserted into equation (3.2.1) to give  $T(a, w, i)$ .

For figure 3.3 the orbital elements  $(a, e, i)$  of the three NEA groups have been transformed to the  $(w, T)$  plane. It is visible that for both Amors and Apollos there is a sub-population that stays around the horizontal line  $T = 3$ , while the parameter  $w$  is increasing. The extended curved tails include objects with high eccentricity and/or inclination. The plot for the Atens is less dense because of the fewer objects in this group.

### 3.3 Results

This section presents the results of the numerical integrations obtained by the Lie and Mercury integration methods discussed in section 2.2.

A comparison is performed focusing on the qualitative differences in the evolution of Near-Earth Asteroids using the defined set of dynamical models. The quantitative measure of the lunar influence on the dynamical evolution of NEAs is then derived from

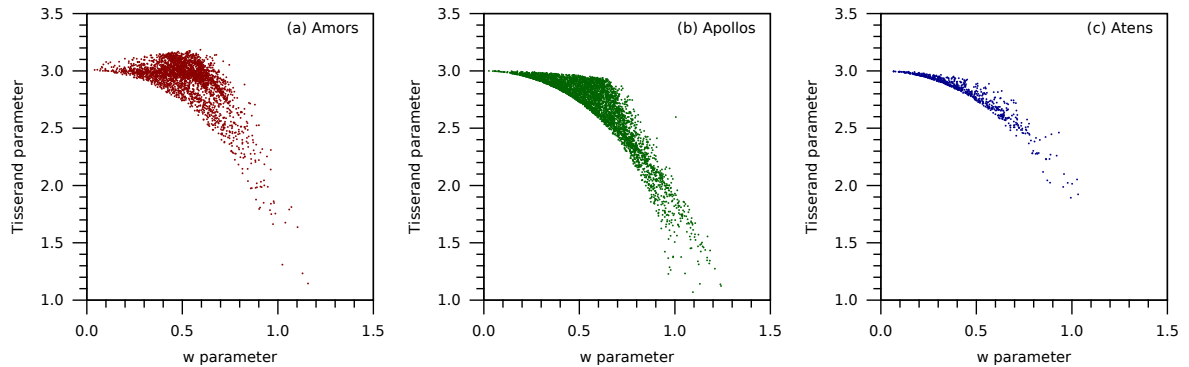


Figure 3.3: A plot of the Tisserand parameter  $T$  versus parameter  $w$  for the different NEA groups. From left to right Amors, Apollos, and Atens. The value  $T = 3, w = 0$  indicates a NEA with circular orbit that is co-planar to Earth’s orbit.

the number of close encounters and impacts with terrestrial planets, but mainly with the Earth.

There is an important difference in the definition of the close encounter distance for the Lie and Mercury integrator. In the first case, for the Lie integrator, the close encounter distance was set to 0.00257 AU, which corresponds to the average lunar distance (LD). In this way only “deep” close encounters are detected where a NEAs would pass the Earth-Moon system within the lunar distance. For the Mercury integrator the close encounter distance was relaxed to one Hill radius, which amounts to about 0.01 AU for Earth (see table 2.1 and figure 2.5). Since the Mercury integrations include far more NEAs than the Lie integrations – and also due to this larger close encounter limit – much more close encounters will be detected in the Mercury data.

### 3.3.1 Preliminary checks

In a first step the reliability of the numerical methods has to be assessed. For this purpose two test runs were performed:

1. The first run checks for the conservation of the integrals of motion, i.e. total energy and angular momentum in the  $N$ -body problem.
2. The second run compares the evolution of the lunar orbit for two models with a different number of perturbers.

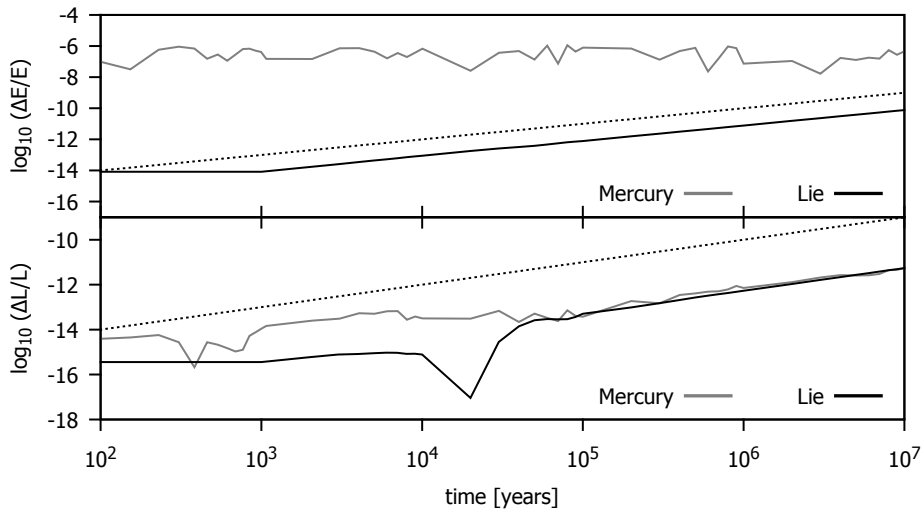


Figure 3.4: Conservation of the total energy (top) and angular momentum (bottom) for the two numerical integration methods used: Mercury hybrid-symplectic integrator (grey), Lie-series integrator (black). The dotted lines show the typical behaviour of numerical errors in case when round-off is the dominant source of error.

### Test I: Conservation of the integrals of motion

A standard test for any numerical method used in  $N$ -body dynamics is how accurately it manages to fulfill the conservation of total energy and total (specific) angular momentum. While the first is a scalar quantity, the latter is a vector, but for the test we take only its absolute value. For our purpose we are interested in the fractional changes  $\Delta E/E$  and  $\Delta L/L$ , i.e. the difference  $\Delta E = E(t) - E(0)$  relative to the initial value  $E(0)$  (the same for  $L$ ).

The test run was performed by using model M7, including the Sun, the planets Venus to Saturn, the Moon, and three massless NEAs, namely (1221) Amor (= 1932 EA1), (1862) Apollo (= 1932 HA), (2062) Aten (= 1976 AA). The total integration time was set to  $10^7$  years, which is the same as for the actual integration runs.

In the analysis of Quinn and Tremaine (1990) it was shown that for long-term integrations of the planetary system round-off error is the dominant source of error. Round-off error leads to a behaviour of the form  $\Delta E/E \simeq n\epsilon$  increasing linearly with the number of integration steps  $n$  (or equivalently linear with time), where  $\epsilon$  is the floating-point precision ( $\epsilon = 2^{-53}$  for double precision calculations).

In figure 3.4 a log-log plot of time versus the fractional change in total energy (top) and angular momentum (bottom) is shown. From this figure it is visible, that both the

Lie-series method (black curve) and the hybrid-symplectic method (grey curve) do a nearly optimal job regarding the conservation of angular momentum. The dotted curves show the typical  $\log_{10} t$  behaviour of round-off error (shifted vertically by an arbitrary constant), after a transient time both numerical methods follow this trend for the angular momentum. In the top panel the fractional change of the total energy is shown, where the intrinsic properties of the two methods – as discussed in the respective sections 2.2.1 and 2.2.2 – are clearly distinguishable. The Lie-series method shows an energy error that is dominated by round-off. The Mercury symplectic method has an oscillating – but on average constant – energy error, that is due to truncation error. One could decrease the truncation error either by using a higher order symplectic method or by choosing a smaller step-size.

### Test II: Lunar orbit in two models

This test calculation aims at detecting any inconsistency in the time evolution of the lunar orbit. Since some of the different dynamical models include a number of perturbing planets, these perturbations could affect the lunar orbit and lead to indirect effects on the motion of NEAs.

As a check let us compute the gravitational forces on the Moon arising from the Sun or any planet, via

$$F_{i,j} = k^2 m_i m_j r_{i,j}^{-2}$$

where  $k$  is the Gaussian gravitational constant (in units of AU, solar masses and days),  $m_i$  is the lunar mass,  $m_j$  and  $r_{i,j}$  are the mass and distance of the planet considered in a coordinate system centered on the Moon. An order-of-magnitude estimate of these forces (normalised relative to the force exerted by the Sun) reveals that the largest effects are due to Sun and Earth; the force due to Earth is about 40 % of that from the Sun. The third strongest force comes Jupiter with a magnitude of about  $10^{-5}$ , followed by Saturn and Venus with  $10^{-6}$ . All other planets contribute with normalised forces of the order of  $10^{-8}$ . The main point here is that the lunar orbit is mainly determined by the Sun and Earth, and that the main perturbers are all included in the model M7.

For the computations the two extreme cases were selected. In the first case the dynamical model is the three-body problem and consists of the Sun, Earth, and Moon. In the second case the model is the full planetary system, including all planets from Mercury to Neptune. The equations of motion were solved numerically for a time-interval of  $10^6$  years, and the Moon's geocentric distance is used to compare the models. Figure 3.5 shows the results. There is no qualitative difference for the lunar orbit for neither model, furthermore even the quantitative differences are small, e.g. the maximum and minimum distances are almost equal for the observed time span. This shows that it is possible and accurate to use Earth and Moon as separated objects (as opposed to both being joined together in the Earth-Moon barycenter) in the various models for at least  $10^7$  years.

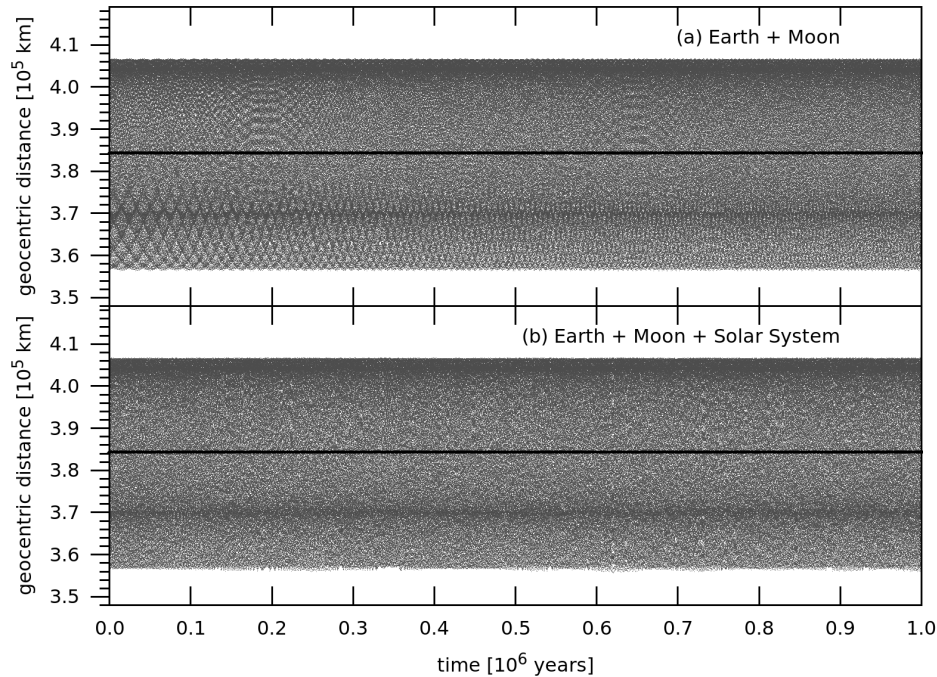


Figure 3.5: Time evolution of the geocentric lunar distance in different models. Top: three-body problem Sun-Earth-Moon; bottom: full planetary system. The bold horizontal line marks the average lunar distance today:  $d = 384\,400$  km.

### 3.3.2 Models M2/M3

The simplest dynamical models used are M2 and M3. The first model is just an elliptic restricted three-body problem, where the dynamics of Near-Earth Asteroids is either dominated by close encounters with Earth, or by a slightly perturbed two-body motion in the absence of close encounters. In the latter model the influence of the Moon introduces more degrees of freedom, but the dynamics is basically still the same. If close encounters happen, then the NEAs will have to pass both Earth and Moon, as the separation between the two is roughly  $0.00257$  AU.

#### Dynamical behaviour of NEAs with individual examples

For these two models one can observe a qualitative difference in the dynamical behaviour of the Amors and Apollos/Atens. Amor group objects are not Earth orbit crossing asteroids in the beginning, whereas Apollos and Atens do have frequent close encounters. The effect of close encounters is markedly visible in the time evolution of the semi-major axis, they appear as discontinuous jumps and lead to a step-function-like behaviour.

Amor group objects have initial perihelion distances between 1.017 and 1.3 AU that do not permit close encounters to Earth immediately. First for some period of time the eccentricity shows a secular variation, and only when it is large enough – or in other words the perihelion distance is low enough – can close encounters occur<sup>3</sup>. Many Amors never reach an eccentricity that is high enough for starting close encounters, and thus the absolute number of encounters and impacts is lowest for the Amors.

A typical example for the evolution of Amors in these models is the object (1943) Anteros (= 1973 EC). Figure 3.6 shows how its Tisserand parameter and semi-major axis (together with the perihelion distance) evolve during the 10 Myr integration time (upper graph). The top half of the image displays the time evolution of the Tisserand parameter; as a single parameter it includes the variations of all three relevant (osculating) orbital elements ( $a, e, i$ ). This object does not have any “deep” close encounters (closer than the lunar distance) to Earth for almost 5 Myr and shows a quasi-periodic signal. Then a sequence of close encounters (indicated by vertical grey lines) modifies its semi-major axis. For comparison the bottom half of the image shows the semi-major axis  $a$  (in black) and perihelion distance  $q$  (in grey), as well as the line  $a = 1$  (dotted horizontal line). The vertical grey lines indicate again close encounters within the lunar distance. Although one can observe from the curve for  $a$  that (distant) encounters also occur before 5 Myr, in the first 1 Myr the eccentricity is not large enough for close encounters to happen anywhere else than in pericenter. After the beginning of the sequence of deep close encounters the semi-major axis shows a chaotic behaviour, like a random walk. For the rest of the integration the perihelion distance remains close to 1 AU.

The evolution of  $a, e$  is also reflected by the Tisserand parameter in the lower graph. During the whole time this object lies between the Tisserand parameter contour lines  $2.95 < T < 3$  (expressed for an inclination of  $i = 0^\circ$ ). The horizontal and vertical extension of the black dots (that represent the instantaneous Tisserand parameter sampled every 1000 years) trace the variation of semi-major axis and eccentricity, respectively.

Atens and Apollos, in general, have frequent close encounters with Earth, because their perihelion distances are initially close to 1 AU, in contrast to Amors.

Figure 3.7 compares the time evolution of the semi-major axis for (1862) Apollo, the prototype object for the Apollo group. After a very short time (only some 1000 years) this NEA shows a completely different evolution in the two models. The reason is the stochastic effect of an early close encounter: in one model the semi-major axis increases after the encounter, while in the other model it decreases. It is obvious that close encounters are the main mechanism for the variation of the semi-major axis, to most of the jumps there is an associated encounter closer than the lunar distance. In the phases between close encounters the semi-major axis is constant or shows only small variations, frequently the NEA is located inside a mean-motion resonance with Earth. This kind of behaviour has already been described by Milani et al. (1990, section 5) and termed as

---

<sup>3</sup>One must be aware about one point: any NEA being initially a member of the Amor group, will belong technically to the Apollo or Aten group at the time when it has close encounters with Earth.

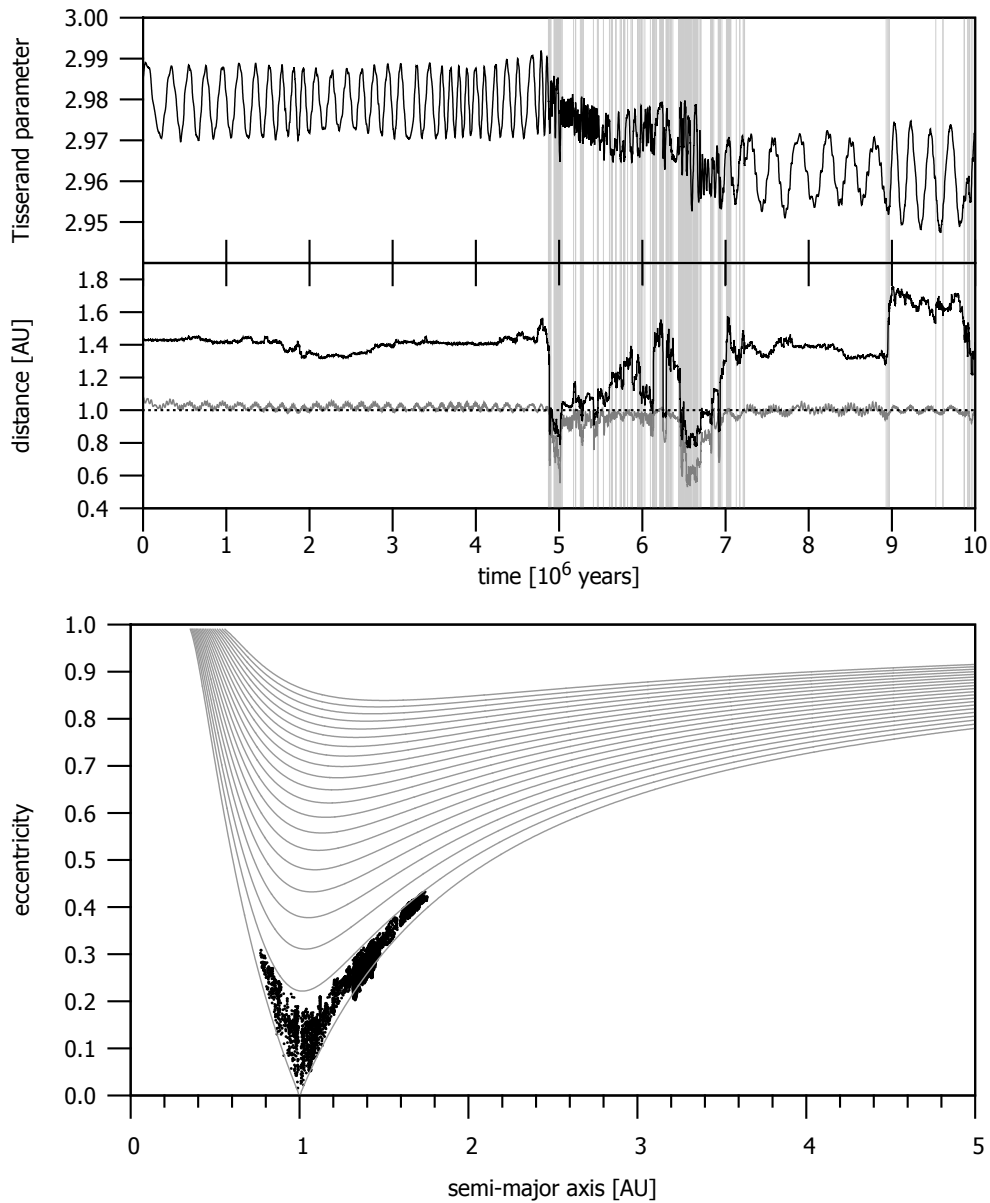


Figure 3.6: The upper graph shows the time evolution of the Tisserand parameter, semi-major axis (black curve) and perihelion distance (grey curve) for the Amor object (1943) Anteros. The vertical grey lines indicate close encounters to Earth within the lunar distance. The lower graph gives the Tisserand parameter evolution in the  $a - e$  space. The grey curves show the Tisserand parameter contours (for  $i = 0$  deg) sampled every 0.05 beginning with  $T = 3$ .

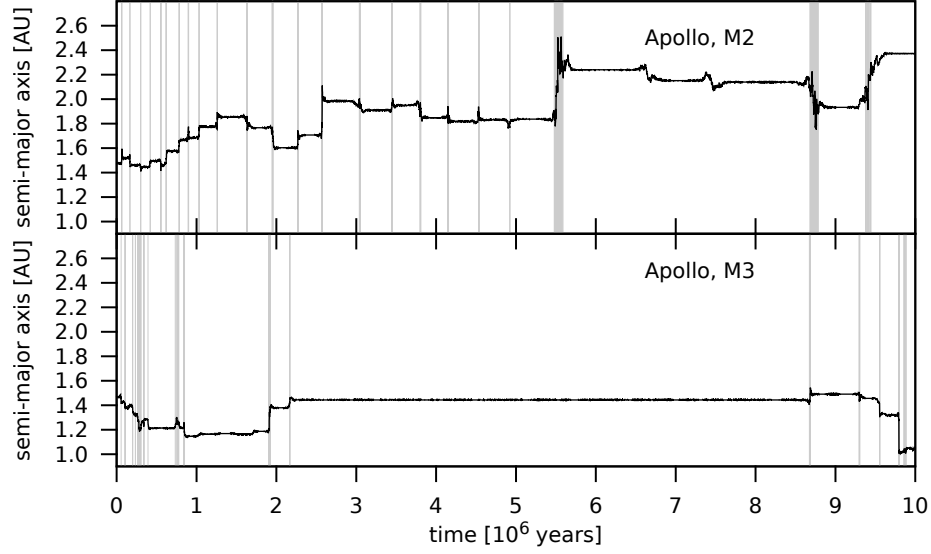


Figure 3.7: Time evolution of the semi-major axis for (1862) Apollo in models M2 (top) and M3 (bottom). The vertical grey lines indicate close encounters to Earth within the lunar distance.

“Geographos class”. In the lower part of figure 3.7 we can see that Apollo is caught in the 19:33 MMR with Earth (at  $a \approx 1.445$  AU) for an extended period of time in model M3.

### Variation in the semi-major axis

The main effect of the Earth and Moon in these two models is in modifying the semi-major axis at close encounters. A simple measure of the combined influence of these two bodies is the relative variation of the semi-major axis

$$\log_{10} \frac{\Delta a}{a} = \log_{10} \left( \frac{\max_{t \leq T}(a) - \min_{t \leq T}(a)}{\langle a \rangle} \right)$$

where we take the difference between the maximum and minimum value and scale it by the mean value of  $a$  over the whole integration time ( $T = 10^7$  years). This variation is then expressed in percent ( $\times 100$  %) before we take the logarithm of it.

A quick example will clarify the details: Let us suppose that a NEA has

$$(a_{\min}, a_{\text{mean}}, a_{\max}) = (0.98, 1.02, 1.10)$$

(all values are in AU). Then from the formula above  $\Delta a/a = 0.118$ , resulting in a variation of 11.8%. Taking the logarithm of this latter number we obtain  $\log_{10}(\Delta a/a) = 1.07$ .

The collection of graphs in figure 3.8 show the relative variation in semi-major axis for all three NEA groups based on the Lie integrator data. We recall that for each group 300 objects were integrated, which are shown along the horizontal axis denoted by their ID number. On the vertical axis the semi-major axis is plotted; each data point gives the mean value of  $a$ , the error bars give the span from the minimum to the maximum value of  $a$ . If for some points the error bars are not visible (specifically this is often the case for the Amors), then this means that the variation is so tiny that it is hidden by the point-size (for reasons of visibility). The colour of each point (see the “thermometer” bar on the right) corresponds to the relative variation in percent, the visible range is from 0.01 % (dark blue) to 1000 % (red).

In some cases the upper end of the error bar extends outside of the image area, there are two reasons for this: (i) a close encounter relocated the NEA to an orbit with semi-major axis well beyond 5 AU, or (ii) the NEA had an “impact” with Earth (or Moon) and escaped from the system<sup>4</sup>.

It is remarkable that all three NEA groups have minimal semi-major axes of  $a_{\min} > 0.5$  AU, there does not form a population of IEOs. The combination of minimal  $a$  with maximal  $e$  for NEAs is still far from being Sun-grazers. NEAs are terminated by collisions with Earth or by ejections after close encounters, rather than being expelled by the Sun. The mechanisms from the study of Gladman et al. (1997, 2000), who found that the majority of Near-Earth objects become Sun-grazers under the influence of orbital resonances, do not act in the current models.

Studying figure 3.8 in detail we can observe that the Amors have variations that are very small ( $< 0.1\%$ ) on average. As discussed above for figure 3.6, Amors evolve on different time scales than the other two groups. At first they are subject to secular effects increasing their eccentricity, on a time scale of some millions of years. Following that their evolution speeds up when they start to have encounters to Earth and switch between various mean-motion resonances.

Apollos and Atens are quite similar regarding the variations in semi-major axis, both show a wide range of variations. On one hand there are still some objects with negligible variations of  $< 1\%$ , but on the other hand the average variation is above 10 %. This is another indication that Apollos and Atens are much more influenced by close encounters with the Earth than Amors. However, there is no systematic qualitative difference between the models in the variation of the semi-major axis, so that we must conclude that the influence of the Moon is rather weak in this respect.

### Orbital elements at close encounters

We can investigate what happens at close encounters, by recording the orbital elements ( $a, e, i$ ) of NEAs at each close encounter. For this task the Mercury integrator data was

<sup>4</sup>Since all objects are point masses there are no real collisions. The impacts mentioned in the text happen when a NEA passes the planet in a distance below the planetary radius. An escape is defined here by reaching a distance of  $\geq 100$  AU from the Sun, or if the eccentricity becomes  $\geq 1$ .

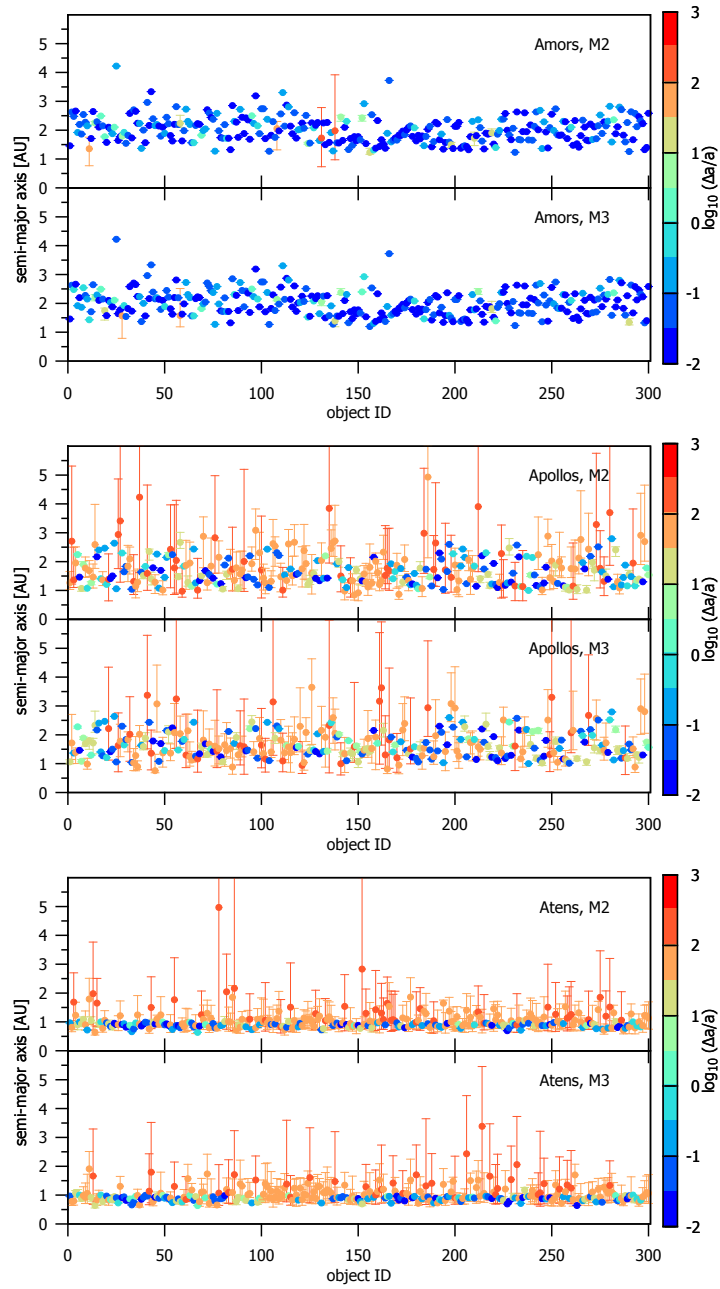


Figure 3.8: The relative variation in semi-major axis for all NEA groups. The point marks the average value of  $a$ , while the minima and maxima are indicated by the error bars; colours correspond to the magnitude of the variation.

selected for the reason that more close encounters were recorded and the whole Near-Earth Asteroid population was sampled, thus having a better statistics. For details about the number of close encounters in the different dynamical models see table 3.7.

In figure 3.9 we can compare the initial distribution (black line, taken from figure 3.2) for the respective orbital element to the resulting distribution for models M2 (red line) and M3 (blue line). The columns are from left to right for Amors, Apollos, and Atens respectively; the top row shows semi-major axis, the middle row eccentricity, and the bottom row inclination.

The distributions are normalised in a way such that the area under the curve sums up to 1, but there is an important difference in the normalising procedure. The initial distribution is normalised by the (fixed) number of asteroids in the group (see table 3.2); for the other curves I normalised by the (variable) number of close encounters. For each row the bin-width is the same, namely  $\Delta a = 0.1$  AU,  $\Delta e = 0.05$ , and  $\Delta i = 5^\circ$ .

On examining figure 3.9 we see that the distribution in  $a$  for the Amors is shifted towards the Earth and the peak is around  $a = 1$  AU, while the initial distribution is completely different. The same shift happens – to a lesser extent – also to the Apollos. Here, the peak is located already at 1 AU for the initial distribution, but certain parts of the distribution are less frequently represented at encounters. The Aten distribution looks in principle the same like for Apollos, except for a steeper decrease in the tail for  $a > 2$  AU. For Atens the initial distribution is heavily peaked around  $a \lesssim 1$  AU, which affects the scaling on the  $y$ -axis. The extended tails of the distributions up to (and beyond)  $a = 5$  AU are produced by only a few objects scattered to such high semi-major axes (and eccentricities) during previous close encounters. In a model including Jupiter these objects would be quickly removed from the solar system.

At the approaches not only semi-major axes around 1 AU are more frequent, but also the eccentricity distributions are significantly different from the initial ones. For Amors the peak is slightly above 0.2, for Apollos at 0.4, while initially it was at 0.5 and 0.6 respectively, compare figure 3.2, for mean (median) values see table 3.3. The distributions in inclination do not show any peculiarities.

It is well known that the discovery of new NEAs is biased towards objects on orbits similar to the Earth’s (Rabinowitz et al., 1994; Muinonen, 1998). NEAs on highly eccentric and/or inclined orbits tend to have a lower probability for Earth approaches (Öpik, 1976). In the simulations we clearly see an accumulation in the number of close encounters for objects with semi-major axes in the range  $0.8 < a < 1.5$ , inclinations below  $i < 30^\circ$ , and eccentricities around 0.4.

Another important observation is that the histograms for the two models are very similar. This demonstrates that the distributions are dominated by the Earth in both cases, and that the Moon hardly makes any contribution.

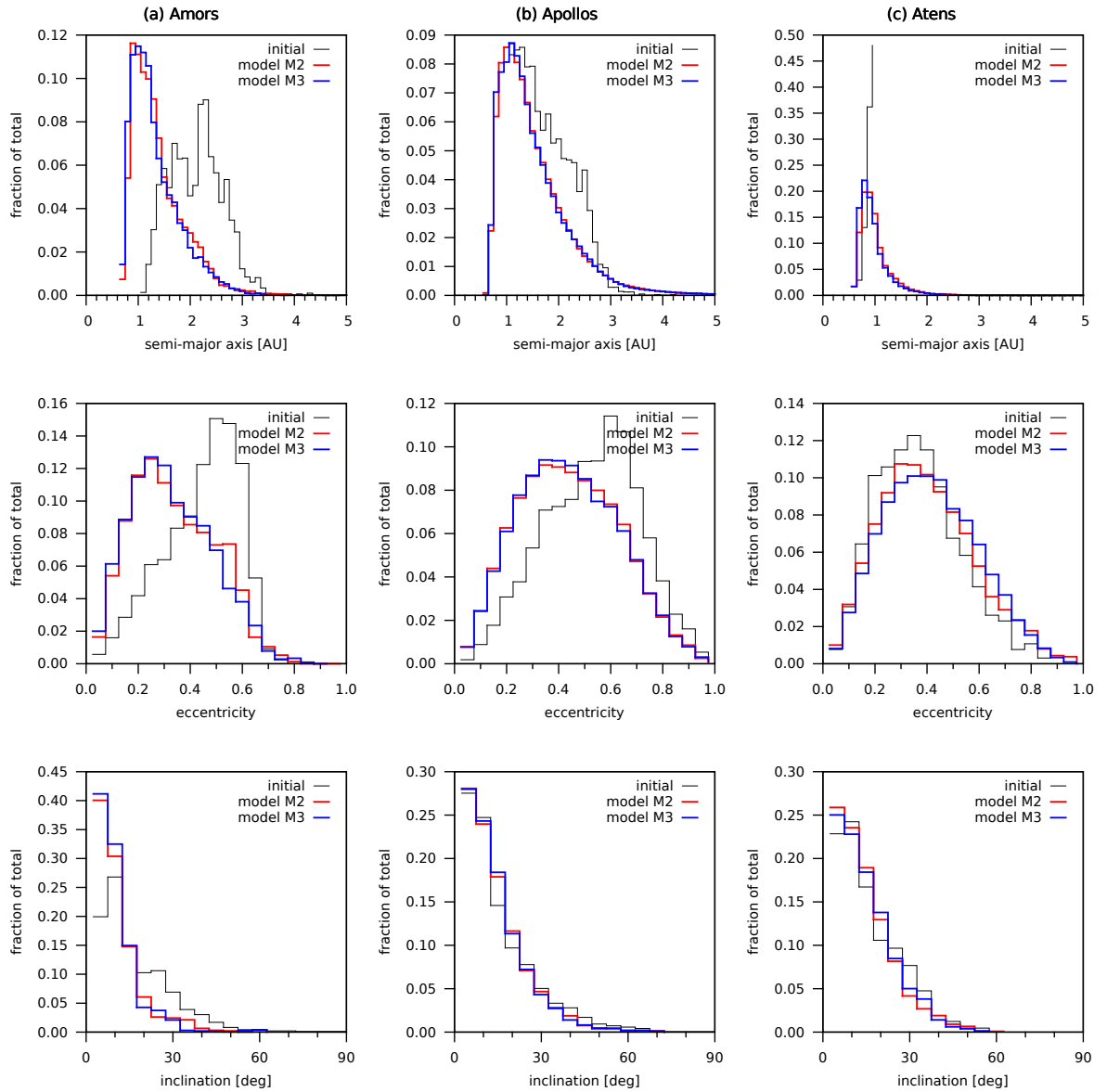


Figure 3.9: Comparison of the distribution of orbital elements ( $a, e, i$ ) at close encounters for all NEA groups in models M2 (red) and M3 (blue) versus the initial distribution (black; from figure 3.2). The vertical axis gives the fraction of events that fall into this box, normalised by the total number of close encounters.

group, model	NEA group membership [%]			
	Amor	Apollo	Aten	other
Amors, M2	$91.0 \pm 20.5$	$5.4 \pm 17.3$	$0.04 \pm 0.4$	$3.6 \pm 12.5$
Amors, M3	$91.0 \pm 21.2$	$5.0 \pm 17.1$	$0.02 \pm 0.4$	$4.0 \pm 14.0$
Apollos, M2	$5.8 \pm 14.6$	$90.0 \pm 19.2$	$4.1 \pm 13.8$	$0.1 \pm 0.5$
Apollos, M3	$5.4 \pm 14.8$	$89.4 \pm 20.8$	$4.9 \pm 15.5$	$0.3 \pm 3.2$
Atens, M2	$2.3 \pm 7.0$	$27.9 \pm 31.7$	$67.6 \pm 33.8$	$2.2 \pm 6.8$
Atens, M3	$3.0 \pm 9.5$	$26.0 \pm 32.0$	$68.3 \pm 34.7$	$2.7 \pm 7.5$

Table 3.4: Statistical summary of the NEA group membership based on Lie-integrator data. The time-averaged percentage (mean and standard deviation) of group membership was monitored for objects initially belonging to a specific NEA group (and model). Objects in the “other” category are non-NEOs, see text for details. All numbers in the table were derived from figures 3.10, 3.11, 3.12.

### NEA group membership and mixing

The Amor, Apollos and Aten groups are not at all separated from each other. As Freistetter (2009) has shown, the NEA groups tend to mix with time, i.e. a NEA starting as an Amor group object can become a member of the Apollo or Aten group at later times, and vice versa. Even the alternative dynamical classification of Milani et al. (1989) is only valid for time-scales of a few  $10^5$  years.

We can investigate this mixing process between the groups over the whole integration time to derive a qualitative indication of the influence of the Moon. Since the group membership depends on the current values of semi-major axis and eccentricity, and both can be modified by close encounters, we are dealing with a strongly chaotic process. In this sense I think that a merely qualitative comparison is justified, without going into further details about which processes play a role for the mixing.

In figures 3.10 (for Amors), 3.11 (for Apollos), 3.12 (for Atens) the group membership is plotted for objects from the Lie sample. The bottom half of each image shows to which NEA group a certain object (identified by the numbers from 1 to 300) belongs to at each instant of time during the  $10^7$  years (on the  $y$ -axis). The membership was sampled every  $10^3$  years. The top half of each image summarises the cumulative fraction of time (in percent) that an individual object spent in the respective group. The groups are defined as usual; Amor group objects are printed in red, Apollos in green, and Atens in blue. If an object does not fit into any NEA class, i.e. asteroids with either  $q > 1.3$  AU (possibly a main-belt object) or  $Q < 0.983$  AU (an Atira object), it is classified as “other” in black colour.

Comparing the images for M2 (top) and M3 (bottom), as well as the statistical summary in table 3.4, one can observe a fair degree of correlation, meaning that in both

models the NEAs have very similar orbital evolution. Table 3.4 details the time-averaged percentage for each group. The large variance in the data follows from the averaging over objects with very different orbital evolution. It is visible in the figures that some objects never change the group, while others do so frequently. Overall the group membership results are consistent for both models. This in turn means that the effect of the Moon in M3 is negligible.

Let us make a final note about the group membership: the data from the table indicate that Amors and Apollos preferably remain in the same group ( $\geq 90\%$ ), but for Atens there is a rather strong migration to the Apollo group. This effect is also visible in figure 3.9, where the Aten semi-major axis distribution forms a tail due to close encounters that extends outwards to  $a \geq 2$  AU.

### 3.3.3 Models M4/M5

The next pair of models includes the planets Venus, Earth, and Mars in M4, with the addition of the Moon in M5. The dynamical evolution of NEAs is more complex with the appearance of numerous mean-motion resonances (MMR) and three-body resonances (TBR); now close encounters can happen to all terrestrial planets.

#### The influence of resonances

Let us start again with an individual example: figure 3.13 shows the time evolution of the semi-major axis of (2062) Aten (= 1976 AA) in both models. The two curves diverge quite early – after about  $7 \times 10^4$  years. However, they show a similar qualitative behaviour regarding the evolution. There are phases of a largely constant semi-major axis (with only small oscillations around an “average” value) lasting for some ten-thousand to a few hundred-thousand years, which are interspersed with phases of one or multiple sudden changes of the semi-major axis cause by close encounters.

This is in principle the same type of dynamical behaviour that we have observed for Apollo for the previous models (see figure 3.7). The situation is just more complex due to the presence of the other terrestrial planets. In the lower part of the figure we have two separate panels showing the evolution in the  $a - e$  plane.

On the left we can observe how Aten in M4 is gradually shifting to larger semi-major axes with time. The dots are coloured according to the vertical colour-bar which displays the time in units of millions of years. The coloured curves indicate planet-orbit crossing values for the perihelia ( $q$ ) and aphelia ( $Q$ ) of NEAs, i.e. in the region bounded by the curves a NEA can have close approaches to the terrestrial planet (Venus at 0.72 AU, Earth at 1.00 AU, and Mars at 1.52 AU).

It is also evident from the left graph that in M4 Aten can only have close encounters with Venus and Earth in the first  $10^6$  years, because it does not cross the curve for Mars. From about 8 Myr until the end of the integration time Aten has orbital elements  $a, e$  which allow it to have close encounters to Earth and Mars, but it is unable to

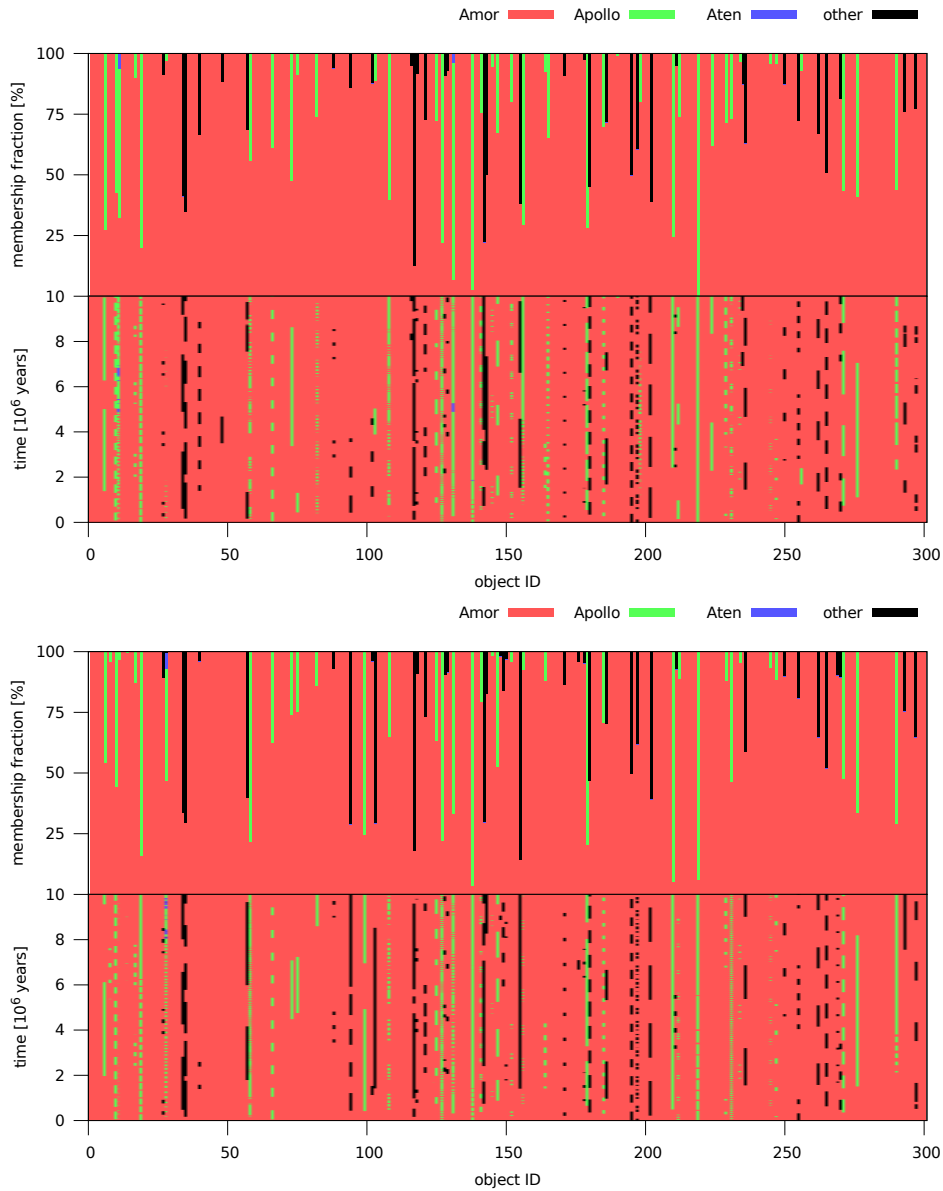


Figure 3.10: Time evolution of individual objects (lower half) and cumulative total fraction of group membership (top half) for NEAs initially belonging to the Amor group. The top figure shows model M2, while the bottom figure is for model M3.

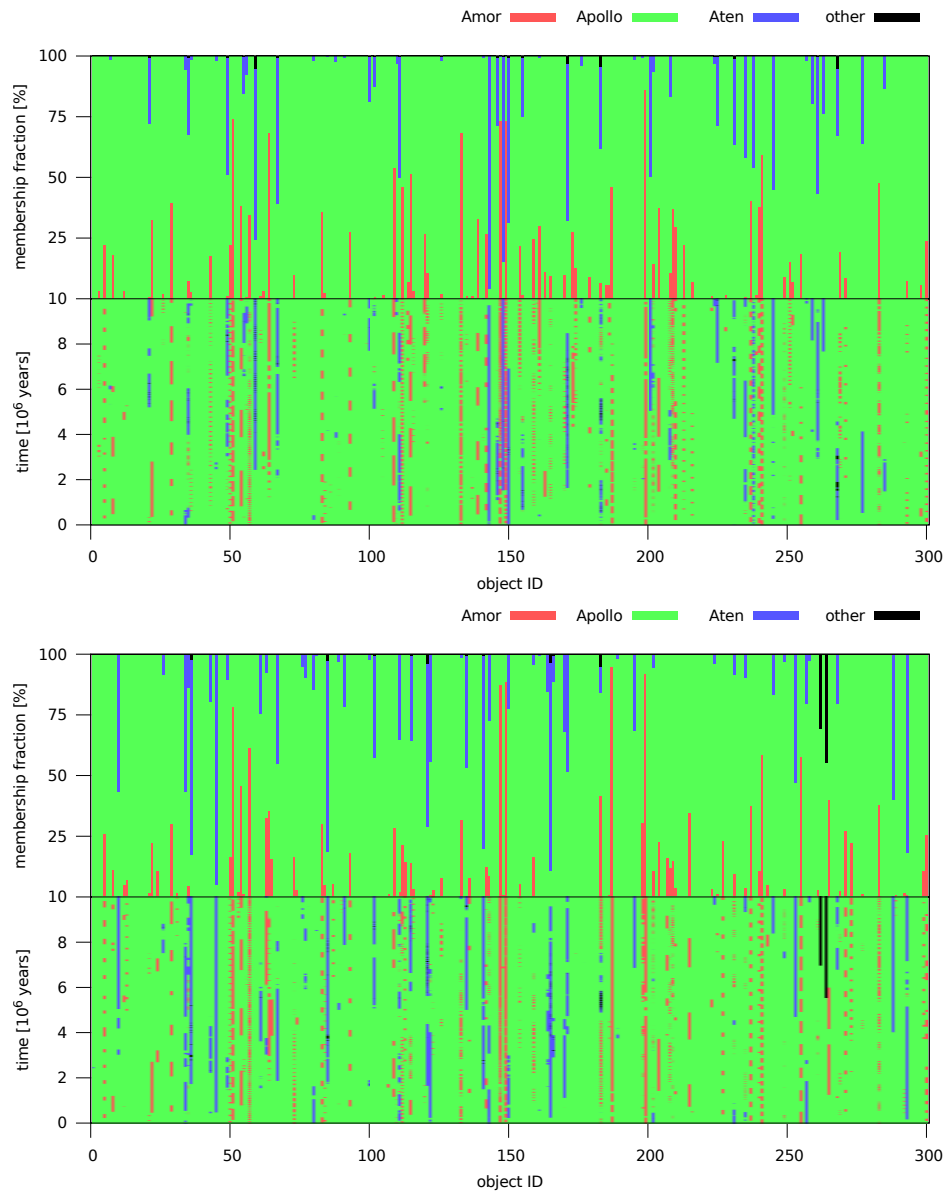


Figure 3.11: Caption like for figure 3.10, but for NEAs initially belonging to the Apollo group.

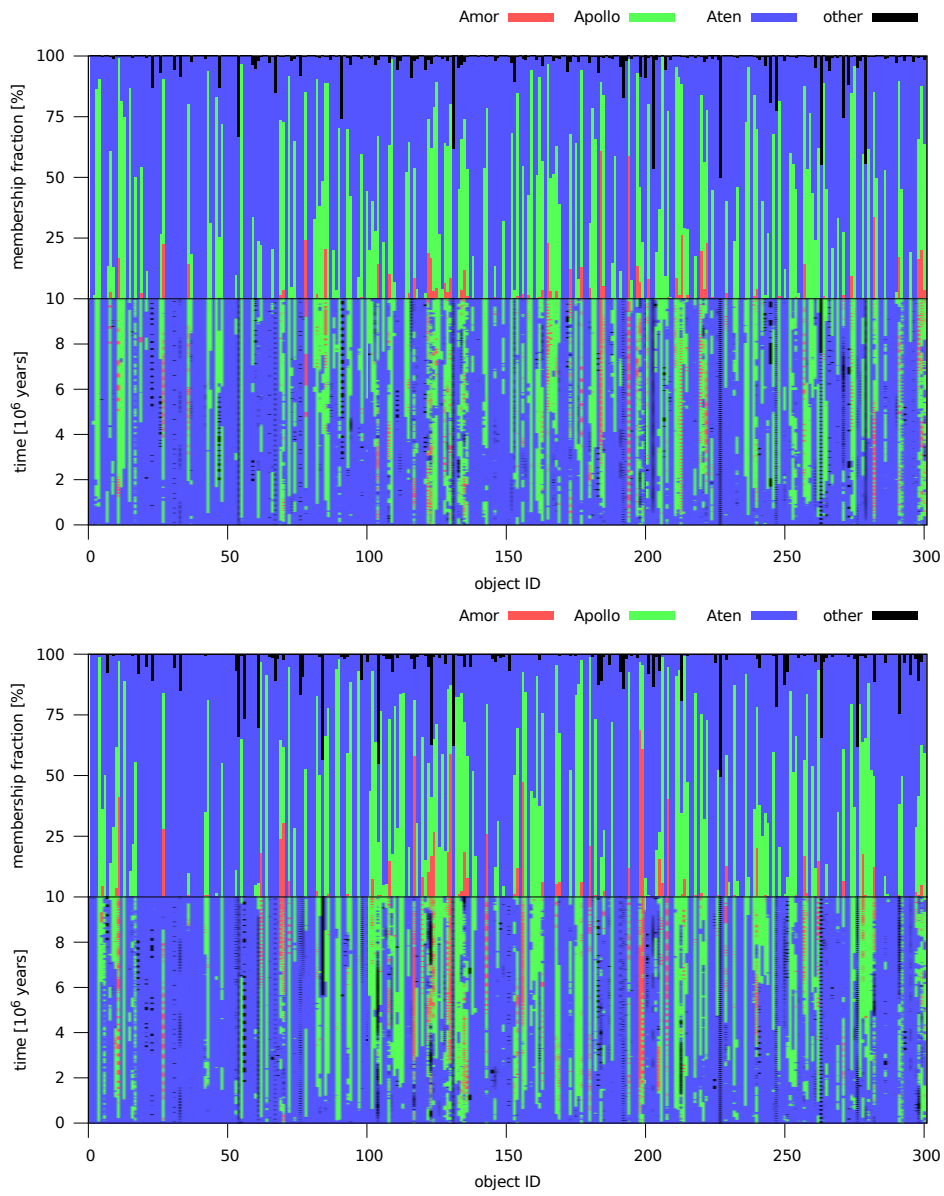


Figure 3.12: Caption like for figure 3.10, but for NEAs initially belonging to the Aten group.

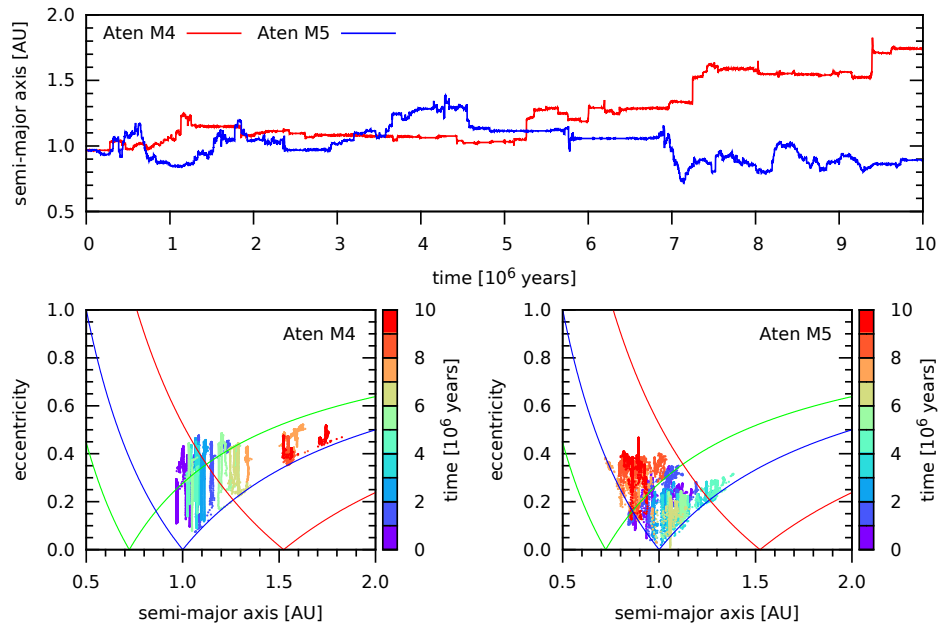


Figure 3.13: Top graph: Time evolution of the semi-major axis of (2062) Aten in models M4 (red curve), M5 (blue curve). The two bottom panels show the time evolution in the  $a - e$  parameter space, the vertical bar indicates the time. The three colour curves represent planet-orbit crossing perihelia and aphelia of NEAs for the planets Venus (green), Earth (blue), and Mars (red).

approach Venus. When tracing the colours we observe that Aten’s eccentricity evolves along vertical stripes for more or less constant semi-major axis; the eccentricity variation is limited by the curve  $q = 1$  AU at the bottom, and to values below  $e \simeq 0.5$ .

In the right panel for M5 Aten is restricted inside a region of the parameter space where it has approaches to Venus and Earth, but – except for a short period of time – not to Mars. This NEA switches frequently between its original Aten group and the Apollo group; towards the end of the integration it becomes an Aten again. The qualitative differences between the models can be explained entirely by the random effects of close encounters at different times to the terrestrial planets, the presence of the Moon in M5 does not play a fundamental role.

I have explicitly analysed the NEA (1221) Amor (= 1932 EA1) to study the influence of resonances in detail. Figure 3.14 gives an impression of the time evolution of its semi-major axis in the two models. In panel (a) the grey curve depicts Amor in M4, in panel (b) the grey curve shows M5. All the horizontal lines extending across the figure show various mean-motion or three-body resonances. The resonances shown here are just a sample, they were selected from a more comprehensive list of possible resonances, based

upon the criterion that they fulfill the relations

$$\begin{aligned} p n_1 - (p + q) n_2 &\approx 0 \\ c_1 n_1 + c_2 n_2 + c_3 n_3 &\approx 0 \end{aligned}$$

where  $p, q, c_i$  are integers, and  $n_i$  are the mean motions of planets and NEAs. The order of the resonance is determined by the value of  $q$  for MMR, while it is  $|c_1 + c_2 + c_3|$  for TBR.

As the analysis is based on osculating elements directly obtained from the numerical integrations, and neither on proper elements (Milani and Knezevic, 1994) nor an analytic model of resonances (Nesvorný and Morbidelli, 1998a), there is some uncertainty associated with the “true” mean motion. The selection of the correct resonance is sometimes made difficult as a consequence of that uncertainty, particularly when keeping in mind that three-body resonances appear as multiplets (Morbidelli and Nesvorný, 1999), and that each low-order MMR is surrounded by higher order resonances (near-multiples). For the low order mean-motion resonances visible in figure 3.14 the critical arguments for the resonance were checked to librate, an example is shown for the E3:8 resonance.

The labels at the right border of the image correspond to the horizontal lines from top to bottom, they denote the respective resonance. Blue lines mark MMR with Earth, red lines are for MMR with Mars, green lines for MMR with Venus, and black lines for the various TBR. Some of the resonances act for just a very short period of time (e.g. E2:3 and V6:13), while others like the E3:8 are active for some  $10^5$  years. It is possible that besides two-body mean-motion and three-body resonances also four-body resonances are acting (e.g. Venus–Earth–Mars–NEA), but this type of resonance was not analysed.

We can conclude from the two examples in figures 3.13 & 3.14 that the dynamics of NEAs is strongly influenced by resonances with the terrestrial planets. The NEAs spend relatively more time inside or near to resonances than in the models M2/3. Close encounters are still important to change the semi-major axis and relocate a NEA to another region of the solar system, but the total number of encounters to Earth in M4/5 is only about 50 % of that in M2/3 for Apollos and Atens (cf. table 3.7). The number of approaches has increased only for the Amors due to the enhanced scattering of NEAs to the inner solar system by close encounters to Mars.

### Relative velocities at close encounters

Although the absolute number of close encounters has diminished, it proves interesting to investigate the distribution of relative velocities and minimum distances at those approaches.

As mentioned earlier two numerical integration methods were used. The Lie series integrator records all close encounters within the lunar distance and provides both geocentric Cartesian position and velocity vector components as well as heliocentric instantaneous osculating elements  $(a, e, i)$ . The Mercury integrator, on the other hand, only supplies

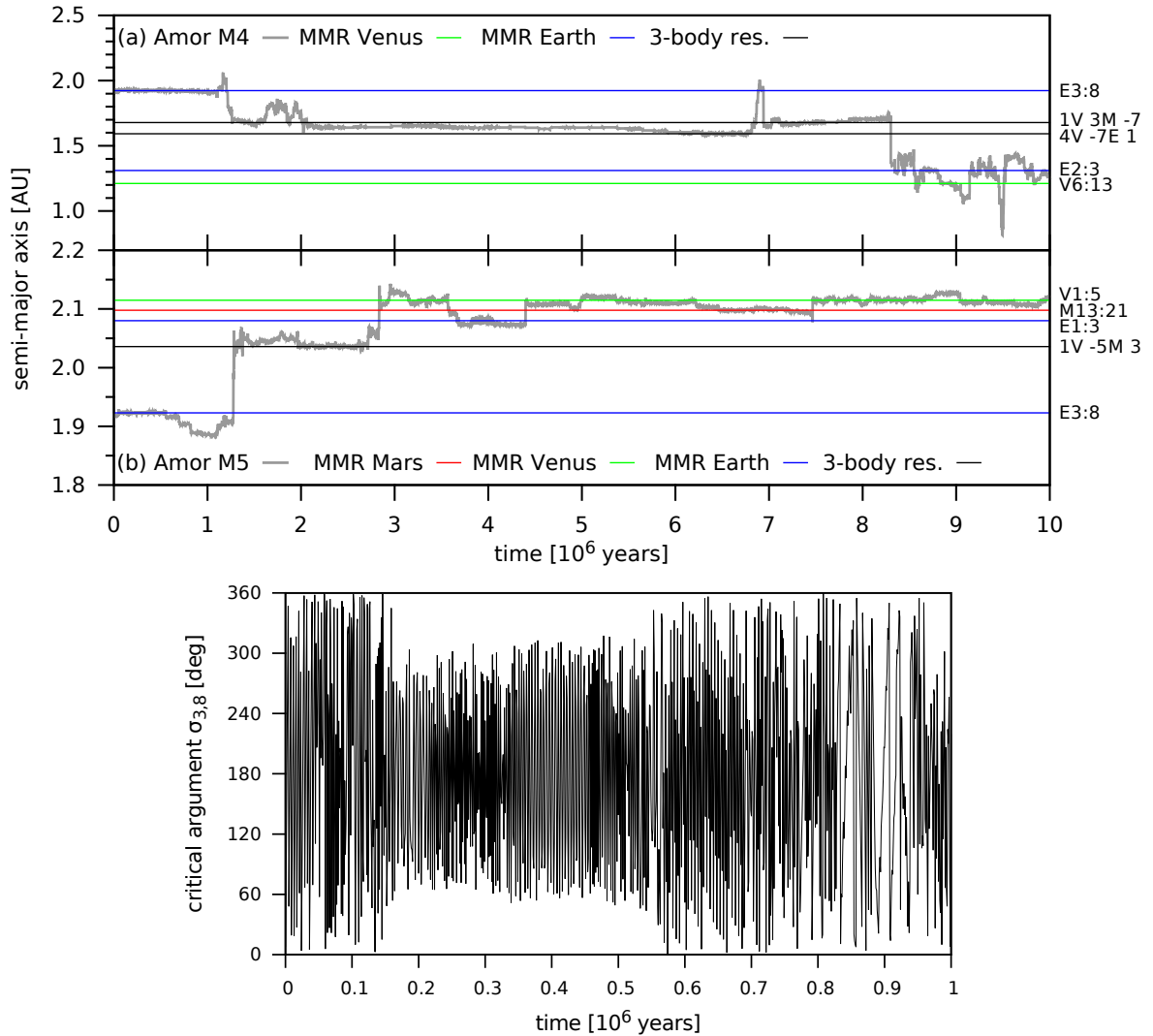


Figure 3.14: Top: Time evolution of the semi-major axis of (1221) Amor in models M4 (panel (a)), M5 (panel (b)). A selection of mean-motion resonances (red, green, and blue) and three-body resonances (black) is plotted as horizontal lines. See text for details. Bottom: The critical argument  $\sigma_{3,8}$  for the E3:8 mean-motion resonance librates around  $180^\circ$  with large amplitude in the time interval  $0.2 - 0.5 \times 10^6$  years.

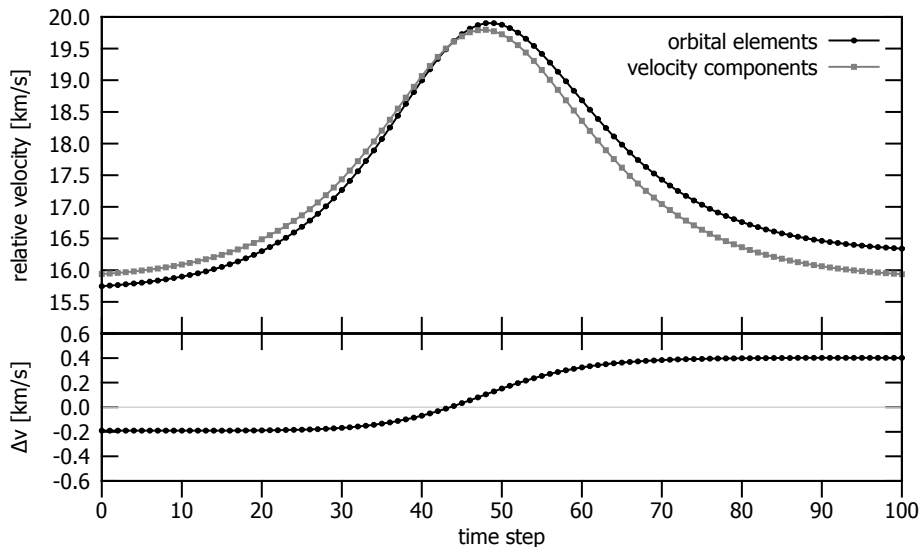


Figure 3.15: Comparing two methods to compute the relative velocity during a close encounter: in black Öpik’s method is used based on heliocentric orbital elements, in grey the planetocentric velocity vector components are used directly (the reference method). The horizontal axis displays the (integer) number of time steps since the begin of the encounter. In the bottom part the difference between the two methods is plotted as a function of the time step.

the heliocentric orbital elements  $(a, e, i)$  for each encounter, which does not allow to compare the planetocentric relative velocities directly.

To alleviate the problem I chose to use the Öpik theory (Öpik, 1976) following the description of Carusi et al. (1990). This theory describes the approach of an asteroid to a planet on a circular orbit (with normalised semi-major axis  $a = 1$ ) by a hyperbolic two-body model. In this way it is possible to compute an approximation of the planetocentric relative velocity  $U$  at a close encounter only from the heliocentric orbital elements  $a, e, i$ :

$$U(a, e, i) = \sqrt{3 - T(a, e, i)} \quad (3.3.1)$$

where  $T$  is the Tisserand parameter relative to the planet, see equation (3.2.1). One only needs to convert  $U$  to the preferred system of units, here I use kilometers per second (km/s) instead of the usual astronomical units per day.

To compare the quality of the approximation figure 3.15 shows the two methods for obtaining the relative velocity. The data is taken from the Lie integrator Apollo sample, and corresponds to a deep close encounter where the NEA comes rather close to the Earth’s surface and consequently has a high relative velocity. The Lie integrator can automatically adjust its global time step over a wide range to accurately follow such

trajectories, in this case the time steps were decreased to some hours (in physical time), so there are enough time steps for a comparison.

The Öpik method (black curve) performs quite well and results in a relative velocity that is close to the reference value (grey curve) computed from the geocentric velocity vector. However, there are two shortcomings:

- The exact location of the peak velocity does not coincide for the two methods, in the Öpik method it is slightly shifted. Additionally, the relative velocities at minimum distance (peak velocities) are also slightly different.
- The other problem is that the curve obtained from the orbital elements is asymmetric, i.e. the velocities at the beginning and the end of the encounter differ.

The first objection from above is not a big problem in practice. As the Mercury integrator provides only a single set of orbital elements per close encounter, we would not be able to detect a shift in the timing of peak velocity. Anyway, we are interested in the magnitude of the relative velocity, not in the moment when it is extremal. There could be a systematic difference between the two methods regarding the magnitude of the relative velocity. This deviation can be partly explained by the assumption of a circular orbit for the planet in Öpik’s theory, which is not realised exactly.

Regarding the latter point we must be careful not to mix the different reference frames. The velocity components are defined in a planetocentric reference system, in this frame the velocity vector is only rotated by an angle which is determined by the encounter geometry (Greenberg et al., 1988). The orbital elements in turn are defined in a heliocentric frame, for which the velocity at the begin and end of the encounter need not be equal, instead in general they will be different. This effect is regularly exploited in orbital mechanics as the “gravity assist maneuver” (Chobotov, 1991, chapter 12). The reason for the asymmetric relative velocity curve based on orbital elements lies in the fact, that the ingredients for the calculation are defined in another reference frame, and so they illustrate the situation in that frame.

For a thorough check of the systematic velocity difference a sample of close encounters for Apollo group NEAs was analysed. The data from the Lie series integrator was used to be able to compare both methods. At each close encounter both relative velocities were computed for every single time step to obtain the sequence of differences (analogous to the bottom part of figure 3.15). Then the mean difference over one encounter and its standard error<sup>5</sup> (SE) were calculated. Figure 3.16 shows this data for nearly 3500 encounters. Every single dot represents the mean difference from an encounter, which is accompanied by the vertical error bars for the standard error of the velocity difference. In general these errors are  $< 0.01$  km/s and are thus negligible. Averaging again the velocity difference over all close encounters we find  $\langle \Delta v \rangle \cong 0.40$  km/s (the dotted horizontal line

---

<sup>5</sup>Another name is standard deviation of mean (SDOM);  $SE = \sigma/\sqrt{N}$  with  $N$  being the number of time steps that the encounter lasts.

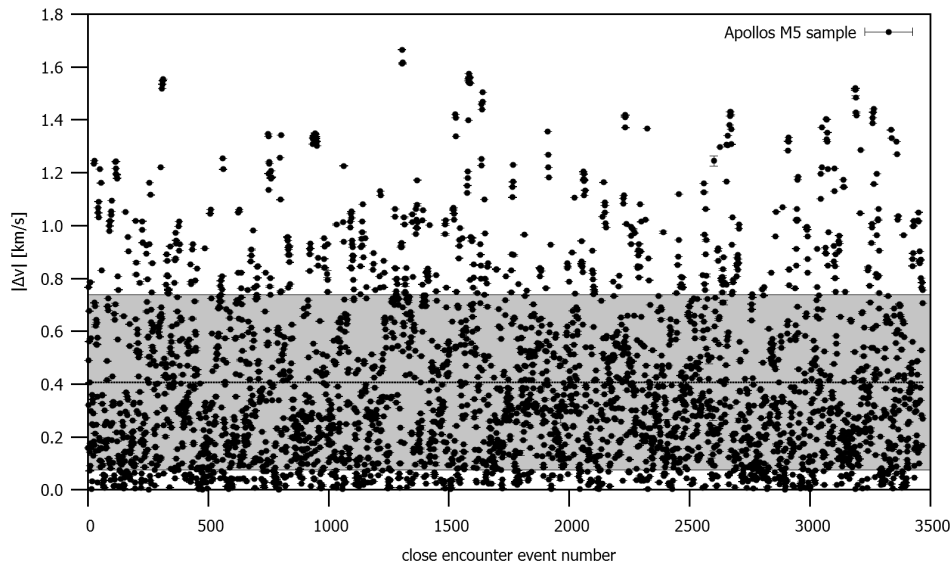


Figure 3.16: A statistical check of the systematic velocity differences between two methods to compute relative velocities. The average and standard error of the individual velocity differences are plotted for a sample of Apollo encounters; each point represents a different encounter. The grey-shaded area indicates the mean difference (dotted horizontal line) and the  $1\text{-}\sigma$  standard deviation over the whole sample.

in the figure) with standard deviation and  $\sigma_{\Delta v} = 0.33$  km/s, whereas the median value is only 0.32 km/s.

These are just formal values, because one can see from the figure that differences up to 1.7 km/s can occur. Nevertheless they assure us that the Öpik method is applicable to extract relative velocities from the Mercury integrator data, and they allow to estimate that on average we will be able to determine the relative velocity with an error less than 10 % for small velocities around 5 km/s, at higher velocities this error will be even lower.

The Öpik method was then applied to the Mercury integrator data to calculate relative velocities for all NEA groups separately. Figure 3.17 compares the relative velocity distributions for Apollos in models M4 and M5. The dotted vertical lines indicate the 5 km/s limit used for selecting a sub-sample of the data, which is presented in figure 3.18.

Figure 3.17 combines data from all close encounters of objects initially in the Apollo group in models M4/5. In case of the Lie integrator (left panel) the relative velocities were measured at the entry to the sphere centered on Earth with radius of the Earth-Moon distance. By choosing a fixed distance avoids to bias the distribution with objects coming very close to Earth which therefore have a high relative velocity. Still there remains a sort of bias at larger velocities above 20 km/s, where the distributions do not decrease monotonically as in the case for the Mercury data. Those spikes are caused by

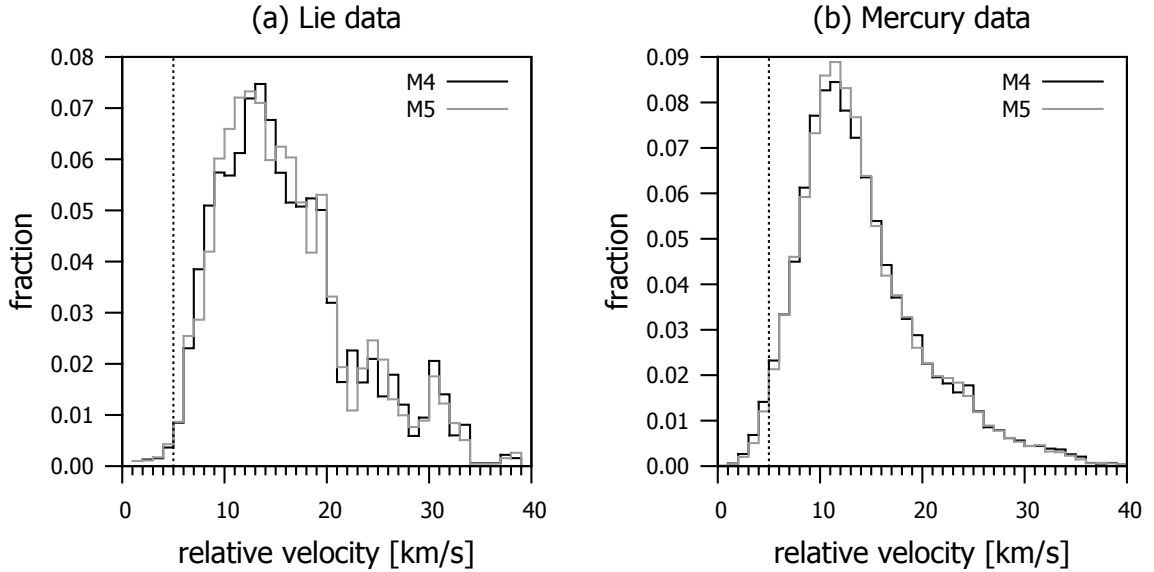


Figure 3.17: The relative velocity distribution for models M4 (black) and M5 (grey) for Apollos based on data from the Lie series integrator (left) and Mercury integrator (right). The distributions are normalised by the total number of encounters; the dotted vertical lines indicate the part of the distribution below 5 km/s.

repeated close encounters of individual Apollo objects, that are not smoothed out due to the rather small size of the sample, compare table 3.8 for the number of close encounters inside the lunar distance. The peaks of the distributions are located at 13–14 km/s for M4 and around 12–13 km/s for M5. There are no events with relative velocities above 40 km/s, at least when the NEAs are at the lunar distance.

For the Mercury integrator data (right panel) the relative velocities in the histograms represent the velocity at minimum distance to Earth (assumed to be the peak velocity during the close encounter). The Apollo group was chosen, since this is the most numerous group and exhibits the largest number of encounters (see table 3.7), so the velocity distributions are expected to be most precise. The minimum distances scatter widely, though, as they range from the physical surface of the Earth up to one Hill radius.

Therefore it has to be cautioned that the two velocity distributions in figure 3.17 are not directly comparable, because the relative velocities were not obtained at the same distance. Apart from this, there is little variation between the two models. Both distributions have their peaks at 11–12 km/s and the tails extend to approximately 40 km/s; only in  $< 0.03$  % of all cases higher relative velocities occur – mainly in connection with impacts.

Taking the distributions as they are, no systematic effect due to the Moon can be

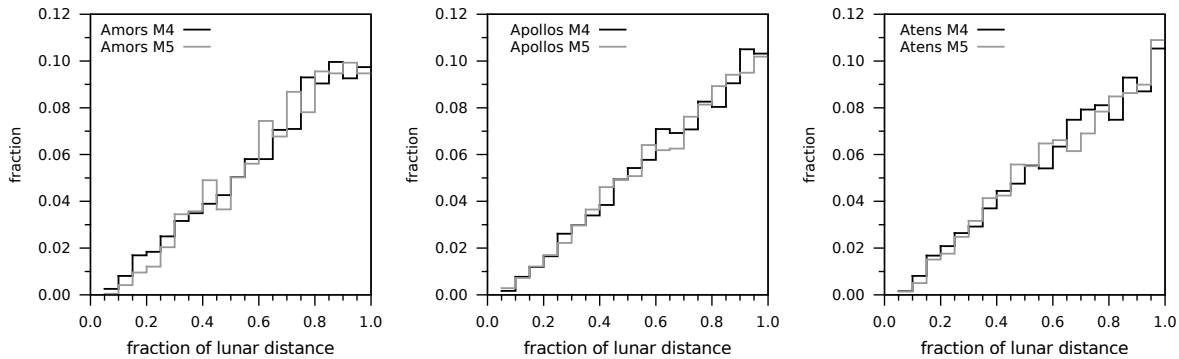


Figure 3.18: The normalised distributions of minimum encounter distances less than the lunar distance for encounters with relative velocities below 5 km/s. From left to right the panels show the distributions for Amors, Apollos and Atens, respectively; the black line is for model M4, the grey line for M5.

derived for M5. There are small variations in the height of individual bins, the peak is shifted by 1 km/s for the Lie data, but overall the data for the two models are too close together to state that the Moon has any appreciable influence on the distribution of relative velocities at close encounters.

Domingos et al. (2004) stated in their study that the Moon is effective in removing asteroids on Earth-impacting trajectories for relative velocities below 5 km/s in 2.6 % of the cases they investigated. I extracted all close encounters with relative velocity below this 5 km/s limit from the Mercury data and checked the distribution of minimum distances to Earth. Another limit was imposed on the minimum distances, they were restricted to be less than or equal to the lunar distance (LD). Applying these selection criteria, the number of close encounter events eligible was reduced from some millions to only a few thousand cases; on average only 0.2 % of the cases from table 3.7 fulfill the constraints.

We can estimate an upper limit for the probability (for independent events) that a deflection by the Moon occurs for a close encounter that meets the requirements ( $v_{\text{rel}} \leq 5$  km/s inside the lunar orbit). Using the percentages from before the probability is  $P(d) = 0.002 \times 0.026 = 0.000052$ , i.e. in one out of 20 000 cases.

The results are presented in figure 3.18 and they show no distinctive difference for any of the three NEA groups. Some data bins show an indication for a depletion of close encounters, but such small differences could also occur by chance. Overall there is no clear sign that the Moon would influence these objects.

### Quantitative analysis of NEA groups

In a part of section 3.3.2 it was investigated how certain NEA groups evolve in time and how the exchange and mixing with other groups works in detail. Here we will extend those results using the additional information gathered from models M4/M5.

For the discussion let us consider again the Apollo group (the results hold for any other group, too). Figure 3.19 shows the count of objects versus time for the sample of 300 Apollo objects in the Lie integrations. In panel (b) we observe the decline of the Apollo population from initially all 300 NEAs to about 230 objects after 10 million years. The other groups gain members proportionally; in this case there are about twice as many Apollos that change to the Amor group (a) than to the Aten group (c). The non-NEO objects<sup>6</sup> in panel (d) remain a small group, but there is a steady fluctuation. This means there is no net drain to a specific end-state, the mixing keeps going on. The observed decay of the Apollo group is in agreement with the logarithmic decay observed by Gladman et al. (2000), except that the decrease is not induced by ejections but by the mixing process with other NEA groups, and ultimately by impacts onto the terrestrial planets.

In case of the other groups the results are similar. Of the initially 300 Amors about 70 % remained in the group at the end of the integration, 15 % became Apollos,  $\sim 1$  % Atens, the rest were non-NEOs. The Aten group decreased more substantially, only 45 % of the initial population finished as Atens, the others became Apollos (36 %) or non-NEOs (14 %, preferentially Atiras). The differences between the models were negligible in all the cases, no increased or decreased transport of NEAs is observable for model M5.

As in the previous models the primary sink for NEAs in the current models are impacts with the planets, rather than ejections or collisions with the Sun. In table 3.9 a summary of the different end-states is given for NEAs that did not survive to the end of the integrations. Figure 3.20 presents the time-evolution of the number of surviving objects for each NEA group. The figure is based on Mercury integrator data for the whole population, scaled with the appropriate numbers from table 3.2. The different impact rates for Atens through Amors can be explained with the orbital periods (connected to the mean motions), which are shortest for Atens. In a given time-interval the Atens will have more revolutions than Apollos or Amors, which in turn increases their impact probability and leads to a higher decay rate.

### 3.3.4 Models M6/M7

The last pair of models include the giant planets Jupiter and Saturn and show a number of features that did not occur until now. Near-Earth Asteroids can now be subject to

---

<sup>6</sup>Based on osculating orbital elements sampled every  $10^3$  years, a “non-NEO” object does not fulfill the  $q < 1.3$  AU and  $Q > 0.983$  AU criteria; these can be Inner Earth Objects (Atiras) or main-belt asteroids.

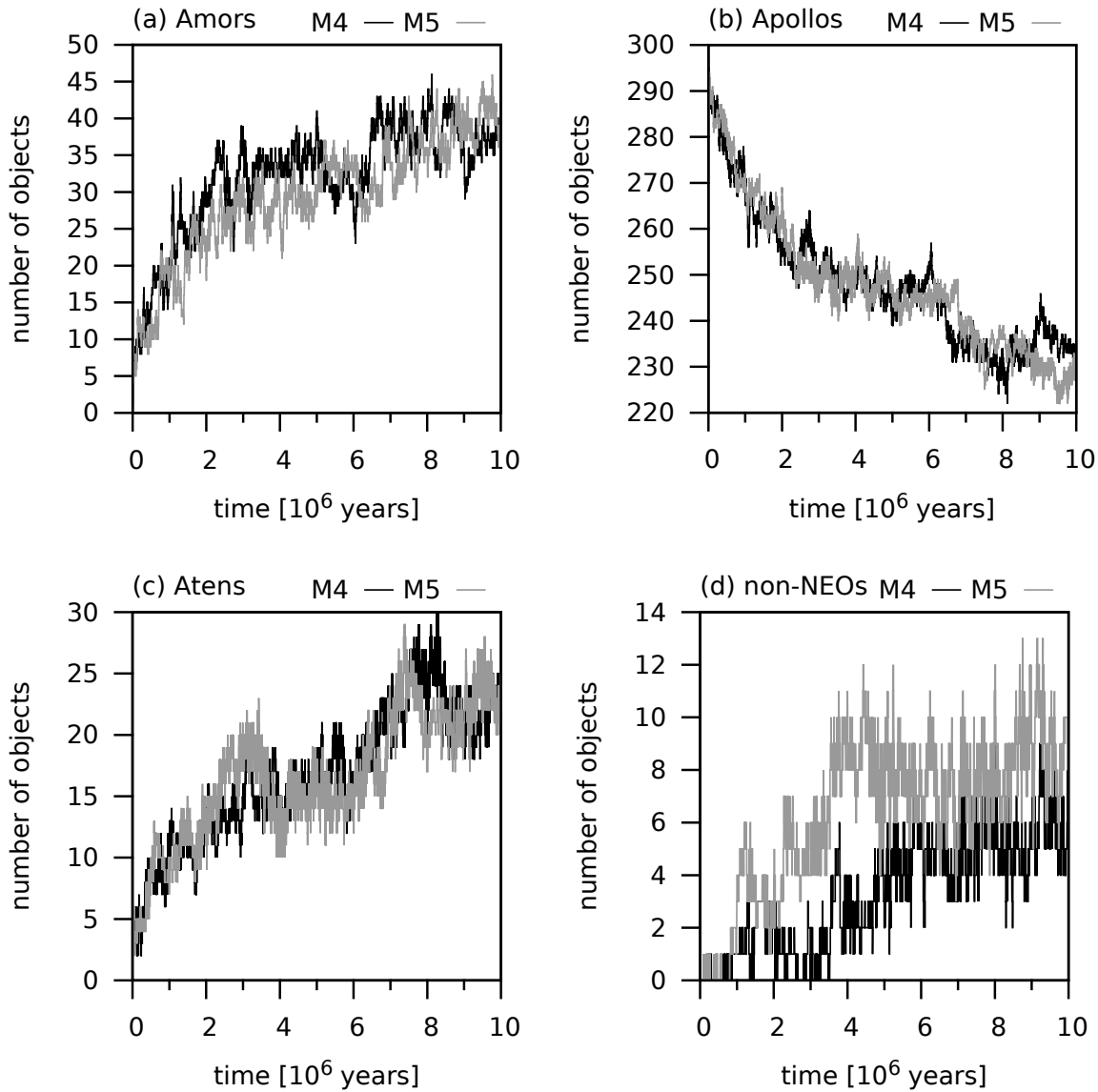


Figure 3.19: The number of objects belonging to a specific NEA group versus time, based on a sample of initially 300 Apollos in (b). Panels (a), (c), (d) show how many of the Apollos became members of the respective group. Different colours are used for the dynamical models, M4 in black and M5 in grey. See text for the definition of non-NEOs.

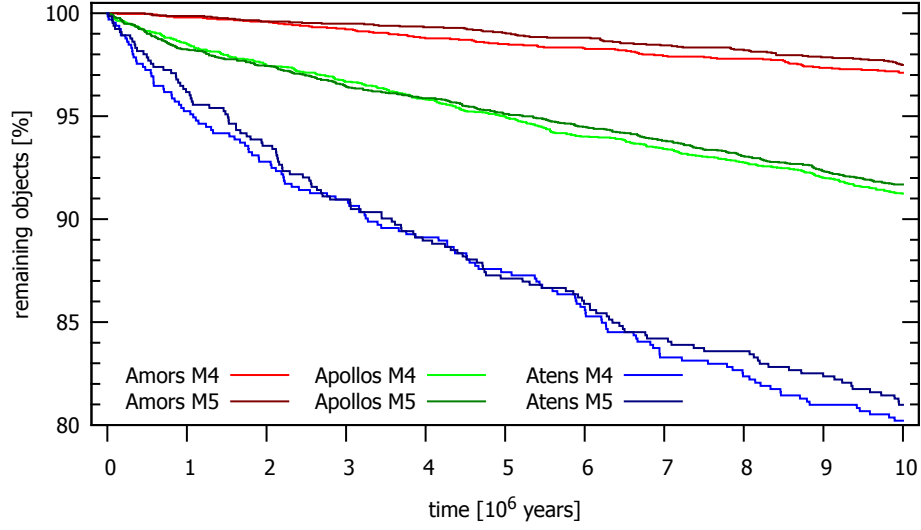


Figure 3.20: Time versus percentage of objects remaining in the simulations, the other objects were removed by impacts.

strong secular resonances ( $g_5$  and  $g_6$ ) with those planets, leading to a rapid increase of eccentricity and an enhanced rate of ejections from the solar system. New mean-motion resonances also occur (e.g. J3:1), and the Kozai resonance can lead to a strong coupling between eccentricity and inclination variations; many of these effects are discussed in Michel et al. (1996) and Gladman et al. (2000).

### Estimating impact velocities from encounter velocity distributions

The current models are best suited among all model pairs to describe the real dynamics of the solar system. In the previous section the NEA velocity distribution at close encounters was discussed; now we are interested in the distribution of impact velocities. Checking tables 3.9 and 3.10 we see that there are too few impacts to extract a reliable impact velocity distribution.

In the following I describe the procedure to estimate (extrapolate) impact velocities. Conforming to the Öpik theory I will assume an unperturbed hyperbolic trajectory for the asteroid relative to the planet. The initial conditions available for the Mercury data are the Earth mass (in units of the solar mass)  $\mu \simeq 3 \times 10^{-6}$ , the minimum planetocentric distance  $r_0$  (in AU), and the (heliocentric) orbital elements  $(a, e, i)$  at this distance.

1. Obtain an estimate of the relative velocity  $v_0$  at the minimum distance by using the relation (3.3.1).
2. We also need the planetocentric semi-major axis which can be calculated from the

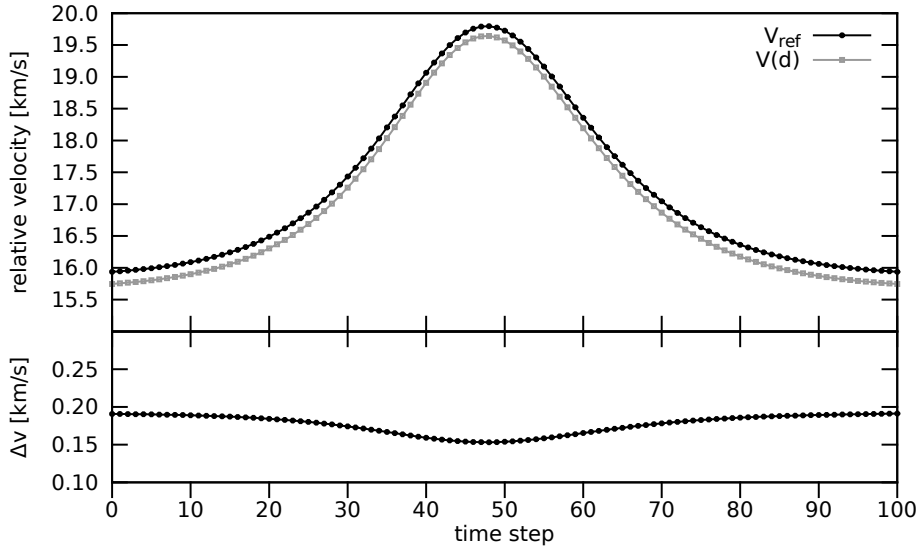


Figure 3.21: A test case to assess the method for computing the relative velocity  $v(r)$  from a given initial distance and velocity. The black curve is the reference velocity obtained directly from the Lie integrator planetocentric velocity components, the grey curve is the approximation. The horizontal axis displays the (integer) number of time steps since the begin of the encounter. In the bottom part the error of the method is plotted.

two-body energy integral

$$a = \left( \frac{2}{r_0} - \frac{v_0^2}{\mu} \right)^{-1}.$$

We will assume that  $a \approx \text{const}$  during the whole close encounter! Note that for a hyperbolic trajectory  $a < 0$ .

3. The velocity relation

$$v^2(r) = \mu \left( \frac{2}{r} - \frac{1}{a} \right) \quad (3.3.2)$$

then allows to calculate the velocity as a function of the distance.

Minton and Malhotra (2010) used a similar relation based on the vis-viva integral, but the resulting impact velocities are essentially the same.

Figure 3.21 presents a test case where the above steps have been used to calculate the relative velocity  $v(r)$  for each time step from a single initial point. The data is the same as for figure 3.15, the reference velocity  $v_{\text{ref}}$  (in black) is taken directly from the Lie integrator. The initial point with index 0 is just inside the lunar orbit, from this point the initial velocity  $v_0$  and semi-major axis  $a_0$  are determined. All other points

(grey line) are calculated from equation (3.3.2) for a given distance  $r$  that coincides with the distance of the reference velocity. The lower part of the figure shows the difference between estimated and reference velocity. This difference is almost entirely dominated by the error with which the initial relative velocity  $v_0$  can be computed from equation (3.3.1). Thus for the approximation errors of the extrapolated velocities with this method the same results hold as for Öpik's method to compute relative velocities: from the statistical analysis (see figure 3.16) the mean error is  $\Delta v = 0.40 \pm 0.33$  km/s.

The histograms in figure 3.22 show the normalised velocity distribution as extrapolated to the Earth's surface (dark grey bars). The distributions obtained from the numerical integrations (light grey) in models M6 and M7 are also included in the figure for comparison. Note that the latter distributions include velocities from different geocentric distances, which is the reason why also very small relative velocities appear (at large planetocentric encounter distances). Impact velocities above 45 km/s are present but amount to less than 0.01 % of all cases.

The impact velocities are consistent with the lower limit of 11.2 km/s for the escape velocity. However, on average in 0.032 % of all cases the method fails and does not provide a physically valid velocity. About 90 % of those cases are due to a Tisserand parameter of  $T > 3$  for the asteroid, as a consequence no relative velocity can be determined from equation (3.3.1). By checking a number of such cases shows that this happens most often when the Earth's eccentricity is  $e > 0.025$ , i.e. close to the peak value in the secular period. It is obvious that the higher the eccentricity the less valid is the assumption of circular orbits; Greenberg et al. (1988) discussed a number of conditions where the Öpik method may fail. In the remaining 10 % of cases the resulting impact velocities are below the escape velocity; in the distributions these cases – although negligible in absolute number – were removed.

In figure 3.23 the data from the previous figure is plotted again to allow for a comparison between the models for each NEA group. Some remarkable features are that for Atens there are more events falling into the 11–14 km/s bins in model M7 than in M6 (the Amors show the same feature for the 11–13 km/s bins to a lesser degree), moreover the modal value for Atens is located at 15–16 km/s in M7 in contrast to 16–17 km/s for M6. Except of these tiny differences no qualitative discrepancy can be found, the lunar effect is yet again hardly discernible. For a discussion of the velocity distributions see section 3.4.5.

### Fitting the collision frequency

After having investigated the impact velocity distributions, next we will focus on the impact frequency. We use the Mercury integrator data to create histograms for the frequency of encounters with a certain minimum distance. The data then will be fitted by a linear function like in Dvorak and Pilat-Lohinger (1999), which allows to calculate the collision frequency with the Earth.

It has to be remarked that – by using an appropriate weighting of the data points

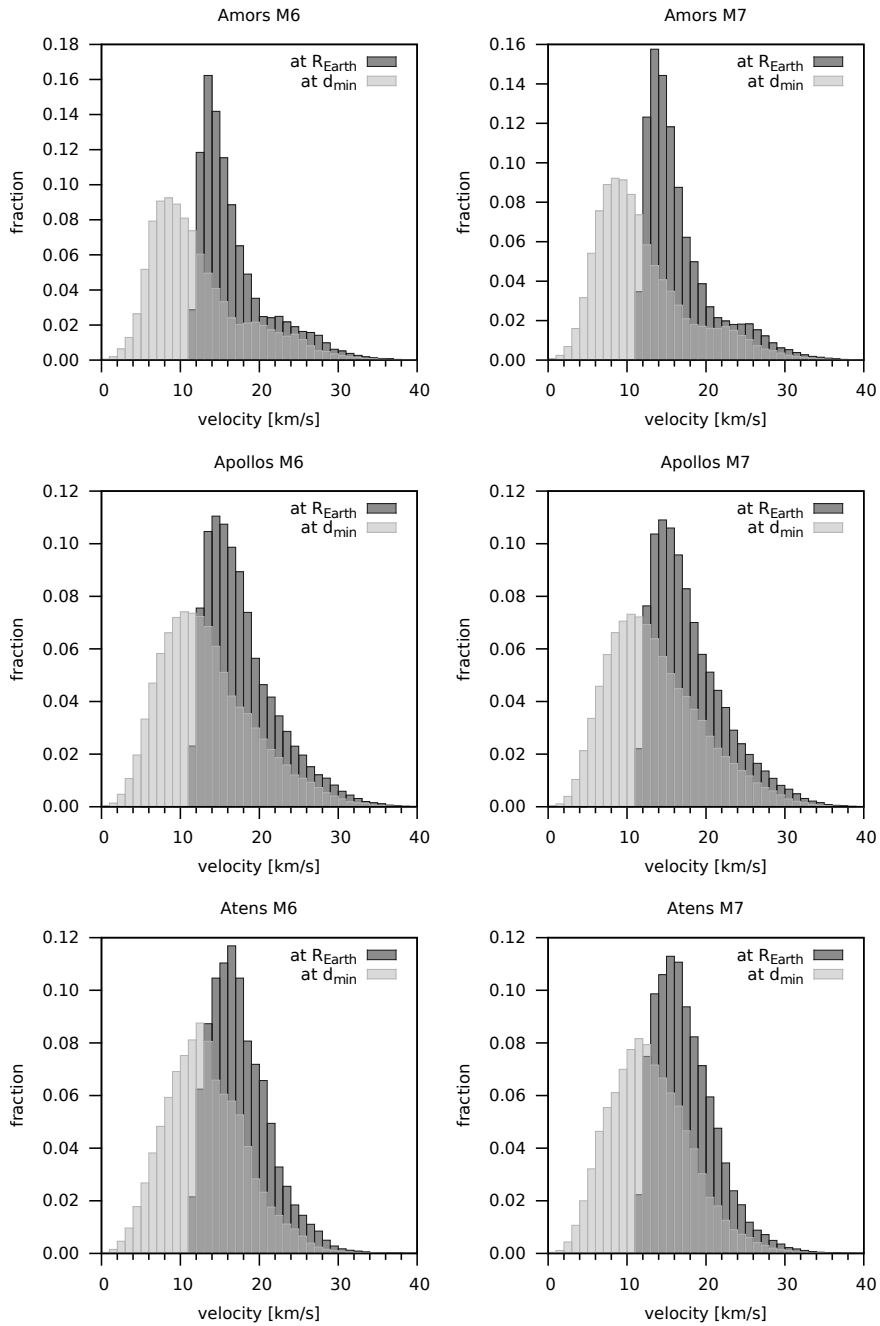


Figure 3.22: Extrapolation of impact velocity distributions (dark grey) from the given velocity distribution at minimum distance (light grey). The velocities at  $d_{\min}$  were extrapolated to the corresponding ones at the Earth surface (for which the escape velocity is  $v_{\min} = 11.2$  km/s).

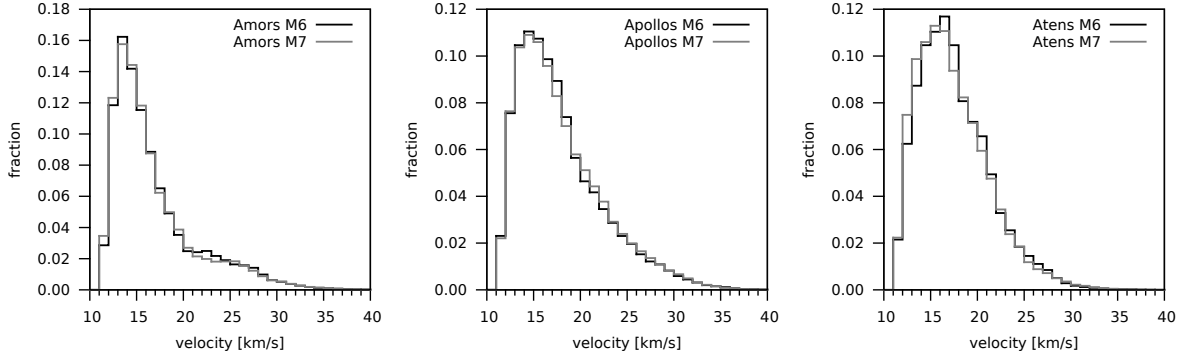


Figure 3.23: Direct comparison of the normalised impact velocity distribution in the models M6 (black curve) and M7 (grey curve). From left to right the Amor, Apollo, and Aten group is visible.

– the linear function could be forced to better fit at smaller or larger distances, but in both cases this would introduce an offset in the residuals. On the one hand it would be advantageous to have a better fit at large distances ( $> 10^6$  km), because distant encounters constitute the majority of the cases and the uncertainty about the encounter frequency grows as the distance shrinks. On the other hand we are interested in the frequency at small distances comparable to the Earth radius, so those points could be assigned a larger weight in the fitting process, which in turn would decrease the accuracy at large distances. In the end I decided to give all points the same weight in the fitting process, which does not bias the residuals.

As an example figure 3.24 shows the two Apollo fits. On the horizontal axis the distance ranges from 0 – 0.01 AU, this interval is covered using a bin-width of 6 378 km, equivalent to one Earth radius ( $R_{\oplus}$ ). Along the vertical axis the encounter frequency is given, which is the absolute number of events per bin normalised by the total number of encounters per  $10^7$  years of integration and by the number of objects. At the bottom the scatter of the residuals is shown, which increases with growing planetocentric distance.

The results of the fitting process are summarised in figure 3.25, separately for models M6 (left) and M7 (right), the collision probabilities (number per year per object) for the NEA groups are directly comparable. It is also visible that the fits generally slightly overestimate the encounter frequency at the smallest distances, except for the Amors in M7. The dots to the extreme left in the figures represent the center of the smallest bin which covers the distance range  $0 \leq r \leq R_{\oplus}$ . For details about the fit parameters and their uncertainties see table 3.5. The slopes  $b$  are rather well constrained, the relative uncertainties  $\sigma_b$  for this parameter are about 0.1 %, while the intercepts  $a$  are harder to determine and the errors are as high as 44 %.

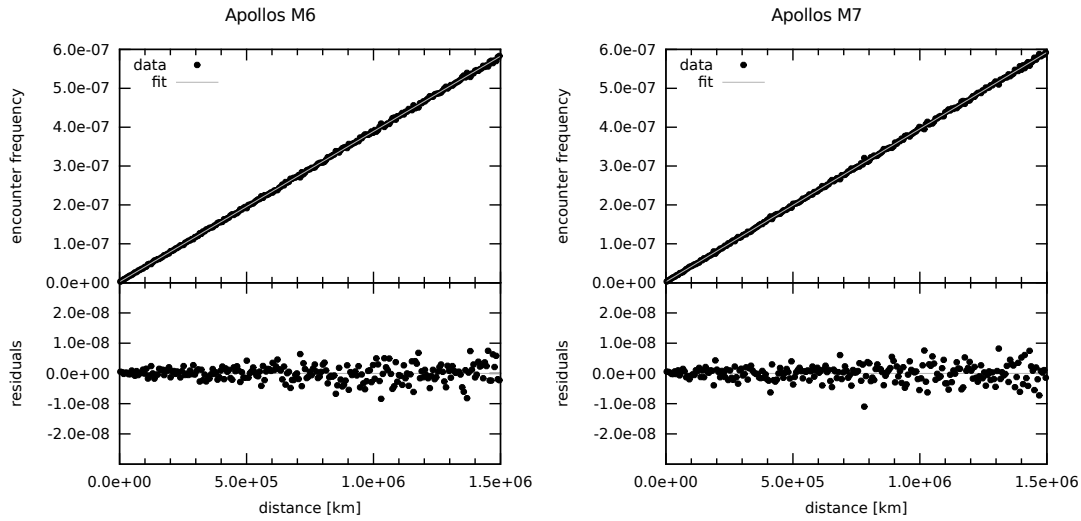


Figure 3.24: Fits for the encounter frequency versus distance for Apollos. For each distance bin (using the Earth radius of 6 378 km as bin-width) the normalised number of encounters per  $10^7$  years per object is plotted. The diagonal line is the linear least-squares fit to the data, the residuals are shown in the bottom panels.

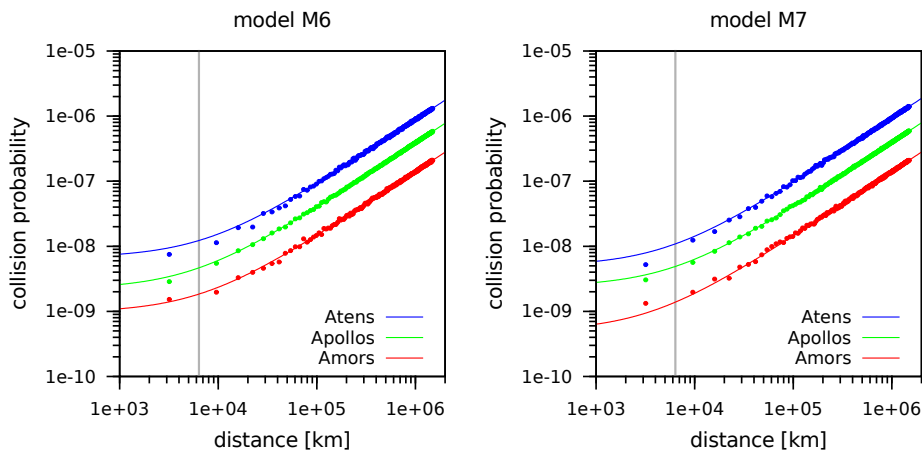


Figure 3.25: Collision probabilities (impacts per object per year) for the three NEA groups (from top to bottom): Atens (blue), Apollos (green), Amors (red). The continuous line is the linear fit to the data points, while the grey vertical line indicates the Earth's radius of 6 378 km; note the logarithmic scaling of both axes.

group, model	parameter $a \pm \sigma_a$ [ $\times 10^{-9}$ ]	parameter $b \pm \sigma_b$ [ $\times 10^{-13}$ ]
Amors, M6	$0.96 \pm 0.25$	$1.392 \pm 0.003$
Amors, M7	$0.50 \pm 0.22$	$1.399 \pm 0.003$
Apollos, M6	$2.20 \pm 0.34$	$3.869 \pm 0.004$
Apollos, M7	$2.39 \pm 0.35$	$3.933 \pm 0.004$
Atens, M6	$6.69 \pm 1.40$	$8.762 \pm 0.016$
Atens, M7	$4.95 \pm 1.33$	$9.328 \pm 0.015$

Table 3.5: Summary of the parameters for the linear fits  $f(x) = a + bx$  to the encounter frequencies ( $x$  in km) given as the number of encounters per object per year. The uncertainties for the parameters  $a$  (the intercept at  $x = 0$ ) and  $b$  (the slope) are also included.

## 3.4 Discussion

This section is intended to summarise and compare data from all models. A statistical analysis of the Lie and Mercury data will be performed. The results obtained so far will be compared to already published data and discussed in that context.

### 3.4.1 Recurrence of close encounters

In the previous sections the investigations were focusing on the lunar influence on NEAs over long time spans. Here the opposite approach will be attempted to reveal any lunar effect on the shortest times scales comparable to the lunar orbital periods (about the Sun and the Earth).

Although the Mercury integrator produced a vast number of close encounter data, it was necessary to use the cumulative data set – irrespective of the different models – to analyse the data for recurrent close encounter events. Here a recurrent close encounter is defined as a Near-Earth Asteroid approaching Earth inside the Hill sphere twice within a time span of one year<sup>7</sup>. Great care was taken to really make sure that close encounters of the same object are considered, and no other asteroid mimics a recurrence.

The extracted data was then binned with a bin-size of 2 days to create the histogram in figure 3.26. Since the vertical axis is scaled logarithmically the height of the boxes is squeezed, but the two most significant peaks are located around the 1/1 and 1/2 fractions of a year. According to that NEAs are – at least temporarily – captured in (or close to) the co-orbital 1:1 resonance with Earth, and a smaller fraction also in the 2:1 resonance, i.e. they encounter the Earth twice per year. No significant evidence

---

<sup>7</sup>For technical reasons I extended the time span to 1.1 years to avoid missing the “stragglers” that might need a few days more than one year to return to Earth.

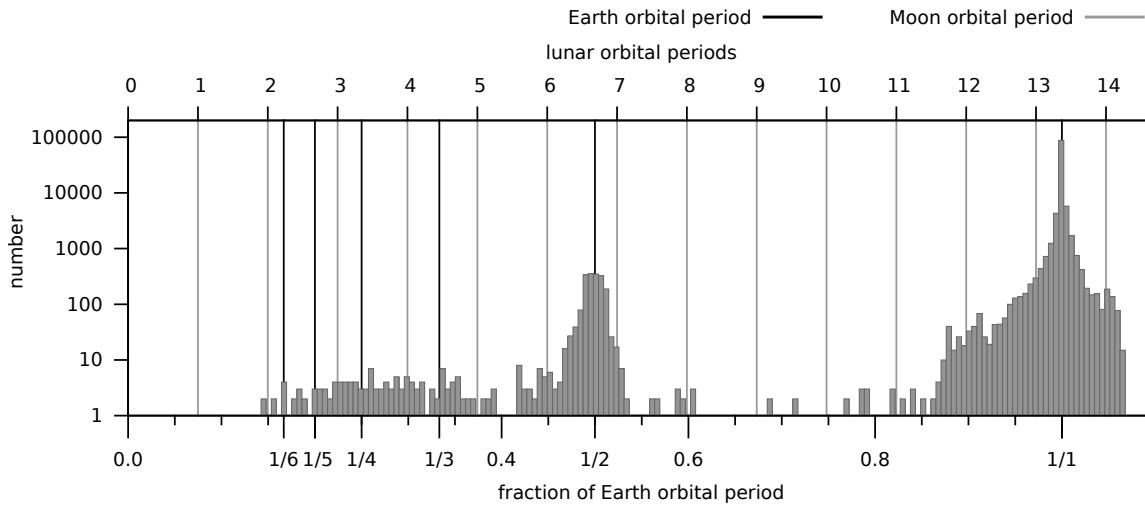


Figure 3.26: Histogram of time spans between recurring close encounters of NEAs within 1 year. The bottom axis is scaled to cover 1.1 years, the vertical black lines indicate the fractions  $1/6$ ,  $1/5$ ,  $1/4$ ,  $1/3$ ,  $1/2$ , and  $1/1$  of a year. The top axis shows multiples of the lunar orbital period with the corresponding grey vertical lines. Note the logarithmic scaling of the vertical axis.

was found for recurrent encounters for other fractions of the Earth’s orbital period, as well as for the multiples of the lunar sidereal orbital period. There are some spikes in the histogram close to these resonant values though, but none of them incorporates enough events to stand out from the noise. Another interesting point is the lack of events between  $0.6 - 0.8$  years, for which I have no explanation.

In Valsecchi et al. (2003) the authors described an analytical theory for handling resonant returns of asteroids and comets. They extended Öpik’s theory to include the times of encounters and were able to compute from the final state of an approach the parameters of the following one. It turns out that only the asteroid’s semi-major axis (for a fixed orbit of the planet) plays a role for resonant returns. Although the authors considered two examples of asteroids, they did not attempt to give a more general picture, specifically they did not suggest or refute that either the  $1/1$  or  $2/1$  resonance could be prominent among the resonant returns.

Schwarz and Dvorak (2012) investigated temporary captures of asteroids by terrestrial planets into the  $1:1$  resonance. They found that temporary captures occur more frequently for the terrestrial planets than in the outer solar system, but captured asteroids in stable orbits are rare.

Brasser and Wiegert (2008) estimated the average lifetimes for non-coorbital asteroids on Earth-like orbits to be shorter than  $10^4$  years. I did not check how many times and for how long a NEA can have recurrent encounters, this remains work for the future.

model	Amors [%]		Apollos [%]		Atens [%]	
	Lie	Mercury	Lie	Mercury	Lie	Mercury
M2	2.0	6.46	56.0	73.15	66.7	76.99
M3	2.0	6.53	55.7	74.43	66.3	79.45
M4	29.7	38.50	87.7	92.82	91.3	93.40
M5	25.7	38.81	88.3	92.45	93.3	93.87
M6	49.0	58.95	90.0	86.16	99.0	98.77
M7	35.0	58.10	92.0	87.02	99.0	98.62

Table 3.6: Percentage of objects from the different NEA groups and models with close encounters to Earth within the lunar distance. Note that the sample sizes for the Lie and Mercury integrator were not equal.

### 3.4.2 Statistics of close encounters

#### Percentage of NEAs with close encounters

We have seen that close encounters happen in all dynamical models and are an essential factor in every NEA's evolution. What is still missing is an overview of what fraction of the NEA population is actually having encounters. Table 3.6 provides the percentage of objects with close encounters to Earth within the lunar distance.

To interpret the numbers it should be recalled that for the Lie integrator the samples contained 300 objects, except for the last two models, where only 100 objects were used. The sample sizes for the Mercury integrator were larger, the numbers can be found in table 3.2.

First of all it is obvious that overall much less Amors approach Earth than Apollos or Atens. The reason is that Amors are not Earth orbit crossers from the beginning, but need some time to evolve and increase their eccentricity under the action of resonances. The sudden increase of the percentage when Mars is added in model M4 reinforces this reasoning. Still it is surprising that even in the most complex models only about 3/5 of Amors have encounters to Earth.

Three runs with the Lie integrator were aborted due to technical problems before they finished. Two of these runs concern the Amor group (for models M6/M7), which partially explains the large difference to the Mercury values. The other case is for the Apollos in M6, but this time the difference is much smaller and in good agreement to the unbiased percentage of the Apollos in M7.

For Apollos and Atens there is quite a good agreement of the percentages, both when comparing the models and the integrators. In the models M2/M3 we can see that the smaller sample size for the Lie runs relative to the Mercury runs decreases the percentage of objects with encounters. The largest differences between the Lie and Mercury runs

are found for Amors and in the models M2/M3, they are probably caused by sampling effects in the Lie runs.

### Close encounters within Hill sphere

Now we turn from relative to absolute numbers for close encounters of NEAs. Table 3.7 summarises the Mercury data on close encounters to all planets inside their Hill spheres for all dynamical models.

Comparing the number of close encounters for the same NEA group between the models we find a gradual decrease when adding more planets. For Apollos and Atens the numbers drop to nearly 50 % in models M4/5 compared to M2/3. This trend also holds for Amors, although at first the numbers increase when Mars is first included into the dynamical models. The lowest number of encounters to Earth (in total) is found for models M6/7, which is clearly due to perturbations by Jupiter and Saturn; in parallel the percentage of escaping objects is highest for these models, this will be discussed below (see table 3.9).

Earth and Venus have a quite similar number of close encounters when considering only Aten group objects<sup>8</sup>. This equivalence also explains why Venus suffers from more impacts of Aten group objects than Earth, see table 3.9.

The data in table 3.7 on close encounters to the Moon fit well with the expectations based on the size of the Hill spheres. The ratio of encounters to the Moon and Earth is  $N_M/N_E = 0.056$ , computed as the average ratio from models M3, M5, M7 over all NEA groups. The corresponding ratio of the Hill radii is  $(R_{H,M}/R_{H,E})^2 = 0.054$ , computed from equation (2.4.1) without using the eccentricity (including the eccentricity the ratio is 0.052). Note that the ratio of close encounters scales as the ratio of the Hill sphere surfaces, not of the volumes; also note that the lunar Hill sphere is completely embedded into the Earth's.

### Close encounters within lunar distance

In table 3.8 only the subset of close encounters inside the lunar distance is given. These are the total number of detected close encounters for the Lie integrator, with three exceptions marked by a star. These exceptions are the three cases mentioned before, where the integration runs were aborted before the full time was reached, hence those numbers should not be considered definitive. The Lie and Mercury data are not directly comparable due to different sample sizes.

The numbers in table 3.8 need to be normalised to adjust for the different sample sizes of the two integrators in order to be able to compare the data. We obtain the normalised number of encounters (inside the lunar distance) per object by dividing the numbers in the table by the number of objects in the respective sample (see section 3.2.2 and table

<sup>8</sup>To make the numbers in table 3.7 really comparable, one would need to rescale them to adjust for the different planetary Hill sphere sizes.

planet	dynamical model					
	M2	M3	M4	M5	M6	M7
Amors						
Earth	486 574	492 835	1 028 513	1 036 769	729 610	729 251
Moon		28 394		57 676		40 495
Venus			239 720	214 204	238 536	254 442
Mars			619 263	615 974	388 144	388 141
Jupiter					161 124	149 672
Saturn					21 364	20 167
Apollos						
Earth	8 146 593	8 222 064	4 919 334	4 911 189	2 955 277	3 003 539
Moon		461 038		272 956		166 707
Venus			2 156 213	2 082 134	1 668 576	1 653 967
Mars			809 170	801 533	480 078	487 240
Jupiter					249 765	261 147
Saturn					33 307	33 164
Atens						
Earth	2 459 552	2 689 286	1 310 621	1 281 895	1 019 455	1 081 269
Moon		151 762		71 217		60 384
Venus			1 015 586	1 137 508	949 455	918 327
Mars			86 357	78 475	67 614	76 505
Jupiter					14 779	17 013
Saturn					2 160	2 067

Table 3.7: Summary of the Mercury data on close encounters of NEAs to all planets (and the Moon) inside the respective Hill spheres depending on the dynamical model. Empty cells mark undefined planet/model combinations. See text for details.

model	Amors		Apollos		Atens	
	Lie	Mercury	Lie	Mercury	Lie	Mercury
M2	1 269	33 003	32 366	555 586	98 317	167 558
M3	364	34 002	34 040	559 945	88 490	184 182
M4	5 374	69 399	22 485	331 568	45 124	87 858
M5	4 610	69 911	21 024	331 810	43 210	86 140
M6	906*	49 347	1 528*	198 760	15 343	68 698
M7	178*	49 001	4 544	202 577	16 503	73 233

\* Integrations aborted before reaching full integration time.

Table 3.8: Absolute number of close encounters to Earth inside the lunar distance in all dynamical models for Lie and Mercury integrator data. Note that a smaller sample was used for the Lie integrator than for the Mercury integrator.

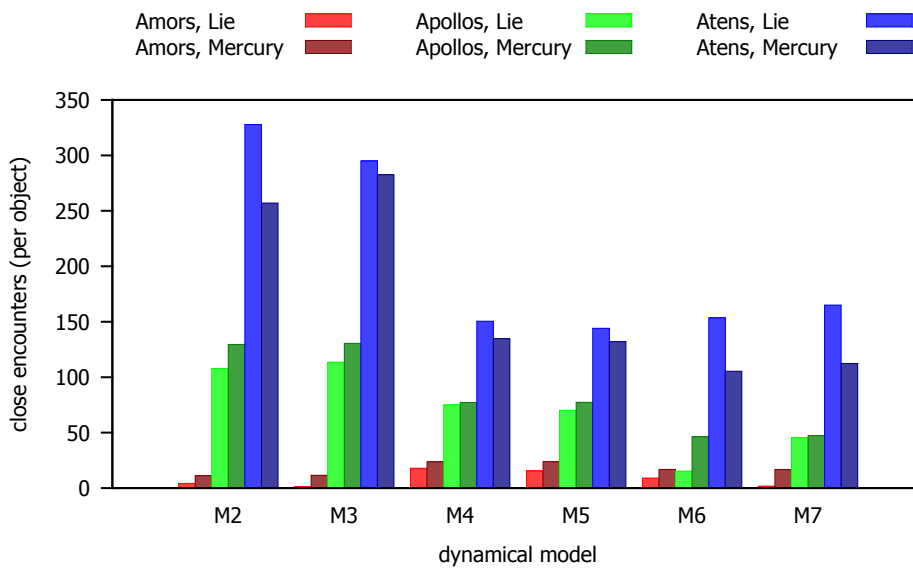


Figure 3.27: Comparison of the normalised number of close encounters per object inside the lunar distance for different dynamical models. The histogram collects data for all three NEA groups (Amors in red, Apollos in green, Atens in blue) and for both integration methods (light colours: Lie integrator, darker colour: Mercury integrator).

3.2). These values should be considered as lower limits, since for a rigorous treatment also the fraction of objects with close encounters (compare table 3.6) must be added as a correction.

Figure 3.27 shows the normalised number of encounters inside the lunar distance per object for all dynamical models. Each bar represents one NEA group with one of the integration methods. The most striking results are a couple of systematic differences between the Lie and Mercury integrator data: (i) in the Lie integrator data the Amors have less encounters by about a factor of 2, but keep in mind the aborted runs for models M6/7; (ii) on the other hand the Atens have more encounters in the Lie data relative to the Mercury data; finally for Apollos both methods agree fairly well.

In models M2/3 the Apollos and Atens have their maximal value of encounters per object, even though just 75 – 80 % of the asteroids contribute (see table 3.6). For these two models it would be easiest to detect any effect of the Moon on the encounters of NEAs, e.g. an enhanced rate of deflections and consequently fewer encounters. In contrast to this, the numbers rather indicate a higher number of encounters in model M3 relative to M2: 11.2 vs 11.6 encounters per object for Amors, 129.5 vs 130.5 for Apollos, and 257.0 vs 282.5 for Atens.

For Amors and Apollos usually the Mercury data agree to  $\pm 1$  in the number of encounters per object, whereas the Atens have a larger scatter. Unsurprisingly, in this direct comparison the Aten group has roughly two times more encounters per object than the Apollos regardless of the dynamical model (e.g. 110 vs 47 in models M6/7); the Amor group has the lowest number (17). The number of encounters per object is of course related to the orbital periods: the Aten group has shorter orbital periods and thus more encounters than the Amors.

As a consistency check for the Mercury integrator close encounter data we take the ratio of the number of close encounters inside the lunar distance  $N_{LD}$  (in table 3.8) to that of all encounters inside the Hill sphere  $N_{HS}$  (in table 3.7). When averaged over all models and all three NEA groups we find a value of  $\langle N_{LD} \rangle / \langle N_{HS} \rangle = 0.0677$ , while the ratio of the average lunar distance of  $D_M = 384400$  km to the Hill radius of Earth gives  $(D_M/R_{H,E})^2 = 0.0679$ . Thus we can be confident that the numbers in table 3.8 are neither too high nor too low.

### Uncertainties for the number of encounters

It is not straight-forward to estimate the uncertainties in the number of close encounters. Each dynamical model represents a single data-point, no strict statistical inference can be made without repeating them several times. Taking spot-checks from the NEA groups does not necessarily lead to valid results. As table 3.6 shows this would work for Atens and maybe Apollos, where over 90 % of objects do have close encounters, but it would be difficult to choose sub-samples for the Amors, and an appreciable uncertainty would remain.

I chose the following way to assess the uncertainties: The ratio of close encounters

inside the lunar distance vs. Hill sphere  $N_{LD}/N_{HS} = 0.0677$  is fairly close to the expected value of 0.0679; the same is true for encounters to the Moon vs. Earth  $N_M/N_E = 0.056$  which is close to the expected 0.054 (see above for the calculations). From the slight deviations we can estimate the relative uncertainty (error) for the number of encounters to be  $100\% \times (1 - 0.0677/0.0679) = 0.3\%$  and  $100\% \times (1 - 0.054/0.056) = 3.6\%$ , respectively. In view of the differences in the number of encounters for pairs of models (see tables 3.7, 3.8) a more conservative estimate for the uncertainty of up to 10% seems adequate. This uncertainty is mainly influenced by the Aten group for models M2/3, but neglecting those models would only decrease the uncertainty to a worst case value of 6% (again for Atens). In other words, I would consider a difference in the number of close encounters above 6 – 10% as a significant sign of the lunar influence. As a matter of fact none of the model pairs exhibits such a large difference, in most cases the differences are  $< 1 - 3\%$ , except for the mentioned larger differences for Atens. To decrease the uncertainty one would require a larger natural or synthetic population, or alternatively longer integration times.

Another check can be performed using the normalised number of encounters per object  $\epsilon$  (derived from table 3.8). The encounters inside the lunar distance can be used to independently estimate (extrapolate) the absolute number of encounters  $E$  inside the Hill sphere for different groups:

$$\frac{E_X}{E_{At}} = \frac{\epsilon_X}{\epsilon_{At}} \times \frac{N_X}{N_{At}},$$

where  $N$  is the absolute number of asteroids in the respective group (see table 3.2),  $X = \text{Amors or Apollos}$ , and the index  $At$  indicates the appropriate value for the Atens. For the Apollos we compute  $47/110 \times 4291/652 = 2.81$ , and from table 3.7 we find the ratios of encounters in models (M6, M7) to be (2.90, 2.78). In a similar way we have for the Amors in the same models 0.70 against (0.72, 0.67). This demonstrates that the quantity “encounters per object” is a useful statistical parameter for NEAs.

### 3.4.3 Statistics of impacts

In connection with close encounters also the occurrence of collisions (impacts) with the planets was monitored. When the dynamical models were introduced, it was stated that in all calculations the Sun, planets and asteroids are treated as point masses. Nevertheless, collisions are defined as encounters for which the planetocentric distance is smaller than the virtual physical radius of that planet, in case of the Earth the radius adopted is 6378 km.

#### Impacts on planets

Table 3.9 gives an overview of the Mercury integrator data about the number of NEA impacts to any massive object in the simulations. In addition to impacts also the number

of ejections<sup>9</sup> of NEAs from the solar system is included, because ejections become a frequent phenomenon in models M6/7.

From the table we see that the impacts on Earth are dominated by the Apollos as the most numerous NEA group. They are followed by the Atens and then Amors, although in models M6/7 there is hardly any difference between the latter two groups. It is also evident that the impacts follow the same trend as the encounters in table 3.7: by adding more planets to the models the number of impacts with Earth decreases. Encounters and impacts are linked to each other, NEA groups with a large number of encounters also produce many collisions. When comparing the model pairs there is no clear trend for collisions with the Earth. Sometimes there are more collisions when the Moon is present, sometimes the opposite case is true.

For Mars the number of collisions with Amors and Apollos matches, while Atens contribute only to a negligible fraction to collisions. Venus is mainly struck by Apollos and Atens, although the majority of impacts is caused by the Aten group when considering the number of impacts relative to the number of objects in the respective group.

In table 3.10 we find a summary of Earth impacts for the Lie integrator data. Since the samples are smaller, so is the number of impacts. The advantage of this data set is that with equal sample sizes (300 objects in the first four models, 100 in the last two) the number of collisions is directly comparable. The general trend of a decreasing number of collisions with increasing number of massive objects is observable, too. Similar to the Mercury integrator data there is no clear indication for a lunar influence on the number of impacts, since the numbers vary by factors of 2 – 4 for model pairs.

Figure 3.28 collects the data from tables 3.9 and 3.10 and shows the normalised number of impacts per object during  $10^7$  years of integration time for all dynamical models. Each bar represents one NEA group with one of the integration methods. The results are similar to those for the normalised number of close encounters: the Lie integrator data results in a higher impacts per object value for Atens, but underestimates collisions of Amors relative to the Mercury integrator data; for Apollos both give essentially the same results in models M6/7. There are two remarks for the Amors: (i) no impacts were detected for Amors in M6 in the Lie data, and (ii) the single event in M7 has to be scaled with 1/100 instead of 1/300 due to the reduced sample size.

### Ejections and Sun-grazers

In models M6/7 there are many NEAs that collide with the Sun, termed “Sun-grazers” by Farinella et al. (1994). This goes along with a strong increase of ejected NEAs, especially Apollos and Amors are suffering from this effect. Up to 50 % of the objects from those two groups are removed by ejections ( $\sim 1400$  Amors and  $\sim 2200$  Apollos), in contrast to only about 25 % ( $\sim 160$ ) of all Atens.

---

<sup>9</sup>An ejection (or escape) happens when the NEA reaches a distance of  $\geq 100$  AU from the Sun, or an eccentricity of  $e \geq 1$ .

target	dynamical model					
	M2	M3	M4	M5	M6	M7
Amors						
Earth	38	52	52	42	45	40
Moon		1		1		1
Venus			20	23	20	20
Mars			13	8	6	3
Jupiter					12	13
Saturn					1	0
Sun	0	0	0	0	103	82
ejected	0	0	0	0	1 386	1 372
Apollos						
Earth	420	393	222	216	124	131
Moon		10		7		3
Venus			141	125	114	121
Mars			13	7	6	4
Jupiter					11	13
Saturn					0	1
Sun	0	0	0	0	188	191
ejected	5	5	0	2	2 250	2 261
Atens						
Earth	129	131	59	58	49	34
Moon		2		1		3
Venus			70	64	55	51
Mars			0	1	1	2
Jupiter					1	0
Saturn					0	0
Sun	1	0	0	0	23	18
ejected	0	0	0	0	158	173

Table 3.9: Summary of the Mercury integrator data on the number of impacts of NEAs onto planets as well as the Moon and Sun depending on the dynamical model. Empty cells mark undefined planet/model combinations. See text for details.

group	dynamical model					
	M2	M3	M4	M5	M6	M7
Amors	1	2	2	8	0*	1*
Apollos	13	39	18	8	3*	3
Atens	73	76	26	32	12	9

\* Integrations aborted before reaching full integration time.

Table 3.10: Number of impacts on Earth in all dynamical models for Lie integrator data. All NEA groups used equal sample sizes, so the numbers should be comparable, except for those cases marked with a star.

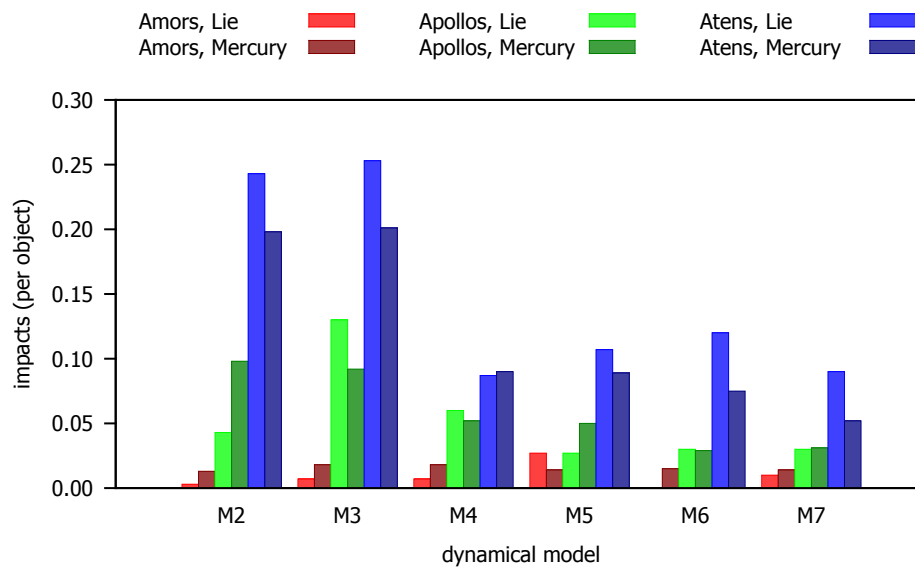


Figure 3.28: Comparing the normalised number of impacts per object for different dynamical models. The histogram collects data for all three NEA groups (Amors in red, Apollos in green, Atens in blue) and for both integration methods (light colours: Lie integrator, darker colour: Mercury integrator).

These results confirm Gladman et al. (2000), who explain the ejections by the action of the J3:1 mean-motion resonance with Jupiter and the  $\nu_6$  secular resonance with Saturn. These resonances are easily accessible for Amors and Apollos, but not for Atens. Atens could be influenced by the  $\nu_5$  secular resonance with Jupiter (see Michel et al., 1997).

However, there is a significant difference: Gladman et al. (2000) reported that more than 50 % of their NEA population (65 out of 117 objects) end as Sun-grazers in their simulations, which is in agreement with the result of 40 % (19 of 47 objects) in Farinella et al. (1994). Another 10 – 15 % of the population are ejected on hyperbolic trajectories (Farinella et al., 1994; Gladman et al., 2000). In my simulations by far most NEAs are ejected (25 – 50 %, depending on the group) and only 3 – 5 % collide with the Sun (see table 3.9). Many of the ejected NEAs might have perihelion distances that are comparable to the solar radius due to large eccentricities, though.

I cannot offer a complete explanation for this discrepancy. In my integrations I used exactly one solar radius ( $\sim 0.005$  AU) for the distance to detect a collision. From my experience with the Swifter RMVS code<sup>10</sup> (Levison and Duncan, 1994), which was employed by Gladman et al. (1997, 2000), I know that there is a parameter for the heliocentric distance at which a test particle is stopped as being too close to the central body. Gladman et al. did not specify the value used for this parameter, but it is clear that the results depend crucially on this parameter. It is also known that symplectic integrators are limited by their fixed step-size when dealing with highly eccentric orbits with small perihelion distances (Levison and Duncan, 2000).

There is another line of reasoning. Gladman et al. (1997) did not observe a high solar impact rate globally, but only for objects injected into the  $\nu_6$  and J3:1 resonances. In those two cases 70 – 80 % of the objects impacted the Sun, while for other resonances typically only 6 – 8 % suffered from that fate. For objects between the J5:2 and J2:1 resonances ejections were more important, 25 – 90 % of the asteroids were removed in this way.

In the end the apparent contradiction could be related to the numerical integration method, or alternatively related to the weighting of different contributions to the percentage of Sun-grazers.

### Impact frequency

Finally, I will estimate the impact frequency to Earth in models M6 and M7 from the data acquired so far. The following estimates all rely solely on the Mercury integrator data, as the larger number of events presumably allows to better constrain the impact frequency.

Three complementary methods will be applied, in the following each method will be discussed.

1. The first and most basic method directly estimates the impact frequency from the

<sup>10</sup>see <http://www.boulder.swri.edu/swifter/>

number of impacts  $I$  in the simulations. This gives the “probability” (or flux) for impacts per year and per object as

$$P_1 = I \times T^{-1} \times N^{-1}$$

which is normalised by the integration time ( $T = 10^7$  years) and by the number of objects  $N$  of the respective NEA group. This method does not provide a measure of the uncertainty directly, but using the assumption that the number of impacts should be the same for any pair of models it is possible to estimate an average uncertainty of  $\pm 12\%$  (with a worst-case value of up to  $\pm 30\%$ ) from table 3.9.

2. In section 3.3.4 the encounter frequencies to the Earth were described by a linear function depending on the geocentric distance, see table 3.5 for details on the parameters. This fit is based on the binned number of encounters with bins of the size of 1 Earth radius ( $R_\oplus = 6\,378$  km). We can use the fit function  $f(x) = a + bx$  to calculate as second estimate the impact frequency at the Earth radius

$$P_2 = f(x = R_\oplus).$$

The fit functions are already appropriately normalised; they also provide estimates of the uncertainty for the impact frequency derived from the parameter uncertainties. One must be careful to use the full form of the error propagation formula to compute the fit uncertainty  $\sigma_f$  (Walser, 2011)

$$\sigma_f^2 = \sigma_{a,a}^2 + 2\sigma_{a,b}^2 R_\oplus + \sigma_{b,b}^2 R_\oplus^2.$$

Here  $\sigma_{a,a}^2$ ,  $\sigma_{b,b}^2$  are the variances of the parameters  $a, b$ , and  $\sigma_{a,b}^2$  is the covariance of the two uncertainties due to a correlation in the two parameters (found to be  $r_{a,b} = -0.866$ ).

3. The final estimate also uses the fit functions  $f(x)$ , but this time the estimate involves the whole interval  $0 \leq x \leq R_\oplus$  instead of a single point. It should be noted that the encounter distance is a continuous variable and as such the probability for it to have the specific value  $x = R_\oplus$  is zero. Therefore the third impact frequency estimate is

$$P_3 = \frac{1}{R_\oplus} \int_0^{R_\oplus} f(x) dx.$$

This integral represents the (continuous) average of  $f(x)$  over the integration interval (in this case equal to the bin-width). The uncertainty for the impact frequency is calculated from the propagation of uncertainty for the fit parameters (variances and covariances) from the function  $g(a, b) = P_3$  by

$$\sigma_g^2 = \left(\frac{\partial g}{\partial a}\right)^2 \sigma_{a,a}^2 + 2\left(\frac{\partial g}{\partial a}\right)\left(\frac{\partial g}{\partial b}\right) \sigma_{a,b}^2 + \left(\frac{\partial g}{\partial b}\right)^2 \sigma_{b,b}^2.$$

group, model	$P_1[\times 10^{-9}]$	$I_1$	$P_2[\times 10^{-9}]$	$I_2$	$P_3[\times 10^{-9}]$	$I_3$
Amors, M6	1.531	45	$1.85 \pm 0.25$	$54 \pm 8$	$1.40 \pm 0.26$	$41 \pm 8$
Amors, M7	1.361	40	$1.39 \pm 0.22$	$41 \pm 6$	$0.94 \pm 0.22$	$28 \pm 6$
Apollos, M6	2.890	124	$4.67 \pm 0.33$	$200 \pm 15$	$3.44 \pm 0.34$	$147 \pm 15$
Apollos, M7	3.053	131	$4.90 \pm 0.35$	$210 \pm 15$	$3.65 \pm 0.35$	$157 \pm 15$
Atens, M6	7.515	49	$12.17 \pm 1.38$	$80 \pm 9$	$9.49 \pm 1.40$	$62 \pm 9$
Atens, M7	5.215	34	$10.81 \pm 1.31$	$71 \pm 9$	$7.92 \pm 1.34$	$52 \pm 9$

Table 3.11: Estimated impact frequencies  $P_k$  (impacts per year per object) on Earth and extrapolated number of impacts  $I_k$  for models M6/7 based on Mercury integrator data. See text for details.

In table 3.11 we find the estimated impact frequencies and the extrapolated number of impacts over  $10^7$  years. This extrapolated number of impacts for a given NEA population size (equal to that used in the simulations) allows to compare the estimates to the actual data.

The numbers in the columns for  $P_1$  and  $I_1$  are taken directly from the numerical integrations, and so no uncertainties are available. As discussed above, a rough estimate of the uncertainties can be calculated by comparing the pairs of models and would give relative errors of 12 % (but up to 30 % for a conservative estimate). The uncertainties for  $P_2$ ,  $P_3$  are of the order of 10 %, which is a consequence of the rather large errors of the fit parameter  $a$  for the intercept (see table 3.5); the smaller errors for the better constrained slopes  $b$  have a weak influence.

In all cases the extrapolated number of impacts  $I_2, I_3$  agree to within the error bars between the models. The reason that  $I_2, I_3$  have identical errors is that they were derived from the same fit parameters (and rounded to the nearest integer). The extrapolated number of impacts  $I_2$  is generally too high when using the impact frequencies  $P_2$ , while  $P_3$  gives results that are closer to the numbers in the simulations ( $I_1$ ).

It is important to note that these impact frequencies (or impact probabilities) represent an average number over an entire NEA group, they can be used for statistical purposes, but for individual objects they are less useful.

The Amor impact frequency should be considered as an upper limit, because the asteroids derived from the Amor group would have become Apollos or Atens once they impact. An improvement would be to split up the Amor impact frequency and distribute it among the other groups according to the determined group mixing rates, which were discussed in sections 3.3.2 and 3.3.3 (see the example for Apollos in figure 3.19).

## A statistical test

A Pearson chi-squared test was performed to distinguish whether or not the differences in the absolute number of impacts are significant. Four categories were defined for a  $2 \times 2$  contingency table with a single degree-of-freedom: (model M6, model M7) vs (impact, non-impact). The “impact” category contains the observed number of impacts  $N_1$  from table 3.11, the complementary “non-impact” category then gives the number of objects without impacts,  $N_{\text{tot}} - N_1$ , where  $N_{\text{tot}}$  is taken from table 3.2 for each group.

The null hypothesis  $H_0$  states that the categories “model” and “impact” are independent, it shall be tested to the significance-level  $\alpha = 0.01$ . Processing the data for Amors/Apollos/Atens results in  $\chi^2$  values of 0.3/0.2/2.9 which are clearly smaller than the critical value  $\chi_{\text{crit}}^2 = 6.63$ .

Consequently the hypothesis  $H_0$  cannot be rejected, which means that the impacts (non-impacts) are statistically independent of the model. In turn this means that with a high probability the Moon has no significant influence on the number of impacts of Near-Earth Asteroids with Earth.

### 3.4.4 Comparison of collision probabilities

In the following paragraphs it will be compared how the collision probabilities derived here relate to those published by other authors.

Shoemaker et al. (1979) provided collision probabilities with Earth based on a secular perturbation theory extending the equations of Öpik. The authors gave probabilities of collision for individual NEAs (Table I) which range from  $0.4 - 14 \times 10^{-9}$  per year for a sample of 35 asteroids. The estimates of Shoemaker et al. for the mean collision probabilities of Atens, Apollos, and Earth-crossing Amors are  $(9.1, 2.6, \approx 1) \times 10^{-9}$  per year (Table II), which agree very well with the data in table 3.11.

Steel and Baggaley (1985) used a method based on the spatial density of asteroids to determine the collision probability for the then known population of 76 NEAs. From the individual collision probabilities the authors calculated the mean probabilities and spreads for Atens and Apollos as  $22 \pm 26 \times 10^{-9}$  and  $5.8 \pm 11.3 \times 10^{-9}$  per year, respectively. These numbers agree fairly well for the Apollos, but are about two times larger than my own estimates for the Atens. They noted that the mean probability for Atens would have been lower by exactly this factor of two, if they had not included a low-inclination asteroid that biased the Aten sample (4 objects in total).

Later Steel (1995) recalculated the collision probabilities for 169 Apollos and Atens, and found similar values to the ones before, namely  $9.33 \times 10^{-9}$  and  $24.30 \times 10^{-9}$  per year for Apollos and Atens. Amors were not included in his calculations, as they are not Earth-orbit crossers at time  $t = 0$ .

Milani et al. (1990) extracted collision probabilities from the data acquired within “Project Spaceguard”. Originally they integrated numerically the orbits of 410 planet crossing asteroids for  $2 \times 10^5$  years, but they used only a subset of 89 asteroids for

their estimates. Since Milani et al. did not use the Shoemaker classification but defined several new dynamical classes, here only the mean collision probabilities spanning all classes can be compared. They found a mean probability of  $2.82 \times 10^{-9}$  per year, whereas their maximum value turns out to be  $5.68 \times 10^{-9}$  per year for the Geographos class. Some of their classes are protected from having approaches to Earth by resonance mechanisms, so the lowest probabilities are  $0.11 \times 10^{-9}$  per year (Kozai class).

Rabinowitz et al. (1994) recalculated the individual collision probabilities for an enlarged sample of 180 Earth-orbit crossing asteroids using the method of Shoemaker et al. (1979). They found values that scatter widely between  $2.9 - 42 \times 10^{-9}$  per year for Atens, and  $0.4 - 30 \times 10^{-9}$  per year for Apollos. From their ‘Table 1’ I estimate a median value somewhere around  $6 \times 10^{-9}$  for Atens, and a mean (median) of  $4.6 \times 10^{-9}$  ( $2.8 \times 10^{-9}$ ) per year for Apollos.

Atens and Apollos were also studied in Dvorak and Pilat-Lohinger (1999) by numerically integrating the orbital evolution of 78 NEAs over  $10^6$  years. The approach in that paper is different from the current one so far as collision probabilities were obtained for any asteroid separately, and then averaged for the whole group. The reported collision probabilities are  $38.6 \pm 22.5 \times 10^{-9}$  for Atens and  $8.2 \pm 5.7 \times 10^{-9}$  for Apollos (units are collisions per year). In a subsequent paper Dvorak and Freistetter (2001) investigated an enlarged sample of 720 fictitious objects for 0.5 million years. They published collision probabilities that are higher by a factor of 2 – 6 than the results reported earlier; this could be an artefact of the regular distribution of the initial conditions in the  $(a, e)$  space.

In the paper of Gladman et al. (2000) 117 NEAs were investigated over 60 Myr. Although they did not specify separate impact rates for the groups (the authors reported 5 impacts to Earth), an overall impact rate of  $4.7 \pm 1.3 \times 10^{-9}$  per year per object was found. That value is very close to the Apollo’s impact frequency found here, which leads me to the speculation that the results of Gladman et al. are dominated by that group.

For the special case of NEAs with Earth-like orbits ( $0.95 \leq a \leq 1.05$  AU,  $0 \leq e \leq 0.1$ , and  $0 \leq i \leq 10$  degrees) Brassier and Wiegert (2008) pointed out that the impact rates can be more than two orders of magnitude higher than the “ordinary” values (up to  $5 \times 10^{-6}$  per year). However, these orbits are very chaotic, they diffuse away from Earth by close encounters on a typical time scale of  $10^4$  years.

Overall there seems to be a good agreement of the impact frequencies obtained from the Mercury integrator data and the values from the cited references. I am aware of the possibility that some publications may contain values different from those mentioned here, but to the best of my knowledge the enumeration above is complete.

### 3.4.5 Impact velocities

In section 3.3.4 the distribution of impact velocities to Earth was estimated from the known velocity distribution for close encounters in models M6/M7, see figures 3.22, 3.23. Here it will be discussed how the obtained distributions compare to previous results.

group, model	impact velocity [km/s]			
	mean $\pm$ std. dev.	median	quartile $v_{0.25}$	quartile $v_{0.75}$
Amors, M6	$16.9 \pm 4.6$	15.4	13.6	18.6
Amors, M7	$16.8 \pm 4.6$	15.3	13.6	18.4
Apollos, M6	$17.9 \pm 4.6$	16.8	14.4	20.2
Apollos, M7	$18.0 \pm 4.6$	16.9	14.4	20.5
Atens, M6	$17.6 \pm 3.8$	17.0	14.8	19.8
Atens, M7	$17.4 \pm 3.8$	16.8	14.5	19.7

Table 3.12: A statistical summary of the impact velocity distributions for Earth in models M6/M7; all velocities are in km/s. The numbers in this table refer to the impact velocity distributions shown in figure 3.23.

A statistical summary of the impact velocities is provided in table 3.12. The table gives the mean impact velocity and the  $1\text{-}\sigma$  standard deviation, the median value, and the values of the 1st and 3rd quartile boundary for each dynamical model. From figure 3.23 the modal values for Amors, Apollos, Atens are found to be 13–14, 14–15, and 16–17 km/s (in M6) (but 15–16 km/s in M7), respectively. The standard deviations are rather large due to the tails that extend to impact velocities of  $v > 45$  km/s, but the cumulative probability for  $v > 45$  km/s is just  $\leq 0.01\%$ . Note that Amors and Apollos have identical standard deviations (when rounded to one decimal digit, differences are present at the second digit), which indicates that the majority of Earth-crossing Amors is in fact Apollo group objects. All mean/median values can be considered to be statistically equivalent, the Moon in M7 does not introduce any shift or decrease of velocity to these distributions.

Bottke et al. (1994, Figure 8) presented the impact velocity-probability distribution for Earth crossers. The mean (median) impact velocities are 17.2 (16.1) km/s averaged over all 128 NEAs in their sample. They remarked that the distributions are quite spiky, as they had to sum separate distributions from their Öpik type method.

Using the method of Steel and Baggaley (1985) collision speeds were calculated in Steel (1995, see Table 1) for 169 Apollos and Atens. Impact speeds were weighted by the collision probabilities; for the two NEA groups the mean values are 15.7 km/s (Apollos) and 15.1 km/s (Atens) – a weighted mean over both groups is 15.5 km/s. When considering the subset of objects with  $e < 0.2$  ( $e > 0.2$ ) an average impact speed of 13.7 (15.8) km/s was determined.

Steel (1998) computed the distributions and moments in impact speeds with an emphasis on objects of size  $\geq 0.5$  km (NEAs and comets). The numbers from his Figure 1 give minimum/mean/maximum impact speeds of 12.6/17.7/40.7 km/s. He also noted

that the distribution is skewed towards low impact speeds with 75 % of cases having  $v < 20$  km/s, and just a few percent with  $v > 30$  km/s.

In Gladman et al. (2000) the distribution of impact speeds was calculated by weighting the encounter velocities with the collision probability, for this they used the velocity distribution over the entire integration time. The reported median impact speeds are 15 km/s at  $t = 0$  and 19 km/s over 60 Myr (for a sample of 117 NEAs).

Jeffers et al. (2001) computed the impact velocity distribution for NEAs (among other impactor populations) by means of an Öpik method that handles also eccentric orbits for both target and impactor. They used a synthetic orbital element distribution to avoid any observational bias and created a population of 20 000 asteroids, from which they obtained a mean impact velocity of 21.7 km/s. However, one must caution that by using a debiased orbital element distribution for NEAs the increased number of objects with high eccentricity and inclination would definitely shift the impact velocity to larger speeds.

A more recent estimate of impact velocities to the terrestrial planets was given in Minton and Malhotra (2010). They found mean (median) velocities of 20.3 (18.9) km/s for an initial population of  $> 17\,000$  particles. These particles were initially located in the asteroid main-belt close to resonances that drive them towards the terrestrial planets. Minton & Malhotra considered only unique encounters between a particle and a planet, i.e. the first encounter only. They noted that the velocity distribution would become skewed by multiple encounters. However, it is possible that they overestimated the velocities for this reason, since at the first encounter the particle has just left the main-belt and probably has a rather high eccentricity which leads to a large impact velocity.

### 3.4.6 Surviving objects

Figure 3.29 shows the details about how many objects have survived until the end of the Mercury integrations. Each NEA is assigned to a group at  $t = 0$  and remains linked to it, regardless of how many times it might change to another group. Amors are shown in light grey, Apollos in medium grey, and Atens have dark grey colour. The plot contains only NEAs that neither had impacts (to a planet, the Moon, or the Sun), nor were ejected from the solar system by a close approach.

It is visible from the figure that in the first four models the fractions are almost constant, while the percentage of surviving objects drops sharply below 50 % for models M6/M7.

In models M2 – M5 objects are predominantly removed by collisions with terrestrial planets; collisions with the Sun or ejections play a minor role. On average about 90 % of all objects survive (when compensating for the group sizes), which evidences that collisions are a rather inefficient way to decrease the NEA population. The small fraction of removed objects would lead to an estimate of the dynamical lifetime of the order of  $10^8$  years, which is in agreement with calculations using the Öpik theory where resonances are

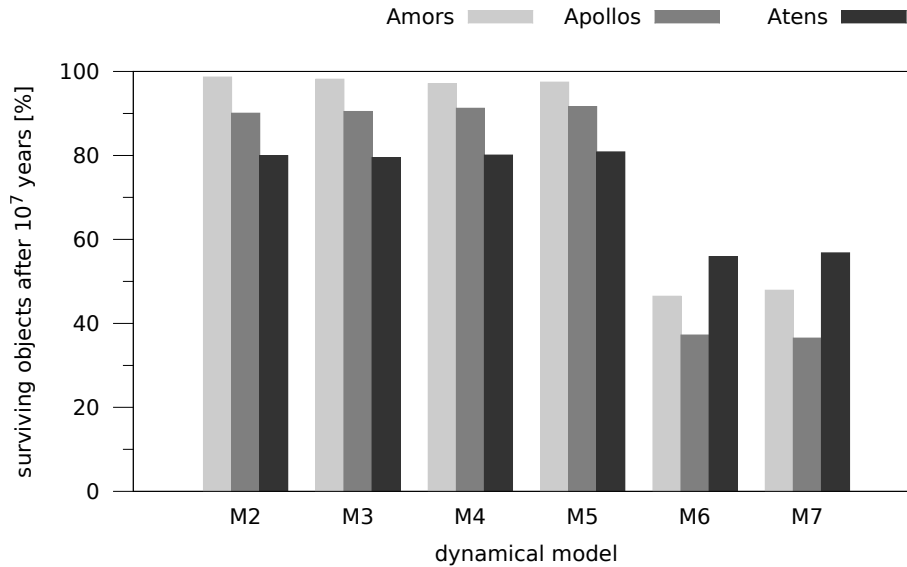


Figure 3.29: The percentage of objects that survived the whole integration time of  $10^7$  years. The grey coloured bars represent the three NEA groups in each dynamical models.

neglected. For the same four models the fraction of surviving objects in each NEA group is dominated by the frequency of approaches, which in turn determines the frequency of impacts. As Atens have the highest number of encounters (see figure 3.27) they also have the lowest fraction of survivors.

The situation changes fundamentally for models M6 and M7, where on average just 42 % of the initial population remains at the end of the integration. In contrast to the other models the Atens are now the group with most survivors (above 50 %). According to Gladman et al. (2000), NEAs (in particular Amors and Apollos) are strongly decimated by the  $\nu_6$  secular resonance with Saturn and the J3:1 mean motion resonance with Jupiter acting for semi-major axes between 2.0 – 2.6 AU – values that are typical for Amors and Apollos, but not for Atens. The low percentage of surviving Amors and Apollos – and the large amount of ejected asteroids (see table 3.9) – can be interpreted in the light of this finding.

It has already been discussed earlier in connection with impacts, that the presence of the Moon does not make any difference. Also here the percentages of surviving objects are equal to within  $\pm 1$  % for all pairs of models.

# Chapter 4

## Impact simulations

This chapter presents the impact simulations that aim to shed light on the lunar influence on possible Earth impacting objects in a simple dynamical model.

At the beginning the dynamical model is introduced in section 4.1. The dynamical model has two complementary variants that investigate the positive and negative effect of the Moon on possible impactors. The two variants and the related configurations are explained in that section.

In section 4.2 the simulation process is described with a focus on the technical details. This section presents the numerical methods for solving the equations of motion, and illustrates the procedures for generating initial conditions for the simulations.

Section 4.3 summarises the results of the simulations. For each variant of the dynamical model different configurations are compared. The quantitative analysis of the simulation outcomes allows to derive a statistical average lunar effect.

The results are finally discussed in section 4.4 and they are compared to published data in the literature.

### 4.1 Dynamical models

#### 4.1.1 Background

Several studies have investigated the dynamical processes of impacts and impact ejecta in the Earth-Moon system and beyond. In the following I will point out key features of those studies that are also relevant for this work.

Gladman et al. (1995) studied the dynamical evolution of lunar impact ejecta to gain insights on the transport processes of lunar material to Earth. In their numerical integrations they used a four-body problem including Earth, Moon, Sun and the ejected particle. They chose initial launch speeds of impact ejecta that are between 2.3 and 3.5 km/s, not very different from the lunar escape speed of 2.4 km/s. They concluded that the amount of ejecta returning to the Moon or delivered to Earth is strongly dependent on the initial velocity, and that the Moon is very efficient in scattering away objects with velocities similar to its orbital speed of  $\approx 1$  km/s.

In a follow-up research Gladman et al. (2005) investigated the spreading of Earth-escaping impact ejecta and the delivery to other planets in the solar system. They considered impactor speeds ranging from the terrestrial escape speed of 11.2 km/s up to 16.4 km/s. From test calculations performed with a model including the Moon the authors found no evidence that it influenced the number of objects returning to Earth.

Scheeres et al. (2002) reviewed the topic of ejecta generated by impacts on asteroids. They discussed the production of ejecta, the relevant dynamical processes and perturbing forces, and gave a classification scheme for the fate of asteroidal ejecta. Although the main focus of their work was different, in this thesis several concepts from that paper are applied.

In Alvarellos et al. (2002) the authors studied the orbital evolution of ejecta from Jupiter's moon Ganymede. They reported the particularly interesting result that particles having sub-escape speed ( $\sim 0.96v_{\text{esc}}$ ) could still orbit Ganymede temporarily, i.e. they do not fall back immediately. The authors chose a launch speed interval of 0.96 – 1.40 times the escape speed for the simulations (in case of Earth this would give an interval of  $11.2 \leq v \leq 15.7$  km/s). These simulations used four different launch angles: 0, 30, 45, and 60 degrees from the vertical.

Another satellite – Saturn's moon Hyperion – was investigated by Dobrovolskis and Lissauer (2004). This work used a much more complex dynamical model (it included several other satellites of Saturn as well as the effect of its rings) and followed the ejecta over a time-span of  $10^5$  years.

Domingos et al. (2004) analysed the lunar effect on collisional processes of asteroids with the Earth. In a restricted four-body model Sun, Earth, Moon and NEA they assessed the strength of the lunar influence on asteroids with relative velocities below 5 km/s. They concluded that the Moon is more likely to help to avoid collision with Earth than to cause them (2.6 % vs 0.6 %). However, their study was restricted to only two dimensions which could severely enhance the interaction probability between Moon and asteroids, besides they used only some hundred particles for the simulations.

In contrast to the other studies discussed so far, Artemieva and Shuvalov (2008) used a 3D hydrodynamical code to model high-velocity impacts of asteroids and comets on the Moon and to estimate the amount of ejecta material generated.

Reyes-Ruiz et al. (2012) continued the research on the collision probability of Earth impact ejecta with other planets in the lines of the Gladman et al. (1995, 2005) papers. In their dynamical model the Moon was included, and they used a larger number of test particles in the simulations than any previous study. They also estimated the effect of the Moon by comparing simulations using separate bodies to the Earth-Moon barycenter model, but found merely minor differences.

Galiazzo et al. (2013b) used a statistical approach to find the most probable source regions of the impactor that created Bosumtwi crater in Ghana. Starting from available geological constraints a number of test particles were traced backwards in time via numerical integrations. The evolution of the “ejected” test-particles was followed for 100 Myr under the influence of the planets and major main-belt asteroids.

### 4.1.2 General aspects

According to Domingos et al. (2004) there are two aspects that need to be taken into account when investigating the role of the Moon: On the one hand it can shield the Earth from Near-Earth Asteroids by direct collisions and indirectly by scattering them away from collision trajectories, but on the other hand it can also contribute to additional impacts by forcing NEAs towards Earth that otherwise would not have hit the planet.

In order to analyse these effects it was necessary to simplify the dynamical model as much as possible, while still retaining the essential ingredients – the Earth and Moon as separate objects. The dynamical model chosen for all simulations is the spatial Circular Restricted Three-Body Problem (CR3BP) in the rotating frame, using the equations of motion (2.3.3) which were derived in section 2.3.

One must be aware of the limitations of this model, especially because the Sun acts as a major perturber on the system (see force estimates on page 60). However, the simulations cover only a rather short time span of the order of several days and it can be safely assumed that for this time-scale the model describes the dynamics sufficiently well. An upper limit for the simulation time-scale can be estimated from the “free-fall” time  $\tau_{ff}$ . An object coming from infinity (with its initial velocity being zero) would arrive to Earth’s sphere of influence ( $R_{\text{SOI}} = 150 R_{\oplus}$ ) with a velocity of  $v_{\text{SOI}} = v(R_{\text{SOI}}) = 0.913$  km/s, which is simply the (parabolic) escape velocity at that distance. If we assume the object to be unaccelerated it will take the free-fall time  $\tau_{ff} = 2R_{\text{SOI}}/v_{\text{SOI}} \approx 24.3$  days to pass through the Earth’s SOI. Note that this is a strict upper limit, because real objects would be accelerated by Earth’s gravity and would take less time.

A possible solution for including the perturbation from the Sun while still having a simple model is to use the Bi-Circular Restricted Four-Body Problem (Simó et al., 1995). This model still allows to express the perturbations from Earth, Moon, and Sun on a massless asteroid in compact form without the need to integrate the orbits of any of the perturbing bodies. A drawback of this model is the fact that it does not fulfil Newton’s laws of motion, as circular orbits are enforced artificially. I have not made any attempt neither to compare the CR3BP to the BCR4BP nor to cross-check the behaviour of the simulations in both models, but a comparison can be found in Castelli (2011).

Another limitation of the CR3BP is naturally that it cannot account for the Moon’s eccentric orbit. This point was ignored for the sake of having a simple form of the equations of motion, as the elliptic restricted three-body problem would introduce such annoyances like an explicit time-dependence into the equations of motion together with a pulsating coordinate system (see Szebehely, 1967) – consequently the unit-length is not constant any more.

To analyse both aspects of the lunar influence I used two special simulation setups (models) in the frame of the CR3BP, the details are explained below. Each of the two model consists of a number of consecutive phases, and depends on certain parameters. Two key parameters are the Earth-Moon mass ratio  $\mu$  and the Earth-Moon distance  $d_{\text{EM}}$ . It has already been discussed in section 3.1 that the Moon’s distance to Earth

increases with time (Goldreich, 1966; Touma and Wisdom, 1994), so that it must have been much closer to Earth at the time of the Late Heavy Bombardment (LHB). The simulations cover three different configurations of the Earth-Moon system by varying the key parameters:

- C1** the default configuration with an Earth-Moon mass ratio of 81.30057 (Roncoli, 2005), this results in  $\mu = 1/82.30057$ , and a constant Earth-Moon distance of  $d_{EM} = 384\,400$  km;
- C2** a configuration with the lunar mass doubled to  $\mu = 1/40$ , the Earth-Moon distance is not changed;
- C3** a configuration where the Moon is at half of its current distance (192 200 km), and the mass ratio is kept at the default value.

The first configuration C1 uses the default parameters for the Earth-Moon system as it is today, so that it is possible to derive the lunar efficiency in deflecting asteroids. Configuration C1 will be used as a benchmark for the other configurations. In the second configuration C2 a more massive Moon is used to check which role the lunar mass plays in the process of deflecting incoming NEAs. The third configuration C3 serves to assess how well the Moon could shield the Earth from impacts some  $10^9$  years ago when it was much closer.

The CR3BP uses normalised non-dimensional units such that the gravitational constant is equal to 1. When using different values for the key parameters one must be careful to choose the right units to satisfy this condition. For the default system the unit-length is 384 400 km, the unit-mass is the total mass of the Earth-Moon system (its value is  $1/328900.5$  solar masses), which fixes the time-unit to roughly 4.34 days (such that one sidereal revolution of the Moon takes  $2\pi$  time units).

### 4.1.3 Model 1: the Moon's role for deflecting impacts

In this first model M1 we are interested in the efficiency of the Moon to prevent impacts on Earth, and the circumstances of such successful deflections. The basic idea is to assume that an impact has already occurred on Earth and to “replay” the situation when the Moon is added to the system.

The simulations are then structured into three consecutive phases:

**Phase 0** A large number<sup>1</sup> of impact sites on the Earth surface is created using a given random distribution in positions and velocities.

**Phase 1** The impactor trajectories are propagated from the Earth surface to a point outside of the Earth's SOI in a two-body problem (i.e. without lunar influence); for this phase the hyperbolic  $f$  and  $g$  functions from section 2.5.1 are employed.

---

<sup>1</sup>The exact number is 40962 random initial conditions per simulation, which is derived from the number of vertices of a polyhedron after 6 iterations, see table 2.2.

**Phase 2** The impactors are released from the SOI towards Earth under the combined gravitational influence of Earth and Moon in the spatial CR3BP.

The final outcomes of **Phase 2** can be:

1. The object reimpacts on Earth at a location usually distinct from its initial point.
2. The object impacts on the Moon if the two trajectories intersect, this case is counted as a deflection.
3. The impactor's trajectory is modified by the Moon in such a way that it misses the Earth and leaves its SOI; since all initial velocities are hyperbolic with respect to Earth the simulation is stopped at this point.
4. The impactor's trajectory is modified by the Moon and it misses the Earth, but it remains captured inside the SOI up to some prescribed time limit.

This model can be considered as analogous to the impact ejecta simulations discussed above. A number of particles is launched from the surface of the target body and it must be determined which fraction of them return to the surface. However, the main goal is slightly different here, since we are interested primarily in those particles that *do not* return.

#### 4.1.4 Model 2: the Moon's contribution to impacts

In the second model M2 we investigate the Moon's contribution to impacts on Earth. The simulation setup is following the concept of a scattering experiment. Particles are started at the border of Earth's sphere of influence on trajectories that avoid impacts with Earth in the absence of the Moon, but the lunar influence could force them to strike Earth.

The simulations have the following structure:

**Phase 0** A large number of particles is set-up at the Earth's SOI using different random distributions for the impact parameter (miss distance to Earth), the initial velocity, and the phase angle of the Moon.

**Phase 1** The particle trajectories are propagated in the spatial CR3BP under the combined gravitational influence of Earth and Moon.

This model does not have a two-body phase, so that the two stages defined above are sufficient.

The final outcomes of **Phase 1** in this model can be:

1. The particle impacts on Earth, in this case the Moon has caused an additional impact.

2. The particle impacts on the Moon, these events are relevant for the statistics but not for the model.
3. The particle misses the Earth and leaves its SOI; the simulation is stopped at this point.
4. The particle misses the Earth, but it remains captured inside the SOI up to some prescribed time limit.

The exact details about the simulations and the choice of the initial conditions are given in section 4.2.

### 4.1.5 Summary

The two complementary models M1 and M2<sup>2</sup> shed light on both aspects of the lunar influence and allow to constrain the dynamical importance of the rather large satellite of Earth.

Here are the main facts about the models:

- The spatial circular restricted three-body problem Earth–Moon–asteroid is the basis of all simulations.
- Model M1 investigates the Moon’s role for deflecting impacts.
- Model M2 investigates the Moon’s contribution to impacts.
- For each model there are three configurations C1, C2, C3 differing in the Earth–Moon distance or the mass ratio.
- A simulation run always consists of 40 962 particles with random initial conditions. The simulations last until a particle impacts either on Earth or Moon, or it leaves the Earth’s SOI.

The simulation phases for the models were mentioned for the sake of completeness. The reader should not care about them, they are not important for understanding the rest of this chapter.

## 4.2 Simulation

This section describes the numerical methods used to accomplish the simulations. It covers the method used to integrate the equations of motion for the spatial CR3BP and the type of distributions for the initial conditions.

---

<sup>2</sup>not to be confused with the model of the same name in section 3.1

### 4.2.1 Numerical integrator and manifold correction

At the core of the simulations the equations of motion (2.3.3) for the spatial CR3BP have to be solved by a numerical integration procedure. For this purpose a Runge-Kutta method introduced by Cash and Karp (1990) was applied following the formulation in Press et al. (1992). This is an explicit embedded Runge-Kutta method combining two methods of order 5 and 4 which uses 6 stages (evaluations of the force function) per basic time step. By construction the method is capable of estimating the local truncation error and thus to adapt the step-size accordingly. This adaptive step-size control is valuable whenever the particles are approaching the Earth or Moon, since then the accelerations grow in magnitude and so would the local errors if a fixed step-size was used; a variable step-size can partly compensate for this effect.

It is well known that explicit Runge-Kutta methods have the tendency to lead to a long-term shift of the conserved quantities, i.e. they cannot keep the Jacobi constant really constant – see Eggl and Dvorak (2010) for a discussion and comparison to other methods.

A way to avoid this behaviour was presented in section 2.3.2 with the manifold correction method (MFC). After each integration step the position and velocity vector are rescaled by a scalar number to comply exactly to the requirement that the Jacobi constant remains fixed to its initial value. This correction adds a little overhead to the numerical method but the increase in accuracy more than compensates the effort.

Figure 4.1 shows the effect of the MFC on the relative error  $|C(t) - C(0)|/C(0)$  of the Jacobi constant  $C$ . On the horizontal axis the number of time steps since the beginning of the integration is shown, the left vertical axis displays the distance of the particle to Earth measured in Earth radii ( $R_{\oplus}$ ). The dotted horizontal line marks the Moon's distance of about  $60 R_{\oplus}$ . From the diagonal red curve we can see that the particle comes closer than the Moon around time step number 250, and that it approaches Earth to within  $10 R_{\oplus}$  at about time step 375, finally it hits Earth. The green curve shows the behaviour of the relative error for  $C(t)$  without MFC, while the blue curve is obtained with active MFC. For this test a fixed step-size was used, which manifests itself in the strong increase of the integration error for the green curve (note the logarithmic scaling of the right vertical axis); the chosen step-size is inappropriate from the point where the green curve starts to rise. The same fixed step-size is used also for the blue curve, but the MFC keeps the integration errors below  $10^{-15}$  as long as the particle is more distant than  $10 R_{\oplus}$ , only after that the error increases, but much more moderately than without MFC. Of course, for the real simulations an adaptive step-size was used which decreases the final error even more; the Jacobi constant is conserved to machine precision ( $2^{-52} \approx 2 \times 10^{-16}$ ) when no impacts occur.

One alternative approach to control the integration errors would be to regularise the equations of motion, which would be particularly helpful in cases with impacts. Érdi (2004) studied the global regularising transformations of the CR3BP, but the transformations he discussed are all valid only for the planar case. A Kustaanheimo-Stiefel type

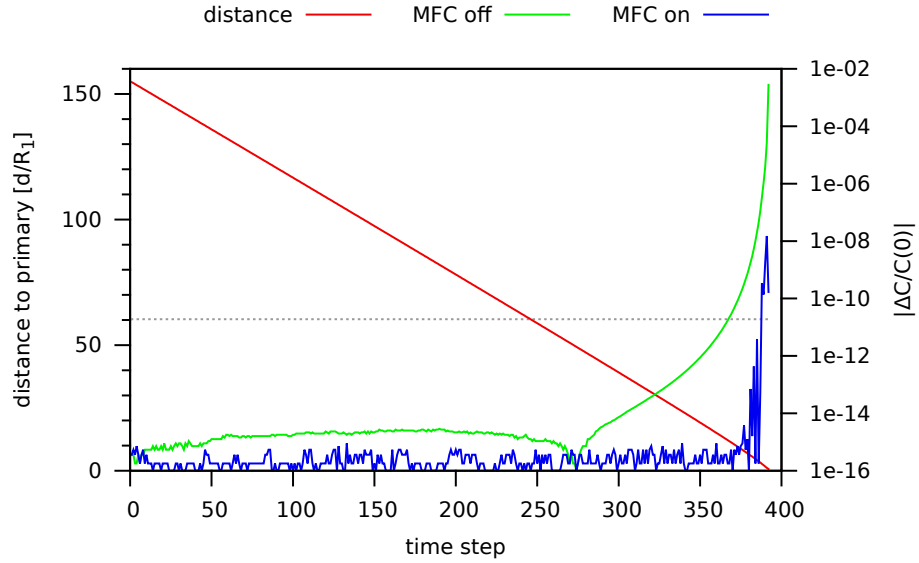


Figure 4.1: The effect of the manifold correction when applied to the CR3BP. A particle starts outside the SOI at slightly more than 150 Earth radii (left axis), its radial distance (red curve) shrinks as it approaches Earth. The local relative error in the Jacobi constant  $C(t)$  is monitored (right axis) as a function of time and distance (green curve: without MFC, blue curve: active MFC). With MFC the final error is 6 orders of magnitude smaller. See text for details.

regularisation (Stiefel and Scheifele, 1971) is also applicable to the spatial CR3BP, but it requires an extended four-dimensional space and leads to a set of completely modified equations of motion.

### 4.2.2 Model 1: initial positions

The six initial conditions  $\{x, y, z, \dot{x}, \dot{y}, \dot{z}\}$  for the components of the position and velocity vector of a particle are equivalent to six degrees of freedom. We can eliminate one degree of freedom by requiring that the boundary condition

$$x^2 + y^2 + z^2 = R_{\oplus}^2$$

is satisfied, since in this model the particles should start at the Earth's surface. The remaining 5 degrees of freedom must be chosen according to some other constraints given by physical restrictions (e.g., the initial speed must be larger than the escape velocity).

For the starting position of a particle two degrees of freedom are left, and these will be represented as the two angles latitude  $\beta$  and longitude  $\lambda$ . The longitude angle is always treated as a uniform random number from the interval  $0 \leq \lambda < 360$  degrees, whereas

the latitude angle is subject to three different random distributions: (i) Equatorial distribution, (ii) Gaussian distribution, and (iii) Spherical distribution.

### Equatorial distribution

In the first case the latitude is taken to be a uniform random number restricted to the range  $-1 \leq \beta \leq +1$  degree. This choice will mimic a two-dimensional distribution of impact sites around the equator, and can be used to compare the results with the purely two-dimensional simulation of Domingos et al. (2004).

For this case we can expect to observe the highest number of particles to be deflected by the Moon. Let us assume the extreme case of a particle starting at  $|\beta| = 1$  deg in perfectly radial direction (along the local surface normal). This particle will then pass the Moon in  $d_{EM} \sin(\beta) \approx 6700$  km or about 4 lunar radii. For any other value of  $\beta$  this distance might be even smaller, provided that the particle's longitude is compatible with the direction to the Moon.

### Gaussian distribution

As the second case I have chosen the Gaussian distribution. The latitude now follows a random normal distribution with mean  $\langle \beta \rangle = 0$  deg (concentration of points around the equator) and standard deviation of  $\sigma_\beta = \pi/6$  rad (30 deg). In this way it is ensured that 99.7 % of all points will fall into the interval  $-\pi/2 \leq \beta \leq +\pi/2$  (3- $\sigma$  interval), any points falling outside this range are rejected.

To generate random numbers having a Gaussian distribution I use the Box and Muller (1958) algorithm that takes a pair of uniform random numbers and transforms them into a Gaussian (pseudo-)random deviate.

The main reason for using the Gaussian distribution is that it does not overestimate the density of points at higher latitudes. This can be demonstrated by comparing the cumulative area integrals for a hemisphere and the Gaussian function:

- The normalised cumulative area integral for a hemisphere is

$$S(\beta) = \frac{1}{4\pi} \int_0^{2\pi} d\lambda \int_0^\beta \cos x dx = \frac{1}{2} \sin \beta.$$

This integral computes the area of the (unit) hemisphere from the equator up to a given latitude  $\beta$  as a fraction of the total area ( $4\pi$ ).

- The normalised integral for the area under the Gaussian function is

$$G(\beta) = \frac{1}{\sqrt{2\pi}\sigma^2} \int_0^\beta \exp\left(-\frac{1}{2}\left(\frac{x}{\sigma}\right)^2\right) dx = \frac{1}{2} \operatorname{erf}\left(\frac{1}{\sqrt{2}} \frac{\beta}{\sigma}\right).$$

Here the integral is substituted by the error-function (Abramowitz and Stegun, 1972);  $\beta$  is assumed to be given in radians, and the standard deviation takes the value  $\sigma = \pi/6 \approx 0.5236$  rad.

latitude [deg]	percentage of total area in interval [%]		
	$0 \leq \beta < 30$	$30 \leq \beta < 60$	$60 \leq \beta \leq 90$
Gauss	34.1	13.6	2.1
Hemisphere	25.0	18.3	6.7

Table 4.1: Percentage of the area in a given latitude interval ( $\beta$  in degrees) relative to the total area; comparison between the area under the Gauss function and the surface of a hemisphere.

Table 4.1 compares the fractional area in three different latitude intervals for the hemisphere and the Gauss function. It is obvious from the table that the Gaussian function distributes a higher number of points (initial conditions) per unit area at lower latitudes than would be present on a sphere, whereas at high latitudes it underestimates the point density. For the current case this behaviour is desired.

Figure 3.2 showed that the majority of NEAs have inclinations  $i < 50$  deg, so impacts at high latitudes should be less frequent than impacts at low latitudes (neglecting the Earth's obliquity). By using the Gaussian distribution we will generate initial conditions with preferably small inclinations and will obtain more impacts from near-ecliptic objects.

### Spherical distribution

The third case does not depend on latitude and longitude, but uses the uniform spherical distribution of points on the surface of a sphere (Saff and Kuijlaars, 1997) that was introduced in section 2.6. Table 2.2 summarises the number of vertices of the resulting polyhedron as a function of the number of iteration steps. I used 6 iterations for 40 962 initial conditions in the simulations.

It must be stressed that all simulations with the spherical distribution will always use the same starting points by construction, but they will differ in the initial velocities. The other two distributions from above result in different starting points for each run (as long as the random number generator is seeded appropriately).

Figure 4.2 visualises all three of the above distributions. The plots show the projected points in the latitude-longitude plane. The origin (0, 0) marks the sub-lunar point, i.e. it is the intersection point of the  $x$ -axis (connecting the centers of Earth and Moon) with the surface.

### 4.2.3 Model 1: initial velocities

There are three degrees of freedom left for the choice of the initial velocities. In order to simulate a broad range of impactor parameters (impact angles, velocities) I impose

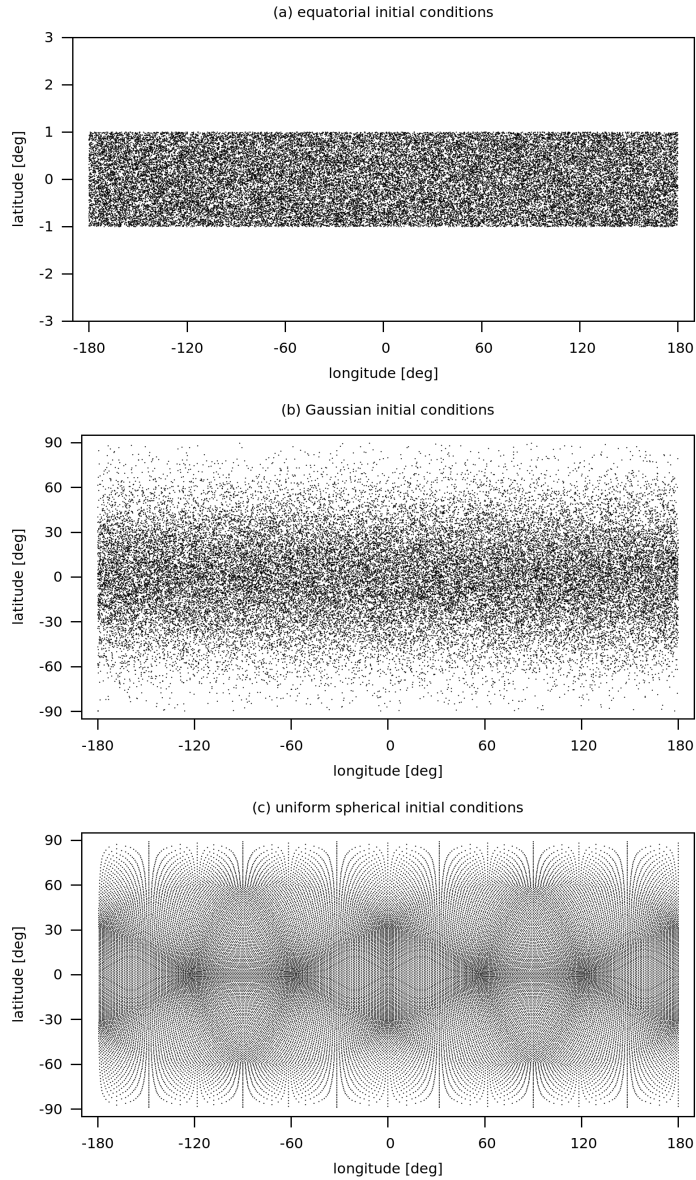


Figure 4.2: The three distribution types for the initial positions, from top: (a) equatorial, (b) Gaussian, and (c) uniform spherical distribution. In each case 40 962 points are distributed on the Earth's surface; note the smaller vertical scale for case (a).

only two weak constraints on the initial velocity. One of the constraints is that the impact angle must not be zero, i.e. perpendicular to the surface. If the position and velocity vectors were parallel, then the angular momentum vector would be zero and the  $f$ - $g$ -functions are not applicable. The other constraint is that the initial velocity must be larger than the escape velocity from Earth ( $v_{\text{esc}} = 11.18$  km/s at the Earth surface).

The velocity vector is generated following the method of Scheeres et al. (2002, eq. (4)). The two angles  $\beta$  and  $\lambda$  (in analogy to latitude and longitude) determine the orientation of the velocity vector with respect to the surface normal represented by the position vector.

The angle  $\beta$  specifies the tilt relative to the surface normal. In the simulations a Gaussian distribution is used for this parameter. For Gaussian and Spherical initial positions the mean impact angle is  $\langle\beta\rangle = 45$  deg with standard deviation  $\sigma_\beta = 15$  deg. For Equatorial initial positions the impact angles are restricted to  $\langle\beta\rangle = 0$  with  $\sigma_\beta = 1$  deg to make sure that the particles remain close to the  $x$ - $y$  plane.

Regarding the direction angle  $\lambda$  a uniform random distribution is used, such that  $0 \leq \lambda < 360$  deg. In this way all possible angles  $\lambda$  describe a cone with the fixed opening angle  $\beta$  for which the surface normal is the symmetry axis.

As the third parameter the initial impact speed must be chosen. In section 3.3.4 figure 3.23 compares the (extrapolated) impact velocity distributions for the NEA groups; table 3.12 summarises the statistical key parameters based on that data. The median impact velocity is between 15–17 km/s, but also higher velocities up to 45 km/s occur. In Gladman et al. (1995) an equation for the residual velocity  $v_\infty$  “at infinity” is given, that relates the initial ( $v_0$ ) and escape velocity ( $v_{\text{esc}}$ ) by

$$v_\infty^2 = v_0^2 - v_{\text{esc}}^2.$$

When using this relation with  $v_0 = 15$  km/s (the lower value for the median impact speed) we obtain a residual speed of  $v_\infty \approx 10$  km/s at the border of Earth’s SOI. Therefore it is clear that we must restrict the range of initial velocities for the simulation to the interval  $v_0 \leq 15$  km/s, because the lunar gravitational influence becomes very inefficient for high relative velocities of 10 km/s or more.

The initial impact speed is given by  $v_0 = v_{\text{esc}} + \Delta v$  with  $0 \leq \Delta v \leq 4$  km/s, and is subject to three different random distributions: (i) Gaussian distribution, (ii) Linear distribution, and (iii) a Poisson-like distribution.

### Gaussian distribution

In the first case the increments  $x = \Delta v$  are chosen according to a standard normal distribution with mean  $\langle x \rangle = 0$  and standard deviation  $\sigma_x = 1$ . The unscaled probability density function (PDF) is given by

$$G(x) \propto \exp\left(-\frac{x^2}{2}\right), 0 \leq x \leq 4.$$

The scaling constant  $\mathcal{N}_G$  must be chosen such that the integral of  $G(x)$  (the cumulative density function, CDF) over the given interval equals to 1, i.e. the total probability is normalised. This is achieved by

$$\mathcal{N}_G = \int_0^4 G(x) dx = \sqrt{\frac{\pi}{2}} \operatorname{erf}(2\sqrt{2}) \approx 1.253235,$$

such that the Gaussian PDF is

$$G(x) = \frac{1}{\mathcal{N}_G} \exp\left(-\frac{x^2}{2}\right). \quad (4.2.1)$$

Random numbers for this PDF are generated from uniformly distributed random numbers by using the mentioned Box-Muller transform.

### Linear distribution

The second type of distribution is a simple linear PDF, which has a maximum probability at  $x = 0$  and vanishes at  $x = 4$ . The monotonic decrease on the interval  $0 \leq x \leq 4$  is chosen as a first order approximation to the behaviour of the empirically found velocity distributions in a surrounding of the peak (see figure 3.23). The scaled probability density function is

$$L(x) = \frac{1}{8}(4 - x), 0 \leq x \leq 4. \quad (4.2.2)$$

From this the CDF can be easily obtained by integration. Then a uniform random number generator can be used to generate random numbers  $u$  that are transformed to this linear PDF:

$$x(u) = 4(1 - \sqrt{1 - u}), 0 \leq u \leq 1.$$

### Poisson distribution

As the third type a Poisson-like distribution was chosen for the reason that the impact velocity distributions in figure 3.23 resemble somewhat a truncated Poisson distribution. This is just a personal impression, in fact other distributions like the Log-Normal distribution<sup>3</sup> could be used as well.

The classical discrete Poisson distribution is defined as

$$P(k) = \frac{\lambda^k}{k!} e^{-\lambda},$$

for real numbers  $\lambda$  and an integer  $k \geq 0$  (Walser, 2011).

<sup>3</sup>see for instance <http://mathworld.wolfram.com/LogNormalDistribution.html>

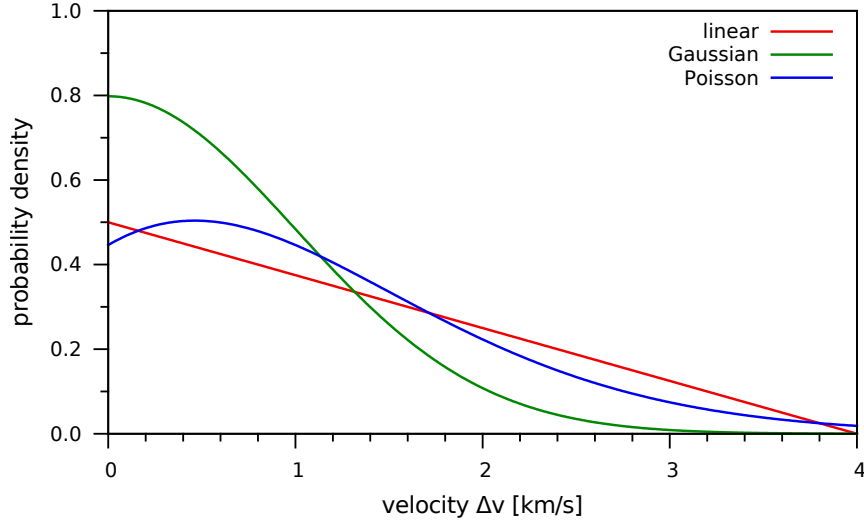


Figure 4.3: A visualisation of the probability density functions for the three velocity distributions. All PDF are restricted to the interval shown, they are scaled for a total probability of 1.  $\Delta v$  is the velocity increment which is added to the escape velocity to give the initial impact velocity.

The continuous form of the above distribution for mean  $\lambda = 1$  and standard deviation  $\sigma = \sqrt{\lambda} = 1$  is obtained (and simplified by this choice) as

$$P(x) \propto \frac{1}{\Gamma(x+1)} e^{-1},$$

where the Gamma-function (Abramowitz and Stegun, 1972) is used for the continuous variable  $x$ . The scaling constant  $\mathcal{N}_P$  for  $P(x)$  cannot be computed analytically, since this involves an integral of the Gamma-function, but numerically it was determined to  $\mathcal{N}_P \simeq 0.824361$ . The scaled Poisson PDF used in the simulations reads

$$P(x) = \frac{1}{\mathcal{N}_P} \frac{e^{-1}}{\Gamma(x+1)}, 0 \leq x \leq 4. \quad (4.2.3)$$

This PDF cannot be sampled directly, because most standard random number generators do not include routines for the Poisson distribution, and in particular not for a continuous variant. To overcome this problem I used a uniform random number generator in combination with acceptance-rejection sampling.

In figure 4.3 one can compare the three normalised PDFs. Note that the linear PDF vanishes exactly at  $\Delta v = 4$ , the Gaussian PDF almost vanishes, while the Poisson PDF is non-zero on the whole interval. The shape of the latter is governed by the choice of  $\lambda = 1$ ; in contrast to the other PDF the peak probability is located at  $x \approx 0.462$  instead

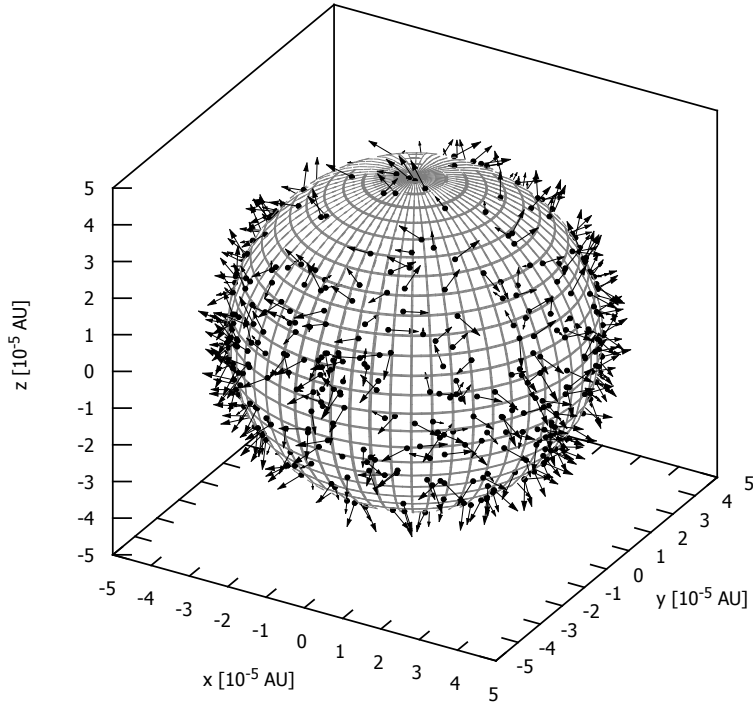


Figure 4.4: A 3D view of a sample of initial conditions on the Earth surface. The black dots mark the initial starting points, the arrows represent the velocity vectors (not to scale).

of  $x = 0$ . Note that the resulting initial impact velocities will fall into the interval  $11.2 \leq v_0 \leq 15.2 \text{ km/s}$  in any case.

Figure 4.4 shows a typical initial setup for the simulations in the 3D space. The points mark the individual impact sites, the arrows indicate the direction and magnitude of the velocity vector (not to scale). Only a limited number of points is drawn; the coordinate system is centered on Earth, and the axes are scaled in astronomical units.

#### 4.2.4 Model 2: initial conditions

In this model all particles start at the border of Earth's SOI at a radial distance of  $R_{\text{SOI}} = 150 R_{\oplus}$ . According to the definitions for the spatial CR3BP in section 2.3 the Earth is located at  $(x_E, y_E, z_E) = (-\mu, 0, 0)$  and the Moon at  $(x_M, y_M, z_M) = (1 - \mu, 0, 0)$ . Both primaries are located on the  $x$ -axis in the rotating frame and their mutual distance is fixed to  $d_{\text{EM}} = 384\,400 \text{ km} (\approx 60 R_{\oplus})$ .

### Initial positions

Initial positions for particles are generated by the following process:

1. Particles are initially positioned at  $(x_P, y_P, z_P) = (R_{\text{SOI}}, 0, 0)$  in the inertial system centered on Earth.
2. Then they are shifted by the impact parameter  $b$  parallel to the positive  $y$ -axis. The impact parameter determines how close a particle would approach Earth in the absence of the Moon. Impact parameters are generated as uniform random numbers in the interval  $5 \leq b \leq 60 R_{\oplus}$ .
3. The shifted particle is then rotated about the  $z$ -axis by the phase angle  $\varphi$ . This phase angle helps to randomise the directions of the incoming particles. The parameter  $\varphi$  is a uniform random number in the interval  $0 \leq \varphi < 360$  deg.
4. In the next step another rotation is performed to move the particle out of the  $x$ - $y$  plane. This angle  $\beta$  is subject to the Equatorial or Gaussian distribution as introduced in M1 for the initial positions. The rotation axis  $\mathbf{a} = (-\sin \varphi, \cos \varphi, 0)$  is the rotated  $y$ -axis from the previous step.
5. Subsequently a final rotation with angle  $\vartheta$  is carried out to further randomise the spatial orientation. This time the rotation axis is the (twice) rotated  $x$ -axis; the angle  $\vartheta$  is a uniform random number with  $0 \leq \vartheta < 360$  deg.
6. As the last step the barycentric correction is applied and the initial position is transformed from the inertial to the rotating system via equation (2.3.2).

The enumeration from above can be summarised in a more formal way. After the first two steps a particle has the planar starting vector

$$\mathbf{r}_0 = R_{\text{SOI}} \hat{\mathbf{e}}_x + b \hat{\mathbf{e}}_y = (R_{\text{SOI}}, b, 0).$$

Note that  $\|\mathbf{r}_0\| > R_{\text{SOI}}$  so that this vector has to be scaled accordingly to represent a particle's position exactly at the SOI. In total three rotations are performed on this vector which result in the effective starting position in the inertial frame

$$\tilde{\mathbf{r}}_0 = \mathbf{R}_{\mathbf{x}'}(\vartheta) \mathbf{R}_{\mathbf{y}'}(\beta) \mathbf{R}_{\mathbf{z}}(\varphi) \mathbf{r}_0.$$

The general matrix  $\mathbf{R}_{\mathbf{a}}(\alpha)$  for a rotation about an axis  $\mathbf{a} = (a_x, a_y, a_z) \in \mathbb{R}^3$  (which must be a unit vector with  $\|\mathbf{a}\| = 1$ ) through an angle  $\alpha$  is given by (Gekeler, 2006)

$$\mathbf{R}_{\mathbf{a}}(\alpha) = \cos \alpha \mathbf{1}_3 + (1 - \cos \alpha) \mathbf{A} + \sin \alpha \mathbf{C},$$

where the three sub-matrices are defined as

$$\mathbf{1}_3 = \begin{pmatrix} 1 & 0 & 0 \\ 0 & 1 & 0 \\ 0 & 0 & 1 \end{pmatrix}, \quad \mathbf{A} = \begin{pmatrix} a_x^2 & a_x a_y & a_x a_z \\ a_x a_y & a_y^2 & a_y a_z \\ a_x a_z & a_y a_z & a_z^2 \end{pmatrix}, \quad \mathbf{C} = \begin{pmatrix} 0 & -a_z & a_y \\ a_z & 0 & -a_x \\ -a_y & a_x & 0 \end{pmatrix}.$$

Model M2 does not make use of the uniform spherical distribution for initial positions, because that distribution is incompatible with the construction procedure described above.

### Initial velocities

The velocity vector must not be parallel to the position vector or otherwise the particle could have an impact with Earth. For this reason the two vectors always form an angle of  $\tan \delta = b/R_{\text{SOI}}$ . It is a consequence of this angle that the velocity vector cannot be modified by adding a random number to any component, as this would change the effective impact parameter  $b$ .

The magnitude of the velocity vector is determined in the same way as in M1:

$$v_0 = v_{\text{esc}} + \Delta v.$$

Here  $v_{\text{esc}} = 0.913$  km/s is the escape speed at the SOI<sup>4</sup>. The velocity increment  $\Delta v$  is a random number in the interval  $0 \leq \Delta v \leq 4$  km/s, it is obtained from one of the three velocity distributions: Gaussian, Linear, or Poisson. These distributions are applied exactly in the same way as for the initial velocity in model M1, with the difference that now the initial speeds cover the range  $0.913 \leq v_0 \leq 4.913$  km/s.

## 4.3 Results

This section presents the results of the simulations for both dynamical models. In the first part (M1) the lunar efficiency in deflecting incoming impactors is studied using various combinations of initial conditions. Afterwards, the second part (M2) presents the results for the lunar contribution to impacts on Earth.

### 4.3.1 Model 1

Model M1 includes three different configurations for the CR3BP, where either the lunar mass or distance are varied (see section 4.1.2). Each of those configurations itself consists of 9 possible combinations of initial positions and velocities, the details can be found in sections 4.2.2 and 4.2.3.

It has already been mentioned that each simulation run includes 40 962 particles. To get statistically meaningful results I repeated each simulation 16 times with random initial conditions. This will not only increase the number of simulated particles, but also allows to calculate mean deflection efficiencies.

Figure 4.5 shows two examples for successful deflections by the Moon (in the rotating frame). The black curves mark the particle's trajectories in Phase 1, where they start

<sup>4</sup>The exact numerical value of the escape speed  $v_{\text{esc}}$  depends on the choice of the scaling constants for the CR3BP; the given value is for C1 with  $\mu = 1/82.30057$  and  $d_{\text{EM}} = 384\,400$  km.

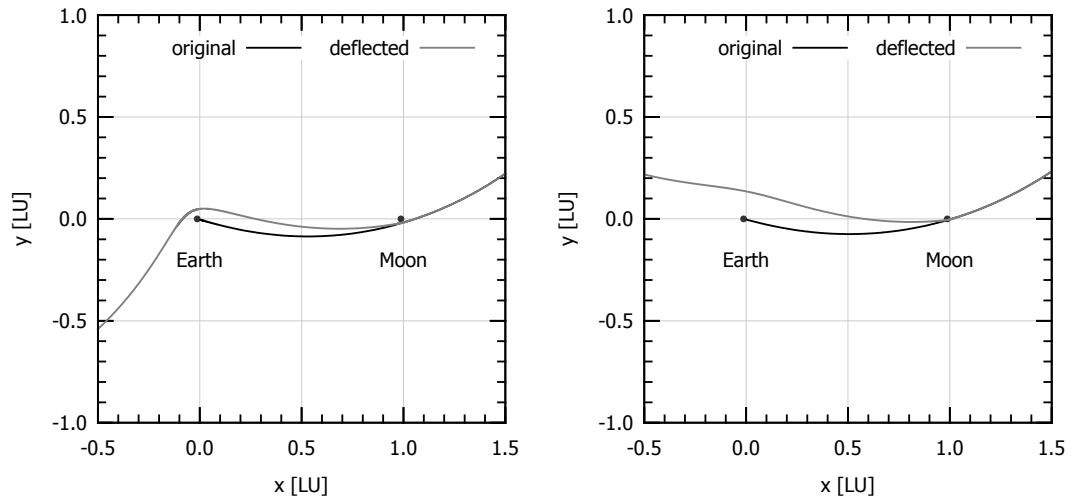


Figure 4.5: Two examples for successful deflections of asteroids on impact trajectories by the Moon. The black curves are the trajectories originating from the Earth’s surface, the grey ones were deflected by close approaches to the Moon. The figures show the projections from 3D onto the  $x$ - $y$  plane; the dots for Earth and Moon are not to scale.

at the Earth surface and move out to the SOI at a radial distance of 2.5 dimensionless length-units (LU; not shown in the image). The grey curves trace the trajectories in Phase 2 with the lunar gravitational influence added, they move from the SOI towards Earth. For both examples shown the particles have a close approach to the Moon, but they do not collide with it; after the deflection they miss Earth and pass in a distance of several Earth radii.

### Standard configuration

The configuration C1 is representative for the Earth-Moon system as it is today. The lunar mass and distance take their default values (see section 4.1.2), i.e. the CR3BP mass-ratio is  $\mu = 1/82.30057$  and the Earth-Moon distance is  $d_{EM} = 384\,400$  km.

Table 4.2 summarises the results of the simulations. The first column lists the 9 possible combinations of initial positions and velocities, e.g. E/G means an Equatorial distribution for the positions with a Gaussian distribution for the velocities. In the second and third column we find the fraction of particles that impact on Earth and Moon, respectively. The fourth column gives the number of deflected particles that leave Earth’s SOI, while the last column contains deflected (non-impacting) particles that remain inside the SOI. For each entry the mean fraction from 16 simulation runs is calculated, the standard deviation is indicated in parentheses. In the very last row

distribution pos./vel.	impact on ...		deflection, particle ... SOI	
	Earth	Moon	outside	inside
E/G	0.99175(39)	0.00075(15)	0.00750(37)	0
E/L	0.99401(39)	0.00058(11)	0.00541(37)	0
E/P	0.99371(27)	0.00063( 9)	0.00567(29)	0
G/G	0.99068(34)	0.00002( 3)	0.00930(34)	0
G/L	0.99284(39)	0.00001( 2)	0.00715(39)	0
G/P	0.99274(34)	0.00001( 1)	0.00726(34)	0
S/G	0.99047(44)	0.00004( 3)	0.00950(42)	0
S/L	0.99260(46)	0.00001( 1)	0.00740(47)	0
S/P	0.99248(50)	0.00002( 2)	0.00751(50)	0
mean	0.99236(119)	0.00023(21)	0.00741(118)	0

Table 4.2: Statistical summary of simulation results for model M1 with configuration C1. Each line represents the mean (standard deviation) of 16 simulation runs with the same combination of position/velocity distribution. The abbreviations for the distribution types are: (E) = Equatorial pos., (G) = Gaussian pos. or vel., (S) Spherical pos., (L) Linear vel., (P) Poisson vel.

the arithmetic mean of all entries is calculated; the average standard deviations were calculated via the error propagation formula. The sum of all numbers in a row should equal 1, but due to rounding there can be slight deviations.

Note that – irrespective of the simulation conditions – at least 99 % of all particles still impact on Earth. The Moon is able to remove at most  $\approx 0.08$  % (on average 0.02 %) of all approaching particles by direct collision. Indirect deflections are somewhat more efficient with  $\approx 0.7$  % of all particles missing Earth and leaving the SOI subsequently. No event occurred where a particle would miss Earth and becomes temporarily captured inside the SOI.

As it was expected impacts on the Moon occur mainly in the equatorial cases. However, even there the fraction of impacts on the Moon is only about 10 % of the number of deflections. This large difference can be explained by the difference in the lunar geometrical and gravitational cross-section. The number of impacts on the Moon becomes insignificant when a more realistic (three-dimensional) distribution of particles is used. From geometrical considerations it follows that the Moon’s apparent angular diameter is  $\alpha \simeq 0.52$  deg, this amounts to a solid angle of  $\Omega \simeq 6.4 \times 10^{-5}$  steradians. In other words, the ratio of the lunar geometrical cross-section to the surface area of a sphere is  $6.4 \times 10^{-5}$ , so we would expect this number to be the fraction of impacts on the Moon in the limit of a perfect coverage of the sphere with particles.

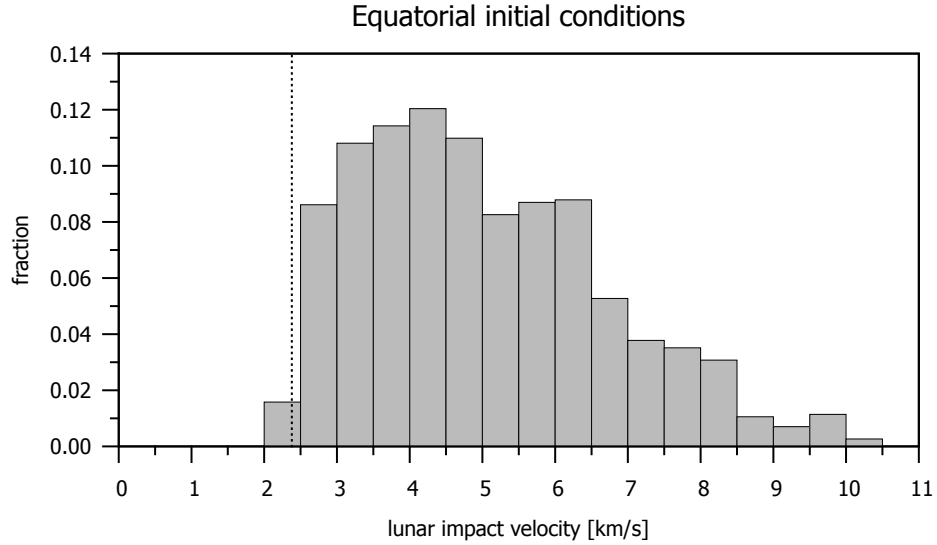


Figure 4.6: Histogram for the impact velocities on the Moon in case of the Equatorial distribution of initial positions. The dotted vertical line indicates the lunar escape speed of 2.38 km/s. Only impacts with  $v \geq 2.38$  km/s were considered for this histogram.

When comparing the velocity distributions we find that in all cases the Gaussian distribution reduces the fraction of impacts on Earth. This decrease in the number of impacts with Gaussian velocities is statistically highly significant; on the contrary the other distributions (Linear and Poisson) are equal within their  $1-\sigma$  errors. The Gaussian velocity distribution (see figure 4.3) leads to a lack of particles with high impact velocities, which in turn diminishes the average relative velocity and leads to a higher deflection efficiency. In the other two distributions relatively high impact velocities are generated with a higher probability.

From the table we see that only in the equatorial case there are enough events for a statistical check of impacts on the Moon. Figure 4.6 shows the lunar impact velocity distribution for equatorial initial conditions. In total more than 1000 objects impact on the Moon and generate this velocity distribution; each bin has a width of 0.5 km/s. The dotted vertical line marks the lunar escape velocity of 2.38 km/s. In the first bin (2.0 – 2.5 km/s) only impact speeds above the escape velocity are included; about 1.5 % of all objects hit the Moon with an impact speed of  $< 2.5$  km/s. The majority of impacts occur at speeds of more than 4 km/s, though.

This impact velocity distribution for the Moon cannot be compared to other distributions obtained from numerical integrations of NEAs or of returning impact ejecta, because the impact speeds depend strongly on the assumptions made for the initial conditions (especially the initial velocity distributions). More realistic lunar impact ve-

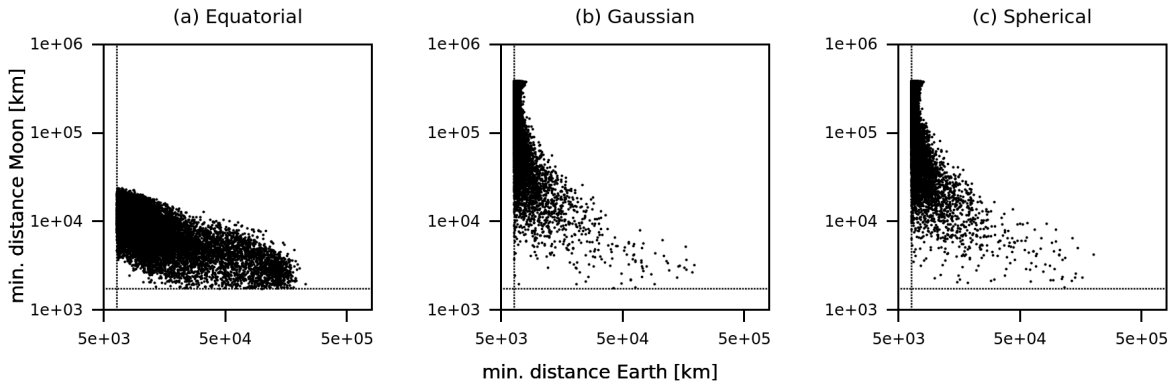


Figure 4.7: A comparison of the minimum distance to Earth versus minimum distance to Moon of deflected particles for all three initial position distributions (a-c). The vertical line indicates Earth’s physical radius, while the horizontal line is the radius for the Moon. Particles that closely approach the Moon tend to have larger miss distances with respect to Earth.

locity distributions were obtained by Ito and Malhotra (2010) and Yue et al. (2013) from large-scale numerical integrations (resulting in 14–70 times more impacts). These simulations show that the impact speeds in figure 4.6 are located in the very low velocity regime, usually lunar impact speeds are similar to those on the Earth with mean value of  $\langle v \rangle > 17$  km/s.

Figure 4.7 shows the minimum distances of deflected particles relative to Earth and Moon. On the vertical axis it is shown how close a particle approached the Moon, the horizontal axis shows the distance by which the particle has missed Earth (note that both axes are scaled logarithmically). The dotted lines indicate the physical radii of the Earth (vertical line) and Moon (horizontal line). It is visible that the closer a particle approaches the Moon (the lower it is on the vertical axis), the higher its miss distance becomes (the farther to the right on the horizontal axis it is situated).

Case (a) is different from cases (b) and (c) in so far as the maximum distance to the Moon is limited by the choice of the initial coordinates (restricted in latitudes and impact angles). For the latter two cases a considerable fraction of deflected particles never comes close to the Moon, but can avoid to collide with Earth (the clumps at the top of the vertical line).

The data for the minimum distances can also be dissected in the form of figure 4.8, which combines the data from all simulations (for a specific initial distribution of positions) into histograms for the minimum distances to Earth and Moon.

In that figure the left column shows the minimum distances to Earth in units of the terrestrial radius; each histogram combines the results for all three velocity distributions. For the Equatorial case the first two bins equal to 56 % and 18 % of all deflected particles,

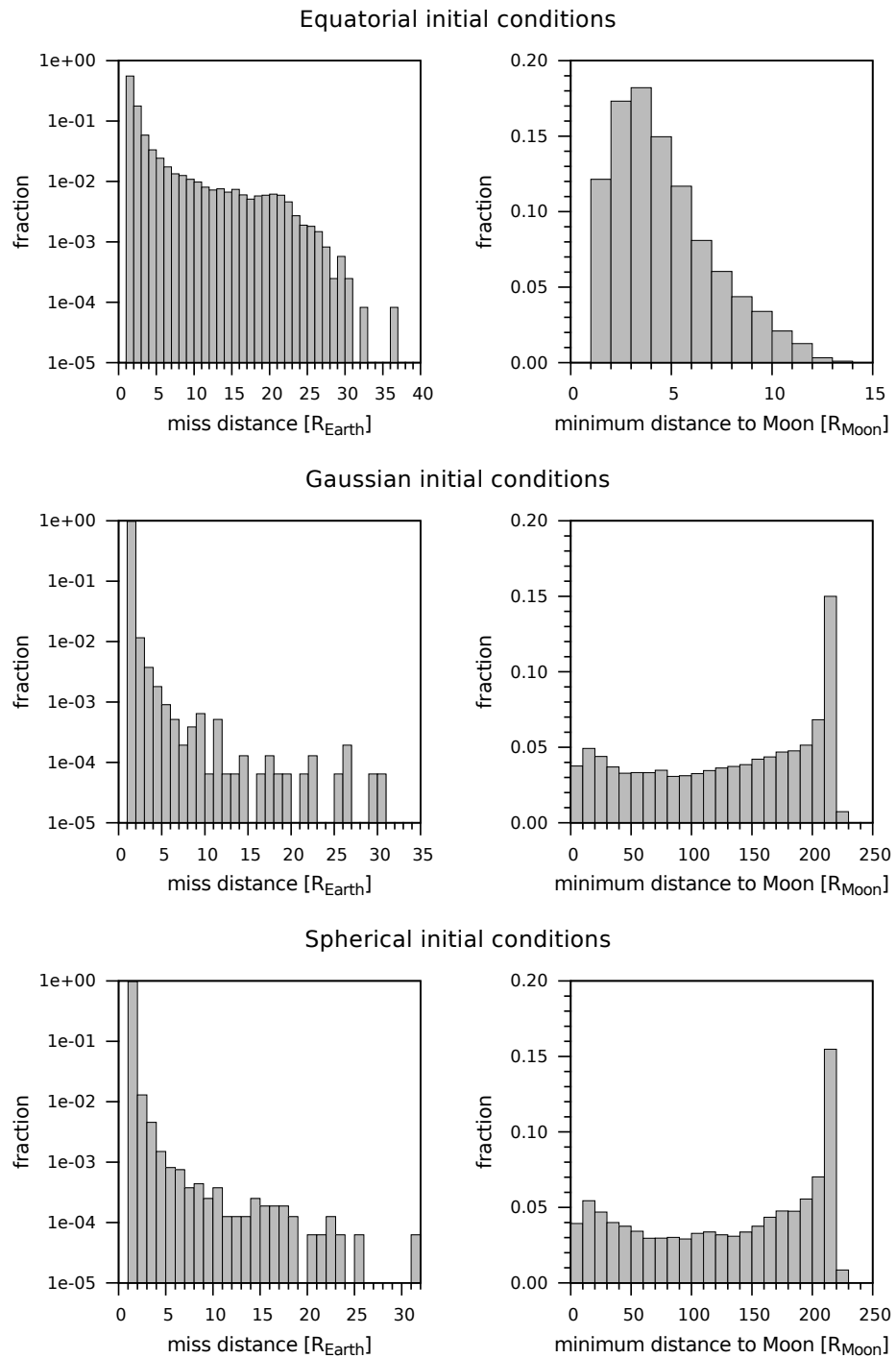


Figure 4.8: Histograms for the minimal distances to Earth and Moon (scaled to the body's radius). Note the different horizontal scale for the top right image, and the logarithmic vertical scale for the left column.

which means that about 3/4 of all particles still approach Earth to within 3 Earth radii. In contrast to that in the Gaussian and Spherical cases one single bin accumulates 98 % of all deflections, while larger miss distances above  $2R_{\oplus}$  are negligible (note the logarithmic scale for the vertical axis).

This fact can be explained by the histograms in the right column, where we can see how close a particle passed to the Moon prior to its Earth fly-by. In the Equatorial case the lunar distance is limited to 15 times the lunar radius (for successful deflections only), but for the other two cases (Gaussian and Spherical) much larger minimum distances are possible. When the particles are not restricted to the primaries' orbital plane they need not approach the Moon, but will definitely come back very close to Earth, where they have started originally. The far side of the Earth (as seen from the Moon) is at a distance of  $\sim 224$  lunar radii (the center of Earth at 220). Those particles in the histograms with minimum distance  $> 200 R_{\text{Moon}}$  (about 20 %) arrive from inclined orbits that never take them near the Moon, they pass the Earth on the “far side” and thus form this largest bar in the histograms.

A special note: in the second and third histogram of figure 4.8 the very first bar (that extends from 0–10 lunar radii) includes in fact only minimum distances from 1–9  $R_{\text{Moon}}$ , as none of the deflected particles may have impacts with the Moon.

It is also of interest where the origin of deflected particles is and how these are distributed. Figure 4.9 shows the maps of the initial latitudes and longitudes with the initial speed added as grey-value.

For case (a) the latitudes are limited (note that the vertical scale is different from the other two images), and there is a gradient in the initial speeds. We have seen in the previous figure 4.8 that all deflected particles encounter the Moon within 15 lunar radii for equatorial initial conditions. At the begin of the simulation the sub-lunar point (the Moon's “shadow”) is at (0;0) on the map and it moves from left to right. As all particles start at the same time, the ones to the right have a shorter arc to the Moon than those to the left. To meet the Moon with given boundary conditions (distance and time), particles to the left must compensate by a higher initial speed. However, this does not mean that on the Earth there would be a similar feature in the distribution of real impact craters, because of the planet's rotation the given distribution will be smeared out in longitudes with time.

In cases (b) and (c) it is well visible that particles from higher latitudes are still deflected in great number, and there is also a striking deficit of deflected particles at the center of the images. The regions with the lack of deflected particles seem to agree roughly with the area from case (a), where deflections were possible. This would indicate that direct deflections by close approaches to the Moon are less efficient than deflections where the Moon is acting as a long-range perturber.

When comparing figures 4.2 and 4.9 note that the size of the dots has been enlarged in the latter to make the colours more visible. The overall density of points is not as large as it would seem from these figures, since the deflected particles make up for only about 0.7 % (on average) of all initial positions per simulation run, but for these figures

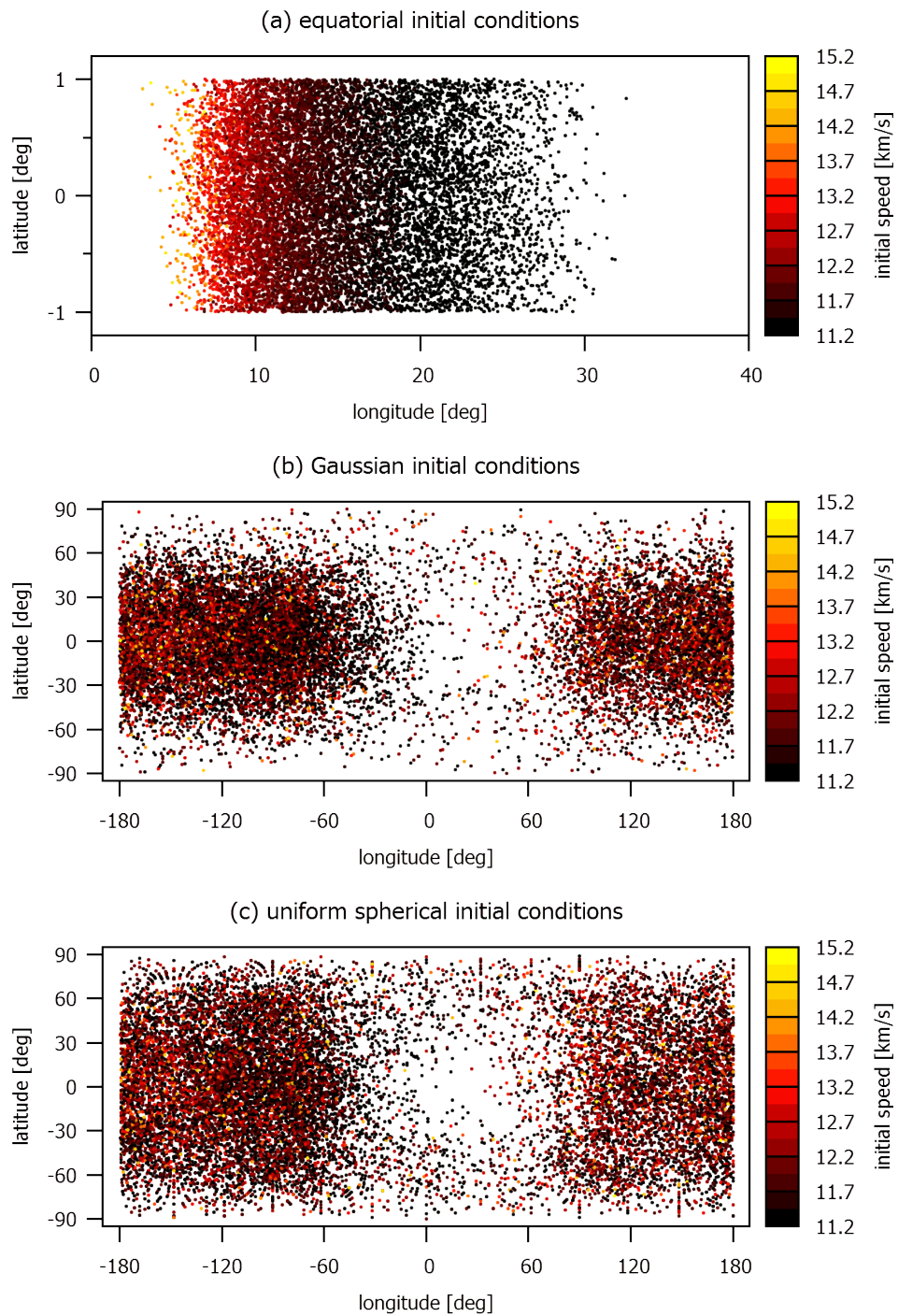


Figure 4.9: Origin of deflected particles on the Earth surface for different initial distributions in C1 of M1. The dots (not to scale) indicate the starting positions, the grey-scale indicates the initial speed.

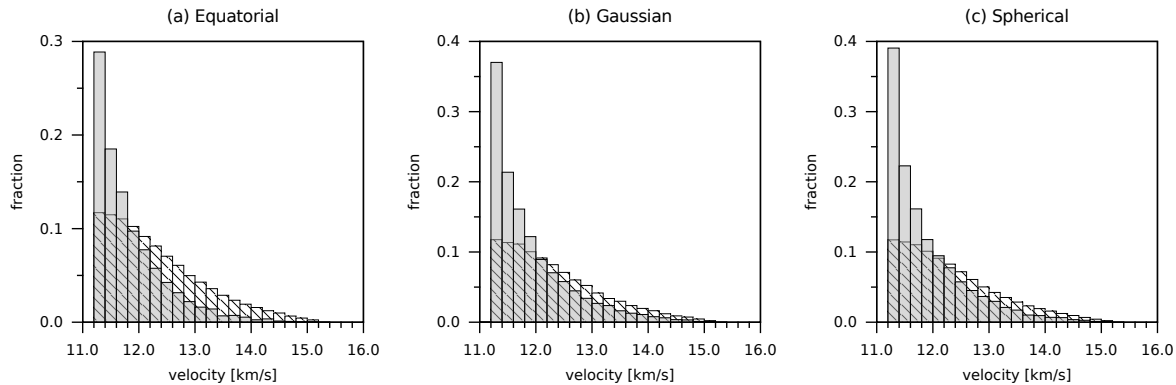


Figure 4.10: Comparison of initial velocities of deflected particles (grey bars) against the initial velocity distribution (shaded bars). Each of the three panels shows the averaged initial velocity distributions for different initial position distributions.

deflected particles from all runs are collected.

Another interesting aspect about the origin of the deflected particles is how their initial velocities relate to the bulk of all particles. Figure 4.10 shows the histograms for all deflected particles (grey bars) relative to the combined initial velocity distribution (shaded bars in the background)<sup>5</sup>. It becomes evident that at speeds  $v < 12$  km/s deflected particles are more abundant, the majority of them even falls into the lowest speed interval. A consequence is that deflections mainly depend on the relative speed of the particle to the Moon, and that the distribution of initial positions is less important.

### Increased lunar mass

In configuration C2 the lunar mass is doubled (Moon/Earth mass ratio  $\mu = 1/40$ ), while the lunar distance remains at the current value ( $d_{EM} = 384\,400$  km). The idea is to check if a more massive satellite would change the rate of impacts on Earth.

The simulation results are summarised in table 4.3. Similar to the results in table 4.2 also here the vast majority of particles return and impact on Earth. In the Equatorial case the percentage of impacts is higher by 0.7 – 1 % than in the Gaussian or Spherical case, this difference is statistically significant, though. These numbers also implicate that the percentage of deflections is lower for near co-planar particles than for inclined ones.

We can observe again that the Gaussian distribution for velocities consistently leads to more deflections; there seems to be a small difference between Linear and Poisson

<sup>5</sup>It has to be remarked that the two histograms are not based on the same population sizes, these are very different indeed: the shaded bars show the fraction relative to all simulated particles, while the grey bars are relative to the number of deflected particles.

distribution pos./vel.	impact on ...		deflection, particle ... SOI	
	Earth	Moon	outside	inside
E/G	0.98015(57)	0.00122(11)	0.01863(54)	0
E/L	0.98439(44)	0.00107(15)	0.01454(43)	0
E/P	0.98352(80)	0.00114(12)	0.01533(75)	0
G/G	0.97120(93)	0.00003( 3)	0.02877(93)	0
G/L	0.97781(67)	0.00003( 3)	0.02217(67)	0
G/P	0.97707(59)	0.00003( 3)	0.02290(58)	0
S/G	0.97130(95)	0.00003( 3)	0.02867(95)	0
S/L	0.97826(79)	0.00002( 2)	0.02172(79)	0
S/P	0.97759(79)	0.00003( 2)	0.02239(79)	0
mean	0.97792(223)	0.00040(23)	0.02168(220)	0

Table 4.3: Statistical summary of simulation results for model M1 with configuration C2. Caption as for table 4.2.

distribution, but their  $1\text{-}\sigma$  intervals marginally overlap. On average 2.2 % of incoming particles were deflected, which is three times higher than for the standard configuration. Impacts on the Moon are still more numerous in the Equatorial case than in the Gaussian or Spherical case by about a factor of 40. The lunar impacts (on average 0.04 %) make up for about 2 % of the total number of all deflections and thus play only a negligible role. No particle was observed to be deflected, miss Earth, and then become captured in the Earth-Moon system (inside the SOI).

All of the figures for C2 would look very similar to those for C1, which is the reason why they are not shown. In the following only the deviations from the presented figures are discussed.

The distribution of lunar impact velocities is shifted to slightly higher values in C2 when compared to figure 4.6; the velocity peak is around 5 km/s and the minimum impact velocity is higher due to the increased lunar mass.

Small Earth miss distances (less than two Earth radii) still dominate with about 98 % of all cases for Gaussian and Spherical initial positions; also in the histogram of the lunar minimum distances the bin at 210 – 220 lunar radii sticks out with 16 % (cf. figure 4.8).

There is a deviation in the Equatorial case, though, now particles were deflected if they approached the Moon within 30 times its radius. In C1 the deflection limit was at  $15 R_{\text{Moon}}$  – this doubling of the deflection distance is consistent with the doubling of the mass.

distribution pos./vel.	impact on ...		deflection, particle ... SOI	
	Earth	Moon	outside	inside
E/G	0.99322( 51)	0.00188(22)	0.00489( 48)	$< 10^{-5}$
E/L	0.99425( 39)	0.00179(21)	0.00396( 33)	$< 10^{-5}$
E/P	0.99412( 33)	0.00180(18)	0.00408( 26)	$< 10^{-5}$
G/G	0.93402(103)	0.00004( 3)	0.06594(104)	0
G/L	0.95005(102)	0.00003( 2)	0.04992(102)	0
G/P	0.94760(118)	0.00003( 3)	0.05237(117)	0
S/G	0.94103( 78)	0.00007( 4)	0.05891( 79)	0
S/L	0.95541( 89)	0.00004( 2)	0.04455( 90)	0
S/P	0.95350(100)	0.00005( 3)	0.04645(100)	0
mean	0.96258(253)	0.00064(36)	0.03678(252)	0

Table 4.4: Statistical summary of simulation results for model M1 with configuration C3. Caption as for table 4.2.

### Decreased lunar distance

For the third configuration C3 the lunar distance is halved to  $d_{EM} = 192\,200$  km, but the lunar mass remains unchanged. This configuration would resemble the Earth-Moon system some  $10^9$  years ago, when the two bodies formed a tighter system.

Table 4.4 contains the results for this configuration. At first glance we find the usual situation: on average more than 96 % of the particles impact on Earth, the ratio of direct to indirect deflections is about 2 %, and there are (almost) no captures inside the sphere of influence.

Looking in more detail there is a pronounced difference of several percent between the Equatorial case and Gaussian/Spherical cases. In contrast to that the fraction of impacts used to be quite equal in all cases for both previous configurations (see tables 4.2 and 4.3).

The fraction of deflections in the Gaussian and Spherical cases increases by more than a factor of 10 when compared to the Equatorial case (see column 4). A possible explanation is that in the latter case particles experience the lunar gravitation at a later time – the lunar Hill sphere is smaller as a result of the decreased distance to Earth. At the time when equatorial particles have their minimum distance to the Moon they have a larger relative velocity, because they are deeper in the terrestrial potential well. Even if the Moon modifies their trajectories the deflection angle might not be large enough to avoid impact with Earth, since the remaining distance to Earth has shrunk.

A figure similar to 4.8 for C3 would show that the Earth-miss distances are in general

less than  $17R_{\oplus}$ , in particular almost exclusively distances of  $< 2R_{\oplus}$  occur for Gaussian and Spherical initial positions (the second highest bin includes only 0.1 % of cases). At the same time minimum distances of  $< 7R_{\text{Moon}}$  are needed for successful deflections in the Equatorial case.

The differences in the velocity distributions are also somewhat more enhanced than for the previous configurations, but the trend continues that the Gaussian velocity distribution leads to more deflections.

In the Equatorial case the table now indicates some captured objects. There were in total 12 particles that stayed inside the SOI until the end of the integrations. A closer investigation of these particles revealed that all of them had very similar starting positions (and velocities), and that they approached the Moon to about 3000 km and subsequently missed Earth by about 10000 km. From a recalculation of their orbits it turned out that they are very sensitive to the integrator time-step size, in the second simulation most of them hit Earth. Consequently, the numbers in the last column of table 4.4 for particles inside the SOI are just included as upper limits, they should be considered to be subject to considerable uncertainty.

### 4.3.2 Model 2

Model M2 investigates the opposite effect to M1. We are interested in the number of cases where the Moon turns an Earth-approaching asteroid into an Earth-impacting one. The three configurations for the CR3BP are studied again; more details on the initial conditions for these simulations can be found in section 4.2.4.

#### Standard configuration

The simulations results for C1 are summarised in table 4.5, which is similar in structure to table 4.2, but the roles of impacts and misses (fly-bys) are exchanged. It has already been mentioned that the uniform spherical distribution for initial positions is not applicable in this model, such that only Equatorial (E) and Gaussian (G) initial positions are considered, along with the three types of velocity distributions: Gaussian (G), Linear (L), and Poisson (P).

The second column in the table shows that impacts on Earth occur on average in 3.5 % of cases, which is a relatively high percentage given the fact that all particles should miss Earth. Impact fractions in this column depend only weakly – if at all – on the initial positions, it is rather the initial velocity that has an influence. In M1 we could observe that the Gaussian velocity distribution led to an increase of deflected particles relative to the other two velocity distributions; here in M2 it significantly increases the number of impacts on Earth.

Lunar impacts are still more probable for Equatorial starting positions than for the Gaussian case, nevertheless they are negligible in total number ( $< 0.02$  %) compared

distribution pos./vel.	impact on ...		deflection, particle ... SOI	
	Earth	Moon	outside	inside
E/G	0.04731(105)	0.00020(6)	0.95249(104)	0
E/L	0.02954(114)	0.00016(5)	0.97030(114)	0
E/P	0.03131( 71)	0.00017(7)	0.96852( 73)	0
G/G	0.04526(100)	0.00008(4)	0.95466(102)	0
G/L	0.02860( 78)	0.00008(3)	0.97132( 79)	0
G/P	0.03022( 78)	0.00008(4)	0.96971( 79)	0
mean	0.03537(226)	0.00013(12)	0.96450(228)	0

Table 4.5: Statistical summary of simulation results for model M2 with configuration C1. Each line represents the mean (standard deviation) of 16 simulation runs with the same combination of position/velocity distribution. The abbreviations for the distribution types are: (E) = Equatorial pos., (G) = Gaussian pos. or vel., (L) Linear vel., (P) Poisson vel.

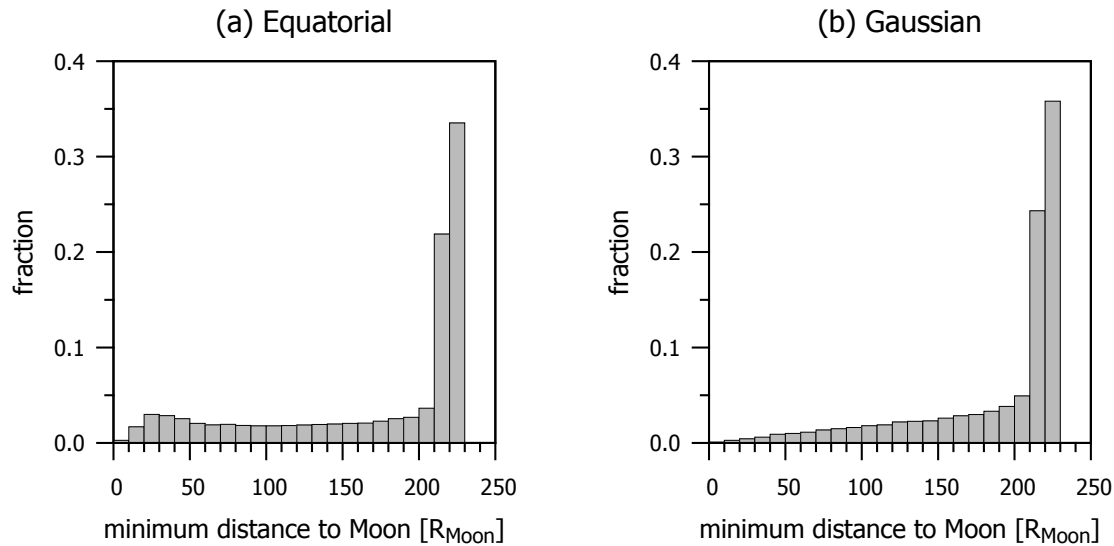


Figure 4.11: Histograms for the minimal distances to the Moon for both initial position distributions. The histograms are based on data for all objects that impact on Earth.

to the other final states. No particles remain inside the Earth’s SOI at the end of the simulations.

Figure 4.11 compares the distribution of minimum distances to the Moon (scaled in lunar radii, bins of width  $10 R_{\text{Moon}}$ ) in the Equatorial and Gaussian case for all impacting particles. The two panels are quite similar qualitatively, both show that the majority of particles never come close to the Moon before they collide with Earth.

In some details the two cases differ, though. For panel (a) there is a bump at around 30 lunar radii, which indicates a slightly enhanced number of particles approaching the Moon (compare to top row in figure 4.8). For panel (b) the histogram is much smoother, the minimum distance to the Moon increases monotonically.

This shape of the histograms is a consequence of having selected only the Earth-impacting objects, which contribute to the large fraction of particles at the 210–230  $R_{\text{Moon}}$  bins (remember that the Earth-Moon distance  $d_{\text{EM}} = 384\,400$  km corresponds to 220 lunar radii).

A more comprehensive analysis of the simulations is given in figure 4.12. For each case – Equatorial (left column) or Gaussian (right column) – four panels show (from top to bottom) the distributions for the initial velocities (at time  $t = 0$  at the SOI), impact velocities, (initial) impact parameters, and the phase angles of impacting particles.

For the initial velocities in row (a) two types of bars are shown: the shaded bars in the background show how the velocity distribution would look like for all particles, which is a combination of Gaussian, Linear, and Poisson velocities ranging from 0.9 to 4.9 km/s with bins of  $\Delta v = 0.1$  km/s; the grey-coloured bars show only the impacting particle’s initial velocities. It is clearly visible that impacting particles form a limited subset of the velocity interval that extends from the escape velocity up to about 2.5 km/s, with the distribution being skewed to lower speeds.

From the initial velocity distribution we obtain the related impact velocity distribution on the Earth in row (b). As the initial speeds were limited to a narrow interval it is not surprising that the impact speeds are limited, too. They are concentrated around 11.2 km/s with an upper limit of 11.5 km/s. In any case these are particles with low relative velocity that are rather susceptible to lunar perturbations.

One row below, the plots (c) show the initial impact parameters in units of the Earth’s radius; these are the distances by which the particles should have missed Earth. There is a clear trend: the smaller the impact parameter is, the higher the impact probability. A closer examination of the results revealed that almost all impacting particles have impact parameters  $b < 15 R_{\oplus}$  ( $b < 96\,000$  km or  $d_{\text{EM}}/4$ ). For the Equatorial case the mean (median) impact parameter is 7.3 (6.9) with the 3<sup>rd</sup> quartile at  $8.4 R_{\oplus}$ , while for the Gaussian case the values are 7.2 (6.8), and  $8.2 R_{\oplus}$ .

In the bottom row (d) we find the histograms for the initial phase angles. The phase angle  $\varphi$  – measured from the positive  $x$ -axis in counter-clockwise direction – gives the direction of the incoming asteroid relative to the direction of the Moon (at  $\varphi = 0$ ). The bump around  $\varphi = 300^\circ$  in the Equatorial case is evidence for particles that approached the Moon; it is also related to the local increase of particles within  $50 R_{\text{Moon}}$  in figure

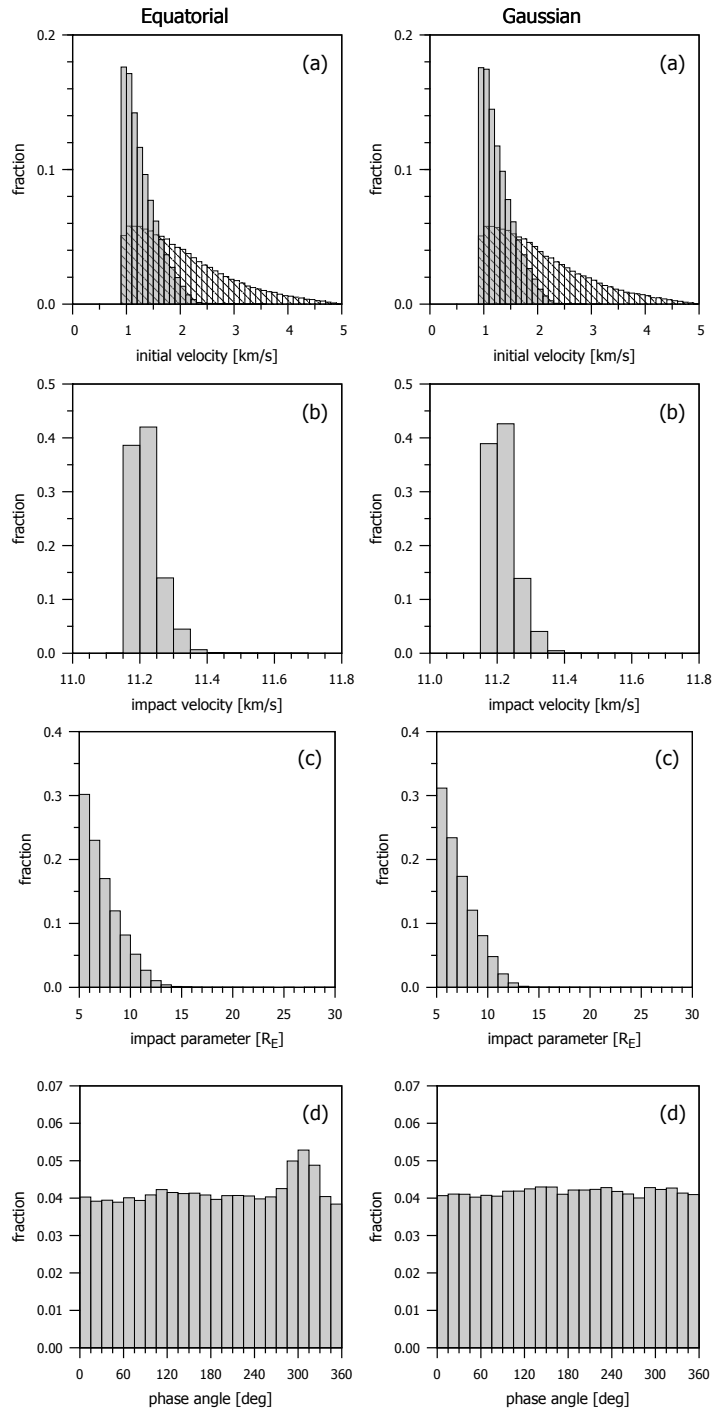


Figure 4.12: Histograms for initial parameters of Earth impacting particles in M2: (a) initial velocity, (b) impact velocity, (c) impact parameter, (d) phase angle; left column for Equatorial and right column for Gaussian initial positions.

distribution pos./vel.	impact on ...		deflection, particle ... SOI	
	Earth	Moon	outside	inside
E/G	0.04727( 98)	0.00030(6)	0.95243( 97)	$< 10^{-5}$
E/L	0.02989(104)	0.00026(7)	0.96984(105)	$< 10^{-5}$
E/P	0.03169( 69)	0.00028(9)	0.96803( 69)	$< 10^{-5}$
G/G	0.04406( 99)	0.00012(6)	0.95582(101)	0
G/L	0.02803( 61)	0.00012(4)	0.97185( 63)	0
G/P	0.02935( 71)	0.00011(5)	0.97054( 71)	0
mean	0.03505(209)	0.00020(15)	0.96475(211)	0

Table 4.6: Statistical summary of simulation results for model M2 with configuration C2. Caption as for table 4.5.

4.11. As of the Gaussian case there is no special feature, all phase angles are more or less equally represented.

### Increased lunar mass

The results of the simulations for C2 are summarised in table 4.6. When comparing these numbers to C1 (in table 4.5) one can notice that they are very similar, indeed the number of deflections (column 3) and impacts on Earth (column 1) are identical to within one standard deviation between the tables.

There is only an increase of impacts on the Moon by about 50 % as a visible effect of the increased lunar mass, this is compatible with the results from model M1. For Equatorial positions there were 8 particles that do not leave Earth’s SOI until the end of the integrations.

In analogy to figure 4.11 also with a more massive Moon there is a bump in the minimal distance histogram for the Equatorial case, but not for the Gaussian case. Still most particles have rather large minimum distances with the peaks located at 210–230 lunar radii. Qualitatively there is no difference of this configuration to the standard configuration, but also quantitatively the fractions in the histograms are varying only minimally.

The same is true for the distribution of initial and impact velocities, which are very similar to figure 4.12. Some noteworthy features for the Equatorial case are that in the third row now also particles with impact parameters beyond  $15 R_{\oplus}$  can impact on Earth; in the phase angle distribution the peak around  $\varphi = 300^{\circ}$  is more pronounced as well when compared to C1.

distribution pos./vel.	impact on ...		deflection, particle ... SOI	
	Earth	Moon	outside	inside
E/G	0.04650(88)	0.00040(7)	0.95295(87)	0.00016(6)
E/L	0.02920(96)	0.00032(9)	0.97039(97)	0.00009(5)
E/P	0.03101(82)	0.00035(8)	0.96852(83)	0.00013(7)
G/G	0.04460(88)	0.00018(9)	0.95511(91)	0.00011(4)
G/L	0.02856(96)	0.00016(6)	0.97123(97)	0.00005(4)
G/P	0.03009(74)	0.00015(4)	0.96970(75)	0.00006(4)
mean	0.03499(214)	0.00026(18)	0.96465(217)	0.00010(12)

Table 4.7: Statistical summary of simulation results for model M2 with configuration C3. Caption as for table 4.5.

### Decreased lunar distance

In the last configuration C3 for model M2 the lunar distance is decreased; table 4.7 collects the data from the simulations.

The results are again very similar to both previous configurations; the mean percentage of deflections is at 96.5 %, and that of forced Earth impacts at 3.5 %. Although impacts on the Moon are negligible in absolute numbers their percentage seems to increase, but note the large uncertainty.

In this configuration the “captured” objects form – for the first time – a non-negligible fraction of the simulation outcomes, similar in magnitude to the lunar impacts. A possible explanation for this behaviour will be discussed in the following section.

For most of the histograms there is nothing special to mention, except that in the Equatorial case the peak in the phase angles is shifted near  $120^\circ$ , but this is a result of the different scaling of the CR3BP when using  $d_{EM} = 192\,200$  km as the unit length.

## 4.4 Discussion

In this section I summarise the main results from the simulations and show how they relate to previously published data. We will also address some open questions related to the deflection efficiency in M2, as well as the circumstances of how and why particles are captured inside the Earth’s sphere of influence.

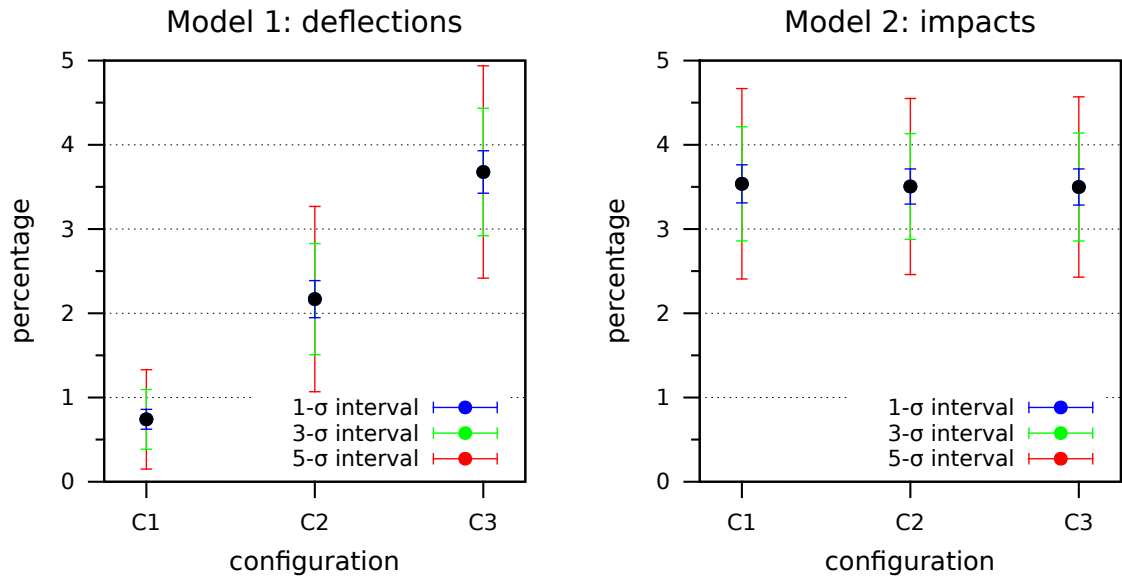


Figure 4.13: Summary of the simulation results for M1 (left) and M2 (right). The three configurations are labelled by C1 for standard configuration, C2 for increased lunar mass, and C3 for decreased lunar distance. The vertical axis shows the resulting percentages, the error bars indicate the multiples of the standard deviation.

#### 4.4.1 Results for Model 1

When comparing the mean values for the deflection efficiency in tables 4.2—4.4 we notice that they depend on the actual values for the basic lunar parameters.

Figure 4.13 collects the data for the two models (left: M1, right: M2) and compares all three configurations.

In M1 the percentage of deflected particles increases from about 0.7 % for C1 to 2.2 % with a more massive Moon (C2); if the Moon was at half of its distance today it could deflect on average about 3.7 % of incoming asteroids (C3). In the figure the respective  $n$ -fold standard deviations are indicated by the error bars. It is clearly visible that the 1- $\sigma$  and 3- $\sigma$  intervals do not overlap, while the 5- $\sigma$  intervals overlap only partly.

The configurations differ by such an amount that there is a high statistical significance for a real physical background. This means that a more massive satellite of Earth would be able to deflect more incoming asteroids (which is no surprise), but it also means that a more compact Earth-Moon system would better shield the Earth from impacts than the current system.

### 4.4.2 Results for Model 2

For M2 always about 3.5 % of all particles impact on Earth, the impact percentage is independent of the actual configuration. The three values for the mean impact efficiency are nearly identical, also no distinction can be made based on their variance (see figure 4.13).

#### Another test case

To address the issue if there is really no correlation of the impact efficiency with any of the lunar parameters (mass or distance), I performed a check with a reduced lunar mass. The chosen mass ratio of  $\mu = 10^{-4}$  is intermediate between that of Titan ( $2.4 \times 10^{-4}$ ) and Ganymede ( $7.8 \times 10^{-5}$ ), while extreme cases like the moons of Mars ( $10^{-8}$ ) or Charon (0.1) were not considered<sup>6</sup>. In the test simulations the impact efficiency was still between 3.5 % (Equatorial case) and 3.6 % (Gaussian case), on average the results turn out to be as high as before.

This raises the question whether or not the observed effect is caused by the Moon. As the three investigated configurations (plus the test case) show, the Moon has only a limited effect in focusing asteroids towards Earth. For the test case the observed impact percentage must be attributed mainly to the terrestrial gravitational focusing. However, in the following section I will demonstrate that the Moon is able to deflect particles strongly enough to impact on Earth, provided that they have low enough relative velocity and impact parameters.

#### Deflection angles

In a study on orbital interactions Greenberg (1982, eq. (36)) provides a formula for the rotation angle (here it is called deflection angle) by which the relative velocity vector of an incoming object is rotated towards the central mass. In that formula the deflection angle  $\chi$  depends on the impact parameter  $b$  and especially on the relative velocity  $v$ ,

$$\sin \chi = \left[ 1 + \left( \frac{bv^2}{G(m_1 + m_2)} \right)^2 \right]^{-1/2}. \quad (4.4.1)$$

A NEA with the lowest impact parameter ( $b = 5R_{\oplus}$ ) at the border of the SOI ( $d = 150R_{\oplus}$ ) would need to be deflected by at least  $\chi = \arctan(b/d) = 1.91^\circ$  to impact on Earth. Any higher value of  $b$  will result in a larger deflection angle, where at some point the Moon will not be able to provide the necessary deflection alone.

Figure 4.14 visualises equation (4.4.1) as a function of the impact parameter for different relative velocities, where the lunar mass is inserted to obtain the deflection angles.

<sup>6</sup>see Satellite Fact Sheet at <http://nssdc.gsfc.nasa.gov/planetary/factsheet/>

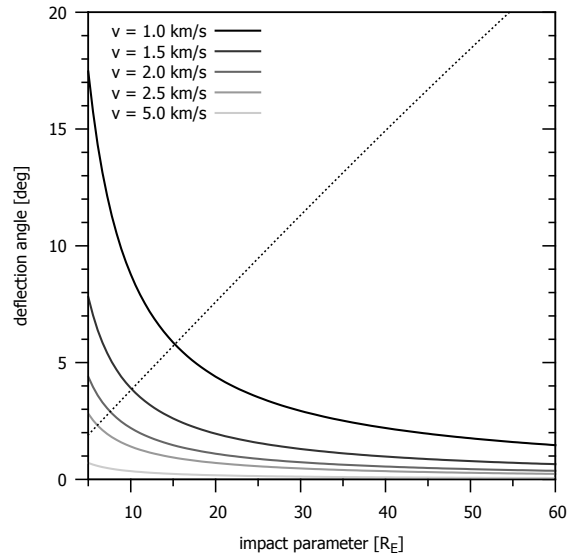


Figure 4.14: The deflection angle due to the Moon as a function of the impact parameter (horizontal axis, scaled in Earth radii) for a given relative velocity; curves are labelled from top to bottom.

The diagonal dotted line (actually this is the more or less linear part of the arctan-function) gives the lower bound for the angle  $\chi$ , any deflection angle below this value is insufficient to lead to a collision with Earth.

From the figure it is visible that impact parameters of  $b \leq 15R_{\oplus}$  are supported at the lower end of the relative velocity interval (for  $v = 1$  km/s). When the relative velocity increases slightly to  $v = 1.5$  km/s the maximum impact parameter shrinks to about  $10R_{\oplus}$ , while for  $v = 2.5$  km/s only impact parameters  $b < 7R_{\oplus}$  are possible.

This must be compared to figure 4.12, where in the top row graphs we saw that impacting particles had initial velocities of less than 2.5 km/s. From the third row of that figure it followed that the impact parameters for those particles were restricted to  $15R_{\oplus}$  or less. These results are consistent with the curves in figure 4.14 based on formula (4.4.1).

Thus it would be conveniently possible to explain the rather high impact efficiency simply by the lunar influence for any of the three configurations of model M2. However, this explanation does not work for the test calculations with reduced lunar mass ( $\mu = 10^{-4}$ ), where the Moon is unable to provide the deflection angles necessary for impacts. In the end it is more likely that the major contribution to the impact efficiency of 3.5 % comes from Earth, with the Moon's contribution being much smaller.

### Isolating the lunar contribution to impacts

It is not straightforward to disentangle the contributions of Earth and Moon to the impact efficiency. A rough estimate can be attempted by using figures 4.8 & 4.11.

From the former figure the Equatorial case (top row, right panel) demonstrated that deflections of asteroids occurred whenever they passed the Moon within  $15 R_{\text{Moon}}$  (lunar radii). This number changes with the configuration, e.g. a higher lunar mass increases the limit to  $30 R_{\text{Moon}}$ .

The latter figure gave the distribution of the minimal lunar fly-by distances for impacting particles. From these histograms we can extract the cumulative fraction of objects that pass the Moon within 30 lunar radii. This number is justified by the fact that the lunar Hill radius equals about 35 lunar radii for configuration C1, see equation (2.4.1). Any particle that passes the Moon within this zone will be subject to strong lunar perturbations.

It follows that roughly 5.0 % and 0.8 % of all impactors in the simulations (for the Equatorial and Gaussian case, respectively) pass the Moon closer than the required limit. We can estimate the Moon's contribution to the mean impact efficiency of 3.5 % as  $0.035 \times 0.008 = 0.00028$  and  $0.035 \times 0.05 = 0.00175$  by using the fractions from above. The lunar effect is between 0.028 – 0.18 %, i.e. the Moon contributes with (well) less than 0.2 % to the determined impact efficiency of 3.5 %; the effect due to Earth is then 3.3 %. As a side-note let us emphasize that the ratio of the two contributions is of the same order as the Moon-Earth mass ratio.

#### 4.4.3 Comparison to other results

In section 4.1.1 a number of previous studies was presented. Among those publications the one of Domingos et al. (2004) is most closely related to the current thesis and was part of the motivation for the investigations above.

Domingos et al. found that below a relative velocity of 5 km/s the lunar gravitational effect becomes significant. They reported as a maximum effect that 2.6 % of objects on collision trajectories were removed when the objects had an initial velocity of 1 km/s; for larger relative velocities the removal percentage decreased to 0.8 % at 5 km/s. In contrast to their results for several discrete values of the relative velocity I found a cumulative effect of 0.7 % in model M1 for a continuous velocity interval. The second main result of Domingos et al. is that lunar perturbations induce on average 0.6 % of the objects to collide with Earth. From my simulations model M2 gives a percentage of 3.5 % for an equivalent case, but as the discussion in the previous section has shown, the Moon's contribution is only 0.2 % to the collisions. Finally, the authors also reported a strong dependence of collisions on the impact parameter.

Gladman et al. (1995) performed simulations of lunar impact ejecta. They found that more than 90 % of the ejecta particles escape to heliocentric orbits for initial speeds larger than the escape velocity, but there is also a velocity interval that favours transport of

material to Earth. The percentage of ejecta returning to the Moon depends strongly on the initial speed, for an initial velocity that is 10 % above escape velocity only 1 % of the material return. These results are in accordance with the simulation results, although I was interested in material that returns to Earth and not to the Moon. In the simulations I considered initial velocities up to 36 % higher than the escape velocity (M1) and found that on average 0.7 % of the objects return.

Gladman et al. (2005) approached the problem of ejecta from another point of view. For impact ejecta originating from Earth they determined that material can be transported to Venus and Mars, and that about 1 % of the original material would return to Earth within 30 000 years. Also these authors found that the fraction of returning material is strictly depending on the ejection speeds, the percentage falls below 1 % for  $v_0 \approx 11.75$  km/s.

Reyes-Ruiz et al. (2012) extended the results of the more recent Gladman et al. paper. Earth impact ejecta (similar to M1) return to Earth in about 1 % of all cases for ejection velocities of 11.7 km/s. The authors also reported the collision probability of these ejecta with the Moon to be 0.02 % which is in excellent agreement with my simulation results (see table 4.2).

All other publications mentioned in section 4.1.1 cannot be compared to the simulations presented, either because the dynamical models are incompatible or because the investigated target objects have nothing in common.

#### 4.4.4 Captured objects

One of the possible end states of the simulations is that particles (originally on hyperbolic trajectories) could be captured temporarily or permanently in the Earth-Moon system. Tables 4.4 and 4.6 show that this outcome is rather rare and occurs preferably in the Equatorial case.

It was already mentioned that the particles had very similar initial starting points and velocities, but also that the trajectories are very chaotic and the outcome is sensitive to the integrator step size.

Alessi et al. (2010) investigated the Earth-Moon CR3BP and how the lunar surface is affected by incoming asteroids. They considered the hyperbolic invariant manifolds associated with the central invariant manifold of the  $L_2$  libration point as “channels” that can deliver asteroids to the Earth-Moon system, which eventually impact on the Moon. For asteroids with appropriate initial conditions there exist tubes that lead or depart from the (quasi) periodic orbits.

Qualitatively the trajectories of captured particles in the simulations resemble to figure 3.1 in Alessi et al. (2010). It is possible that the few particles observed to become captured start close to or inside those tubes that bring them close to  $L_2$ . However, before they get captured they must get rid of their excessive velocity. They can do so by a flyby (or gravity assist maneuver) to the Moon, during which the velocity can decrease or increase (Chobotov, 1991).

This process could explain why captures occur preferentially in the equatorial case, why the initial conditions are so similar, and why the objects need to closely approach the Moon. This process would not explain the results for C3 in table 4.7, which are somewhat different in this respect. I did not investigate those cases in detail, since they belong to a final state that is not of primary interest, and the fraction of cases is negligible compared to the impacts on Earth. One hypothesis is that the decreased lunar distance could influence the geometry of fly-bys in such a way that particles have two gravity assist maneuvers with Moon and Earth, where in both cases they decrease their velocity and end in a bounded state.



# Chapter 5

## Summary

This final chapter summarises the main results and conclusions of the main chapters 3 on the dynamics of NEAs and chapter 4 on impact simulations. Section 1.4 established three key points that will be addressed in the following.

### How does the Moon influence the trajectories of real NEAs in the long-term?

The long-term dynamics of NEAs was investigated by means of two numerical integration methods, the Lie-series integrator (section 2.2.1) and the Mercury integrator (section 2.2.2). Both methods are well suited to handle the frequent close approaches of NEAs to planets. By using two different types of integrators I intended to exclude spurious results and to increase the confidence in the data.

Three pairs of models were defined in section 3.1, and then used to investigate the lunar effect on NEAs in increasingly more complex dynamical systems.

In models M2/M3 close encounters to Earth or the Earth-Moon system are very frequent (cf. table 3.7). When comparing the orbital element distributions of NEAs at close encounters in figure 3.9, no qualitative difference is found apart from small statistical fluctuations. In all cases the distributions are very similar, which indicates that they are dominated by the Earth and that the Moon has almost no effect. The class membership statistics (figures 3.10 – 3.12 and table 3.4) also demonstrates that the percentage of objects belonging to a specific NEA group is independent from the Moon's presence.

The models M4/M5 introduce mean-motion resonances as another key factor for the dynamics of NEAs. Figure 3.20 shows the percentage of NEAs remaining in the simulation versus time. It is obvious that impacts decrease the total number, but the decrease is rather slow ( $\geq 80\%$  of objects are remaining). The curves have a similar trend for both models, although there is a slight excess in M4 ( $\leq 1\%$ ) for all NEA groups. If this trend continued for a longer integration time (at least until reaching 50% of the original population), then one could deduce some lunar influence. However, in the close encounter relative velocity distributions (figure 3.17) no observable lunar effect is visible; this is true in particular for the  $v_{\text{rel}} \leq 5$  km/s encounters in figure 3.18. It is possible

to estimate the lunar deflection efficiency from the data in figure 3.18 which gives a probability of  $P(d \leq 384\,400\text{km} | v_{\text{rel}} \leq 5\text{km/s}) = 0.0052\%$ ; a similar number to this can be derived for models M6/M7. This shows that the events are rare where the presence of the Moon would make a difference.

The last pair of models M6/M7 include the powerful perturbations of Jupiter and Saturn. Similar to the previous model pair also this time no qualitative difference can be observed in the relative velocity distributions in figure 3.22. The same holds for figure 3.29 when comparing the number of surviving objects. In all cases the percentages agree to within  $\pm 1\%$  between the models, thus the Moon has only a marginal effect on NEAs over time-spans of  $10^7$  years.

In table 3.7 the number of close encounters inside the Hill sphere is summarised, for most cases the numbers differ by  $< 2\%$ . It is also visible from table 3.6 that the percentage of NEAs with close encounters to Earth within the lunar distance agrees to  $\pm 1\%$  for most models. These data were converted to the normalised number of encounters per object, shown in figure 3.27, which demonstrates that there are no systematic effects when the Moon is included into the models.

## Does the presence of the Moon increase or decrease the number of impacts on Earth?

In section 3.3.4 the collision frequency for each NEA group was estimated directly from the integrations. From the encounter frequency to the Hill sphere the impact frequency was fitted by a linear model, see figure 3.24 and table 3.5.

The observed number of impacts in the simulations can be found in table 3.9. Table 3.11 summarises the estimated impact frequencies based on three methods (see section 3.4.3). A Pearson chi-squared test was performed to test the hypothesis that the Moon significantly modifies the number of impacts. This test yields a negative result, i.e. the data imply that the Moon does not increase or decrease the number of impacts.

An alternative approach was taken in section 4.1. The circular restricted three-body problem Earth–Moon–NEA was employed to simulate impacts on the Earth. For this task a novel variant of the manifold correction method was implemented (see sections 2.3.2 and 4.2.1).

In the first simulation model (M1/C1) I checked how many impactors the Moon could deflect (section 4.3.1). The results in table 4.2 show that still 99.2% of incoming objects hit the Earth, but in 0.8% of the cases the Moon could deflect the impactor. This percentage is lower than the corresponding value reported in Domingos et al. (2004), but there it was obtained for a 2D model. In figure 4.8 the histograms indicate that successful deflection mainly occur when the asteroid passes the Moon within 30 times the lunar radius – which is roughly equal to the Moon’s Hill radius.

The second simulation model (M2/C1) was designed to quantify the lunar contribution

---

to impacts (section 4.3.2). The results are given in table 4.5, which shows that in about 3.5 % of all cases an impact happens. Section 4.4.2 discusses the reasons for this rather high percentage. It was shown that for the given limits in impact parameter and relative velocity the Moon can provide deflection angles that are large enough to allow for an impact (figure 4.14). When the lunar effect is isolated then less than 0.2 % of the impacts can be attributed to its effect.

In total I can confirm that the Moon is slightly more effective in removing potentially impacting NEAs (in  $\sim 0.8$  % of all simulated cases) than in focussing NEAs towards Earth (in  $< 0.2$  % of cases). Of course, one should not forget that these deflections depend on the relative velocity, and just for 0.2 – 0.3 % of all close encounters the relative velocity is low enough.

## Would changes in the lunar parameters affect the impact rate?

This question was treated along with the simulations in chapter 4. The basic models (section 4.1) were modified to account for a higher lunar mass or a smaller lunar distance.

In the standard configuration C1 (with lunar mass and distance as in reality) the Moon deflects  $0.74 \pm 0.12$  % of impactors. The percentage of deflections increases to  $2.17 \pm 0.22$  % with increased lunar mass in C2, these results are consistently higher than for the default mass in all simulation runs. After decreasing the lunar distance there are still more deflections in C3, this time  $3.68 \pm 0.25$  % of all cases. This means that under special circumstances – preferably for low relative velocity encounters – the Moon can modify the impact rate, and the effect depends on the physical parameters (at least mass and geocentric distance).

For the complementary model, which investigated the forced impacts, the data were indecisive (see figure 4.13). Irrespective of the Moon's actual physical parameters the simulations have always resulted in 3.5 % of additional impacts. The same percentage was found for a strongly decreased mass ratio (see section 4.4.2), which indicates that the Moon's real influence would be much weaker than the 3.5 %. An estimate for the default lunar mass yields a best-case value of 0.2 % additional impacts caused by the Moon. This analysis was not extended to other parameter values.

As the bottom line and conclusion no real influence is detectable for the Moon on the trajectories of Near-Earth Asteroids. For investigations covering long time intervals and aimed at a statistical description of NEA dynamics the Moon can be safely ignored. The lunar gravitational influence will become important only in the special case of deep close encounters with low relative velocity.



# Bibliography

- Aarseth, S. J., Lin, D. N. C., and Palmer, P. L. (1993). *Evolution of Planetesimals. II. Numerical Simulations*. *Astrophysical Journal* **403**, pp. 351–376.
- Abramowitz, M. and Stegun, I. A. (editors) (1972). *Handbook of Mathematical Functions*. Dover, 9th edition.
- Alessi, E. M., Gómez, G., and Masdemont, J. J. (2010). *A motivating exploration on lunar craters and low-energy dynamics in the Earth-Moon system*. *Celestial Mechanics and Dynamical Astronomy* **107**, pp. 187–207.
- Alibert, Y., Broeg, C., Benz, W., and 23 coauthors (2010). *Origin and Formation of Planetary Systems*. *Astrobiology* **10**, pp. 19–32.
- Alvarellos, J. L., Zahnle, K. J., Dobrovolskis, A. R., and Hamill, P. (2002). *Orbital Evolution of Impact Ejecta from Ganymede*. *Icarus* **160**, pp. 108–123.
- Artemieva, N. A. and Shuvalov, V. V. (2008). *Numerical simulation of high-velocity impact ejecta following falls of comets and asteroids onto the Moon*. *Solar System Research* **42**, pp. 329–334.
- Baer, J. and Chesley, S. R. (2008). *Astrometric masses of 21 asteroids, and an integrated asteroid ephemeris*. *Celestial Mechanics and Dynamical Astronomy* **100**, pp. 27–42.
- Bailey, M. E., Chambers, J. E., and Hahn, G. (1992). *Origin of sungrazers - A frequent cometary end-state*. *Astronomy & Astrophysics* **257**, pp. 315–322.
- Bancelin, D., Hestroffer, D., and Thuillot, W. (2012). *Numerical integration of dynamical systems with Lie series. Relativistic acceleration and non-gravitational forces*. *Celestial Mechanics and Dynamical Astronomy* **112**, pp. 221–234.
- Bazsó, Á., Dvorak, R., Pilat-Lohinger, E., Eybl, V., and Lhotka, C. (2010). *A survey of near-mean-motion resonances between Venus and Earth*. *Celestial Mechanics and Dynamical Astronomy* **107**, pp. 63–76.
- Beaugé, C., Ferraz-Mello, S., and Michtchenko, T. A. (2007). *Planetary Masses and Orbital Parameters from Radial Velocity Measurements*. In: R. Dvorak (editor), *Extrasolar Planets. Formation, Detection and Dynamics*, pp. 1–25. Wiley-VCH.

- Bertini, I. (2013). *Asteroids Close-Up: What We Have Learned from Twenty Years of Space Exploration*. In: V. Badescu (editor), *Asteroids: Prospective Energy and Material Resources*, pp. 1–33. Springer.
- Binzel, R. P. and Xu, S. (1993). *Chips off of asteroid 4 Vesta - Evidence for the parent body of basaltic achondrite meteorites*. *Science* **260**, pp. 186–191.
- Bottke, W. F., Morbidelli, A., Jedicke, R., Petit, J.-M., Levison, H. F., Michel, P., and Metcalfe, T. S. (2002). *Debiased Orbital and Absolute Magnitude Distribution of the Near-Earth Objects*. *Icarus* **156**, pp. 399–433.
- Bottke, W. F., Jr., Nolan, M. C., Greenberg, R., and Kolvoord, R. A. (1994). *Collisional Lifetimes and Impact Statistics of Near-earth Asteroids*. In: T. Gehrels, M. S. Matthews, and A. M. Schumann (editors), *Hazards Due to Comets and Asteroids*, pp. 337–357.
- Box, G. E. P. and Muller, M. E. (1958). *A Note on the Generation of Random Normal Deviates*. *The Annals of Mathematical Statistics* **29**(2), pp. 610–611.
- Brasser, R. and Wiegert, P. (2008). *Asteroids on Earth-like orbits and their origin*. *Monthly Notices of the RAS* **386**, pp. 2031–2038.
- Brown, P., Spalding, R. E., ReVelle, D. O., Tagliaferri, E., and Worden, S. P. (2002). *The flux of small near-Earth objects colliding with the Earth*. *Nature* **420**, pp. 294–296.
- Burkardt, T. M. and Danby, J. M. A. (1983). *The solutions of Kepler’s equation. II*. *Celestial Mechanics* **31**, pp. 317–328.
- Bus, S. J. and Binzel, R. P. (2002). *Phase II of the Small Main-Belt Asteroid Spectroscopic Survey. A Feature-Based Taxonomy*. *Icarus* **158**, pp. 146–177.
- Calame, O. and Mulholland, J. D. (1978). *Lunar tidal acceleration determined from laser range measures*. *Science* **199**, pp. 977–978.
- Carry, B. (2012). *Density of asteroids*. *Planetary and Space Science* **73**, pp. 98–118.
- Carusi, A., Valsecchi, G. B., and Greenberg, R. (1990). *Planetary close encounters - Geometry of approach and post-encounter orbital parameters*. *Celestial Mechanics and Dynamical Astronomy* **49**, pp. 111–131.
- Cash, J. R. and Karp, A. H. (1990). *A Variable Order Runge-Kutta Method for Initial Value Problems with Rapidly Varying Right-hand Sides*. *ACM Trans. Math. Softw.* **16**(3), pp. 201–222.
- Castelli, R. (2011). *On the Relation Between the Bicircular Model and the Coupled Circular Restricted Three-Body Problem Approximation*. In: *Nonlinear and Complex Dynamics*, pp. 53–68. Springer.

- Cellino, A. and Dell’Oro, A. (2010). *Asteroid Dynamical Families*. In: J. Souchay and R. Dvorak (editors), *Lecture Notes in Physics*, volume 790, pp. 137–193. Springer.
- Chambers, J. E. (1999). *A hybrid symplectic integrator that permits close encounters between massive bodies*. *Monthly Notices of the RAS* **304**, pp. 793–799.
- Chapman, C. R. (1979). *The asteroids - Nature, interrelations, origin, and evolution*. In: T. Gehrels (editor), *Asteroids*, pp. 25–60.
- Charles, E. D. and Tatum, J. B. (1997). *The Convergence of Newton-Raphson Iteration with Kepler’s Equation*. *Celestial Mechanics and Dynamical Astronomy* **69**, pp. 357–372.
- Chesley, S. R. (2006). *Potential impact detection for Near-Earth asteroids: the case of 99942 Apophis (2004 MN<sub>4</sub>)*. In: L. Daniela, S. Ferraz-Mello, and F. J. Angel (editors), *Asteroids, Comets, Meteors, IAU Symposium*, volume 229, pp. 215–228.
- Chobotov, V. A. (editor) (1991). *Orbital mechanics*. AIAA education series. AIAA Inc.
- Danby, J. M. A. (2003). *Fundamentals of Celestial Mechanics*. Willmann-Bell Inc., 2nd edition.
- DeMeo, F. E., Binzel, R. P., Slivan, S. M., and Bus, S. J. (2009). *An extension of the Bus asteroid taxonomy into the near-infrared*. *Icarus* **202**, pp. 160–180.
- Dobrovolskis, A. R. and Lissauer, J. J. (2004). *The fate of ejecta from Hyperion*. *Icarus* **169**, pp. 462–473.
- Domingos, R. C., Winter, O. C., and Neto, E. V. (2004). *Collisions with the Earth: the Moon’s contribution*. *Advances in Space Research* **33**, pp. 1534–1538.
- Dvorak, R. and Freistetter, F. (2001). *Dynamical evolution and collisions of asteroids with the earth*. *Planetary and Space Science* **49**, pp. 803–809.
- Dvorak, R. and Lhotka, C. (2013). *Celestial Dynamics: Chaoticity and Dynamics of Celestial Systems*. Wiley-VCH.
- Dvorak, R. and Pilat-Lohinger, E. (1999). *On the dynamical evolution of the Atens and the Apollos*. *Planetary and Space Science* **47**, pp. 665–677.
- Eggl, S. and Dvorak, R. (2010). *An Introduction to Common Numerical Integration Codes Used in Dynamical Astronomy*. In: J. Souchay and R. Dvorak (editors), *Lecture Notes in Physics*, volume 790, pp. 431–480. Springer.
- Érdi, B. (2004). *Global Regularization of the Restricted Problem of Three Bodies*. *Celestial Mechanics and Dynamical Astronomy* **90**, pp. 35–42.

- Farinella, P., Froeschle, C., Froeschle, C., Gonczi, R., Hahn, G., Morbidelli, A., and Valsecchi, G. B. (1994). *Asteroids falling into the Sun*. *Nature* **371**, pp. 315–318.
- Freistetter, F. (2009). *Fuzzy characterization of near-earth-asteroids*. *Celestial Mechanics and Dynamical Astronomy* **104**, pp. 93–102.
- Froeschle, C. and Scholl, H. (1989). *The three principal secular resonances  $nu(5)$ ,  $nu(6)$ , and  $nu(16)$  in the asteroidal belt*. *Celestial Mechanics and Dynamical Astronomy* **46**, pp. 231–251.
- Fukushima, T. (1997). *A Procedure Solving the Extended Kepler's Equation for the Hyperbolic Case*. *Astronomical Journal* **113**, pp. 1920–1924.
- Fukushima, T. (2003). *Efficient Orbit Integration by Scaling for Kepler Energy Consistency*. *Astronomical Journal* **126**, pp. 1097–1111.
- Galiazzo, M. A., Bazzó, Á., and Dvorak, R. (2013a). *Fugitives from the Hungaria region: Close encounters and impacts with terrestrial planets*. *Planetary and Space Science* **84**, pp. 5–13.
- Galiazzo, M. A., Bazzó, Á., Huber, M. S., Losiak, A., Dvorak, R., and Koeberl, C. (2013b). *A statistical dynamical study of meteorite impactors: A case study based on parameters derived from the Bosumtwi impact event*. *Astronomische Nachrichten* **334**, pp. 936–939.
- Gallardo, T. (2006). *Atlas of the mean motion resonances in the Solar System*. *Icarus* **184**, pp. 29–38.
- Gekeler, E. W. (2006). *Mathematische Methoden zur Mechanik*. Springer.
- Giorgini, J. D., Yeomans, D. K., Chamberlin, A. B., Chodas, P. W., Jacobson, R. A., Keesey, M. S., Lieske, J. H., Ostro, S. J., Standish, E. M., and Wimberly, R. (1996). *JPL's On-Line Solar System Data Service*. *Bulletin of the American Astronomical Society* **28**(3), p. 1158.
- Gladman, B., Dones, L., Levison, H. F., and Burns, J. A. (2005). *Impact Seeding and Reseeding in the Inner Solar System*. *Astrobiology* **5**, pp. 483–496.
- Gladman, B., Michel, P., and Froeschlé, C. (2000). *The Near-Earth Object Population*. *Icarus* **146**, pp. 176–189.
- Gladman, B. J., Burns, J. A., Duncan, M. J., and Levison, H. F. (1995). *The dynamical evolution of lunar impact ejecta*. *Icarus* **118**, pp. 302–321.
- Gladman, B. J., Migliorini, F., Morbidelli, A., Zappala, V., Michel, P., Cellino, A., Froeschle, C., Levison, H. F., Bailey, M., and Duncan, M. (1997). *Dynamical lifetimes of objects injected into asteroid belt resonances*. *Science* **277**, pp. 197–201.

- Goldreich, P. (1966). *History of the Lunar Orbit*. Reviews of Geophysics and Space Physics **4**, pp. 411–439.
- Greenberg, R. (1982). *Orbital interactions - A new geometrical formalism*. Astronomical Journal **87**, pp. 184–195.
- Greenberg, R., Carusi, A., and Valsecchi, G. B. (1988). *Outcomes of planetary close encounters - A systematic comparison of methodologies*. Icarus **75**, pp. 1–29.
- Greenberg, R. and Nolan, M. C. (1993). *Dynamical relationships of near-Earth asteroids to main-belt asteroids*. In: J. S. Lewis, M. S. Matthews, and M. L. Guerrieri (editors), *Resources of near-earth space*, pp. 473–492.
- Greenstreet, S., Ngo, H., and Gladman, B. (2012). *The orbital distribution of Near-Earth Objects inside Earth's orbit*. Icarus **217**, pp. 355–366.
- Gröbner, W. and Knapp, H. (1967). *Contributions to the method of Lie series*. B.I.-Hochschulschriften. Bibliographisches Institut.
- Hahn, G. and Lagerkvist, C.-I. (1988). *Orbital evolution studies of planet-crossing asteroids*. Celestial Mechanics **43**, pp. 285–302.
- Hairer, E., Lubich, C., and Wanner, G. (2006). *Geometric Numerical Integration: Structure-Preserving Algorithms for Ordinary Differential Equations*. Springer Series in Computational Mathematics. Springer, 2nd edition.
- Hanslmeier, A. and Dvorak, R. (1984). *Numerical Integration with Lie Series*. Astronomy & Astrophysics **132**, pp. 203–207.
- Hartmann, W. K., Farinella, P., Vokrouhlický, D., Weidenschilling, S. J., Morbidelli, A., Marzari, F., Davis, D. R., and Ryan, E. (1999). *Reviewing the Yarkovsky effect: New light on the delivery of stone and iron meteorites from the asteroid belt*. Meteoritics and Planetary Science **34**, pp. 161–167.
- Helin, E. F. and Shoemaker, E. M. (1979). *The Palomar planet-crossing asteroid survey, 1973-1978*. Icarus **40**, pp. 321–328.
- Hilton, J. L. (2002). *Asteroid Masses and Densities*. In: W. F. Bottke, A. Cellino, P. Paolicchi, and R. P. Binzel (editors), *Asteroids III*, pp. 103–112. University of Arizona Press.
- Huang, J., Ji, J., Ye, P., and 26 coauthors (2013). *The Ginger-shaped Asteroid 4179 Toutatis: New Observations from a Successful Flyby of Chang'e-2*. Nature Scientific Reports **3**, pp. 3411–3416.

- Ito, T. and Malhotra, R. (2010). *Asymmetric impacts of near-Earth asteroids on the Moon*. *Astronomy & Astrophysics* **519**, pp. A63–A71.
- Ivanov, B. (2008). *Geologic Effects of Large Terrestrial Impact Crater Formation*. In: V. V. Adushkin and I. V. Nemchinov (editors), *Catastrophic Events Caused by Cosmic Objects*, pp. 163–205.
- Jeffers, S. V., Manley, S. P., Bailey, M. E., and Asher, D. J. (2001). *Near-Earth object velocity distributions and consequences for the Chicxulub impactor*. *Monthly Notices of the RAS* **327**, pp. 126–132.
- Jorba, Á. and Zou, M. (2005). *A software package for the numerical integration of ODEs by means of high-order Taylor methods*. *Experimental Mathematics* **14**(1), pp. 99–117.
- Kamo, S. L., Reimold, W. U., Krogh, T. E., and Colliston, W. P. (1996). *A 2.023 Ga age for the Vredefort impact event and a first report of shock metamorphosed zircons in pseudotachylitic breccias and Granophyre*. *Earth and Planetary Science Letters* **144**, pp. 369–387.
- Kankiewicz, P. (2002). *Earth-Moon Separation Problem In The Motion Of Near Earth Asteroids*. *Earth Moon and Planets* **91**, pp. 43–51.
- Kinoshita, H., Yoshida, H., and Nakai, H. (1990). *Symplectic integrators and their application to dynamical astronomy*. *Celestial Mechanics and Dynamical Astronomy* **50**, pp. 59–71.
- Koeberl, C. (2006). *The record of impact processes on the early Earth: A review of the first 2.5 billion years*. *Geological Society of America Special Papers* **405**, pp. 1–22.
- Kokubo, E. and Ida, S. (2002). *Formation of Protoplanet Systems and Diversity of Planetary Systems*. *Astrophysical Journal* **581**, pp. 666–680.
- Laskar, J. (1990). *The chaotic motion of the solar system - A numerical estimate of the size of the chaotic zones*. *Icarus* **88**, pp. 266–291.
- Levison, H. F. and Duncan, M. J. (1994). *The long-term dynamical behavior of short-period comets*. *Icarus* **108**, pp. 18–36.
- Levison, H. F. and Duncan, M. J. (2000). *Symplectically Integrating Close Encounters with the Sun*. *Astronomical Journal* **120**, pp. 2117–2123.
- Levison, H. F., Morbidelli, A., Van Laerhoven, C., Gomes, R., and Tsiganis, K. (2008). *Origin of the structure of the Kuiper belt during a dynamical instability in the orbits of Uranus and Neptune*. *Icarus* **196**, pp. 258–273.

- Lupishko, D. F., Martino, M. D., and Binzel, R. P. (2007). *Near-Earth objects as principal impactors of the Earth: Physical properties and sources of origin*. In: G. B. Valsecchi, D. Vokrouhlický, and A. Milani (editors), *IAU Symposium*, volume 236, pp. 251–260.
- Mainzer, A., Grav, T., Bauer, J., and 34 coauthors (2011). *NEOWISE Observations of Near-Earth Objects: Preliminary Results*. *Astrophysical Journal* **743**, pp. 156–172.
- McSween, H. Y., Mittlefehldt, D. W., Beck, A. W., Mayne, R. G., and McCoy, T. J. (2011). *HED Meteorites and Their Relationship to the Geology of Vesta and the Dawn Mission*. *Space Science Reviews* **163**, pp. 141–174.
- Michel, P., Froeschlé, C., and Farinella, P. (1996). *Dynamical Evolution of NEAs: Close Encounters, Secular Perturbations and Resonances*. *Earth Moon and Planets* **72**, pp. 151–164.
- Michel, P., Froeschlé, C., and Farinella, P. (1997). *Secular Dynamics of Asteroids in the Inner Solar System*. *Celestial Mechanics and Dynamical Astronomy* **69**, pp. 133–147.
- Michel, P., Migliorini, F., Morbidelli, A., and Zappalà, V. (2000). *The Population of Mars-Crossers: Classification and Dynamical Evolution*. *Icarus* **145**, pp. 332–347.
- Migliorini, F., Michel, P., Morbidelli, A., Nesvorný, D., and Zappala, V. (1998). *Origin of Multikilometer Earth- and Mars-Crossing Asteroids: A Quantitative Simulation*. *Science* **281**, pp. 2022–2024.
- Milani, A., Carpino, M., Hahn, G., and Nobili, A. M. (1989). *Dynamics of planet-crossing asteroids - Classes of orbital behavior*. *Icarus* **78**, pp. 212–269.
- Milani, A., Carpino, M., and Marzari, F. (1990). *Statistics of close approaches between asteroids and planets - Project Spaceguard*. *Icarus* **88**, pp. 292–335.
- Milani, A. and Gronchi, G. F. (2010). *Theory of Orbital Determination*. Cambridge University Press.
- Milani, A. and Knezevic, Z. (1994). *Asteroid proper elements and the dynamical structure of the asteroid main belt*. *Icarus* **107**, pp. 219–254.
- Minton, D. A. and Malhotra, R. (2010). *Dynamical erosion of the asteroid belt and implications for large impacts in the inner Solar System*. *Icarus* **207**, pp. 744–757.
- Morbidelli, A., Bottke, W. F., Jr., Froeschlé, C., and Michel, P. (2002). *Origin and Evolution of Near-Earth Objects*. In: W. F. Bottke, A. Cellino, P. Paolicchi, and R. P. Binzel (editors), *Asteroids III*, pp. 409–422. University of Arizona Press.

- Morbidelli, A., Lunine, J. I., O'Brien, D. P., Raymond, S. N., and Walsh, K. J. (2012). *Building Terrestrial Planets*. Annual Review of Earth and Planetary Sciences **40**, pp. 251–275.
- Morbidelli, A. and Nesvorný, D. (1999). *Numerous Weak Resonances Drive Asteroids toward Terrestrial Planets Orbits*. Icarus **139**, pp. 295–308.
- Muironen, K. (1998). *Discovery and follow-up simulations for small Earth-crossing asteroids*. Planetary and Space Science **46**, pp. 291–297.
- Murison, M. A. (1989). *On an efficient and accurate method to integrate restricted three-body orbits*. Astronomical Journal **97**, pp. 1496–1509.
- Murray, C. D. and Dermott, S. F. (1999). *Solar System Dynamics*. Cambridge University Press.
- Murray, N., Holman, M., and Potter, M. (1998). *On the Origin of Chaos in the Asteroid Belt*. Astronomical Journal **116**, pp. 2583–2589.
- Nacozy, P. E. (1971). *The Use of Integrals in Numerical Integrations of the N-Body Problem*. Astrophysics and Space Science **14**, pp. 40–51.
- Nesvorný, D. and Morbidelli, A. (1998a). *An Analytic Model of Three-Body Mean Motion Resonances*. Celestial Mechanics and Dynamical Astronomy **71**, pp. 243–271.
- Nesvorný, D. and Morbidelli, A. (1998b). *Three-Body Mean Motion Resonances and the Chaotic Structure of the Asteroid Belt*. Astronomical Journal **116**, pp. 3029–3037.
- Novaković, B. (2013). *Orbital and Dynamical Characteristics of Small Bodies in the Region of Inner Planets*. In: V. Badescu (editor), *Asteroids: Prospective Energy and Material Resources*, pp. 45–79. Springer.
- Öpik, E. J. (1976). *Interplanetary encounters: close-range gravitational interactions*. Elsevier Scientific Publishing.
- Pilat-Lohinger, E., Süli, Á., Robutel, P., and Freistetter, F. (2008). *The Influence of Giant Planets Near a Mean Motion Resonance on Earth-like Planets in the Habitable Zone of Sun-like Stars*. Astrophysical Journal **681**, pp. 1639–1645.
- Press, W. H., Teukolsky, S. A., Vetterling, W. T., and Flannery, B. P. (1992). *Numerical recipes in C. The art of scientific computing*. Cambridge University Press, 2nd edition.
- Quinn, T. and Tremaine, S. (1990). *Roundoff error in long-term planetary orbit integrations*. Astronomical Journal **99**, pp. 1016–1023.

- 
- Rabinowitz, D. L., Bowell, E., Shoemaker, E. M., and Muinonen, K. (1994). *The Population of Earth-crossing Asteroids*. In: T. Gehrels, M. S. Matthews, and A. M. Schumann (editors), *Hazards Due to Comets and Asteroids*, pp. 285–312.
- Reddy, V., Nathues, A., Gaffey, M. J., and Schaeff, S. (2011). *Mineralogical characterization of potential targets for the ASTEX mission scenario*. *Planetary and Space Science* **59**, pp. 772–778.
- Reyes-Ruiz, M., Chavez, C. E., Aceves, H., Hernandez, M. S., Vazquez, R., and Nuñez, P. G. (2012). *Dynamics of escaping Earth ejecta and their collision probabilities with different Solar System bodies*. *Icarus* **220**, pp. 777–786.
- Rickman, H. (2010). *Cometary Dynamics*. In: J. Souchay and R. Dvorak (editors), *Lecture Notes in Physics*, volume 790, pp. 341–399. Springer.
- Roncoli, R. B. (2005). *Lunar Constants and Models Document*. JPL Technical Document D-32296 .
- Saff, E. B. and Kuijlaars, A. B. J. (1997). *Distributing many points on a sphere*. *The Mathematical Intelligencer* **19**(1), pp. 5–11.
- Scheeres, D. J., Durda, D. D., and Geissler, P. E. (2002). *The Fate of Asteroid Ejecta*. In: W. F. Bottke, A. Cellino, P. Paolicchi, and R. P. Binzel (editors), *Asteroids III*, pp. 527–544. University of Arizona Press.
- Schmadel, L. D. (2012). *Dictionary of Minor Planet Names*. Springer, 6th edition.
- Schwarz, R. and Dvorak, R. (2012). *Trojan capture by terrestrial planets*. *Celestial Mechanics and Dynamical Astronomy* **113**, pp. 23–34.
- Shevchenko, V. G. and Mohamed, R. A. (2005). *Spacecraft exploration of asteroids*. *Solar System Research* **39**, pp. 73–81.
- Shoemaker, E. M., Williams, J. G., Helin, E. F., and Wolfe, R. F. (1979). *Earth-crossing asteroids - Orbital classes, collision rates with earth, and origin*. In: T. Gehrels (editor), *Asteroids*, pp. 253–282.
- Simó, C., Gómez, G., Jorba, A., and Masdemont, J. (1995). *The bicircular model near the triangular libration points of the RTBP*. In: A. E. Roy and B. A. Steves (editors), *From Newton to Chaos. Modern Techniques for Understanding and Coping with Chaos in N-Body Dynamical Systems, NATO ASI Series B: Physics*, volume 336, pp. 343–370. Plenum Press.
- Steel, D. (1998). *Distributions and moments of asteroid and comet impact speeds upon the Earth and Mars*. *Planetary and Space Science* **46**, pp. 473–478.

- Steel, D. I. (1995). *Collisions in the Solar system - VI. Terrestrial impact probabilities for the known asteroid population*. Monthly Notices of the RAS **273**, pp. 1091–1096.
- Steel, D. I. and Baggaley, W. J. (1985). *Collisions in the solar system. I - Impacts of the Apollo-Amor-Aten asteroids upon the terrestrial planets*. Monthly Notices of the RAS **212**, pp. 817–836.
- Stiefel, E. L. and Scheifele, G. (1971). *Linear and Regular Celestial Mechanics: Perturbed Two-body Motion, Numerical Methods, Canonical Theory*. Grundlehren der mathematischen Wissenschaften. Springer.
- Stumpff, K. (1965). *Himmelsmechanik. Bd.2: Das Dreikörperproblem*. Hochschulbuecher für Physik. VEB Deutscher Verlag der Wissenschaften.
- Szebehely, V. (1967). *Theory of orbits. The restricted problem of three bodies*. Academic Press.
- Taff, L. G. (1985). *Celestial mechanics: A computational Guide for the Practitioner*. Wiley-Interscience.
- Tholen, D. J. (1989). *Asteroid taxonomic classifications*. In: R. P. Binzel, T. Gehrels, and M. S. Matthews (editors), *Asteroids II*, pp. 1139–1150.
- Touma, J. and Wisdom, J. (1994). *Evolution of the Earth-Moon system*. Astronomical Journal **108**, pp. 1943–1961.
- Tsiganis, K., Gomes, R., Morbidelli, A., and Levison, H. F. (2005). *Origin of the orbital architecture of the giant planets of the Solar System*. Nature **435**, pp. 459–461.
- Valsecchi, G. B., Milani, A., Gronchi, G. F., and Chesley, S. R. (2003). *Resonant returns to close approaches: Analytical theory*. Astronomy & Astrophysics **408**, pp. 1179–1196.
- Vokrouhlický, D., Milani, A., and Chesley, S. R. (2000). *Yarkovsky Effect on Small Near-Earth Asteroids: Mathematical Formulation and Examples*. Icarus **148**, pp. 118–138.
- Walser, H. (2011). *Statistik für Naturwissenschaftler*. Uni-Taschenbücher. Haupt GmbH.
- Weidenschilling, S. J. (2011). *Initial sizes of planetesimals and accretion of the asteroids*. Icarus **214**, pp. 671–684.
- Wetherill, G. W. (1979). *Steady state populations of Apollo-Amor objects*. Icarus **37**, pp. 96–112.
- Williams, J. G., Sinclair, W. S., and Yoder, C. F. (1978). *Tidal acceleration of the moon*. Geophysical Research Letters **5**, pp. 943–946.

- Wisdom, J. (1982). *The origin of the Kirkwood gaps - A mapping for asteroidal motion near the 3/1 commensurability*. *Astronomical Journal* **87**, pp. 577–593.
- Yeomans, D. K. and Chodas, P. W. (1994). *Predicting Close Approaches of Asteroids and Comets to Earth*. In: T. Gehrels, M. S. Matthews, and A. M. Schumann (editors), *Hazards Due to Comets and Asteroids*, pp. 241–258.
- Yoshida, H. (1993). *Recent Progress in the Theory and Application of Symplectic Integrators*. *Celestial Mechanics and Dynamical Astronomy* **56**, pp. 27–43.
- Yue, Z., Johnson, B. C., Minton, D. A., Melosh, H. J., Di, K., Hu, W., and Liu, Y. (2013). *Projectile remnants in central peaks of lunar impact craters*. *Nature Geoscience* **6**, pp. 435–437.



# Acknowledgements

I am grateful to the University of Vienna and Dr. Christian Koeberl and Rudolf Dvorak for the opportunity to be a member of the Doctoral School (IK) “Planetology: From Asteroids to Impact Craters” at the Department of Lithospheric Research, University of Vienna.

I want to thank especially my PhD advisor Dr. Rudolf Dvorak for all his patience and goodwill while this thesis was still work in progress. He was ever supporting and motivating me to do yet another step.

Personally, I am proud to be a member of the AstroDynamics group, where so many people were helping me. First of all I want to appreciate the help of Christoph Lhotka, Thomas Maindl and Richard Schwarz in reading parts of the manuscript and helping to improve it. I also owe thanks to these same people plus David Bancelin, Siegfried Ettl, Barbara Funk, Mattia Galiazzo, Markus Gyergyovits, Elke Pilat-Lohinger, and others for numerous informative discussions.

Last but not least I acknowledge funding by the IK at the University of Vienna and FWF projects P-22603 and P-23810. I also thank Elke Pilat-Lohinger and Richard Schwarz for additional financial support.

My parents and my brother have always been ready to encourage me and to support me mentally in any possible way. To them I send my very deepest thank you!



---

# Curriculum Vitae

## Personal data

Name (First, Last)	Ákos Bazsó
Place of birth	Cluj, Romania
Citizenship	Austria
E-Mail	akos.bazso@univie.ac.at

## Education

2010 – today	PhD studies in Astronomy & Astrophysics at the University of Vienna
March 2008	Master of Science in Astronomy, diploma thesis: “Störungsrechnung mit Lie-Reihen” (Perturbation theory with Lie-series)
2001 – February 2008	graduate studies in Astronomy at the University of Vienna
June 2001	high-school (Realgymnasium) in Vienna, Austria

## Conferences and Meetings (contribution type)

September 2013 (Poster)	6 <sup>th</sup> International Meeting on Celestial Mechanics (CELM-EC VI) in San Martino al Cimino, Viterbo, Italy
January 2013	1 <sup>st</sup> AstroNet-II training school in Rome, Italy
September 2012 (Talk)	6 <sup>th</sup> Workshop of Young Researchers in Astronomy & Astrophysics in Budapest, Hungary
July 2012	2 <sup>nd</sup> International Summer School on Scientific Computing in Waidhofen/Ybbs, Austria
March 2012 (Poster)	43 <sup>rd</sup> Lunar and Planetary Science Conference in The Woodlands – Houston, USA
September 2011 (Talk)	Journées 2011 in Vienna, Austria
March 2011 (Talk)	8 <sup>th</sup> Alexander von Humboldt Colloquium on Celestial Mechanics in Bad Hofgastein, Austria
May 2010 (Talk)	École thématique du CNRS en Mécanique Céleste in Cusac, France

---

April 2010 (Talk)	5 <sup>th</sup> Austrian-Hungarian Workshop on Celestial Mechanics in Vienna, Austria
September 2009 (Poster)	5 <sup>th</sup> International Meeting on Celestial Mechanics (CELMEC V) in San Martino al Cimino, Viterbo, Italy
March 2008	7 <sup>th</sup> Alexander von Humboldt Colloquium on Celestial Mechanics in Bad Hofgastein, Austria
March 2007	École thématique du CNRS en Mécanique Céleste in Bad Hofgastein, Austria
May 2006	Meeting on Asteroids and Comets in Europe (MACE) in Vienna, Austria
June 2005	4 <sup>th</sup> Austrian-Hungarian Workshop on Celestial Mechanics in Budapest, Hungary

### **Research experience**

October 2014 – January 2015	Scientific project staff in FWF project P-22603-N16 “Exoplanetary systems: architecture, evolution, habitability” at the Institute of Astrophysics, University of Vienna
November 2013 – April 2014	Scientific project staff in FWF project P-23810-N16 “Dynamics of co-orbital planets in double-stars” at the Institute of Astrophysics, University of Vienna
March 2010 – April 2013	Scientific assistant in doctoral school “Planetology: From Asteroids to Impact Craters” at the Department of Lithospheric Research, University of Vienna
June 2009 – January 2010	continuation of work on FWF project P-18930 at the Institute of Astronomy, University of Vienna
July 2006 – June 2007	Scientific project staff in FWF project P-18930 “Effective stability of equilateral Lagrange-points” at the Institute of Astronomy, University of Vienna

## Refereed publications

- Bazsó, Á., Dvorak, R., Pilat-Lohinger, E., Eybl, V., and Lhotka, C. (2010). *A survey of near-mean-motion resonances between Venus and Earth*. *Celestial Mechanics and Dynamical Astronomy* **107**, pp. 63–76.
- Bazsó, Á., Schwarz, R., Érdi, B., and Funk, B. (2013). *Stability of librational motion in the spatial circular restricted three-body problem for high inclinations and mass ratios*. *Astronomische Nachrichten* **334**, pp. 1008–1011.
- Dvorak, R. and Bazsó, Á. (2008a). *On the Stability of the Lagrange Points: Analytical and Numerical Results*. *Nonlinear Phenomena in Complex Systems* **11**, pp. 177–183.
- Dvorak, R. and Bazsó, Á. (2008b). *The search for extrasolar planets with BRITTE*. *Communications in Asteroseismology* **152**, pp. 166–174.
- Dvorak, R. and Bazsó, Á. (2011). *The Three Trojan Problem*. *International Journal of Bifurcation and Chaos* **21**(08), pp. 2235–2243.
- Dvorak, R., Bazsó, Á., and Zhou, L.-Y. (2010). *Where are the Uranus Trojans?* *Celestial Mechanics and Dynamical Astronomy* **107**, pp. 51–62.
- Galiazzo, M. A., Bazsó, Á., and Dvorak, R. (2013a). *Fugitives from the Hungaria region: Close encounters and impacts with terrestrial planets*. *Planetary and Space Science* **84**, pp. 5–13.
- Galiazzo, M. A., Bazsó, Á., Huber, M. S., Losiak, A., Dvorak, R., and Koeberl, C. (2013b). *A statistical dynamical study of meteorite impactors: A case study based on parameters derived from the Bosumtwi impact event*. *Astronomische Nachrichten* **334**, pp. 936–939.
- Grandl, W. and Bazsó, Á. (2013). *Near Earth Asteroids - Prospection, Orbit Modification, Mining and Habitation*. In: V. Badescu (editor), *Asteroids: Prospective Energy and Material Resources*, pp. 415–438. Springer.
- Posch, T., Aspaas, P. P., Bazsó, Á., and Müller, I. (2013). *Austrian-Hungarian Astronomical Observatories Run by the Society of Jesus at the Time of the 18th Century Venus Transits*. *Journal of Astronomical Data* **19**, pp. 121–130.
- Schwarz, R., Bazsó, Á., Érdi, B., and Funk, B. (2012). *Stability of the Lagrangian point  $L_4$  in the spatial restricted three-body problem - application to exoplanetary systems*. *Monthly Notices of the Royal Astronomical Society* **427**, pp. 397–402.
- Schwarz, R., Bazsó, Á., Érdi, B., and Funk, B. (2014). *Stability and secondary resonances in the spatial restricted three-body problem for small mass ratios*. *Monthly Notices of the Royal Astronomical Society* **443**, pp. 2437–2443.

Schwarz, R., Funk, B., and Bazsó, Á. (2013). *New insights into the stability of  $L_4$  in the spatial restricted three-body problem*. Monthly Notices of the Royal Astronomical Society **436**, pp. 3663–3667.

## Non-refereed publications

Aspaas, P. P., Posch, T., Müller, I., and Bazsó, Á. (2014). *Astronomische Observatorien der Jesuiten in der “Provincia Austriae” im 18. Jahrhundert*. In: W. R. Dick and D. Fürst (editors), *Acta Historica Astronomiae*, volume 52, pp. 89–110.

Bazsó, Á. (2012). *Lunar Effects on Close Encounters of Near Earth Asteroids*. In: *Lunar and Planetary Institute Science Conference Abstracts, Lunar and Planetary Inst. Technical Report*, volume 43, p. 1809.

Bazsó, Á. and Dvorak, R. (2011). *Dynamics of possible Uranus Trojans*. In: Á. Süli (editor), *Publications of the Astronomy Department of the Eötvös University*, volume 20, pp. 5–14.

Bazsó, Á. and Galiazzo, M. (2012). *Lunar effects on close encounters of hungaria asteroids and near-Earth asteroids with the Earth*. In: H. Schuh, S. Böhm, T. Nilsson, and N. Capitaine (editors), *Proceedings of the Journées 2011 “Systèmes de référence spatio-temporels”*, pp. 217–220.

Dvorak, R. and Bazsó, Á. (2011). *The Three Trojan Problem*. In: Á. Süli (editor), *Publications of the Astronomy Department of the Eötvös University*, volume 20, pp. 15–22.

Galiazzo, M. A., Bazsó, Á., and Dvorak, R. (2012). *Fugitives from the Hungaria region: close encounters and impacts with terrestrial planets*. ArXiv e-prints **1210.1418**.

Galiazzo, M. A., Bazsó, Á., and Dvorak, R. (2014). *The Hungaria Asteroids: close encounters and impacts with terrestrial planets*. *Memorie della Societa Astronomica Italiana Supplementi* **26**, pp. 38–46.

Grandl, W. and Bazso, A. (2014). *Near Earth Asteroids- Prospection, Orbit Modification and Mining*. European Planetary Science Congress 2014 Abstracts **9**, p. 245.

Vienna, March 2015